G LUXFORD

EXPERIMENTAL AND MODELLING INVESTIGATION OF THE DEFORMATION, DRAG AND BREAK-UP OF DRIZZLE DROPLETS SUBJECTED TO STRONG AERODYNAMIC FORCES IN RELATION TO SLD AIRCRAFT ICING

SCHOOL of ENGINEERING

PhD THESIS

SCHOOL of ENGINEERING

PhD THESIS

Academic Year 2004 - 2005

G LUXFORD

Experimental and Modelling Investigation of the Deformation, Drag and Break-up of Drizzle Droplets Subjected to Strong Aerodynamics Forces in Relation to SLD Aircraft Icing

Supervisor: D W Hammond

March 2005

This thesis is submitted in partial fulfilment of the requirements for the degree of Doctor of Philosophy

© Cranfield University 2005. All rights reserved. No part of this publication may be reproduced without the written permission of the copyright owner

Abstract

The distortion, drag and break-up of drizzle droplets subjected to strong aerodynamic forces was investigated to understand the pre-impact behaviour of droplets in aircraft icing from supercooled freezing drizzle. The objective was to obtain a formulation and data for the drag properties of droplets distorted by the aerodynamic forces, which were beyond the scope of available experimental and modelling methods.

A practical and efficient semi-empirical computer model was developed for small water droplets in air, 100µm < D < 500µm, at moderate Reynolds numbers, 350 < Re < 1500, and high Weber numbers 3 < We < 20. This used available experimental terminal velocity data for free-falling droplets, extrapolated to higher Weber numbers, and the numerical solution for sessile droplets on a horizontal unwettable surface, with corrections for the Reynolds number.

A theory for bag break-up was developed based on the Rayleigh-Taylor instability of the windward droplet surface. The critical Bond number was 13.7, with a critical diameter of 10.1mm for free-falling water droplets, compared to the experimental value of 10mm diameter. The equivalent Weber number was 14.2 for free falling water droplets.

Aerodynamic interaction between the closely-spaced droplets from a vibrating nozzle droplet generator resulted in irregular spacing and coalescence of droplets. In an alternative design a laminar jet impinged on a rotating slotted disk to achieve the necessary droplet spacing, but the significant size variability of the droplets degraded the experimental measurements.

High-speed videos, to 50,000pps, and photographs were obtained of droplet distortion, break-up, coalescence and splashes using a high-intensity LED strobe flash.

A specially-designed convergent wind tunnel was developed for experimental measurements, to validated the drag model and provide data for droplets distorted by aerodynamic forces. The convergent profile produced a rapidly-increasing Weber number at a sufficiently slow rate to avoid transients or droplet vibrations.

A special instrument was developed, with three equispaced parallel laser beams and photo detectors, to determine the droplet velocity and acceleration. Droplet drag characteristics were measured up to Weber numbers of 16.

Good agreement was obtained between droplet drag model and experimental results. The greatest discrepancy was about 20% at a Weber number of about 8.

Note:- This thesis is available as a PDF file from the Cranfield University Library, www.cranfieldlibrary.cranfield.ac.uk, or Icing Group, Cranfield University, Bedfordshire MK43 0AL, UK, Tel +44 (0)1234 750 111. www.cranfield.ac.uk/contact.htm .

.

Table of Principal Sections and Chapters

Abstract.....i
Table of Principal Sections and Chapters.....ii
Table of Contents.....iii
List of Figures.....vii
List of Tables.....xiii
Acknowledgments.....xiv
Author's Background.....xv
Nomenclature.....xv
Structure of the Thesis.....xvii
Overview.....1
Chapter 1: Distortion, Drag and Break-up of Droplets.....13
Overall Conclusions.....49
Chapter 2: Scaling and Transient issues.....51
Chapter 3: Drag Model for Deformable Droplets.....61
Chapter 4: Imaging and Evaluation of Droplets.....91
Chapter 5: Measurement and Evaluation of Droplet Velocity and Acceleration.....97
Chapter 6: Droplet Distortion Modelling.....103
Chapter 7: Approximate Evaluation of Bag Break-up.....115
Chapter 8: Development of Simulation for Droplet Motion Dynamics.....121
Chapter 9: Design of Droplet Research Tunnel.....133
Chapter 10: Air Flow Calculation for Convergent Droplet Tunnel.....143
Chapter 11: Calibration of Convergent Droplet Tunnel.....157
Chapter 12: Development of Droplet Generator.....163
Chapter 13: Instrumentation to measure Droplet Velocity and Acceleration.....171
Chapter 14: Derivation for Determining Droplet Velocity and Acceleration.....179
Chapter 15: Development of the Strobe Flash Light.....185
References, Bibliography and Literature.....193
End.....209

– –

Table of Contents

Abstract i
Table of Principal Sections and Chapters ii
Table of Contents iii
List of Figures vii
List of Tables xiii
Acknowledgments xiv
Author's Background xv
Nomenclature xv
Structure of the Thesis xvii
Overview 1
The Roselawn Incident 1
The Cranfield Main Icing Tunnel 1
The Vertical Tunnel 3
Relevance of Droplet Distortion to SLD Icing. 4
Scale and Transient Issues 4
The need for Drag Data, or Formulation, for Distorted Droplets 5
Development of a Droplet Drag Computer Model 5
Experimental Drag Measurement and Model Verification 8
Conclusions 12
Chapter 1: Distortion, Drag and Break-up of Droplets. 13
Reasons for and Objective of the Investigation 13
Icing Tunnel Facilities 14
Need for Droplet Drag Data for Numerical Modelling 14
Use of Dimensionless Parameter Groups 15
What is drag 20
Effect of Turbulence in the surrounding flow 20
Conditions of Interest to SLD Icing 20
Literature Survey and References 21
The Difficulties with determining drag for deformable droplets 23
Scaling and Transient Issues 30
Organisation of the Investigation 31
Development of simulation for droplet motion dynamics 31
Development of the droplet drag model 32

Development of the experimental facilities 36
LED Flash Light development 39
Instrument for measuring droplet acceleration and velocity 40
Other Measuring Errors 41
Experimental measurements 43
Comparison between the drag model and experiment 45
Outcomes of the Investigation 48
Overall Conclusions 49
Further Work 50
Chapter 2: Scaling and Transient issues 51
Scaling effects on droplet motion 52
Scaling effects on droplet transient response 55
Simulation of droplet dynamic conditions 56
Conclusions 60
Chapter 3: Drag Model for Deformable Droplets. 61
Introduction 61
Definition of Drag 61
Turbulence Length Scale 62
Drag Data for Spherical Droplets 63
Drag on a flat circular disk normal to airflow 65
Drag Data for Distorted Droplets 66
Survey of the droplet literature 67
Evaluation of free-falling droplet data 69
Interpretation of data for free-falling droplets 71
Extrapolation and Representation of the free-fall data. 71
Analysis of free-falling spheres 74
Drag correction factor in relation to free-falling droplets 76
Issues related to droplet size and Reynolds number 78
Revised drag model for deformable droplets 81
Computing drag for other droplet sizes 86
Results and Sensitivity of the Droplet Drag Model 87
Conclusions 90
Chapter 4: Imaging and Evaluation of Droplets 91
Introduction 91

Development of an Imaging system 91
Application of the Imaging System 93
Video Image Sequences..... 94
Single Shot photographs 95
Conclusions 96
Chapter 5: Measurement and Evaluation of Droplet Velocity and Acceleration. 97
Introduction 97
Equipment..... 97
Method of Measurement..... 99
Evaluation of the Results..... 101
Conclusions 102
Chapter 6: Droplet Distortion Modelling 103
The issues 103
Sessile droplet model..... 105
Use of surface equations with CFD analysis 106
Comparison of Droplet Distortion by Weber number 110
Conclusions 113
Chapter 7: Approximate Evaluation of Bag Break-up 115
The Rayleigh-Taylor Instability Model..... 115
Numerical Solution..... 117
Conclusion 120
Chapter 8: Development of Simulation for Droplet Motion Dynamics 121
Method of analysis..... 121
Numerical Solution of Equations 121
4th order Runge-Kutta solution method 123
Changing the independent variable 124
Computation at fixed-distance intervals 125
Stability criterion for the numerical solution..... 125
Determining the Overall Airflow 126
Alternative Mode of operation 128
Determining the Droplet Drag force..... 128
Vertical Tunnel Analysis 129
Droplet Heat Transfer..... 129
Principal Subprograms for the droplet simulation program 130

Chapter 9: Design of Droplet Research Tunnel.....133
Introduction 133
Tunnel Configuration 133
The Diffuser..... 134
Diffuser Flow Stability 135
The Fan Requirement 136
Convergent Working Section 137
Plenum Chamber 138
Plenum Chamber Inlet Screen 139
Flow Straightener 141
Support Bench 142
Fan Specification 142
Chapter 10: Air Flow Calculation for Convergent Droplet Tunnel.....143
Convergent Nozzle Flow Calculations 143
Flow Validation 146
Convergence Correction..... 147
Verification of the convergent tunnel airflow calculations 151
Droplet Tunnel Contraction Profile 153
Excel VBA macro for Nozzle Calculations..... 154
Excel VBA Macro for convergent tunnel flow correction 155
Chapter 11: Calibration of Convergent Droplet Tunnel.....157
Determination of Air Velocity..... 158
Other potential errors..... 161
Conclusions 162
Chapter 12: Development of Droplet Generator 163
Introduction 163
Principles of operation..... 163
Hardware Implementation 165
Droplet Coalescence..... 166
Electrostatic Removal of Surplus Droplets 167
Alternative Droplet Generator..... 167
Using the spinning disk droplet generator..... 169
Chapter 13: Instrumentation to measure Droplet Velocity and Acceleration.....171
Introduction 171

The Methods used 171
The Diode Laser Unit 172
Photo Detector unit 174
Example Measurement Results 175
Typical result file from the droplet measurement 178
Chapter 14: Derivation for Determining Droplet Velocity and Acceleration 179
Droplet Acceleration Measurement 179
More detailed acceleration analysis 181
Constant Acceleration 181
Constant rate of change of acceleration with time 183
Chapter 15: Development of the Strobe Flash Light 185
Introduction 185
Images from a Single Flash 186
Improved LED Driver 188
Use of LED flash unit with high-speed Video 191
References, Bibliography and Literature 193
End 209

- -

List of Figures

Figure 1: Under view of an ATR72 turboprop aircraft. 1
Figure 2: Cross-section of the main icing tunnel, shown with Dr Hammond to scale 2
Figure 3: Convergent entry (left) to 760mm square working section (right) 2
Figure 4: The Vertical Wind Tunnel 3
Figure 5: Typical droplet deformation for a Weber number of 8. 3
Figure 6: Transient distortion of a droplet 5
Figure 7: High-speed video of a droplet bag break-up 6
Figure 8: Example of droplets obtained from a vibrating nozzle generator. 8
Figure 9: Spinning disc droplet generator. 8
Figure 10: Convergent Droplet Tunnel with Plenum chamber, Diffuser and Fan 9
Figure 11: LED flash unit with 80mm Collimating Lens 10
Figure 12: Arrangement for measurement of droplet velocity and acceleration 11
Figure 13: The Vertical Wind Tunnel 14
Figure 14: The Main Horizontal Refrigerated Icing Tunnel. 14

Figure 15: Relationship between droplet size, Reynolds number and Weber number. 21
Figure 16: Properties of supercooled water. 26
Figure 17: Effect of Altitude on Air properties 26
Figure 18: Stream of uniform droplets produced with a vibrating nozzle generator. 28
Figure 19: Simulated measuring errors. 30
Figure 20: Typical distorted drops. 32
Figure 21: Droplet distortion in the stagnation region of vertical tunnel target for We ≈ 30 33
Figure 22: Typical shape of distorted droplets. 35
Figure 23: Picture of the droplet research tunnel 36
Figure 24: Droplet Generator, construction and appearance 37
Figure 25: Stream of 270µm droplets from vibrating nozzle droplet generator 37
Figure 26: Image of droplet formation at the exit of the droplet generator. 37
Figure 27: Irregular spacing and coalescence of droplets 38
Figure 28: Video of droplet coalescence 38
Figure 29: Effect of droplet spacing and Reynolds number on the drag coefficient. 38
Figure 30: Typical low-resolution droplet image pair from a PIV imaging system. 40
Figure 31: Preliminary test of LED flash light. 40
Figure 32: Typical droplet shapes 42
Figure 33: Three axis manipulator for droplet measuring instrumentation. 43
Figure 34: Tunnel flow calibration. 45
Figure 35: Comparison of Bond number measurements and computer model with Massey data 46
Figure 36: Comparison of Drag Coefficient measurements and computer model with Massey data 47
Figure 37: Deceleration of a sphere with a constant drag coefficient, Cd, in still air. 54
Figure 38: Air velocity approaching the stagnation region of a cylinder and NACA 0012 aerofoil 57
Figure 39: NACA0012 CFD inviscid flow 57
Figure 40: Transient loading on 200µm droplets 58
Figure 41: Droplet distortion in the stagnation region 59
Figure 42: Separation of Boundary Layer 62
Figure 43: Wake behind an object 62
Figure 44: Recirculation in the wake 62
Figure 45: Pressure distribution around a sphere. 62

Figure 46: Effect of turbulence on distribution of initially uniformly spaced droplets.. 63
Figure 47: Sphere drag data, from Boundary-Layer Theory, H. Schlichting..... 63
Figure 48: Sphere Drag Data, from Massey 1989, 6th Ed..... 64
Figure 49: Comparison of various Sphere drag data. 64
Figure 50: Distortion of free-falling droplets 65
Figure 51: Drag coefficients for Flat Circular Disks. 65
Figure 52: Test disk for drag measurement 65
Figure 53: Air flow over a flat circular disc for Re = 290..... 66
Figure 54: Drag correction derived from Kennedy and Roberts..... 67
Figure 55: Terminal free-fall velocity of water droplets in ambient air at 1g gravity.... 68
Figure 56: Drag on free-fall droplets against Reynolds number 71
Figure 57: Drag of free-fall droplets against Weber number 71
Figure 58: Extrapolation of data for free-falling water droplet in ambient air..... 72
Figure 59: Curve fitting for extrapolation of drag data for free-falling droplets..... 73
Figure 60: Curve fitting of drag data for free-falling droplets and We < 5.3..... 74
Figure 61: Original drag correction for high Weber no..... 76
Figure 62: Various droplet drag models using the drag correction method 78
Figure 63: Relationship between Weber number, Reynolds number and droplet size... 79
Figure 64: Droplet drag interpolation between spheres and disks..... 82
Figure 65: Drag Interpolation between a sphere and disk against Bond number..... 84
Figure 66: Ratio of Disk drag to Sphere drag coefficients. 84
Figure 67: Drag Interpolation against Droplet aspect ratio 85
Figure 68: Model results with Streeter disk drag data for 50 & 250μm droplets..... 88
Figure 69: Model results with the Massey disk drag data for 50 & 250μm droplets 88
Figure 70: Effect of the Disk Drag Data on the Droplet Drag..... 89
Figure 71: Drag discrepancy between droplet distortion models; Streeter data..... 89
Figure 72: Drag discrepancy between droplet distortion models; Massey data..... 89
Figure 73: Still Image of Jet Break-up and droplet formation 91
Figure 74: Astronomy camera with Extension Tubes and 135mm Lens. 92
Figure 75: Wind tunnel test with prototype LED flash and Astronomy camera..... 92
Figure 76: Various Droplet Images from the Astronomical Camera. 92
Figure 77: Setup for high-speed video imaging of droplets. 93
Figure 78: Setup for flash photography of droplets..... 93
Figure 79: Using calibration grid inside the tunnel 93

Figure 80: Close-up of 0.6mm pitch calibration grid 93
Figure 81: Image sequences of droplets 94
Figure 82: Bond number droplet distortion 94
Figure 83: Droplets with 2.86 times elongation 94
Figure 84: Typical images of distorted droplets 95
Figure 85: Distortion & break-up of droplets 95
Figure 86: Experimental arrangement for measuring droplet aerodynamic forces 97
Figure 87: Close-up view of the laser beam block and photo detectors 98
Figure 88: Precision Manometers 98
Figure 89: Laser beams intercepting the droplet stream and tunnel walls 98
Figure 90: Typical Signals from Oscilloscope 100
Figure 91: Typical signals after Normalisation 100
Figure 92: Typical Signals after alignment 101
Figure 93: Experimental drag results for 250μm droplets 102
Figure 94: Distorted shape of Sessile Droplets 108
Figure 95: Droplet distortion data, Clift, Grace and Weber 109
Figure 96: Linearised plot of Droplet Distortion for free-falling Droplets 110
Figure 97: View of distorted droplet 111
Figure 98: Droplet distortion in the stagnation region 115
Figure 99: Varying pressure distribution on a droplet 115
Figure 100: Sessile droplet model of instability 116
Figure 101: Piston stability in bottom of tank 116
Figure 102: Deflection of water interface 117
Figure 103: Large deflection of water interface 117
Figure 104: Stability limit against deflection 117
Figure 105: Diameter ratio for distorted droplets 118
Figure 106: Sessile droplet on PTFE 119
Figure 107: Thickness of Sessile Droplet 119
Figure 108: Terminal velocity of droplets 119
Figure 109: General arrangement of droplet research tunnel 133
Figure 110: Photograph of droplet research tunnel 134
Figure 111: Characteristics of a conical diffuser 135
Figure 112: Details of tunnel diffuser design 135
Figure 113: Diffuser flow stability. 136

Figure 114: Performance characteristics of the suction fan..... 137
Figure 115: Fan Geometry and Dimensions..... 137
Figure 116: Frame of wind tunnel working section. 138
Figure 117: Smoke Test in the convergent tunnel..... 138
Figure 118: Interior of the Plenum chamber 138
Figure 119: Enlarged view of fibre inlet screen 139
Figure 120: Pressure drop of tunnel and inlet screen 139
Figure 121: Inlet Screen Pressure loss vs. Flow Velocity 140
Figure 122: Improvements to tunnel flow stability 140
Figure 123: Flow straightener for tunnel entrance 141
Figure 124: Characteristics of Adiabatic Flow in a Convergent Tunnel..... 145
Figure 125: Convergence rate for iteration..... 145
Figure 126: Shape of Convergent Square Section Droplet Tunnel 146
Figure 127: CFD analysis of air velocity in the convergent droplet tunnel. 146
Figure 128: Comparison between Nozzle theory, CFD analysis and measured results 147
Figure 129: CFD flow analysis of the vertical tunnel 148
Figure 130: Area Correction for a Steeply-Convergent Tunnel 151
Figure 131: Comparison between CFD analysis and Simulation for Vertical Tunnel. 152
Figure 132: Pressure distribution in convergent tunnel from CFD analysis. 157
Figure 133: Comparison between the model predictions and pressure tappings 158
Figure 134: Direct plot of Air speed against Fan speed. 160
Figure 135: Tunnel velocity calibration against fan speed..... 161
Figure 136: Growth rate of surface ripples on a laminar jet..... 163
Figure 137: Development of surface wave and droplet formation..... 163
Figure 138: Delay of droplet formation without nozzle vibration..... 164
Figure 139: Irregular droplets formed without nozzle vibration 164
Figure 140: Droplet Generator, construction and appearance..... 165
Figure 141: Implementations of the droplet generator 165
Figure 142: Droplets being formed 165
Figure 143: Uniform droplet stream after becoming spherical. 165
Figure 144: Displacement of droplets due to airflow along the droplet stream. 166
Figure 145: Drag Interactions between Discs and Cylinders 166
Figure 146: Effect of droplet spacing and Reynolds number on the drag coefficient.. 166
Figure 147: Image sequence of droplet coalescence 167

Figure 148: Irregular droplets due to aerodynamic interactions..... 167
Figure 149: Typical arrangement for droplet deflection used in an ink-jet printer. 167
Figure 150: Spinning disc droplet generator. 168
Figure 151: Testing of spinning disc droplet generator..... 168
Figure 152: Droplets formed from the spinning slotted disc. 168
Figure 153: Stream of droplets produced by the spinning slotted disc. 168
Figure 154: Spinning slotted disc droplet generator..... 169
Figure 155: Arrangement for measurement of droplet velocity and acceleration..... 171
Figure 156: Triple laser mounting block 172
Figure 157: Dimensions and photograph of 1mW diode laser units 172
Figure 158: Alignment of diode lasers on milling machine bed 173
Figure 159: Arrangement for supporting and inverting the diode laser block. 173
Figure 160: Photograph of interior of photo detector unit..... 174
Figure 161: Diagram and results of the Whirling Wire test rig..... 174
Figure 162: Typical signals from the droplet measurement 175
Figure 163: Typical result obtained with droplet detector. 176
Figure 164: Measured droplet characteristics at high velocity. 177
Figure 165: Further result at high droplet velocity 177
Figure 166: Velocity vs. Time diagram for droplet 181
Figure 167: Droplet image obtained from strobe illumination with low-power LED.. 185
Figure 168: Initial wire image from a single LED flash..... 186
Figure 169: Test for evaluating LED response speed..... 186
Figure 170: Prototype LED flash unit and Starlight Express astronomy camera..... 186
Figure 171: Optical arrangement of Droplet Imaging 187
Figure 172: Test of LED flash unit and camera with resulting images at 100m/s. 187
Figure 173: Circuit diagram for LED flash unit 188
Figure 174: Circuit board layout 189
Figure 175: Component arrangement. 189
Figure 176: LED Flash unit, showing controls and collimation lens 189
Figure 177: Response of LED driver circuit 190
Figure 178: Whirling wire test at 100m/s with revised LED flash unit. 190
Figure 179: LED flash unit with Collimating Lens 191
Figure 180: Example of high-speed video imaging with the LED strobe flash unit. ... 191

List of Tables

Table 1: Comparison between experimental and calculated results for 250µm droplets45
Table 2; Sphere drag formulation; from Clift, Grace and Weber, table 5.2 64
Table 3: Drag coefficient formulation for a flat disk, data from Nakayama 1961 66
Table 4: Formulation for drag coefficient of a flat disk, from Massey, 1989. 66
Table 5: Terminal Velocities for free-falling Drops 70
Table 6: Terminal free-fall velocity of water droplets, from Scott 1964........................ 70
Table 7: Free-falling droplet drag properties in ambient conditions 74
Table 8: Procedure for calculating droplet drag coefficient 86
Table 9: Procedure for determining drag interpolation factor. 87
Table 10: Average Experimental Results 101
Table 11: Tunnel condition... 159

Acknowledgments

Many thanks to all those who helped with this research, without which it would not have been possible. In particular thanks to;

Paul Spooner and the CAA for their support and sponsorship of this research.

Thomas Bond and Dean Miller of NASA for the sponsorship of the LED flash lamp and their help and advice on this research and to Gene Hill of the FAA for his support.

My Tutor Dr David Hammond and the department head Professor Paul Ivey for their help, support and tolerance that enabled this research to be carried out.

Ingrid Howes and Sally Pearson of the departmental office for their help.

Professor Chris Freeman and Dr David Cameron for their help and advice on the research and in reviewing the thesis.

ADINA for the loan of their CFD and FEA computer software.

Dr Roland Schmehl of ESA for his extensive help, support and communications on the research issues and in providing many useful references.

Dr Jason Tan of Wichita University (formerly my Tutor at Cranfield) for his help and advice on the research.

Dr Joao Amaral Teixeira for the CFX analysis of the droplet wind tunnel and Robin Stanfield for CFD analysis of external airflow.

Dr Heather Almond at Cranfield for the etching of the slotted disks.

Dave Woodhouse and Kevin McEneny of Darchem for the flow straightener.

Steve Cooke of Linx Inkjet Printers for help with component parts.

Keith Hastings of EPSRC loan pool for use of the Phantom 7 high-speed video camera

Jolyon Cleaves of Photosonics for help with the Phantom 7 video camera.

Roger Groves for help and advice on optics and testing of the LED flash units.

Steve Markham for the electronic design and construction of the flash units.

Michael Hattey of Starlight Xpress Ltd. for help with the astronomy camera.

John Boaler of LaVision for the evaluation of high-speed imaging equipment.

John Witton, Mark Jermy, David Binks, Mathew Harrison, Helen Ford and all other colleagues at Cranfield University who provided valued help and advice.

Derek Brown, Alan Hutchings, Pat Sweeny, George Lipinski, Clive Wood and all other staff of the DMG Cranfield workshop, for help and advice with the development and construction of the experimental facilities.

Bernard Charnley, Brian Stapleton and Cranfield stores for various help and materials.

Professor Anthony Pearson for his support and helpful advice and guidance.

All others I have not mentioned who helped with this research, and

Finally to my Wife Rosemary for her tolerance and support through this research and to our cats Harrod, Stripey and Commy for their attention and distraction.

Author's Background

Prior to undertaking this research, to obtain his PhD at Cranfield University, the author previously had some forty-two years of experience in industry, of which the first five years were as an engineering apprentice. The rest were mostly concerned with research and development of various kinds, followed by three years at Cranfield University, with the PhD thesis submitted in 2005.

His qualifications include a 1st Hons. BSc in Mech. Eng. from The City University in 1974, followed by membership of the Institute of Mechanical Engineers and registration as a Chartered Engineer. Other qualifications included an HNC in Electronics and Computing.

After completing his engineering apprenticeship in 1965 and prior to starting at the City University in 1971, the author carried out development of heaters and furnaces at Calor Gas Engineering, and then research and development of artificial limbs for the Department of Health at Roehampton.

On finishing at the City University in 1974 he then carried out research into the Thermo-ElastoHydrodynamics of industrial rotary pump seals at the Tube Investments Research Laboratories, Hinxton Hall, near Cambridge, until 1977. He then continued applied Research and Development of pump seals for Crane Packing (now John Crane) and then at Borg Warner until 1986.

The author then carried out research and development of Laboratory equipment for Fisons Scientific Equipment, in particular the roto-dynamic stability of high-performance centrifuges. In 1988 he worked as a Principal Engineering Consultant for CREATE Ltd at Cranfield University for 4 years, then as an independent consultant.

Following a successful contract to develop a prototype spiral groove ink pump for Domino Inkjet Printing he joined the company in 1994 to continue the pump development and also carry out research for and development for inkjet printers and droplet generators.

In 2001 this was followed by a period with Inca Digital on the development of large format inkjet printers for large posters. He then joined Cranfield University in 2002 to support the development of the new Icing Wind Tunnel facilities and to carry out PhD research into aircraft icing issues, for which this is the thesis.

Nomenclature

CCD	=	Charge Coupled Detector
SLD	=	Supercooled Large Droplets
VeD	=	Volume Equivalent spherical diameter
VMD	=	Volume Mean spherical diameter
D	=	Droplet volume equivalent spherical diameter
De	=	Droplet equator diameter
h	=	Thickness, or length, of oblate droplet
U	=	Velocity of droplet, or velocity difference between air and droplet.

U_0	=	free stream velocity, or droplet velocity entering the stagnation region	
U_r	=	radial velocity towards cylinder	
U_θ	=	tangential velocity around cylinder	
R	=	cylinder or leading edge radius, or other aerofoil reference dimension	
r	=	distance from the cylinder axis	
θ	=	tangential angle from the stagnation line	
a, g	=	Acceleration and gravity respectively	
ρ, μ	=	Fluid density and viscosity respectively	
σ	=	Surface tension	
$_a$	=	Subscript for air	
$_d$	=	Subscript for droplet	
Bo	=	Bond number for VeD	$= (\rho_d - \rho_a).g.D^2/\sigma \approx \rho_d.g.D^2/\sigma$
			$= ¾\ We.Cd$
Cd	=	Drag coeff for droplet VeD.	$= F/(\pi.D^2.\rho_a.U^2/8)$
			$= {}^4/_3.(\rho_d - \rho_a).a.D/\rho_a.U^2 = {}^4/_3.Bo/We$
Ci	=	Interpolated drag coefficient	$= Cs^k.Cq^{(1-k)}$
Cq	=	Disk drag coefficient	
Cs	=	Sphere drag coefficient	
F	=	Drag force on a droplet	$= a.(\rho_d - \rho_a).\pi.D^3/6 = Cd.\rho_a.U^2.\pi.D^2/8$
La	=	Laplace number	$= \rho_a.\sigma.D / \mu_a^2$
			$= Re^2/We = 1/Oh^2$ (with gas properties)
k	=	Drag interpolation factor	$= Log_{10}(Ci/Cq) / Log_{10}(Cs/Cq)$
Mo	=	Morton number	$= g.\mu_a^4.(\rho_d - \rho_a)/\rho_a^2.\sigma^3 \approx g.\mu_a^4.\rho_d/\rho_a^2.\sigma^3$
			$= We^2.Bo/Re^4$
Oh	=	Ohnesorge No.	$= \mu_d/\sqrt{(\rho_d.\sigma.D)}$
Re	=	VeD Droplet Reynolds number	$= \rho_a.U.D/\mu_a$,
Rq	=	Reynolds number for De	$= \rho_a.U.De/\mu_a$,
R	=	Leading edge radius of aerofoil, or other relevant dimension	
T_d	=	Droplet oscillation period	$= (\pi/4).\sqrt{(\rho_d.D^3/\sigma)}$
t	=	time from entering the stagnation region	
x	=	distance travelled in the stagnation region	
t_t	=	R / U_0	
t_0	=	$({}^4/_3).(\rho_w / \rho_a).(D / (Cd.U_0))$	
x_0	=	$U_0.t_0$	
We	=	VeD Droplet Weber number	$= \rho_a.U^2.D/\sigma$,
We^2/Bo	=	Drag parameter for VeD	$= (\rho_a.U^4/g.\sigma).(\rho_a/\rho_d)$
			$\rightarrow$ 14.75 for free-fall drops
ρ_d/ρ_a	=	Density ratio	

Unless otherwise indicated the droplet dimensionless groups assume the VeD, or D, velocity difference between droplet and air, $Abs(U_a - U_d)$, and local air properties, ρ_a, μ_a.

Structure of the Thesis

This Thesis has, quite deliberately, not been written as a book to be read from cover to cover. It has a modular structure, with some similarities to the structure of a computer program, in which the main body, Chapter 1, is equivalent to the main program, with other Chapters equivalent to subprograms.

The thesis is intended to be a source of useful information concerning the various issues associated with the investigation of distortion, drag and break-up of liquid droplets subjected to strong aerodynamic forces, or any other application where relevant chapters of the thesis may be useful to other investigations.

There is first an overview of the investigation, explaining why the research was carried out, the primary issues considered and some conclusions. This has been written in as informal manner, as far as possible, for those who do not need, or wish, to consider the more technical aspects of the investigation.

There is then the "Main Body" of the thesis, Chapter 1. This gives a much more complete technical explanation of the research. It is intended to be useable as a stand-alone document, without reference to the other chapters. It does not give the full depth and completeness of explanation and derivations, so refers to the relevant chapters for a more complete discussion on particular issues.

The remaining chapters of the thesis each deal with a particular aspect of the investigation. There is no particular order to these chapters, since they are not intended to be read sequentially. However the first seven chapters are considered to be of the greatest relevance to this investigation. Otherwise the chapters have been arranged so that related chapters are grouped together. Some of the chapters are, by nature, quite technical and it was anticipated that these would only be read by someone who needs to fully understand the details of a particular issue, possibly to apply it to some other research. For various reasons these sections have been called Chapters, rather than Appendices, in part because these chapters could have their own appendices.

Each of these chapters is, so far as reasonably feasible, intended to be self-contained to its specific topic and can, within reason, be used independently of the rest of the thesis, but with cross-reference to other related chapters where necessary.

It is anticipated that the overview will be read first and then, as necessary, the "Main Body", Chapter 1, can be read, but other chapters will only be read if they are of specific interest and relevance to the reader.

It was also anticipated that some readers may only be interested in specific chapters, possibly for application to other research, so they will not be interested in any of the other discussion in the thesis and may only wish to study the particular chapters relevant to their application.

Note:- This thesis was prepared with Microsoft Word (2003) and then converted to a PDF file. A digital copy should be obtainable from the Cranfield University Library, www.cranfieldlibrary.cranfield.ac.uk, or Icing Group, Cranfield University, Bedfordshire MK43 0AL, England, Tel +44 (0)1234 750 111. www.cranfield.ac.uk/contact.htm.

Overview

The Roselawn Incident

On 31 October 1994, over Roselawn, Indiana, USA, an ATR72 turbo-prop aircraft, similar to that in Figure 1, was in a holding pattern at 8,000 to 10,000 feet, 2,400 to 3,000m. Unexpectedly the autopilot disengaged and, before the pilots could regain control, the aircraft rolled over, resulting in the loss of 68 people with the aircraft.

Figure 1: Under view of an ATR72 turboprop aircraft.

It was subsequently concluded that an important contributing factor was the accumulation of an ice ridge on the upper surface of the wing aft of the de-icing facilities, (NTSB/AAR-96/01, July 1996). This ice ridge so disturbed the airflow over the aileron surfaces that it caused the autopilot to disengage, after which the ailerons uncontrollably deflected to cause the loss of control. After a substantial investigation it was concluded that the ice accumulation had resulted from flying through supercooled drizzle.

While this kind of ice formation was already known, it seemed that, up to then, most understanding about aircraft icing had been related to freezing fog and clouds, where the size of the water droplets were much smaller, typically less than 100µm.

With supercooled drizzle, the droplets tend to be much larger, typically 100µm to 500µm diameter, with the range of 200µm to 300µm being of particular relevance. Since these are much larger than those in the more familiar cloud icing this is commonly referred to as Supercooled Large Droplet icing, otherwise known as SLD icing.

SLD icing droplets are large compared to clouds and fog droplets. They are, however, still very small compared to the more familiar rain drops, which are typically several mm in diameter, the size range considered in much of the previous droplet research.

Due to the Roselawn and other aircraft icing incidents, many SLD icing research investigations were started around the world. Because of the larger droplet size involved it was found that this icing process was very much more complex than for the small droplet icing. With larger droplets the surface tension force, which retained the droplet shape and integrity, tended to be less dominant. The dynamic response times also tended to increase, so it would take substantially longer for heat transfer on contact with the wing. The distortion and vibration responses also tended to be slower and it could be substantially more difficult to deflect the droplets from a straight-line ballistic motion.

The Cranfield Main Icing Tunnel

To investigate aircraft icing, various low temperature icing tunnel facilities were instigated by Professor Robin Elder and Dr Jason Tan at Cranfield University. After the basic facilities had been developed, the project came to a standstill. Professor Elder and Dr Tan left to take up other activities and, in March 2002, Dr David Hammond was recruited from British Aerospace to complete these developments. The author joined his icing team in April 2002 to help with the developments of these facilities whilst also carrying out related research for a PhD, for which this is the resulting thesis.

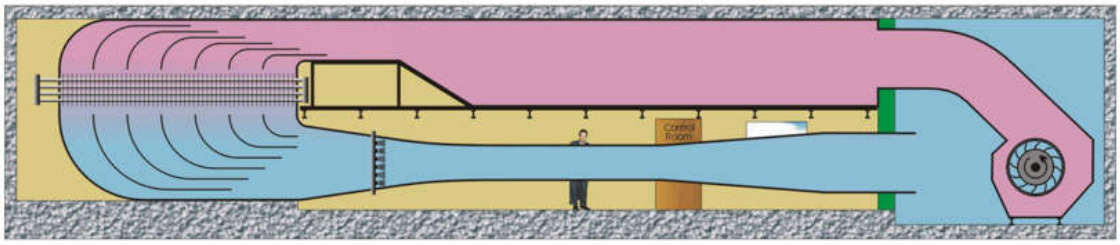

Figure 2: Cross-section of the main icing tunnel, shown with Dr Hammond to scale

One of the initial issues was to redesign the convergent entry to the main icing tunnel, shown in Figure 2 and Figure 3. This was required, since the initial design was found to have too steep a convergent rate for the larger droplets to follow the air flow. In this it was necessary to ensure that the droplet spray introduced into the low-velocity airflow would be accelerated to the required velocity, supercooled to the required temperature, and provide an adequate distribution of spray in the working section.

Figure 3: Convergent entry (left) to 760mm square working section (right)

To help with the design of the convergent entry, a computer simulation of the droplet motion dynamics and cooling was developed. This made use of a numerical simulation package, which the author had previously developed and used for many and various applications. One of these was to model the motion dynamics of ink droplets, when subjected to aerodynamic and electrostatic forces, in a continuous ink-jet printer. This was then adapted to model the motion dynamics of water droplets in a convergent wind tunnel. The main additional requirement was to model the airflow, which was achieved by treating the tunnel as a large convergent nozzle with 1D adiabatic compressible flow.

For this application the aerodynamic forces on the droplets were quite moderate and it was adequate to assume the droplets remained spherical, for which suitable data on the aerodynamic drag forces was available.

The Vertical Tunnel

A vertical convergent wind tunnel, Figure 4, was also being developed to accelerate droplets vertically downward to impact onto a splash target, where observations and measurements could be made. A requirement of this was to accelerate the larger droplets, up to 400µm diameter, to a velocity of up to 100m/s without them breaking up due to the aerodynamic accelerating force. The design study for this was carried out by Dr Tan, then at Wichita University, in particular to determine the contraction shape of the convergent tunnel.

Figure 4: The Vertical Wind Tunnel

The droplets were to be accelerated down the tunnel by the aerodynamic drag force in the higher-velocity airflow. For the droplets to be continuously accelerated, the air velocity had to be sufficiently greater than the droplets to maintain the necessary drag force. This required the tunnel cross-section to be continually contracting to maintain the necessary excess air velocity over the droplets.

An issue with this was the height of the tunnel and whether it would be able to fit within the available building height without any major difficulties. Hence it was beneficial to minimise the tunnel height.

In the tunnel design study by Dr Tan it was assumed that the droplets remained spherical, although it was known that the larger 400µm droplets would be significantly distorted, as shown in Figure 5, which shows a 5.8mm droplet falling through ambient air at terminal velocity. The distortion of the 400µm droplets in the vertical tunnel would have been similar, but inverted, due to aerodynamic forces accelerating the droplets down the tunnel.

Droplets distortion increased the air drag for two reasons;

1. The increased equator diameter and hence frontal area on which the aerodynamic pressure could act.
2. The sharper curvature at the equator causing the airflow to separate earlier, so reducing the flow recovery on the downwind side, thus giving a larger wake in relation to the equator diameter.

Figure 5: Typical droplet deformation for a Weber number of 8.

At the time it was known that such droplet distortion would be sufficient to increase its air drag by at least 30%, which meant that the vertical tunnel could have been significantly shorter in height.

With the subsequent droplet research it was found that the droplet air drag, for the relevant conditions, was at least 70% greater than for the spherical droplet assumption, so the vertical tunnel height may have been reduced by as much as 2 metres.

Using the simulation and the drag correction for droplet distortion, as then understood, the tunnel contraction profile was re-evaluated and it was found that this could have been at least a metre shorter in height whilst still achieving the required performance. A

difficulty with the analysis was the lack of suitable data or formulation for the effect of distortion on the droplet drag at the relevant conditions. It was realised that this could be a significant impediment in the design and development of equipment and facilities, like the vertical tunnel, involving such effects, and that such data was required.

Relevance of Droplet Distortion to SLD Icing.

It was deduced that the changes in air velocity in the flow field around an aircraft wing would be similar to those in the vertical tunnel, but this change would occur in a much shorter distance, with a steeper velocity gradient. As a result any droplets within the airflow would experience more extreme aerodynamic forces than in the vertical tunnel, which was designed to limit such forces. This could have a significant effect on the way that droplets behaved in the airflow around the aerofoil and hence could have a significant effect on the icing process in freezing drizzle.

The difficulty in this was that the droplets conditions in the airflow around an aerofoil were outside the scope of previous investigations, both in terms of the severity of conditions and the range of droplet sizes. While there was some data on the break-up criterion, it was not clear if that was relevant to the SLD icing conditions and there did not seem to be any available data on the drag properties for the relevant conditions and droplet size range.

At the time, the significance of this issue was not appreciated by the aircraft icing community, where the SLD icing models still assumed the droplets remained spherical. The suggestion that aerodynamic droplet distortion and break-up would have a significant effect was greeted with some scepticism. It would seem that part of the reason for the doubt was that such effects had not been observed in any of the high-speed imaging of droplets in scale model tests, such as the investigation by Gent, Ford, Moser and Miller (AIAA 2003-389). The reason for this was attributed to the fact that the thickness of the flow field around the small-scale aerofoil did not allow sufficient time for the droplets to respond to the aerodynamic forces, although some small amount of droplet deformation was noticed.

From this it was concluded that both Scaling and Transient effects were important in determining the behaviour of drizzle droplets in SLD icing. However it was not possible to fully investigate such effects. It was agreed that the investigation would, at least, consider the quasi-static behaviour of droplet distortion, drag and break-up. Some consideration was, however, given to the scaling and transient issues, as discussed below.

Scale and Transient Issues

It would seem that the prevailing view of SLD icing was that the momentum of the larger droplets would be such that aerodynamic forces would have little effect on them. The reasoning for this seemed to be based on observations and modelling with small-scale aerofoils, where the thickness of the aerofoil flowfield was not sufficient to significantly affect the droplets before they reached the aerofoil surface.

When the effect of the size and scale of the aerofoil was evaluated, it was found that this could have a substantial effect on the behaviour of the droplets, since a full scale aerofoil provides both the time and distance for the droplet distortion to have a substantial effect on their speed and trajectory, Chapter 2. It also indicated the possibility of the aerodynamic break-up of droplets before they reached the aerofoil surface, so the remnants might then be swept away in the airflow.

A further issue for the range of conditions relevant to SLD icing was that the amplitude and duration of the aerodynamic loading of the droplets could induce a dynamic and/or a vibration response in the droplets that could also cause droplet break-up. With scale-model testing the duration of these forces was often too short for such effects to be significant. In the vertical tunnel it was, however, found that the conditions were sufficient to cause significant droplet distortion, as shown in Figure 6 for a droplet approaching a target surface. It can be seen that this becomes increasingly distorted as it enters the more stagnant air near the target surface.

Figure 6: Transient distortion of a droplet

The need for Drag Data, or Formulation, for Distorted Droplets

Whilst various researchers had investigated the drag of distorted droplets several mm in size, they had not considered the more aggressive conditions experienced by the smaller droplets in SLD icing conditions.

For this research it was concluded that there would need to be two parallel paths to obtain the necessary formulation and data;

1. To develop and refine a useable, practical and efficient formulation of drag for distorted droplets, by combining and harmonising available data and analysis.
2. To develop test facilities to obtain experimental data so as to validate and refine the droplet drag formulation.

Development of a Droplet Drag Computer Model

The behaviour of a droplet depends on many factors, such as;

1. Aerodynamic drag force
2. Droplet size
3. Droplet velocity, relative to the air
4. Droplet acceleration, or gravity
5. Air density
6. Air viscosity
7. Surface tension
8. Droplet density
9. Droplet viscosity

Providing the droplet shape only changed reasonably slowly and there is no significant internal flow, then the droplet viscosity is not relevant.

Given no other forces on the droplet, the aerodynamic drag force had to equal the gravity force, or acceleration force where gravity was negligible. Hence there were seven relevant independent parameters to consider.

It was not reasonable to try to obtain an effective model by directly using all the parameters. To reduce them to a manageable number, the method of Dimensional Analysis was used. The Buckingham Pi theory states that the number of dimensional groups will be the number of parameters, seven, less the number of fundamental dimensions, mass, length and time. This indicated that there were four possible dimensional groups.

The air density and droplet density were dimensionally equivalent so could only be counted once, but the ratio of these densities provided a relevant parameter group.

This then left three independent parameter groups. These could take various forms, but the preferred ones were the Reynolds number, Weber number and Bond number.

There were a variety of other dimensionless parameters that were also used to help with the modelling, which were derived from a combination of the primary three parameter groups and the density ratio. These are explained in subsequent Chapters.

In the case of spherical droplets, or fixed shapes, the surface tension plays no role, so this only allows for two parameter groups, which are normally the Reynolds number and the drag coefficient. The drag coefficient could be obtained from the ratio of the Bond number and Weber number, which cancelled out the surface tension. For the purpose of this investigation, when a droplet was assumed to remain spherical it would still have a surface tension, even though this did not have any effect, hence the Weber number and Bond number could still be used for comparison with the deformable droplets.

The approach first considered was to use the well-established data for the drag force on a sphere and then see if it was possible to determine some correction factor for the droplet distortion in relation to this.

The one established source of suitable experimental data was that for water droplets falling through ambient air in normal gravity at terminal velocity. In this the Reynolds number and Weber number could be determined from the fall velocity and the Bond number could be determined from the gravity force.

As the droplet size increased it resulted in increasing distortion of the droplet. This enabled the effect of the distortion on the drag to be determined in relation to the drag on a sphere for the same conditions.

The initial drag model derived from data for free-falling droplets and spheres was used to design the convergent droplet tunnel for the experimental measurements. While this initial model contained discrepancies, it was sufficiently correct, for the conditions of interest, so as not to have any significant effect on the subsequent droplets experiments.

A limitation of the droplet free-fall data was that it was only available for a maximum Weber number of 11, at a Bond number of 8.4, Reynolds number of 4700 and droplet size of 8mm. Beyond this the flattened windward side of the droplet tended to become unstable, collapse inward to form a bubble on the downstream side, which would then result in the bag break-up of the droplet.

Figure 7 shows a high-speed video of this process with a droplet of around 270μm in the droplet wind tunnel. Both airflow and droplet were travelling from right to left.

Figure 7: High-speed video of a droplet bag break-up

It was, however, later found that if the aerodynamic force on the droplet was rapidly increasing, but not at such a rate to cause any transient shock or vibration of the droplet, then the droplet could remain intact in more severe conditions, at least to a Weber number of 16, and even more so in transient conditions, such as shown in Figure 6.

It was considered essential to obtain droplet drag data for higher Weber numbers. That, however, required the relevant drag data to design the experimental equipment needed to obtain that data. Hence an approximate formulation had to initially be used for this.

This difficulty was resolved by extrapolating the available data for free-falling droplets. Initially this was achieved by directly extrapolating a curve fitted to the data. Such a method can be uncertain if taken too far, but it provided a workable formulation which allowed the necessary tunnel design analysis to be carried out.

Subsequently a more effective method was developed for extrapolating and applying the available data.

The "Drag Correction" approach was found to be suitable for water droplets greater than about 1.3mm, since at low velocities, for Weber numbers less than 3, there was little distortion. The droplets could then be treated as spherical, in which the drag characteristics only depended on the Reynolds number. At high velocities, Weber numbers greater than 3, it was found that the Reynolds number had little effect and the drag correction, which mostly depended on the Weber number, so the data for free-falling droplets could be directly used.

For SLD icing the droplet size of most interest was between 200μm and 300μm. With such small droplets there could be significant effects from both the Reynolds number and the Weber number, so it was not possible to directly separate these effects.

It was realised that the free-falling droplet experiments provided the necessary data for other conditions, but required a means to reliably extrapolate this to higher Weber numbers and to apply a Reynolds number correction for smaller droplets.

It was found that by plotting the relationship between the Bond number and Weber number, for the free-falling droplets, in an appropriate way, the resulting curve asymptotically tended to a constant value above a Weber number of 10. Through various considerations it was concluded that, provided the droplets remained intact, this relationship would apply to higher Weber numbers for a near steady Weber number.

The other issue was to correct for the Reynolds number effects. In this it was reasoned that, with respect to the equator diameter of an oblate distorted droplet, the drag characteristics would, for the same equator Reynolds number, lie somewhere between that of a sphere and a flat circular disc perpendicular to the air flow. This could be represented as an interpolation factor between the sphere and disk.

The presumption made was that, for a given distorted shape, this interpolation factor would be independent of the Reynolds number. It was also concluded that the shape of a distorted droplet was primarily determined by the Bond number and that the Reynolds number was unlikely to have more than a minor effect on this shape. Given these assumptions, it was possible to combine the drag data for free-falling droplets, a droplet distortion model for the Bond number and the drag data for spheres and flat circular discs together to produce a semi-empirical computer model for the drag characteristics of deformable droplets for the required range of Reynolds numbers and Weber numbers.

Experimental Drag Measurement and Model Verification

To obtain the necessary experimental data and to verify the computer model it was necessary to obtain relevant experimental data. For the results to be dimensionally similar to the relevant SLD icing conditions, for both the Weber number and Reynolds number, it required droplets of a similar size, typically 200µm to 300µm diameter.

This would require the following facilities.

1. A means of generating calibrated droplets of the required size.
2. A means of subjecting these droplets to the required aerodynamic forces.
3. A means to image, observe and check the behaviour of the droplets.
4. A means to measure the droplet drag force and velocities of the air and droplets.

Droplet Generation

Initially the droplets were generated using a vibrating nozzle. This was capable of generating a very consistent stream of droplets that could be accurately calibrated for size, as shown in the top row of Figure 8.

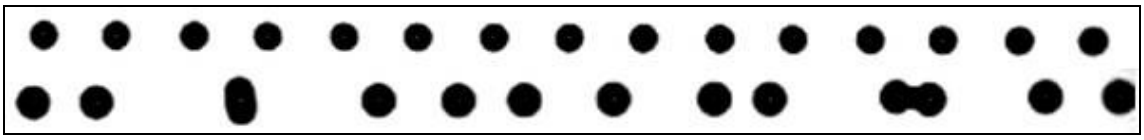

Figure 8: Example of droplets obtained from a vibrating nozzle generator.

As these droplets were accelerated in the airflow, the aerodynamic interactions between them caused them to become irregularly spaced, clump together and then coalesce into large droplets, the initial stages of which are shown in the bottom row of Figure 8.

This was the preferred way to generate calibrated droplets and it was possible to electrostatically remove the surplus droplets to increase the droplet spacing, so reducing aerodynamic interactions to prevent the coalescence. By the time it was possible to observe and understand this effect, it was, however, not possible to develop the necessary equipment, but that could be considered in further work to refine the method.

A remedial solution for producing droplets with the required spacing had to be quickly developed and the method used was to impinge a uniform jet of water onto a spinning slotted disk, as shown in Figure 9 The process of droplet generation is shown by the high-speed video sequence on the right side of Figure 9..

Figure 9: Spinning disc droplet generator.

While this produced droplets of the required spacing, the droplets were of irregular size. The frequency of droplets was known, so by weighing the droplets produced in a given time it was possible to determine the average droplet mass.

Conditioning the Droplets

For the droplet size of interest the earth's gravity was far too weak to create the necessary distortion forces. In practice acceleration in excess of 1000g was required. The possibility of using a centrifuge was considered, but the resulting droplet velocities would have introduced substantial and indeterminate Coriolis accelerations. Also it was likely that such a centrifuge would have to be quite large, and hence costly, to construct.

The method adopted was to try to approximate the equivalent SLD icing conditions experienced by droplets of the required size in the vicinity of an aerofoil. For this investigation it was preferable to avoid curvilinear motion and to minimise transient effects, but it was necessary that the droplets should experience rapidly-increasing aerodynamic forces and accelerations, particularly above a Weber number of 10, so that the droplets did not break-up before achieving the required conditions.

This resulted in the development of a convergent tunnel, in which the air was being increasingly accelerated. A decelerating flow would have better represented the condition near the leading edge of an aerofoil, but that would have been significantly more difficult and costly to achieve. It was a comparatively simple matter to produce a stable accelerating flow, using ambient air, with the required characteristics. This did, however, mean that the air density was decreasing, rather than increasing, but this could be compensated for by further increasing the air velocity to retain the necessary conditions. This did, however, result in a slightly different variation in the Reynolds number, which was considered acceptable.

Using the simulation and the available droplet drag data, the convergent profile of the tunnel was designed to produce a steadily and rapidly-increasing aerodynamic force on the droplets, with respect to time, but not at such a rate that this induced a transient response or vibrations of the droplets.

The resulting transparent convergent tunnel, shown in Figure 10, was 520mm long, with a 290mm square inlet and 76.5mm square exit. At maximum speed this could achieve Mach 0.5 at the tunnel exit, to keep compressibility effects and air density variations within acceptable limits.

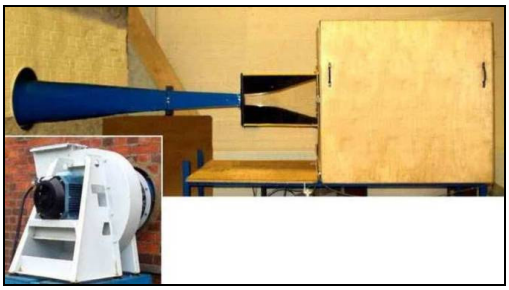

Figure 10: Convergent Droplet Tunnel with Plenum chamber, Diffuser and Fan

For this a suitable fibrous filter inlet screen and plenum chamber had to be designed and constructed to condition the inlet air. The outlet diffuser was optimised and constructed to maximise the kinetic energy recovery from the airflow, so that a low-cost commercial suction fan could be used. The fan had an accurate electronic speed control to allow infinite variability of the tunnel airflow. The tunnel air velocity and density was determined and calibrated from pressure tappings along one of the tunnel walls. Two sides of the tunnel were transparent so that droplets could be observed and measured with optical equipment and instruments.

The droplets were injected from the plenum chamber at a velocity of around 10m/s, which was similar to the maximum inlet air velocity to the tunnel entry.

The imaging and measurement of the droplets was at a fixed location 40mm upstream of the tunnel exit and the droplet conditions were varied by changing the fan speed.

Imaging of the Droplets

In principle it was not necessary to obtain images of the droplets, since the primary requirement was to measure their drag characteristics. In practice it was essential to obtain images to ensure the droplets were being injected, conditioned and delivered to the measuring location as required.

Because of irregularities in the motion of the droplet, their small size and high velocities, some special imaging methods were required. Whilst suitable equipment for this existed it was not available for use on a regular basis.

It was concluded that, if a sufficiently short and powerful flash could be produced, then any conventional camera technology, with suitable optics, could be used to capture the required images. The normal method for generating such flashes was a pulsed laser, but such equipment was not available on a regular basis.

It was known that a Light Emitting Diode (LED), could produce very short flashes, at least down to 1µs, but previously the light energy per flash was not sufficient to obtain an image from a single flash with an available camera. Where the conditions were exactly repeated, such as at the exit of the vibrating-nozzle droplet generator, the resulting image could be obtained from the accumulation of many thousands of flashes.

Such an approach was not possible with the irregular conditions in the tunnel, so a much brighter flash light was developed, using recently-available high-power Light Emitting Diodes and MOSFET transistors.

The requirement was to obtain droplet images from a single flash with a resolution of 5µm and maximum motion blur of 5µm at a velocity of up to 100m/s. This required a flash duration as short as 0.05µs, or 50ns. To achieve sufficient intensity required a special high-power LED subjected to a current pulse of up to 15 amps with a rise and fall time of 25ns. In practice useable images were obtained with flashes of 100ns to 200ns duration with a peak current of a few Amps from a 30V supply.

Figure 11: LED flash unit with 80mm Collimating Lens

Figure 11 shows the resulting LED flash unit, together with an aspheric 80mm diameter by 80mm focal length collimating lens. This flash unit was able to produce a flash rate of up to 100kHz that could be synchronised with a high-speed video camera to produce video sequences, such as shown in Figure 7 and the right hand side of Figure 9.

Measurement of the droplet motion

An essential part of the investigation was the need to determine the droplet velocity relative to the airflow and the aerodynamic drag force applied to the droplets.

From this data and knowing the droplet size and properties, the Reynolds number, Weber number, Bond number and Drag Coefficient could be determined. This would then provide the necessary experimental data for comparison with predictions from the computer model for droplet drag.

The most difficult and critical part in this was to determine the drag force on the drop-

lets. The only known practical way was to determine the acceleration of the droplets. Knowing the droplet size and mass the drag force could then be determined.

Measuring the droplet velocity could have been achieved with various standard methods, but such equipment was not available to this project. To accurately measure acceleration required determining small changes in velocity over a short interval of time and in the shortest possible distance. An evaluation of the standard velocity measuring instruments indicated that they would be unlikely to have the necessary resolution and precision needed for the droplet acceleration to be determined with adequate accuracy.

This resulted in the need for a specially-developed low-cost instrument that could determine the droplet acceleration with the necessary accuracy.

The arrangement used to achieve this is shown in Figure 12. In this three parallel laser beams were projected across the path of droplets and onto photo detectors to determine when they were interrupted by a droplet. Periodically a single droplet would intercept all three beams, to produce a sequence of electronic pulses from the three photo detectors.

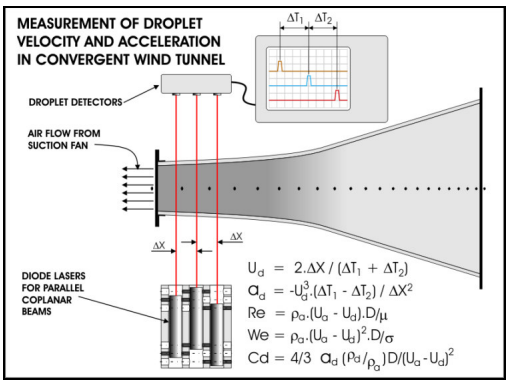

Figure 12: Arrangement for measurement of droplet velocity and acceleration

From knowing the spacing of the laser beams and the time intervals between the pulses, it was then possible to calculate the velocity and acceleration of the droplet. Knowing the droplet size and properties and the air velocity in the tunnel, the experimental drag characteristics for the droplet could then be determined for the prevailing conditions.

For this it was advantageous to have equal spacing between the laser beams. This method was subjected to a careful error analysis and it was found that the design, construction and alignment of the laser beam unit was critical.

With a beam spacing of 25mm the most critical issue, for the required accuracy, was that the middle beam should be within 30μm of the central location between the two outer beams. In practice this was aligned to within about 15μm. As an additional safeguard the block carrying the three lasers could be inverted, so that any asymmetry of the beam spacing would then be reversed. By taking the average of measurements with the laser block in the normal position and then inverted, for the same conditions, the errors due to beam asymmetry would be cancelled out.

The signal pulses were recorded by an 8 bit digital oscilloscope and then transferred to a computer via an interface. Typically the signals were sampled at 1μs intervals and, using interpolation, it was possible to determine the pulse timing to within 0.1μs.

It was determined that this system could measure the droplet acceleration with an accuracy of 2% to 3% for the particular experimental conditions. The velocity measurement was far more accurate. In the event it was not, however, possible to obtain data to this level of accuracy due to the variability of droplet size from the droplet generator, as discussed in Chapter 12. To try to alleviate this a large number of measurements were made for each condition and these were then averaged to reduce the uncertainty. For the high Weber numbers, 12 to 16, with droplets of 250μm, there was remarkably close agreement between the computer model and the experimental result.

The greatest discrepancy between the model and the measurement was at a Weber number of about 8, where the difference was about 20% with 250µm droplets. Given the experimental uncertainties the worst case was more than two times more accurate than assuming spherical droplets. For a Weber number of 10.5, it was at least three time more accurate and above a Weber number of 13 about ten times more accurate.

Conclusions

1. A practical effective and efficient semi empirical computer model for the drag of deformable droplets was developed from available experimental data and a distortion model of sessile droplets.
2. The necessary experimental facilities were developed to produce, inject and condition the droplets with the required aerodynamic forces in a convergent wind tunnel. This enabled imaging of the distorted droplet in the wind tunnel and instrumentation was developed to measure the droplet velocity and acceleration, from which the drag characteristics could be determined.
3. The measured drag characteristics were found to be in acceptable agreement with predictions from the computer model. The discrepancies between the model and the measurements were very much less that the discrepancy between the measurements and the drag predictions for the spherical droplet assumption.

Chapter 1: Distortion, Drag and Break-up of Droplets.

Reasons for and Objective of the Investigation

A new group was set up at Cranfield University in about April 2002 to carry out research into the icing of aircraft due to freezing drizzle from Supercooled Large Droplets, or SLD. These were typically 100μm to 500μm diameter and large compared to the droplets of about 50μm, or less, considered in previous icing investigations, but much smaller than the droplets of several millimetres considered in most droplet research.

The aim of this research was to better understand the distortion and break-up of small supercooled drizzle drops as they interact with the airflow near the leading edge of an aircraft aerofoil and what effects this might have on the icing process. The resulting findings could then contribute to new icing simulation codes that were being developed.

The aims and objective were;

- To consider if the aerodynamic conditions in the vicinity of the leading edge of an aerofoil and whether this could result in significant effects on the distortion, drag, motion and break-up of drizzle droplets.
- To determine the resulting aerodynamic forces acting on the droplet distortion and resulting effect on their aerodynamic drag characteristics.
- To evaluate and predict the minimum quasi-steady aerodynamic conditions for the break-up of droplets.
- To develop an effective method for calculating and predicting the distortion and drag of droplets when distorted by aerodynamic forces.
- To develop a computer model for calculating and predicting the distortion and motion of droplets in a given airflow while taking into account the effect of the distortion and resulting increased drag due to the aerodynamic forces.
- To asses the significance of size scaling and dynamic response of in-flight droplets in relation to the SLD icing process and derive relevant dimensional parameter groups to provide appropriate scaling rules.
- To develop experimental facilities to create the required droplets and subject them to relevant aerodynamic forces.
- To develop the necessary facilities to enable the behaviour of the distorted droplets to be imaged and measured.
- To compare the experimental results against and validate the predicted results
- To evaluate the relevant magnitude and significance of the effect in SLD icing and how this may be affected by the relevant conditions and aerofoil scale.

Relevant conditions considered and investigated

The typical relevant conditions considered in this research were;

- Water droplet size from 100μm to 500μm, or $26\times10^3 < La < 130\times10^3$.
- Approximate range of free-stream air velocity considered, 70m/s to 160m/s
- Experimental conditions; water droplets in ground level ambient air. Results and

model applicable to other relevant conditions with dimensional scaling.

- Application, from ground level to 10,000 feet, from 20C to supercooled at -20C, scaled using parametric groups from ground level atmospheric conditions.
- Droplet Weber numbers up to 16 for quasi-static conditions and up to about 30 for some transient conditions.
- Approximate range of droplet Reynolds number; 700 to 1500.

Effects on Icing

The combination of the larger droplets, together with the severe aerodynamic forces near an aircraft wing, could cause substantial distortion and even the break-up of the droplets prior to contact with the aerofoil. The resulting distortion of the droplets could greatly increase their aerodynamic drag, by as much as a factor of three or more, which could then substantially affect the motion of the droplet and the manner in which the ice accumulates on an aerofoil.

Hence it was anticipated that such issues could have a significant effect on the aircraft icing process in supercooled drizzle.

Icing Tunnel Facilities

The Icing Group was developing wind tunnel facilities to reproduce the icing conditions. One of these was the main horizontal refrigerated icing tunnel, Figure 14, with an air flow of up to about 100kg/s at a velocity up to about 140m/s through a working section of 760mm square.

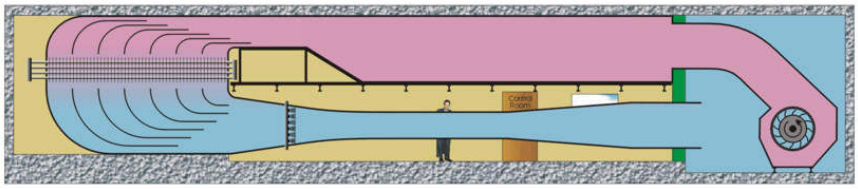

Figure 14: The Main Horizontal Refrigerated Icing Tunnel.

The other facility developed was a 5.5m tall vertical refrigerated tunnel, Figure 13, with an airflow of up to about 7.8kg/s, a minimum section of about 216mm square and velocity of around 133m/s. This was to accelerate droplets towards a wetted target, at up to 100m/s, to investigate the splash behaviour of droplets.

Figure 13: The Vertical Wind Tunnel

For both these facilities it was necessary to analyse, optimise and design the contraction profiles to achieve the necessary acceleration, cooling and distribution of water droplets.

Need for Droplet Drag Data for Numerical Modelling

To better understand the icing process with freezing drizzle and to help with the tunnel analysis and design, it was necessary to develop a numerical computer model of the cooling and dynamic motion of the droplets in an airflow with a steep velocity gradient.

Whilst modelling the dynamic motion of the droplets was reasonably straightforward, the necessary data about the droplet drag characteristics was required. Although such data was available for spherical droplets, there appeared to be very little useful data for droplets that were substantially distorted by aerodynamic forces.

As a result this research was undertaken to obtain the necessary data and model to represent the drag characteristics of distorted droplets for the required range of conditions.

Use of Dimensionless Parameter Groups

As discussed in the overview, the droplet behaviour depends on many factors, such as;

1. Aerodynamic drag force
2. Droplet size
3. Droplet velocity, relative to the air
4. Droplet acceleration, or gravity
5. Air density
6. Air viscosity
7. Surface tension
8. Droplet density
9. Droplet viscosity

To try to develop an understanding of droplet behaviour by directly relating it to all these parameters, or experimental measurements, was likely to be impractical.

It was thus necessary to reduce the quantity of relevant parameters to a more manageable number.

A first step in this was to asses if any of the parameters were unnecessary, or were directly dependent on the other parameters by some obvious relationship. In this way several of the of the parameter could be eliminated.

Providing the droplet shape only changed reasonably slowly and there was no significant internal flow, then the droplet viscosity could be neglected.

Given no other forces on the droplet, then from considerations of force balance, see Chapter 3, the aerodynamic drag force had to equal the acceleration, and/or gravity, force. Hence there were seven relevant parameters to consider.

To further reduce the parameters to a manageable number the method of Dimensional Analysis was used (Doebelin 1995), (Jerrard & McNeil 1980), (Taylor 1974), (Brinkworth 1971), (Ipsen 1960), (Buckingham 1914). In this the normal dimensioned parameters were replaced with fewer dimensionless parameters, normally referred to as dimensionless numbers.

For this the Buckingham Pi theory states that the number of dimensionless groups will be the number of parameters, seven, less the number of fundamental dimensions, which were mass, length and time. This indicated that there should be four possible dimensional numbers from the remaining seven dimensional parameters.

	Parameter	**Symbol**	**Units**
1.	Drag force	F	$kg.m/s^2$
2.	Droplet dimension	D	m
3.	Droplet velocity	U	m/s
4.	Acceleration, or gravity	a	m/s^2
5.	Density	ρ	kg/m^3
6.	Viscosity	μ	kg/(m.s)
7.	Surface tension	σ	kg/s^2

From the Buckingham Pi theory this would give four dimensionless numbers. These

could take various forms, but the well know ones normally adopted were

- Reynolds number $24.(\rho.U^2/2).(\pi.D/4)/(3.\pi\mu U.D) = \rho.U.D/\mu$
- Weber number $8.(\rho.U^2/2).(\pi.D^2/4) / (\pi.D.\sigma) = \rho.U^2.D / \sigma$
- Bond number $6.a.(\rho.\pi.D^3/6) / (\pi.D.\sigma) = \rho.a.D^2/\sigma$
- Drag Coefficient. $F/((\rho.U^2/2).(\pi.D^2/4)) = 8.F/(\pi.D^2.\rho.U^2)$

Variants of the Dimensional Groups

In these parameters the relevant droplet dimension, D, would normally be the diameter of a sphere with the same volume as the droplet, known as the Volume Equivalent Diameter (VeD). When the droplet is distorted then for some considerations another dimension may be relevant, such as the equator diameter, De, or droplet thickness, h.

Which fluids properties and parameters were used in the dimensionless parameters depended on the circumstance. For example in the case of the Weber and Reynolds number this could either use the properties of the droplet fluid or of the surrounding fluid. For a droplet impacting against a surface the fluid properties of the droplet fluid would be used, however when considering the distortion and drag forces of a droplet the properties of the surrounding fluid would then be used. In both cases the same interfacial surface tension would be used.

With respect to the drag forces the relevant velocity was the differential velocity between the droplet and the surrounding fluid. In some cases this velocity may not be known, so some other known velocity may then be used, such as the free stream velocity. This would then give a nominal value for the relevant parameter group.

This could give rise to different variants of each parameter group, so where necessary the parameters used for a dimensionless group where explicitly stated. Unless otherwise stated the equivalent diameter and the differential velocity of the droplet with the surrounding fluid were assumed, for the Bond number the droplet density was assumed, while for other dimensionless numbers the properties of the surrounding fluid were assumed.

Reynolds number

The Reynolds number relates the force on the droplet from the dynamic pressure of the surrounding fluid, due to its velocity relative to the droplet, $\rho_a.U^2/2$, acting over the projected area of the droplet, $\pi.D^2/4$, in relation to the viscous drag force, as represented by Stokes law, $3.\pi.\mu_a.U.D$.

Weber number

The Weber number relates the force from the dynamic air pressure, $\pi.\rho.U^2.D^2/8$, to the surface tension force, $\pi.D.\sigma$, around the droplet perimeter. This relates the external pressure distribution to droplet distortion.

Bond number

The Bond number, relates the body and/or inertial force, $\pi.\rho_d.a.D^3/6$, due to gravity, **g**, and/or acceleration, **a**, to the perimeter surface tension force, $\pi.D.\sigma$. This also known as the Eötvös (pronounced Ertversh) number which is normally written without the umlauts as Eotvos (Clift, et al 1978).

The parameter was originally used for droplets and bubbles sinking/falling or rising at

constant velocity due to the force of gravity in a surrounding fluid. Where the density of the surrounding fluid produced a significant buoyancy effect then the mass of the fluid displaced by the droplet, or bubble, has to be taken into account by allowing for the buoyancy effect from the displaced fluid. This modifies the Bond number to give $Bo = (\rho_d - \rho_a).a.D^2/\sigma$, however with respect to aircraft icing, the density of air, with respect to water, was sufficiently small that this buoyancy correction could be neglected.

With respect to droplets in free flight in the flow field around an aerofoil, the droplet acceleration was typically 1000 times that of gravity, so that gravity effects in the Bond number could be neglected, with gravity, **g**, replaced with the droplet acceleration, **a**.

Drag coefficient

The Drag coefficient relates the aerodynamic drag force, **F**, to the aerodynamic pressure force on the projected area, $\pi.\rho_a.U^2.D^2/8$. This is normally used to define the drag characteristics of rigid items, such as aircraft. It is also applied to rigid particles, such as cylinders, spheres and ellipsoids.

This parameter could also be applied the deformable droplets, however it does not incorporate the surface tension effect related to the deformation and also it is only indirectly related to the droplet acceleration. Hence for deformable droplets the Bond number was seen as a better parameter to represent the drag force.

Force Balance Considerations

The previous consideration resulted in four dimensionless parameters, when according to the Buckingham Pi theory only three were required. Hence one of the parameters must be capable of being expressed in terms of the other three parameters.

The required relationship could be determined by considering the force balance between the aerodynamic drag force and the force required to accelerate the droplet mass, as defined by Newton's 2nd law of motion.

hence	$F = Cd.(\rho_a.U^2/2).(\pi.D^2/4)$	=	$(\rho_d.\pi.D^3/6).a$
so that	$\frac{1}{4}.Cd.(\rho_a.U^2.D/\sigma)$	=	$\frac{1}{3}.(\rho_d.D^2.a/\sigma)$
and	$Cd\ .We$	=	$^4/_3.Bo$
thus	Cd	=	$^4/_3.Bo/We$

Hence we see that the drag coefficient is, essentially, the ratio of the Bond number to the Weber number, which cancels out the surface tension.

Added Mass

The assumption made was that the effective mass of the droplet was that of the water in the droplet, possibly corrected for the displaced air. Because of the increased air velocity as it flows around the droplet, this increased the kinetic energy in the airflow, which contributes to the kinetic energy of the droplet. This then produces an apparent increase in the droplet mass. This is known as the added mass, induced mass, or hydraulic mass, (Massey 1989). For inviscid flow around a sphere the added mass is half the mass of the displaced fluid. For viscid flow the added mass will be less. Since the mass of the displaced air was anyway negligible, compared to the mass of the droplet, the effect of the added mass was also neglected.

Purpose of the droplet drag analysis

From the preceding evaluation it was found that the drag coefficient was a function of the Bond number and Weber number. Hence the drag coefficient could be dispensed with. The forces acting on the droplet could then be represented by the Bond number and this would then also incorporate the surface tension effects, which the drag coefficient did not represent.

The purpose of this research was to enable the motion of deformable droplets to be more correctly determined in the flow field around the leading edge of an aerofoil. In this the requirement was to determine the droplet acceleration given the velocity differential between the droplet and surrounding air. The incremental changes in the droplet velocity were then determined by numerical integration, as discussed in Chapter 8.

The established aeronautical perspective is, however, more familiar with defining the aerodynamic drag in terms of a drag coefficient. This is appropriate for a rigid item, which does not involve surface tension and is travelling at constant speed, relative to the surrounding fluid. With items where substantial deformation is related to the aerodynamic loading and acceleration, in conjunction with surface tension, the Bond number, in relation to the Weber number and Reynolds number, better represent the behaviour of a deformable droplet.

Where it is preferred that the drag is given as the drag coefficient this can be achieved from the Weber number and Bond number with the relationship, $Cd = {}^{4}/_{3}.Bo/We$.

Other Useful Dimensionless Numbers, or Parameters

The four basic dimensionless numbers previously considered are the ones that would normally be used to represent the drag characteristics of a droplet. As has been shown one of these can be derived from the three primary parameter of the Weber number, Reynolds number and Bond number.

The use of any two dimensionless parameter is sufficient to define the droplet situation, from which any other parameter, to represent the droplet response, can be determined.

In practice there can be circumstances where the necessary dimensions and parameters are not available to allow the required dimensionless parameters to be determined. This can then make it difficult to proceed to a solution.

In such circumstance the primary dimensionless groups can be combined together in such a way as to eliminate the need for the unknown dimensioned parameter. For convenience the new groups have various names. Relationships between the various parameter groups can then be determined so as to allow the necessary manipulation to achieve the required solution.

Some of the relevant alternative dimensionless parameter groupings are;

- the Froude number
- the Laplace number.
- the Ohnesorge number
- the Morton number
- the drag parameter We^2/Bo
- the Rabin number

Froude number

The Froude number is normally associated with surface gravity waves for scaling the wave drag of ships. It can, however, also be a useful parameter for some aspects of droplet dynamics, in which gravity, **g**, is replaced with the acceleration, **a**.

There seems to be different versions of this number, but the one normally used is;

$$Fr = U^2/g.D, \text{ or } U^2/a.D, = (\rho_d/\rho_a).(We/Bo) = {}^4/_3.(\rho_d/\rho_a) / Cd$$

After allowing for the density ratio of the droplet fluid to the surrounding fluid and the factor of $^4/_3$, the Froude number is found to be the reciprocal of the drag coefficient, Cd.

Laplace number

The Laplace number is given by;

$$La = Re^2/We = D.(\rho_a.\sigma/\mu_a^2)$$

In this parameter group the properties of the surrounding fluid were used.

The particular value of this parameter is that it does not include velocity, or acceleration, and for given fluid properties it is directly related to the droplet size. Hence it primarily represents the droplet size, while also taking account of the fluid properties.

For given conditions in air, with water droplets of a given surface tension, this shows that for a given droplet size there is a specific relationship between the Reynolds number and Weber number. Hence to achieve specific values for both Weber number and Reynolds number, for given fluid properties, this can only be achieved with a given droplet size. Hence changing the droplet size in scaled tests, to retain other scaling relationships, such as the Weber number, the Reynolds number may not be correctly scaled.

Ohnesorge number

The Ohnesorge number is the inverse square root of the Laplace number, but is normally used in relation to the droplet fluid properties. Hence;

$$Oh = 1 / \sqrt{La} \text{ (with droplet properties)} = \mu_d / \sqrt{(\rho_d.\sigma.D)}$$

A feature of this parameter is that it gives the damping coefficient of droplet vibrations. For the 1st vibration mode the damping factor, $\eta \approx (\sqrt{2}).Oh$, giving a vibration-damping factor of about 1% for water (O.A. Basaran, 1992), for the droplet size range of interest.

Morton number

The Morton number, Mo, was also originally used in relation to bubbles and droplets rising, or sinking in a surrounding fluid due to gravity (Clift, 1978). This is given as;

$$Mo = We^2.Bo/Re^4 = g.\mu_a^4.\rho_d/\rho_a^2.\sigma^3 \text{ or } a.\mu_a^4.\rho_d/\rho_a^2.\sigma^3 = (a.\mu_a^4/\rho_a.\sigma^3).(\rho_d/\rho_a)$$

A useful feature of this is that it does not contain either velocity or droplet size and, apart from gravity, or acceleration, only contains fluid and surface properties.

The value of this parameter is for situations where the fluid properties are known and gravity, or acceleration, is known, or is to be determined from the Morton number. This is particularly useful for of droplets freefalling in ambient air and standard gravity, with $Mo = 1.98\times10^{-12}$, where neither the droplet size or velocity may be defined.

Other useful dimensionless parameters

One useful group considered was;

$$We^2/Bo = Mo.Re^4 = {}^4/_3.We/Cd = (\rho_a.U^4/g.\sigma).(\rho_a/\rho_d) \text{ or } (\rho_a.U^4/a.\sigma).(\rho_a/\rho_d)$$

The advantage of this parameter group is that it relates acceleration, or gravity, to droplet velocity without involving droplet size.

A useful property of this was, as discussed in Chapter 3, that for free-falling droplets at We > 10 this tends to a constant value, of about 14.75.

A parameter used by some researchers was the Rabin number, (Rabin & Lawhead, 1960), $Ra = We/\sqrt{Re}$. This was an empirical parameter used to define various modes of droplet break-up. This parameter can, however, also be rewritten as $Ra = (We^3/La)^{1/4}$, which shows that the parameter is essentially an alternative version of the Weber number, with some correction for droplet size. An evaluation of droplet break-up criterion in Chapter 7 indicated that break-up was more likely to be a function of Bond number, but with respect to droplet break-up there is a functional relationship between We, La and Bo, which it would seem the Rabin number was intended to express.

What is drag

The definition of drag, with respect to droplet motion, is considered in Chapter 3. This is given as the vector component of the aerodynamic force vector acting in the direction of the flow velocity of the surrounding air relative to a droplet. Hence, for example, where the airflow is in the same direction and at a higher velocity than the droplet, then the drag will cause the droplet to be accelerated, rather than produce a retarding force.

The magnitude of the drag force will be a function of the magnitude of the velocity difference between the droplet and surrounding fluid.

Effect of Turbulence in the surrounding flow

The effect of turbulence on the droplet behaviour is discussed in Chapter 3. The assumption made was that the length scale of the surrounding turbulence was large compared to the scale of the droplet, so that the droplet "experiences" this as a fluctuating flow velocity in the surrounding air. These fluctuations were assumed to have a sufficiently short period that their effect was averaged out and there was no significant effect on the average velocity and trajectory of the droplets, but there may have been some dispersion of the velocity and trajectory of droplets.

It is, however, possible that in appropriate condition the period of the drag fluctuations from turbulence will interact with the natural resonance of the droplet, perhaps causing its premature break-up. This issue was beyond the scope of this research.

Conditions of Interest to SLD Icing

These issues are briefly discussed here, but are considered in greater detail in Chapter 3, with an enlarged version of Figure 15. The shaded region of Figure 15 shows the problematic conditions.

The conditions of interest to SLD icing are, typically, supercooled water droplets of between 100µm and 500µm and Weber numbers greater than 3, where droplet distortion begins to have a significant aerodynamic effect. For a Weber number less than 3 the droplet could be treated as being nearly spherical.

For water droplets greater than 1.3mm diameter, La > 340×10^3, at a Weber number greater than 3 the Reynolds number would be greater than 1,000, as shown in Figure 15, where the air drag was adequately indifferent to Reynolds number, so mostly just the Weber number effects needed to be considered.

For spherical droplets there is adequate drag data available (Massey 1989). For 3 < We < 10 and Re > 1000, drag data could be derived from free-falling distorted droplets at terminal velocity in ambient air and standard gravity, (Maybank 1961), (Scott 1964).

Below a diameter of 100µm, La < 26×10^3, in typical SLD icing conditions, with a full-size aerofoil, it would seem that the Weber number was unlikely to be sufficient to cause significant droplet distortion.

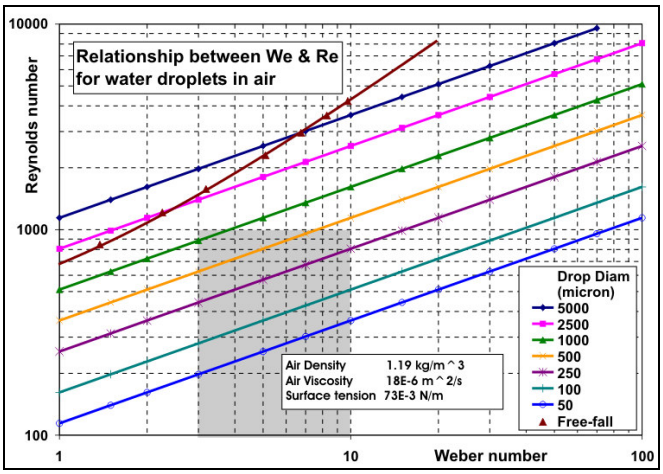

Figure 15: Relationship between droplet size, Reynolds number and Weber number

For a sustained Weber number greater than 11 droplets can be unstable and likely to break-up (Maybank and Briosi, 1961), so little data was available for such conditions. It would seem, however, that where the Weber number was increasing at a sufficient rate, but not enough to cause transient effects, droplets could exist to Weber numbers of 20 or more, (Liu 2000).

For Reynolds numbers less than 1000, the air viscosity could have a significant effect. If at the same time the Weber number was greater than 3, then both the viscosity and droplet distortion effects could become significant and interact, so a more elaborate droplet drag model would be required, which was the primary issue for this investigation.

Above a Weber number of 10 the oblate deformation of the droplet could reduce the sensitivity of the drag to Reynolds number. This is because of both the higher Reynolds number for the larger equatorial diameter and also the more acute surface curvature at the equator which would encourage more stable flow separation.

Literature Survey and References

More than 480 literature items were identified related to droplets and icing, as shown in the References, Bibliography and Literature, of which about 70 had become available during the investigation.

The references and bibliography are listed in chronological order, as far as possible, with the most recent first, where the most relevant papers were likely to be. This has been found to be an effect way to organise references as it brings contemporary papers, research and authors together, so it is then possible to follow the various developing trends through the references. The references are grouped into each year, back to 1967, when several years may be grouped together. All 1900 to 1949 references are in one group with two pre 1900 papers. Where the reference date was uncertain this was taken as being the year of the latest reference it contained and the following year, i.e. 97-98.

Of these references, some 218 items were considered relevant and could be obtained. These were reviewed, but none of these contained the necessary data, or model formulation, for the drag of deformable droplets in the range of small droplet sizes for the more severe aerodynamic conditions relevant to aircraft icing in supercooled drizzle.

Whilst the references were numbered, the numbering was not fixed, so the convention adopted for references within the text was to enclose these within brackets with author and year, such as, "(Maybank and Briosi 1961)", unless it was being directly referred to, such as "this used the method of Maybank and Briosi (1961)."

The relevant literature on droplet drag is discussed in more detail in Chapter 3.

A substantial number of references on droplet distortions, drag and break-up were obtained and evaluated, (Hase, Weigand, 2004, 2002), (Schmehl, 2002, 2003), (Helenbrook, Edwards, 2002), (Aalburg, Faeth, van Leer, 2002), (Risso, 2000), (Bartley, Martinez, Baron, Secker, Hirst, 2000), (Schmelz, Walzel, 1999), (Fyfe, Oran, Fritts, 1987), (Simpkins, 1971), but non of these covered the conditions for in-flight droplets relevant to SLD icing. In general they either dealt with droplets outside the size range of interest, or they did not cover the necessary range of Weber number and Reynolds number.

Wright and Potapczuk (AIAA-2004-0412) did consider the increase in drag due to the distortion of larger droplets in modelling the trajectories of droplets in SLD icing, but concluded that the drag "at most is 15% higher than the drag of a sphere". In the same publication they calculated Weber numbers of 16 and higher, with break-up occurring for $10 < We < 20$, or Bo (or Eotvos) > 16. At a Weber number of 16 it has been shown in this research for a droplet size of 250µm that the drag increase is about a factor of 3.3, which far exceeds that suggested by Wright and Potapczuk. For the same Weber number of 16 for a 1mm droplets an increase in drag of at least a factor of three would be expected. It is considered that such an increase in the droplet drag could have a significant effect on the droplet trajectory and distribution of ice accretion.

It is considered that the reason for the incorrect conclusion by Wright and Potapczuk was that they based their drag correction on the droplet Reynolds number using data obtained for free-falling droplets. It would seem that they did not appreciate that the droplet distortion, which is mostly responsible for the increase in drag, is dependent on surface tension, as represented by the Weber number and Bond number. Since the Reynolds number does not include surface tension it is an unsuitable indicator of droplet distortion and the related increase in drag. Figure 15 shows that for a given Weber number the Reynolds number is proportional to the square-root of the droplet size. Hence to correctly adjust the drag for a droplet size of 1mm, using data for a free-falling droplet of 9mm, would require that the Reynolds number for the free-fall droplet data would need to be increased by a factor of three. When this is done it gives a drag increase much more in keeping with the findings of this research.

The best quality data obtained was that for the terminal velocity of free-falling droplets in ambient air and standard gravity, (Scott, 1964, data of Gunn & Kinzer, 1949), (Maybank, Briosi 1961). This was, however, for lager droplets and only provided data up to a Weber number of 10, or so, and at much higher Reynolds numbers, but it provided the necessary quality of data to enable a semi-empirical computer model to be developed.

Many references on Scaling and Icing issues were also obtained and evaluated, as discussed in Chapter 2. It would seem that none of these considered the issue of droplet

distortion prior to impact with the aerofoil, or the consequent effect on the droplet drag characteristics and the icing processes. In general it seems that they all assumed the droplets remained spherical. This seems to have been an implicit presumption made without any reasonable justification.

The Difficulties with determining drag for deformable droplets

Given the state of knowledge with fluid dynamics and aerodynamics it seemed remarkable that the necessary data for the drag of deformable droplets had not already been obtained, or a suitable model already derived.

The drag characteristics for spheres was adequately determined by Lapple and Shepherd (1940) for the range of interest and some data went back much earlier (Allen 1900). The drag resistance of free-fall deformable droplets was accurately determined in the experiments of Gunn & G.D. Kinzer (1949), which could be used to correct drag for the distortion of large droplets greater than 1.3mm for Weber numbers less than 10. With smaller deformable droplets there were, however, other issues to be considered, due to the combined effect of both the higher Weber number and also Reynolds number.

The question was why the necessary data, or model, for the drag of deformable droplets was not available. It would seem that that there must have been some particular difficulties in obtaining the necessary data, or in developing a suitable model. This Chapter considers some of the issues and difficulties of obtaining the necessary data or in developing an appropriate model.

There would appear to be two approaches to obtaining the required data.

1. To first determine the shape of the deformed droplet and then determine the resulting drag of that shape, possibly by assuming a fixed distorted shape.
2. To directly determine the aerodynamic forces on the droplets as they deform naturally due to the aerodynamic forces.

Determining Droplet Shape

With the first approach the shape of the droplet could be determined from measurements of photographic images and it would seem that various researchers had done this (Clift, Grace and Weber, 1978).

Alternatively the droplet shape could be determined by the numerical solution of the differential equations for the curvature of the droplet surface resulting from the pressure differential across this surface, as elaborated in Chapter 6. For this the internal pressure would be determined from the acceleration and density of the droplet.

One difficulty was that neither the external pressure distribution or droplet acceleration may be known, since these would depend on and affect the shape of the droplet. To determine the external airflow and pressure could require sophisticated computer analysis, such as Computer Fluid Dynamics (CFD), which might not be available, or effective.

It would seem, however, that the distorted droplet shape was not so greatly affected by details of the external pressure distribution and that a first approximation of this might suffice. In Chapter 6 the shape of a sessile droplet, resting on a horizontal unwettable surface, was computed and found to be a reasonable approximation to the shape of a free-falling droplet at the same Bond number. Alternatives, such as assuming a floating droplet on a denser immiscible fluid, might have achieved a better approximation, but

this was not investigated any further.

Due to the moderate effect that the external flow seemed to have on the droplet distortion, it was concluded that the range of Reynolds numbers was not likely to have a sufficient effect on the external pressure distribution or a significant effect on the droplet shape for a given Bond number.

A more accurate computation of the droplet shape could be obtained with an iterative procedure. In this an approximate shape would first be computed by numerical integration using an assumed external pressure distribution. The pressure distribution around the resulting shape could then be experimentally measured, or computed with CFD modelling. The resulting shape could then be recomputed from the revised external pressure distribution. Starting with a sessile droplet, it was anticipated that this would adequately converge to the correct shape in a few iterations.

A more sophisticated option was Direct Numerical Simulation, allowing the free movement of the droplet surface within CFD modelling. These methods were improving and still being developed (Schmehl 2002) but required substantial amounts of computing power that might not be available for many applications. It would seem that at the time the method was not suitable for Weber number greater than 10. There also appeared to be substantial difficulties for Reynolds numbers greater than 300, relative to the equatorial diameter, where it would seem the flow was neither axisymmetric or steady (Johnson and Patel, 1999).

Obtaining drag data for a given droplet shape

There would appear to be three basic methods for determining the drag of a distorted droplet of a prescribed shape;

1. CFD computer modelling.
2. Experiments with free-fall in air, or sinking/rising through a fluid, at terminal velocity due to gravity.
3. Directly measured drag force on the component in a wind tunnel, or liquid flow.

With CFD modelling there were substantial potential difficulties in accurately modelling the flow around fixed geometry spheres and droplets at Reynolds numbers greater than 300 (Johnson, Patel 1999). This was because the flow was neither axisymmetric nor steady, so it required full 3D transient modelling. It was also necessary to have a very fine element mesh in the vicinity of the flow separation to achieve accurate results. All this meant that the computing effort required was substantial. Appreciable effort had been applied to modelling the drag of spheres, but even so there would seem to have been appreciable difficulties. These issues would have been substantially compounded by the range of geometry variation required for distorted droplets. At the time it was more effective to obtain the require data by experimental means.

In free-falling experiments the difficulty could be in maintaining the orientation of the object to be the same as for a free-falling droplet. These may have been naturally stable, or could be stabilised by adding fins, where it would be necessary to ensure that these had a negligible effect on the drag, or that the effect could be adequately allowed for. In experimentally obtaining the drag on a flat circular disk, sinking through water at terminal velocity, it was found that the motion could be stabilised by making the disk slightly dished, but this option might not have been possible for an oblate droplet shape.

Directly measuring the drag force of a fixed object in a flow at low Reynolds numbers could require very sensitive instruments to measure the tiny force with adequate accuracy. Such a method was used by Simmons and Dewey (1930) to determine the drag of flat circular disks at Reynolds numbers of 282, with an air velocity of about 0.5m/s and diameter of 7.7mm, giving a drag force of only about 7.8μN for a drag coefficient of 0.92. Such a tiny force would be difficult to measure reliably with modern instruments.

It was considered that it would be easier to carry out such measurements in a liquid, either with a forced flow, or towing tests, because of the higher fluid density. It would also have been possible to use a higher fluid viscosity, to allow a higher velocity for the same Reynolds number. The resulting drag force, F, was found to be;

$$F = (\pi/8).Cd.Re^2.(\mu^2/\rho)$$

It was interesting to note that this was independent of size, but depended on the ratio of viscosity squared to density. Hence water produced nearly four times more drag force than air for the same Reynolds number. Surprisingly a lower density gave a higher force for the same viscosity and Reynolds number. With a viscosity of 100cP and density of 800kg/m^3, such as a light oil, with Cd = 0.92 and Re= 282, this gave a drag force of 0.36N, which was about 46,000 times that obtained by Simmons and Dewy in air flow. For a 10mm diameter object this required a velocity of about 3.5m/s.

From the preceding evaluation it seemed quite feasible to measure the drag force on a solid droplet shape with reasonable accuracy in readily-achievable flow in a hydrodynamic tunnel of around 100mm diameter using a light oil. No examples of such drag measurements for oblate spheroids were found in the literature.

In the Reynolds number range of 125 to 500 there would seem to be appreciable uncertainty about the drag on a flat circular disk, with differences of up to 50% for Re = 267 (Massey 1989) and (Nakayama & Boucher 1999). Some of this uncertainty could apply to highly oblate droplets until better experimental data becomes available.

Direct experimental drag measurements with deformable droplets

The preferred option was to directly determine the drag force on droplets of the required size and when subjected to conditions similar to those in aircraft icing with supercooled drizzle droplets.

Reproducing all the relevant conditions was not feasible, or necessary. In particular it was much simpler and less costly to carry out the experiments using ambient air and at room temperature. This affected the fluid properties, such as surface tension, density and viscosity. These effects could, however, be allowed for by dimensional scaling with the Reynolds number, Weber number and Bond number.

It did not seem possible to fully maintain all the dimensional similarities, in particular the viscosity ratio of water to air. It was, however, considered that the primary two parameters, Reynolds number and Weber number could be maintained, but this required a droplet of about actual size to maintain the relationship between Weber number and Reynolds number, as represented by the Laplace number.

Figure 16 shows the viscosity of supercooled water is substantially greater than for water at 20C. At −20C the viscosity is about four times that at 20C (Trinh and Ohsaka 1994). The water viscosity was only an issue if there was internal flow within the droplet, due to recirculation from surface friction, droplet vibration or surface ripples. It was

found that the effect of surface friction was negligible, Chapter 3. The presumption made for quasi-static conditions was that droplet viscosity had only a minor effect on surface ripples and droplet vibration, since the vibration damping factor was low, typically a few percent (Basaran 1992), having a similar value to the Ohnesorge number.

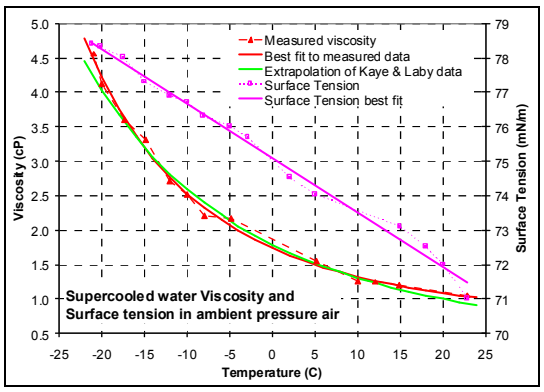

Figure 16: Properties of supercooled water.

Water temperature also affected its surface tension, as shown in Figure 16, but much less than viscosity. Typically at -20C it was about 8% higher than at +20C (Trinh & Ohsaka 1994), but surface tension had a more direct effect on droplet distortion and drag.

Air density and viscosity were also affected by temperature and pressure, which were affected by altitude. Figure 17 shows the resulting effect on density and viscosity for standard atmospheric conditions (Kaye & Laby 1995). It can be seen that this may have a substantial effect on air density and at 12km altitude this is only about a quarter of that at ground level. In comparison the reduction in air viscosity is about 17% at 12km altitude.

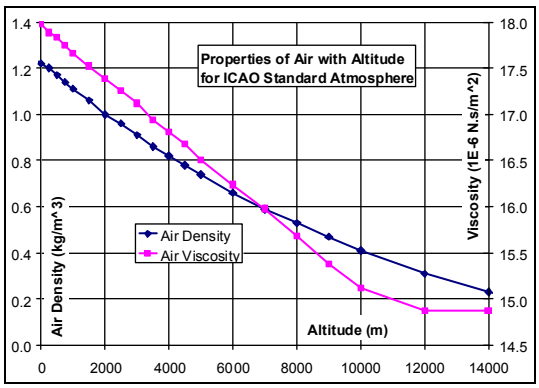

Figure 17: Effect of Altitude on Air properties

It was, however, understood that icing from supercooled drizzle tended to occur at much lower altitudes, where the effects on air density and viscosity were much less. At around 1,500m, or 5,000ft, altitude the air density is reduced by about 16% and the viscosity by about 3%. This amount of variation in air properties could readily be allowed for by maintaining the values of Reynolds number and Weber number. The Roselawn SLD icing incident occurred at less than 3,000m, or 10,000ft, altitude.

A substantial problem with measuring the force acting on deformable droplets was that it was not possible to attach them to any form of force transducer, since this would affect the droplet deformation.

If it had been possible the preferred option was to apply a known body force to the droplet. On the earth surface gravity is always 1g, which requires larger droplets to achieve the required Weber numbers, since achieving a higher gravitational force was not practicable. The use of a centrifuge was considered, see Chapter 3, but Coriolis effects were likely to be a problem. Electrostatic forces were unlikely to be sufficient and would also have affected the distortion of the droplet. Electromagnetic forces required dosing the droplets with magnetic particles, which could have caused other difficulties.

It was concluded that the preferred option was to depend on the acceleration force acting on the droplet. This could be achieved by having an airflow with a steep velocity gradient, similar to the actual conditions around an aircraft aerofoil.

One method was to directly reproduce the flow around an aerofoil. Since, however, it

was found that the droplet behaviour could be affected by the scale size of the aerofoil, in particular the transient effects, Chapter 2, it was concluded that the aerofoil would have to be full scale. Whilst, in principle, this was quite feasible, the test facilities needed would have been too large and costly for the resources and space available.

A further issue with an aerofoil was that the flow would have been curvilinear. Whilst this might be a better representation of the icing conditions, the measurement, data gathering and processing would have been beyond the capability of the facilities, time and resources available.

With the present state of knowledge it was considered that it would be enough to obtain droplet drag data for linear motion in quasi-static conditions. The investigation of transient effects in curvilinear flow could come later, as further work, when the necessary facilities and resources where available.

For linear motion, the droplet drag characteristic could be investigated either in an accelerating, or decelerating, flow. In a free-stream flow approaching the stagnation region at the leading edge of a stationary aerofoil, the droplet would be decelerating relative to the aerofoil. With an aircraft in flight, in near stationary air, a droplet would initially be stationary and then be rapidly accelerated as the aerofoil stagnation region engulfed it. In comparison, one could consider a droplet approaching the upper surface of an aerofoil. In this case with a stationary aerofoil, the droplet would enter an accelerating flow. It would thus seem to make little difference to droplets whether they were in an accelerating or decelerating flow.

One difference would be that in a decelerating flow the air temperature and density would be increasing, while the viscosity would be decreasing. In an accelerating flow the reverse would occur.

In reproducing the droplet conditions, with respect to time, in a decelerating flow, by using an accelerating flow, there could be some mismatch due to the resulting changes in air properties, in particular the air density. It was considered that this could be adequately resolved by ensuring that the variation in Weber number was the same in both cases, to reproduce the same variation in aerodynamic force. That could be achieved with accelerating flow by increasing the velocity difference between the droplet and air to compensate for any changes in air density and surface tension. A consequence of this could be a few percent mismatch in the Reynolds number, which in the range of interest would have only a very minor effect on the droplet drag.

In curvilinear flow the situation would be much more complicated to investigate, since the oblate distortion might, at least momentarily, not be aligned to the relative velocity of the air flow, so resulting in lift (lateral force), as well as drag.

In practice a linear accelerating flow and the required aerodynamic droplets forces could readily be achieved in a convergent wind tunnel. The converse was not so practicable, without elaborate design, since with a divergent tunnel the flow was likely to separate from the walls unless the divergent angle was kept to just a few degrees, as in a diffuser.

Having applied the required force to the droplets, a means of determining these forces was required. If the droplet mass was known then, in principle, the force could be determined from the droplet acceleration. It would seem, however, there could be significant practical difficulties in accurately determining the droplet mass and acceleration, which were some of the primary issues considered in this investigation.

In principle a regular stream of droplets with equal mass (mono dispersed) could be readily produced, as shown in Figure 18. Whilst it may not have been possible to exactly control the droplet size, the frequency at which they were produced could be accurately controlled. By collecting the droplets for a given period, accurately weighing what was collected, knowing the number of droplets for that period and that they were of equal mass, it was possible to accurately determine the droplet mass.

Figure 18: Stream of uniform droplets produced with a vibrating nozzle generator

There were, however, significant difficulties in dispersing the droplets into the airflow while retaining the uniform droplet mass. These issues are considered in Chapter 12 about the droplet generator, since this proved to be a major difficulty.

The other issue in determining the drag force was that of measuring the droplet acceleration. In principle this could simply be achieved by determining the change in velocity in a given time, or distance.

The problem was that the change in velocity, over a given time, or distance, could be quite small, perhaps just a few percent, so the difference between the two velocities, would be a small fraction of the measured velocity. Hence any errors in the velocity readings would, in proportionate terms, be greatly magnified. Typically the accuracy of the velocity measurements would have to be more than an order of magnitude better than the accuracy required for the acceleration results. Hence for 5% acceleration accuracy the velocity measurement would have typically needed to be accurate to 0.5%, or better. This could be difficult to achieve, unless sophisticated, hence expensive, instrumentation was used, but that was not available.

It was possible to increase the distance, or time, between the velocity sensors to produce a greater velocity difference. This would help to reduce errors due to discrepancies in the velocity measurements. However it required the necessary distance in which to carry out the measurement. If conditions changed significantly in the measuring distance, or time, then the acceleration measurement errors could have been appreciable.

One of the issues was how to measure the velocity with the necessary accuracy. Typical velocity measurement methods were PIV (Particle Image Velocimetry) and PDA (Phase Doppler Anemometry).

Particle Image Velocimetry (PIV)

PIV determines droplet velocity by taking two successive images, normally with a sheet of pulsed laser light to illuminate the droplets. Cross-correlation between the two images then determines how far the droplets had moved between the successive images, from which the velocity would be determined. Such equipment would have needed two pulsed lasers together with a sophisticated imaging and data processing system, which results in quite an expensive instrumentation system.

It would seem that such a system would have worked better with a fairly dense spray, to average out the individual errors, and would have had an accuracy limit of about 1%, which required a droplet movement of at least 10 pixel between images. For this investigation the droplets distribution was quite sparse, so the position errors could not be averaged out, thus resulting in reduced accuracy.

It would have been necessary to obtain two velocities, which would have required at least three successive images, hence three pulsed lasers and more elaborate processing. Regardless of whether such a system had been available, or could have been developed, it was concluded that given the constraints applicable to this investigation, the equipment would have not been available and, anyway, the required acceleration accuracy would not have been achievable.

Phase Doppler Anemometry (PDA)

The PDA method works by determining the Doppler frequency as the droplet intercepts two intersecting laser beams (Lacoste et al, 2002-03), (Lehmann, Nobach, Tropea 2002-03). It would seem that, with spherical droplets very good velocity accuracy could be achieved, approaching 0.1%. The measurement was, however, best suited to a reasonably dense spray and was adversely affected by droplet distortion. Such equipment was, anyway, not available, particularly given that two systems could have been required to measure the change in velocity between two locations.

Direct Measurement

A more direct approach by some researchers was to obtain image sequences of the droplets and then determine the droplet acceleration by double differentiation of the droplet position (Rabin and Lawhead 1959). The difficulty with this was the requirement for accurate measurement of the droplet position on successive frames and then the need to double difference the droplet positions to obtain the acceleration, from which the drag coefficient could be calculated. In general such a differencing process tends to greatly amplify errors and it was difficult to obtain even a moderate level of accuracy. The analysis in Chapter 4 shows that extremely accurate droplet position measurements were required to achieve a reasonable degree of acceleration accuracy.

For spherical droplets and particles Ingebo (1956) used a rotating mirror to track the motion of the droplets and photograph them. When this resulted in a sharp image, the droplet velocity could be determined from the rotation speed of the mirror at its distance from the droplets. This velocity measurement was claimed to be accurate to 1.5m/s, or around 5% for a typical droplet velocity of about 30m/s. To reduce the data variability, curves were fitted to plots of velocity against droplet diameter at a given position in the wind tunnel. This presumed a given relationship between these two parameters. From the resulting curve fitting, the velocity for a given size of droplet was plotted against distance along the tunnel, from the slope of which the acceleration was calculated. This appeared to have a variability of about 30% for the acceleration.

An appreciable difficulty with the methods of Rabin and Lawhead, and Ingebo was that they were very labour intensive and not particularly accurate. With modern imaging and data processing it was possible that the process could have been more automated, but the intrinsic limitations would have remained. The data processing method used by Ingebo could, anyway, only be applied to near spherical droplets.

A more practical, cost effective and accurate method had to be obtained. A system was developed which measured the time intervals between droplets interrupting laser beams. Low cost diode lasers could be used for this, with photo detector circuits to determine when a beam was interrupted. A limitation of this was that, to be measured, a droplet had to cut all the beams, so this required that the motion of the droplet had to be in the plane of the beams. Given linear acceleration along the axis of a straight convergent tunnel this requirement could readily be achieved.

The obvious system was to have two pairs of parallel laser beams and to measure the velocity between the first pair and then between the second pair to determine the velocity change. It was, however, found advantageous to simplify this to three laser beams, the centre beam being used in conjunction with both the first and last beam. The resulting measuring system is discussed in Chapter 13. In Chapter 14 the equations are derived for calculating the acceleration and velocity from the signals. This includes the necessary corrections for the beam spacing and errors due to variation of conditions over the measuring distance.

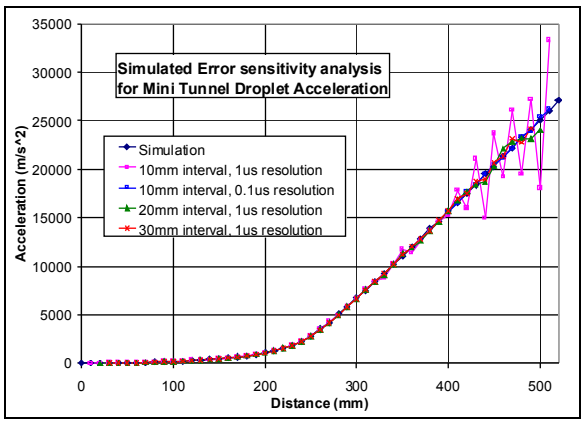

Figure 19: Simulated measuring errors.

The potential magnitude of the acceleration errors is shown in Figure 19. This was a simulated measurement using the numerical model of droplet motion to generate time and position data for a droplet at regular intervals along the tunnel axis. This was rounded to a given resolution and then used to compute the acceleration as if it were measured data. The results were then compared with the acceleration directly available from the computer model. It can be seen that with a beam spacing of 10mm and 1µs time resolution there were substantial errors above an acceleration of 15000m/s^2. With 20mm beam spacing and 1µm resolution the accuracy was greatly improved, and with 30mm beam spacing and 1µs resolution, the results were in good agreement with the acceleration directly obtained from the simulation.

Eventually a beam spacing of 25mm was adopted. With the diode laser units used it would have been difficult to achieve much less of a beam spacing. Increasing the beam spacing beyond 30mm limited the proximity of the measurements to the end of the wind tunnel.

A critical issue was found to be the symmetry of the spacing between the 1st and 2nd and the 2nd and 3rd beams. To achieve an acceleration accuracy of about 3% with 25mm beam spacing, the middle beam had to be within about 35µm of the central location between the two outer beams, or within 0.14% of the beam spacing. Appreciable care was taken in the design and calibration of the instrument to ensure this was achieved, as described in Chapter 13. Typically this alignment was within 10µm to 15µm.

A further enhancement was that the block carrying the diode lasers could be inverted, so any asymmetry in the beam spacing would be reversed. Measurements obtained with the normal and inverted orientation, for the same conditions, could then be averaged to cancel out any asymmetry errors in the beam spacing.

Scaling and Transient Issues

The behaviour of droplets in SLD icing is more complex, due to their large size and their ability to deform and even break-up when subjected to strong aerodynamic forces.

A consequence was that droplets could behave in a different way in the vicinity of a full-scale aerofoil, in comparison to that with a small-scale test model. This issue is considered in more detail in Chapter 2. No references were found which adequately considered this issue. In this it was found that there were two relevant dimensional groups,

which were;

$\mathbf{(D / R).(\rho_d / \rho_a).Cd}$ for the droplet motion dynamics

and $\mathbf{(D / R).\sqrt{((\rho_d/\rho_a).We_{nom})}}$ for transient and dynamic droplet distortion

Given that aircraft icing is concerned with the behaviour or water droplets in air at a reasonably low altitude, the density ratio, ρ_d / ρ_a, would only vary over a moderate range. Also for given droplet conditions the Weber number, We, which is directly linked to the drag coefficient, Cd, would also need to be similar for droplets in the vicinity of both the scale-model and full-size aerofoils. Hence, if correct scaling was to be achieved with a scale model then it would also be necessary for the size of the water droplets, **D**, to be directly scaled with the size of the aerofoil, as represented by its leading edge radius, **R**, or some other suitable reference dimension of the aerofoil. To achieve this, the airflow velocity for the scale model would have to be increased appropriately, compared to that for the full-scale aerofoil. In this there is a square root relationship, so that a four to one reduction modelling scale size would require a two to one increase in the air speed. Such an increase in air speed would be likely to cause other difficulties, not least of which could be significant compressibility effects in the airflow.

Scaling the droplet size to maintain the scaling ratio, D/R, with the aerofoil scaling, would, anyway, not maintain similarity of the droplet Laplace number, La, hence would not maintain the correct Reynolds number for a given Weber number.

One of the reasons for using a convergent tunnel was that it enabled the conditions experienced by droplet in the vicinity of medium to large aircraft aerofoil to be adequately reproduced in a small and inexpensive test facility, without any need to scale the droplet size.

Organisation of the Investigation

The investigation was essentially in three parts

1. Computer and mathematical modelling to develop;
    a. a computer simulation to help with development of the facilities and instrumentation, to evaluate the effect of drag models on the droplet motion and trajectories and to help with the design and organisation of experiments.
    b. a computer model of the droplet drag using available data, reasoned analysis and simpler numerical modelling methods.
2. Experimental investigation to;
    a. develop and set up the required experimental facilities
    b. obtain Droplet video and still images
    c. experimentally obtain the drag data for deformable droplets
3. Evaluation and comparison of the computer model against the experimental results for the droplet drag.

Development of simulation for droplet motion dynamics

A simulation was required to model the motion and trajectory of droplets in a given airflow distribution. This was mostly for flow in a convergent tunnel, but some special

cases for external flow were also evaluated. This was to help assess the situation, such as the design and development of the wind tunnels and experimental facilities and to evaluate the behaviour of droplets in freezing drizzle conditions for aircraft icing.

The development of the simulation is explained in Chapter 8. This provided a numerical solution for the motion and trajectory of droplets in a given flow. Essentially this calculated the drag force on a droplet at a known location and velocity in the airflow. From this the acceleration force on the droplet was calculated, from which the change in position and velocity were computed for the next incremental step using the 4th order Runge Kutta numerical method.

Particular features of this simulation were;

1. It was possible for the incremental step to be established with respect to time, distance, or various other parameters. This, for example, enabled the droplet motion and trajectory in a convergent tunnel to be determined with equal distance increments along the tunnel length.
2. The motion characteristics required for a droplet could be prescribed and the simulation could then be used to directly determine the convergent profile of the tunnel required to achieve that motion.
3. The airflow calculations for the convergent tunnel assumed 1D adiabatic compressible flow. In this a correction could be made for the convergent angle of the tunnel, up to a semi-angle of 90° to the axis, as described in Chapter 10.

The simulation was used to help with the design of the convergent entry of the main icing tunnel, to evaluate the design of the convergent vertical droplet splash tunnel and to optimise the design of the droplet research tunnel. It was also used to assess the conditions near the leading edge of an aerofoil, as approximately represented by the inviscid flow on the windward side of a cylinder, for droplets approaching the stagnation region.

The simulation was mostly used with an early form of the droplet drag model, using the drag correction factor, discussed in Chapter 3. Whilst there were discrepancies, it was adequate for the required analysis and optimisation and did not detract from the effectiveness of the resulting wind tunnel facilities.

Development of the droplet drag model

The development of the droplet drag model is discussed in Chapter 3.

At high Weber numbers, We > 3, droplets can no longer be assumed to be spherical and they distort into an oblate shape that presents the larger frontal area to the airflow. Figure 20 shows photographs of some typical highly distorted droplets in the horizontal convergent wind tunnel. The scale has a pitch of 0.5mm. The droplet deformation substantially increased their aerodynamic drag. This drag force must have an equal and opposite body force, which would be either gravity or acceleration force.

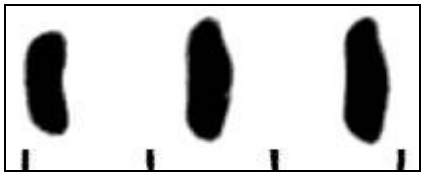

Figure 20: Typical distorted drops

At a Weber number of 10 the drag coefficient was likely to be more than double that of a sphere of the same volume-equivalent diameter.

There were two reasons for the increase in drag;

1. The larger equatorial diameter increased the droplet frontal area.
2. The increased curvature at the equator resulted in earlier and more stable flow separation at lower Reynolds numbers, with respect to the equatorial diameter.

The drag characteristics can be subdivided into a number of regions;

1. Droplets with a Weber number less than 3. These can mostly be treated as spherical, possibly with a minor correction.
2. Droplets with a Laplace number greater than about 340×10^3, or 1.3mm diameter for water at ambient air conditions, and at a Weber number greater than 3. For these the effect of Reynolds number can mostly be neglected and the data for the drag properties of free-falling droplets in ambient air could be used, with a drag correction related to the Weber number.
3. Above a sustained Weber number of 10 it would seem that droplets could become unstable and break-up, but if the Weber number was rapidly increasing, but not at a sufficient rate to cause a transient response or droplet vibration, then higher Weber numbers could be achieved for a short period. In these conditions the sensitivity to Reynolds number effects would seem to be much less and it was the Weber number effects that mostly needed to be considered. For these conditions no published data was available due to the droplet instability.
4. Where the rate of increase in Weber number occurs in a short time period, compared to the droplet vibration period. For these droplets transient effects could become important, as that the droplet dynamic response and vibration could then be a significant issue (Luxford et al 2004). In the vertical tunnel it was observed that droplets could survive Weber numbers of 30, or more, for a short period, as shown in Figure 21. This could have a significant effect on the velocity and trajectory of a droplet as it approaches an aerofoil. Such transient issues are, however, only briefly considered in this investigation, Chapter 2.

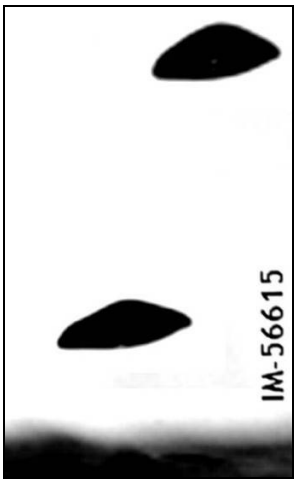

Figure 21: Droplet distortion in the stagnation region of vertical tunnel target for We ≈ 30

5. Droplets with a Laplace number less than about 340×10^3, or 1.3mm for water droplets, at a Reynolds number less than 1000 and Weber number between 3 and 10. For these there is an interaction between the Weber number and Reynolds number, which increases as the droplet size decreases. In this region the drag data for free-falling droplets could be used, but with a correction for Reynolds number. These are the most complicated conditions for which to model the drag of droplets, but it also happens to be an important range of conditions with respect to aircraft icing in supercooled drizzle.
6. For aircraft icing it is unlikely that a Weber number greater than 3 will be achieved for droplets less than 100μm diameter, so they could mostly be treated as spherical. This may not hold true in small-scale model tests where the velocity gradients could be much steeper than with full-size aerofoils.

7. With small scale aerofoil models the transit time of the droplet through the flow field may be too short for the droplet to have time to deform, or for the aerodynamic forces to have a significant effect on the velocity and trajectory of a droplet. It is possible that this could result in significantly different icing patterns compared to that of full size aerofoils, particularly for larger aircraft, where there is much more time and distance for the droplets to be affected.

Free-fall Droplet Data

The primary data for the droplet model was that for free-falling droplets at terminal velocity in ambient air. This provided drag data up to a Weber number of at least 10. Beyond that, droplets could be unstable, but could also remain intact for a limited period.

Investigation of the data for free-falling droplets showed that the value of We^2/Bo asymptotically tended to an upper limit of 14.75 at a Weber number of about 10. The presumption made was that this would be retained for higher Weber numbers while the droplet remained intact, Chapter 7. Hence if the Weber number was increasing rapidly enough that the droplet could achieve these higher Weber numbers, while not inducing significant transient effects or droplet vibration, then this assumption would apply. This was an observation made from the available data, which required experimental validation. This issue is discussed in more detail in Chapter 3.

This extrapolation enables the available data to be extended to higher Weber numbers, possibly up to a Weber number of 20, or more. As discussed in Chapter 5, experimental results had so far been obtained, in the droplet tunnel, for Weber numbers up to 16.

Sessile Droplet Distortion

Whilst it could be difficult to experimentally study droplets at sustained Weber numbers much greater than 10, because of their instability, it was possible to consider the distortion of droplets in comparable conditions. One of the simplest was for a droplet resting on a horizontal surface, known as a sessile droplet. In practice the shape of this depends on the contact angle between the droplet surface and the horizontal surface. With some combinations of liquid and surface this would cause the droplet to wet the surface and spread out into a thin film. However the presumption made was that the surface was unwettable and that there was no surface interaction between the droplet and the horizontal surface, other than the mechanical support provided by the surface.

A sessile droplet can be subjected to gravitational, or acceleration, forces which can cause the droplet to flatten into an oblate shape, but with a flat contact surface. In such circumstances the droplet cannot have a Weber, or Reynolds, number, as that required a velocity. The condition can, however, be represented by the Bond number, which relates the gravitational, or acceleration, force to the surface tension.

When a comparison was made between a distorted free-falling and sessile droplet on the basis of equal Bond numbers, there was very good similarity between them, as shown in Figure 22, despite the very different way in which the distortion was produced, in particular the external pressure distribution. The shape of the sessile droplet was obtained using numerical integration. The Weber number given to the sessile droplet was that which would apply to a free-falling droplet at the same Bond number.

It might be possible to obtain a better approximation to the free-falling droplet shape with a sessile droplet floating on the unwettable surface of a denser liquid, but that option was not investigated.

The benefit of the sessile droplet was that it allowed the evaluation of the distorted shapes which were well beyond what could be obtained for free-falling droplets. Clift, Grace and Weber (1978) gave an equation for the aspect ratio of a free-falling droplet. Whilst this was based on experimental data for Bond numbers of less than 8, the resulting formulation could be extrapolated to much higher Bond numbers, where it remained consistent with that obtained for the sessile droplets, see Chapter 6.

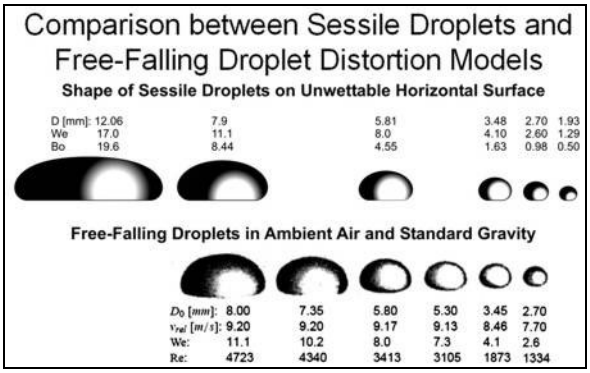

Figure 22: Typical shape of distorted droplets. From Chapter 6 and Schmehl 2002

The preceding discussion shows that, if the droplet distortion was determined from the Bond number, rather than from the Weber number, it allowed the distorted shape to also be determined from other situations which did not involve velocity. Despite the very different circumstances, this produced reasonably similar shapes. It was found that, in calculating the drag on the droplet, the exact shape of the distorted droplet was not critical and it only affected the droplet drag by less than 1% for most conditions of interest.

Solving for Droplet Acceleration

A difficulty with using the Bond number to calculate the droplet distortion was that the reason for calculating the droplet drag was mostly to determine its acceleration. To determine the Bond number, however, requires the acceleration to be known. This could be resolved by an iterative procedure in which an initial condition was assumed and then revised in successive iterations until the required solution was obtained.

Reynolds number correction

The previous discussion indicated a way in which the effects of the Weber number and droplet distortion could be determined. The principal issue remaining in determining the drag on a droplet was found to be that of adequately correcting for the Reynolds number, particularly for distorted water droplets of less than about 1.3mm. How this was achieved is considered in Chapter 3, but the essential issues were;

1. The distorted droplet shape was defined by the Bond number and was effectively independent of the Reynolds number. The distorted shape could be determined from experimental data for free-falling droplets, or for adequately similar conditions, such as a sessile droplet resting on a horizontal unwettable surface.
2. For an oblate distorted droplet, of a given shape, the drag coefficient, with respect to the equatorial diameter, would be bounded between that for a sphere and that for a flat circular disc. It was then assumed that the drag coefficient for the given distorted droplet shape, relative to equatorial diameter, would be the interpolated value between that of the sphere and disk and that this interpolated proportion would be independent of the equatorial Reynolds number.

An issue was that for low Reynolds numbers, $200 < Re < 300$, the various data for the disk drag coefficient data differed by as much as 40% to 50% (Nakayama and Boucher, 1999), (Massey, 1989) . For water droplets of 250µm, or larger, this made a maximum difference of only about 5% at a Weber number of 6 to 7. For droplets of 50µm diame-

ter, it could make a difference of up to 20% for similar Weber numbers. Such small droplets were, however, unlikely to achieve such Weber numbers in practical aircraft icing conditions, so the discrepancy was not too important. For other applications and in icing experiments with small-scale models, the discrepancy could be more relevant.

This interpolation procedure enables a correction to be made for the Reynolds number, so that in conjunction with the extrapolation of the data for free-falling droplets it was possible to develop a model for the drag of distorted droplets for the required range of conditions relevant to aircraft icing in supercooled drizzle.

The details for the development of this model are considered further in Chapter 3.

Development of the experimental facilities

The purpose of the experimental facilities was to apply the necessary aerodynamic forces to appropriate water droplets and then observe and measure the resulting effects. The design of the various facilities is expanded in the following chapters;

- Droplet research tunnel — Chapter 9
- Droplet generator — Chapter 12
- LED flash light — Chapter 15
- Measurement instrument for droplet velocity and acceleration. — Chapter 13

Droplet Tunnel design

Figure 23 shows the droplet wind tunnel. From right to left this consisted of the Plenum chamber, transparent convergent working section, outlet diffuser and suction fan.

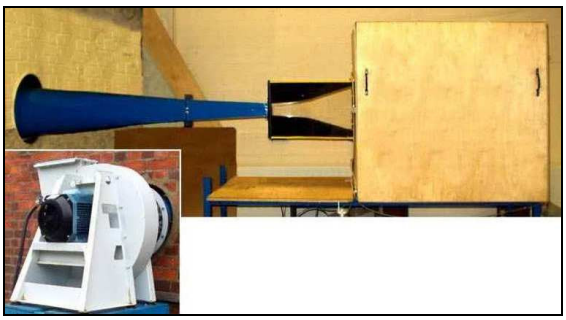

Figure 23: Picture of the droplet research tunnel

The plenum chamber was required to remove unwanted disturbances from the inlet air, such as from the heating fans in the laboratory. This was achieved with an inlet screen on the right hand side of the plenum chamber, which consisted of several layers of fibre matting normally used in air filters. Various measurements and analysis was carried out to ensure the inlet screen did not cause too much pressure loss, while ensuring it would remove unwanted disturbance in the inlet air, Chapter 9.

It would have been preferable to have also included a honeycomb airflow straightener with the inlet screen, but that was not available. A smaller piece of honeycomb flow straightener was obtained to fit over the entrance to the working section.

Droplet Generator

In order to carry out the required observations and experiments, it was necessary to introduce a stream of calibrated droplets into the accelerating airflow of the convergent tunnel. How this was achieved and the various issues related to this are discussed in greater detail in Chapter 12.

The first method used was a vibrating nozzle generator as shown in Figure 24. A larger scale version is shown in Chapter 12.

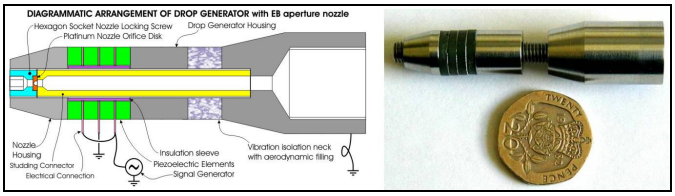

Figure 24: Droplet Generator, construction and appearance

The exact frequency at which the droplets were produced was controlled by a signal generator. To achieve consistent droplets this frequency was limited to a particular range related to the droplet size and velocity, as discussed in Chapter 12. A typical 270µm droplet stream produced by this is shown in Figure 25.

Figure 25: Stream of 270µm droplets from vibrating nozzle droplet generator

This method was capable of producing a very uniform stream of identical droplets at a precisely calibrated frequency. Whilst the mass and diameter of the droplets could not be precisely controlled, these could be accurately calibrated by collecting the droplets for a given period and weighing them on precision scales. This could determine the droplet size to better than 1% accuracy.

Such a droplet stream could not be used with the instrumentation for measuring the droplet acceleration and velocity. This consisted of three parallel laser beams, as explained in Chapter 13, and it was necessary that only one droplet should be intercepting the laser beams at any given time. Since, however, the spacing of the laser beams was much greater than the spacing of the droplets, this was a potential problem.

It was, however, found that the acceleration of the droplets greatly increased their spacing and the turbulence in the wind tunnel dispersed the stream. As a result, the likelihood of more than one droplet interrupting the laser beams in a given period was reduced to an acceptable level.

During the development of the laser beam droplet detection and measuring instrumentation it became increasingly apparent, from observing the resulting signals, that the droplets were not being delivered into the airflow as intended and that very irregular droplets were being detected, even though very regular droplets were being generated. It was not possible to observe what was happening, since no means of imaging the irregular high-speed droplets was then available.

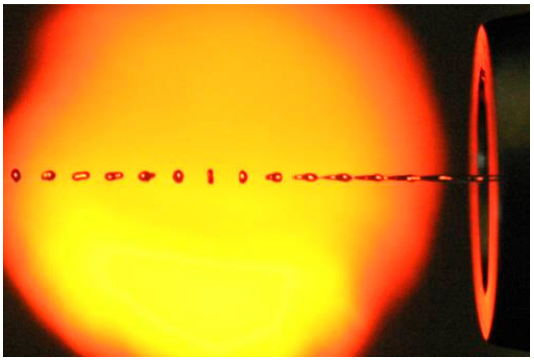

Figure 26: Image of droplet formation at the exit of the droplet generator.

It was possible to image the repetitive droplets as they were generated, as shown in Figure 26. This was obtained with back illumination from a low-power LED, when viewed through a low-power microscope. The LED was directly driven from a pulse generator that was triggered from the signal generator driving the piezoelectric elements of the droplet generator.

Since each LED flash was very weak, each image required many thousands of flashes. This was only possible because the image was identically repeated for each flash. This approach was not possible within the wind tunnel because the images were irregular.

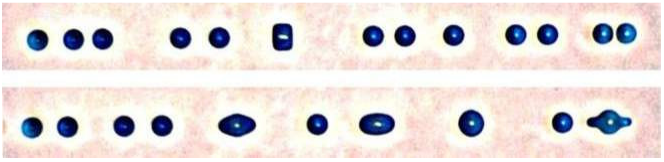

Figure 27: Irregular spacing and coalescence of droplets

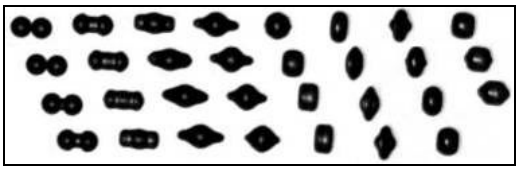

Figure 28: Video of droplet coalescence

To overcome this a much more powerful flash light, with much shorter flashes, was required, as discussed in Chapter 15.

With the development of a suitable flash light it was then possible to obtain images of the droplets in the wind tunnel and determine what was happening, as shown in Figure 27. With increasing distance from the droplet generator there was decreasing regularity in the droplet spacing due to aerodynamic interactions, until they came into contact to coalesce. Figure 28 shows a high-speed video sequence, taken at 50,000 pictures per second, of two droplets coalescing.

Figure 29, given in more detail in Chapter 12, shows that for regularly-spaced droplets the drag coefficient decreases as the distance between them decreases. This also occurs for one object following another.

It seemed reasonable to deduce that where there is a stream of identical and equally-spaced droplets that if some disturbance, such as turbulence, caused a droplet to be displaced along the stream then that would increase the drag on the droplet downstream of the increased gap and decrease the drag on the droplet downstream of the reduced gap. The result is to further increase the displacement of the initially displaced droplet and also displace the down wind droplet in the opposite direction. As a result the irregularity of the droplet spacing would increase, typically forming the droplets into groups of two or three, until they coalesce together, as shown in Figure 27 and discussed in Chapter 12.

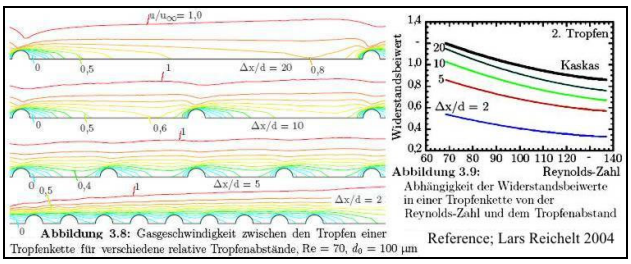

Figure 29: Effect of droplet spacing and Reynolds number on the drag coefficient.

Various tests were carried out to accelerate the droplets more rapidly, to more quickly increase their separation and reduce their interaction, by introducing them into higher-velocity air. Unfortunately this also just accelerated the coalescence process even more and provided no benefit.

It was concluded that to prevent this difficulty the droplet generator would have to produce droplets with a greater spacing. This was not directly possible with a vibrating-nozzle generator, since just reducing the vibration frequency, to increase the droplet spacing, was only possible over a very limited range, as this could, itself, result in the generation of irregular droplets and irregular droplet spacing.

One option, as considered in Chapter 12, was to use electrostatic charging of the droplets to remove the surplus ones. This would increase the spacing between the remaining

droplets and so reduce the aerodynamic interaction between them. Such technology has already been developed for continuous ink-jet printers, with which the author was very familiar. However, there was not sufficient time nor resources to develop this.

An alternative option, also considered in Chapter 12, was to place a spinning slotted disk in the path of the droplet stream. This could be synchronised so that selected droplets could pass through the slots, while the intervening droplet would be stopped by the disk. It was, however, observed with a high-speed video camera that it was effectively impossible for a droplet to pass cleanly through a slot due to the run-off across the slots from preceding droplets that had struck the disk. There were anyway appreciable difficulties in accurately synchronising the slots with the droplets.

It was reasoned that a more effective approach might be to place the spinning slotted disk close to a non-vibrating nozzle producing a uniform parallel jet which impinged on the rotating slotted disc. Passing slots would then allow through sections of the jet, which would subsequently form into a spherical droplets, as discussed in Chapter 12.

Unfortunately this method of droplet generation did not produce particularly uniform droplets, but it was possible to calibrate the volume mean diameter of the droplets by collecting and weighing the droplet stream for a given period. From knowing the slot passing frequency it was then possible to determine the average droplet mass.

Whilst this method was far from ideal, it did produce droplets of a known average mass and with the necessary spacing to minimise droplet coalescence. In this respect it was preferred to the vibrating nozzle method. Within the constraints of the time and resources available it was not possible to develop any better alternative.

The variability of the droplet size from the spinning slotted disk was considered to be the primary reason for most of the scatter in the experimental results. However when the results were averaged and fitted with the best regression line it was found that the variability of the average was much reduced.

LED Flash Light development

As discussed above, in order to observe what was happening with the droplet generation and delivery, it was necessary to have a means of imaging the small, irregular, high-speed droplets. An essential requirement of this was to have a very short exposure time. Given droplet diameters down to about 200μm, travelling at up to 100m/s, it was concluded that an exposure time of 50ns, or 0.05μs, would ensure a motion blur of no more than 5μm, which was consistent with the potential resolution of a suitable camera.

Such short exposure times could not be achieved with normal mechanical, or electronic, shutters. The one shutter method with the required capability was that of an image intensifier camera. In this the visible image was converted into an electron image which could then be manipulated at very high speed by an electrostatic field to achieve the required shutter speed, whilst also intensifying the image. Such a camera was too expensive to purchase and the image resolution and quality was appreciably degraded by the image intensifying process. An old version of such a camera was available later on, but it would have required a significant supply of Polaroid film and lacked the many benefits and flexibility of digital image processing.

It was deduced that if the illumination could be wholly provided by a flash of sufficient intensity and of sufficiently short duration, then almost any camera with the necessary

lens and optics could be used to obtain photographic images of the droplets.

Initially the preferred option for this was a high-power pulsed laser, which could produce high-intensity flashes as short as 10ns. Such equipment was too expensive to purchase and was not otherwise available. From a demonstration of such equipment, a LaVision PIV system, it was possible to obtain some initial low-resolution images of the droplets. A typical example, with droplets of about 270µm, is shown in Figure 30.

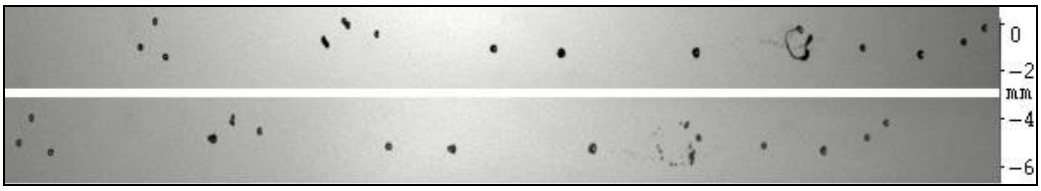

Figure 30: Typical low-resolution droplet image pair from a PIV imaging system.

The two images in Figure 30 were taken with a short time interval between them, with the droplets travelling from right to left. They show how irregular the droplets became, despite having been injected as a coherent stream of droplets. One of the coalesced droplets can be seen in the process of break-up, due to the aerodynamic forces from the increasing acceleration.

The same camera trial included a preliminary test of an early version of an LED (Light Emitting Diode) flash unit, as shown in Figure 31. Although the image quality was limited, it showed the potential of the method.

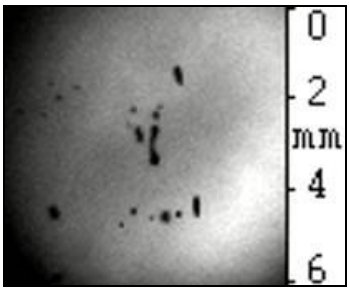

Figure 31: Preliminary test of LED flash light.

As discussed in Chapter 15, the LED flash unit was developed into a much more powerful unit, capable of 50ns flashes at 100kHz, with each flash capable of recording an individual image in a high-speed video camera, as shown in Figure 28 for a video sequence taken at 50kHz.

Obtaining droplet video and still images

For still photographs the LED flash unit was initially used with a digital astronomy camera. This was capable of recording the very low light levels from the shortest 50ns flash duration. It was, however, a difficult piece of equipment to use and this was later replaced with a standard SLR digital camera. Whilst this did not produce such good image quality, quite adequate pictures were obtained with the increased light output from the LED flash unit and the camera was much easier to set up and align.

Later a high-speed video camera became available on loan for a short period. This was used to obtain most of the droplet video sequences, such as Figure 28.

It was anticipated that the droplet images might be used to determine the droplet distortion for various conditions, however the image quality and repeatability was never really sufficient for this and it was, in any case, unnecessary since the required data was otherwise available, as discussed in Chapter 6.

Instrument for measuring droplet acceleration and velocity

A low cost means for accurately measuring the droplet velocity and acceleration was a requirement for this research. Knowing the droplet diameter and mass its parameters could then be determined in terms of the Reynolds number, Weber number, Bond number and Drag coefficient.

The more conventional methods of measuring droplet motion, such as PIV and laser Doppler, were not available and were anyway not capable of directly determining the droplet acceleration, with the necessary accuracy, in such a sparse droplets distribution.

An alternative method was developed for this, as explained further is Chapter 13. This used three parallel and equally spaced laser beams laying in a plane, produced from low-cost diode lasers. These were shone across the transparent wind tunnel, in which the accelerating air flow carried a stream of droplets to be measured. The beams were orientated so that any droplet could intercept all three beams at right angles near their focal points. These beams were each detected by a photo detector, which transmitted the resulting electronic pulses to a digital oscilloscope with a computer interface.

Chapter 14 gives the detailed analysis of the calculations required to obtain the droplet velocity and acceleration from the time intervals between the resulting pulses.

In this x_1 and x_2 were the respective spacing between the 1st and 2nd and 2nd and 3rd laser beams and t_1 and t_2 were the respective time intervals between the 1st and 2nd and 2nd and 3rd pulses from the beam interruptions.

From this the droplet velocity, $\mathbf{U_0}$, and acceleration, **a**, were calculated at the location of the middle beam with the following equations;

$$\mathbf{U_0} = \mathbf{(x/t).(1+\beta.(\beta - 2.\alpha))/(1-\beta^2) - b.t^2.(1-\beta^2)/6}$$

$$\mathbf{a} = \mathbf{(2.x/t^2).(\beta - \alpha)/(1-\beta^2) + 2.b.t.\beta/3}$$

where $\alpha = (x_1 - x_2) / (x_1 + x_2)$

$\beta = (t_1 - t_2) / (t_1 + t_2)$

$x = (x_1 + x_2) / 2$

and $t = (t_1 + t_2) / 2$

The parameter, **b**, was the rate of change of acceleration, or jerk, of the droplet, which represented the changing conditions along the tunnel. The jerk could not be determined with only three laser beams, since at least four beams would be required for that. It was neither necessary nor practical to use more than three beams due to the constraints of geometry, resources and time. It was possible to evaluate the droplet jerk from the pressure gradient along the tunnel or using the droplet motion simulator. For the conditions of interest, the jerk had a very minor effect on the results compared to more significant uncertainties, such as droplet size variability from the droplet generator.

When a suitable sequence of signals were obtained, these were transmitted to and stored in the computer as text files. These files were later analysed with a computer program to determine the droplet velocity and acceleration and the resulting drag properties.

Other Measuring Errors

In additions to errors due to the basic principles and alignment, there were also other potential errors in the measurement of droplet velocity and acceleration due to incorrect determination of the droplet location or signal timing.

One of these was refraction of the laser beams as they passed at an angle through the transparent wall of the tunnel. This would introduce a slight parallel offset of the beam. Providing the transparent sides of the tunnel were of uniform thickness and flat then the beam offset would be equally applied to all three beams, so would cancel out any ef-

fects. This would, very slightly, shift the location at which the measurement was made, but that effect was neglected.

In practice the transparent tunnel walls were slightly curved, so this could mean that the different beams passed through the walls at slightly different angles. Hence each beam would have a slightly different refraction offset. If the refraction offset was proportional to the distance along the tunnel, which would almost be the case with a constant curvature of the tunnel walls, then this would slightly change the spacing of the laser beams to very slightly affect the velocity measurement, but it would not affect the symmetry of beam spacing, so would also only have a small effect on acceleration measurement. Given that, at the measuring location, the thickness, angle and curvature of the tunnel wall was quite small, these refraction effects were considered negligible compared to other much more significant uncertainties.

Another issue was to what extent the position of the droplet along the tunnel, in particular its centre of mass, could be determined when passing through a laser beam. The time at which the droplet was deemed to be at the laser beam location was taken to be midway between the time for 50% pulse height of the rising and falling pulse edge, when the droplet interrupted the beam. If the droplet shape was irregular then it would be possible for the centre of mass to be slightly displaced from the location determined by the laser beam. Figure 32 shows the typical shape of distorted droplets of about 250μm, volume mean diameter.

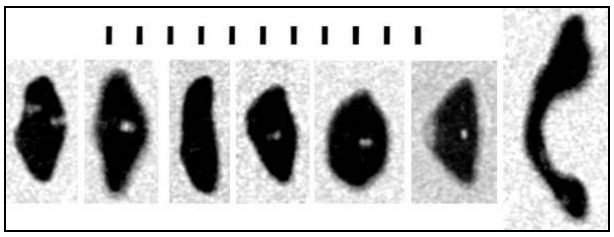

Figure 32: Typical droplet shapes

If the droplet shape remained reasonably constant while intercepting the three beams across the same section of the droplet, then there would be an equal offset discrepancy for all three beams, which would cancel out any errors. If, however, the droplets were changing shape, or the beams intercepted across different sections of the droplet, then this could result in a different offset error for each beam, which could be interpreted as an error, particularly with respect to the droplet acceleration.

A critical issue was the offset of the middle beam from the central location between the two outer beams. Normally this would be aligned to be within about 10μm. The beams had a spacing of 25mm, so if the outer beams had an offset of 17.5μm in one direction and the middle beam an equal and opposite offset this would respectively give beam spacing of (25mm – 35μm) and (25mm + 35um), which would then give a value for α = 70μm/50mm = 0.14%. The important issue was the value of this as a proportion relative to the time asymmetry parameter, β, which was typically around 7%. Given these conditions the additional error in the acceleration would be about 2%.

It was reasoned that the maximum offset error would be a small fraction of the 200μm droplet thickness. It was thus considered that this offset error was likely to be less than 17.5μm and it was unlikely that the worst combination of offset errors would occur. It was thus concluded that the acceleration error due to these measuring offsets would be very much less than 2%. Since these errors would be random and of either sign the average acceleration error expected from this effect would be much less than 1%.

Experimental measurements

Once the necessary experimental facilities and methodology had been developed, a series of experimental measurements were then carried out. This and the calibration procedure are discussed further in Chapter 5 and Chapter 11.

Due to various delays in the equipment development, there was not sufficient time available for the comprehensive range of experiments intended. In practice the experiments had to be limited to one droplet size. The volume mean diameter used was 250µm, which was in the middle of the critical range relevant to icing with supercooled drizzle and also the most difficult range for the computer modelling of droplet drag.

Originally it had been intended to run the tunnel fan at a fixed speed and then traverse the instrumentation along the tunnel length to observe the resulting variations in droplet velocity and acceleration. These results were then to be compared against the predicted characteristics of the convergent tunnel. It was, however, not practicable to carry out the experimental measurements in this way, as a suitable carriageway for the instrumentation was not available.

The tunnel suction fan was, however, equipped with an accurate variable speed control. This enabled all measurements and imaging to be at a fixed location, near the tunnel exit, with the fan speed varied to achieve the required droplet conditions. This allowed use of a much simpler fixed support for the imaging and measuring equipment.

A three axis manual manipulator was used to support the measuring instrumentation, as shown in Figure 33. This provided fine adjustment of the height and position along the tunnel. The unit also had to be tilted to align the laser beams with the droplet trajectories, which was achieved with a wedge under one edge of the manipulator base.

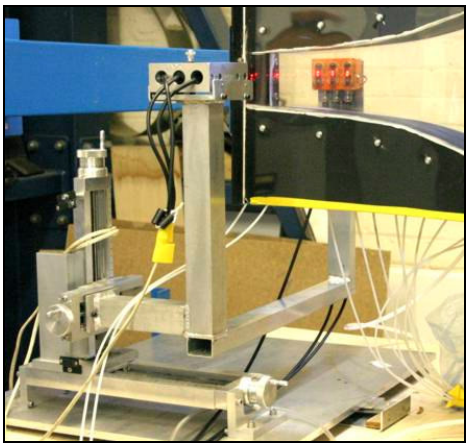

Figure 33: Three axis manipulator for droplet measuring instrumentation.

A requirement of the experiment was to determine the velocity difference between the droplet and airflow to obtain the Reynolds and Weber numbers. This required that both the droplet velocity and the air velocity be known.

The tunnel air velocity was determined from pressure tappings in the tunnel wall. These were at 40mm intervals, with the last tapping 20mm from the tunnel exit. From CFD modelling it was found that the pressure distribution across the tunnel section was sufficiently uniform and that the static pressure at the tunnel axis was the same as at the tunnel wall, Chapter 10 and 11. No total pressure measurements were made in the tunnel, since it was concluded that the flow along the tunnel axis was isentropic and that the total pressure at the axis would be the same as the total pressure in the plenum chamber. Since the air velocity in the plenum chamber was negligible, the static pressure in the plenum chamber was assumed to be the same as the total pressure along the tunnel axis.

Near the tunnel walls the total pressure was expected to be lower due to the reduced air velocity within the boundary layer. CFD analysis showed that the boundary layer at the tunnel section of interest was typically only about 1mm or so thick.

The imaging and measurements were located 40mm from the tunnel exit, midway between the last two pressure tappings. This allowed sufficient clearance from the tunnel end for the required imaging and measurement, but was also sufficiently near the exit that the required aerodynamic forces could be achieved with the 250μm droplets.

For this it was necessary to calibrate the tunnel flow against fan speed. The details of this are discussed in Chapter 11. The essential requirement was to measure the pressure difference between the plenum chamber and last two pressure tappings. From these measurements the air velocity was calculated by assuming ideal adiabatic compressible airflow. In this calculation the ambient air temperature and pressure were measured and allowed for. The plenum chamber temperature was obtained from a mercury thermometer on the inlet screen. The pressure in the plenum chamber was assumed to be the same as the barometric pressure, obtained from a high precision digital manometer in a neighbouring laboratory. The pressure difference across the inlet screen was less than 0.5mb, or 50Pa, at the maximum fan speed.

It was recognised that there could be a small pressure difference between the laboratory pressure and barometric pressure due to the airflow into the open circuit tunnel from the laboratory and then exhausted outside. This then had to be replenished from outside through vents, which could cause a small pressure drop. The maximum airflow was about $1m^3/s$, or about 1m/s, velocity through the inlet screen. It was concluded that, providing the external door of the laboratory was open during the tunnel operation, then this would provide the necessary air replenishment with a negligible difference between the laboratory pressure and barometric pressure.

It was also possible that there was a small discrepancy between the plenum chamber pressure and barometric pressure due to the temperature difference between the laboratory and the outside temperature, with the resulting difference in air densities. Once the tunnel was running, the air change in the laboratory quickly brought the laboratory to the atmospheric temperature, so such differences were minimal.

The airflow calibration was carried out for a particular set of atmospheric conditions, in terms of temperature, pressure and humidity, Chapter 11. The air humidity was not recorded and its effects were neglected. During the calibration and experiments there were no days in which there were exceptional conditions. The main concern with humidity was that this might affect evaporation from the droplets, but the droplet exposure to the air was so short it was considered that such effects could be neglected.

It was recognised that the tunnel calibration would depend on the particular conditions at the time. It was, however, not possible to fully recalibrate each time the tunnel was used. It was accepted that the inlet air density would depend on the ambient temperature and pressure, but it was found that, in general, these tended to be related in such a way that variations in the ambient air density were quite small.

It was presumed that, for small changes in ambient air density, the relationship between the tunnel air velocity and the fan speed would remain reasonably independent of air density. This presumption was not investigated any further due to the limitations of time and the fact that it was considered to be a minor issue in comparison to other larger uncertainties, such as droplet size variability.

Since the tunnel air velocity was expected to be approximately proportional to fan speed, the calibration was plotted as the ratio of air velocity to fan speed against fan

speed, as shown in Figure 34, to provide the maximum resolution of the graph. It can be seen that there was a variation of about 15% in the proportion of air velocity to fan speed, which was attributed to differences in Reynolds number and Mach number effects in the tunnel and fan. In practice most of the experimental measurements were carried out at a fan speed between 1200rpm and 2400rpm, or between 40% and 80% of the maximum fan speed. Over this speed range the ratio of air velocity to fan speed varied by less than 2%.

Each calibration point in Figure 34 for the two pressure tappings was the average of at least nine pressure readings for the same conditions.

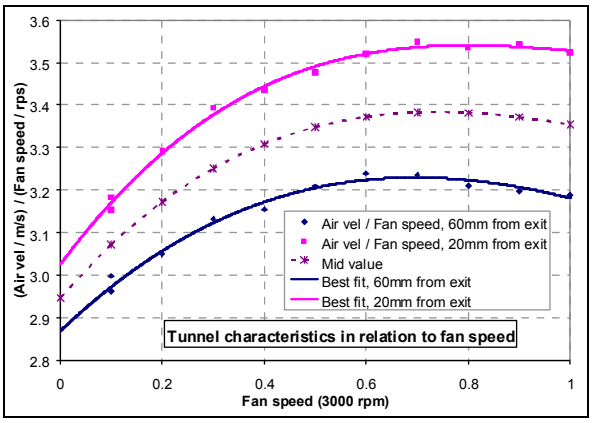

Figure 34: Tunnel flow calibration.

From the geometry of the tunnel convergence and airflow analysis, it was found that the velocity gradient along the tunnel was near to constant in the section of interest, so the air velocity midway between the pressure tappings was taken as their average velocity. The variance in the mean velocity calibration was evaluated to be less than 0.4%.

When the tunnel was run for an experiment, the conditions were allowed to stabilise for about 30minutes, so that the conditions in the laboratory were similar to the external atmosphere. The ambient pressure and temperature were recorded and used to determine the inlet air density for the necessary flow analysis.

Comparison between the drag model and experiment

From the computer model, discussed in Chapter 3, and the experimental measurements, as described in Chapter 5, the two set of results for 250µm droplets were compared, as shown in Table 1and Figure 35.

Reynolds number	**Weber Number**	Measured Bond No.	Calculated Bond No.	Sphere Bond No.	Measured Cd	Calculated Cd	Sphere Cd	Cd difference, Measured to Calculated	Calculated Cd ratio, droplet to Sphere
558	**4.81**	2.79	2.77	1.94	0.773	0.768	0.538	0.8%	1.427
708	**7.75**	4.55	5.63	2.95	0.782	0.969	0.507	-19.2%	1.912
824	**10.57**	7.85	9.29	3.88	0.990	1.172	0.489	-15.5%	2.396
910	**12.97**	12.88	13.08	4.66	1.324	1.345	0.479	-1.6%	2.809
1003	**15.88**	18.41	18.45	5.59	1.546	1.549	0.470	-0.2%	3.299

Table 1: Comparison between experimental and calculated results for 250µm droplets

This shows the experimental results for five different fan speeds, 1200rpm to 2400rpm, giving an air velocity from 67m/s to 136m/s. It can be seen that there was substantial scatter in the experimental results and most of this was attributed to the difficulties of generating and delivering uniform (monodispersed) droplets to the measuring location.

Results were obtained for average Weber numbers of 4.8, 7.8, 10.6, 13.0 and 15.9. When the average of each data group was taken, for the Weber numbers of 4.8, 13.0 and 15.9 there was very good agreement between the experimental results and the computer model to within 1.6%. The worst discrepancy was at a Weber number of 7.8, where the average experimental Bond number and drag coefficient was 19% below the computer model. At a Weber number of 10.6, the average experimental result was about 15.5% below the computer model.

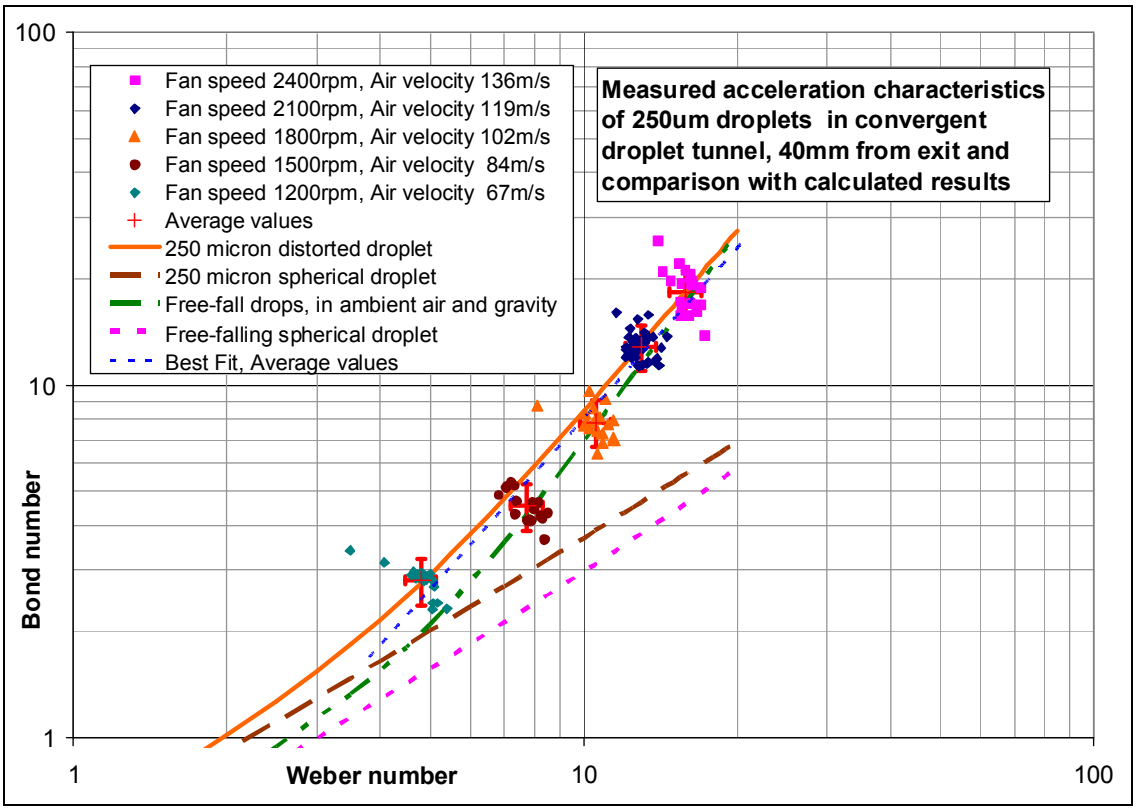

Figure 35: Comparison of Bond number measurements and computer model with Massey data

Because of the variability of droplet size and limited amount of the experimental results, it was not possible to determine if the discrepancies between the experimental and modelling results were due to errors in the measurements, the computer drag model, or both.

It can be seen from Figure 35 that the average experimental results for We = 7.8 and 10.6 were close to the curve for free-falling droplet data, which indicates that the experimental results were lower than expected. To resolve this would have required repeating the measurements with a better droplet generator and at more speed increments.

In this comparison the computer model used the disk drag data from Massey. When the disc drag data from Streeter was used, then at a Weber number of 7.8 this increased the discrepancy between the model and the average experimental result by a further 5%, to around 24%. From this it would appear that the disk drag data from Massey gave the better correlation with the experimental results.

Also shown in Figure 35 is a regression line through the average experimental results and it can be seen that it was in good agreement with the computer model between a Weber number of 7 and 14. With Excel it was only possible to fit a straight line.

Whilst the quality of the experimental results were more variable than intended and

there were uncertainties in the computer mode, the resulting agreement was sufficiently good to provide a practical means of evaluating the drag properties of deformable droplets, at least up to a Weber number of 16.

Clearly the droplet drag computer model was a substantial improvement on the spherical droplet assumption, as shown by Figure 35. It is understood that previous to this investigation the droplets were assumed to be spherical in the SLD aircraft icing analysis.

Table 1 shows that for 250µm droplets and We > 8 the drag was at least double that for the equivalent spherical droplet. At a Weber number of 15.9, for a 250micron water droplet, the measured and calculated drag on the deformed droplet was about 3.3 time that for a spherical droplet. For a Weber number of 20 the increase in drag, compared to sphere, would be about 4 to 1, assuming the droplet remained intact for such conditions.

The results in Figure 35 were plotted as Bond number against Weber number since this was found to be a better way of presenting the drag effects for deformable droplets. This was because of the significance of surface tension and the benefit of directly representing the droplet acceleration, which is normally the required result.

It is understood, however, that to those more familiar with the drag forces on rigid objects this may be an unfamiliar method of representing such data and the more conventional drag coefficient was preferred. From that the drag force can be calculated, which can then be used to determine the droplet acceleration.

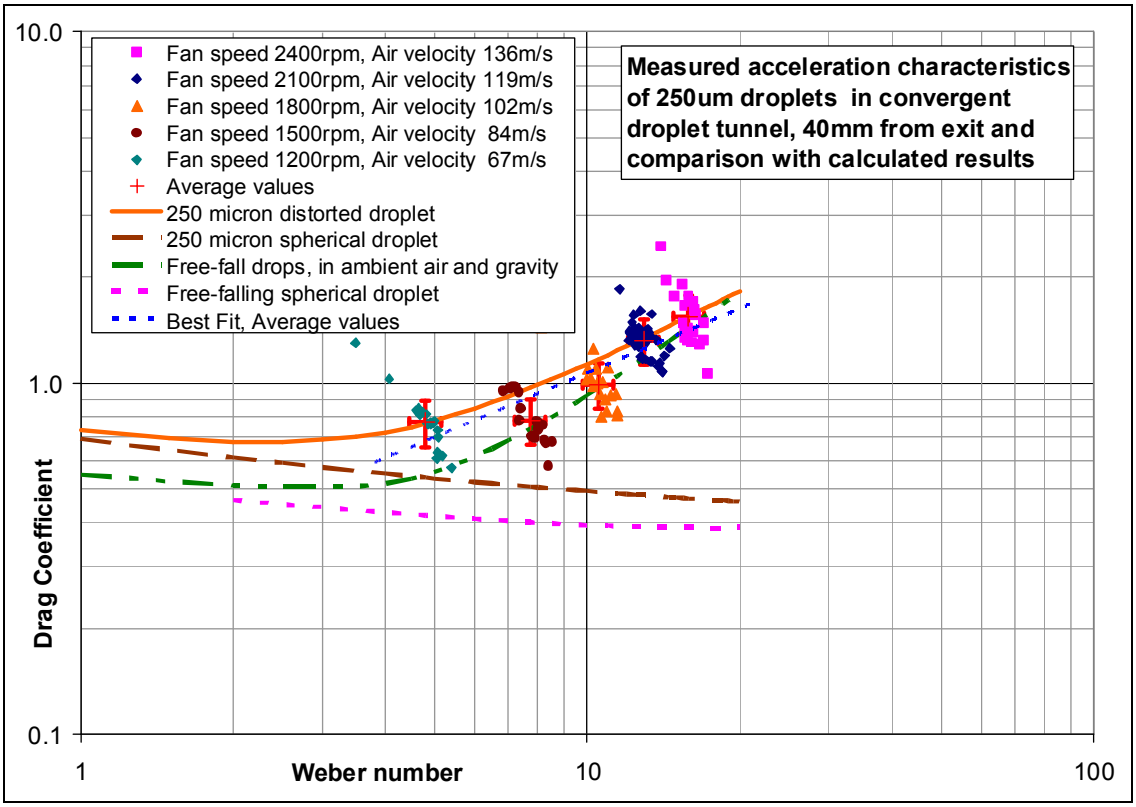

Figure 36: Comparison of Drag Coefficient measurements and computer model with Massey data

The drag coefficient can readily be determined from the Bond number and Weber number using the relationship; $Cd = {}^{4}/_{3}.Bo/We$. This was applied to present the results in terms of drag coefficient, as shown in Figure 36.

In this the drag coefficient is still plotted against Weber, rather than Reynolds number, as it would be for a rigid object. This because the Weber number takes into account surface tension and droplet deformation. For a given droplet size, or more specifically a given Laplace number, the relationship between Weber number and Reynolds number remains consistent. Changing the Reynolds number, with respect to the Weber number, is best characterised with a change in Laplace number, which represents a change in droplet size. Hence the results can then best be plotted as either Bond number, or Drag coefficient, against Weber number for various values of the Laplace number.

For water droplets of 250μm diameter in ambient air conditions, with $\rho_a = 1.19 kg/m^3$, $\mu_a = 18.\mu m^2/s$, $\sigma = 70.mN/m$, the Laplace number is 65.2×10^3. For other droplet diameters the Laplace number is proportional to droplet size.

Outcomes of the Investigation

1. A numerical computer simulation was developed from an earlier version to model droplet motion dynamics, allowing for the increased drag due to droplet distortion. For droplet modelling in convergent tunnels this included a correction for the tunnel convergence, the ability to directly calculate the required convergent profile to achieve specified droplet conditions and the facility to compute the solution with respect to various independent variables, such as time and distance along the tunnel.
2. An effective method of bright field still and video imaging was developed with an LED flash lamp capable of 100,000 flashes per second with a flash duration down to 50ns. This enabled video and still images to be obtained of distortion, aerodynamic break-up and splashes of droplets with a resolution down to 10μm or better and at a video rate of at least 50,000 pictures per second.
3. Special instrumentation was developed to measure the linear velocity and, in particular, acceleration of droplets to better than 5% accuracy. This used three parallel and equispaced coplanar laser beams to determine the droplet motion.
4. A transparent convergent droplet research tunnel was developed to apply the necessary aerodynamic forces to droplets in a controlled manner to approximate the aerodynamic conditions in the vicinity of a full-scale aerofoil. This enabled the behaviour of the affected droplets to be observed and measured.
5. A vibrating-nozzle droplet generator was developed to produce a stream of monodispersed droplets. It was, however, found that the close droplet spacing and resulting aerodynamic interactions caused irregular droplet spacing, droplet coalescence and irregular droplet size. An alternative droplet generator was developed, in which a uniform jet impinged on a rotating slotted disk. This achieved the required droplet spacing, but the droplet size distribution was more irregular than intended and resulted in significant variability in the experimental results for droplet drag characteristics.

Overall Conclusions

1. In the vicinity of an aerofoil the strong aerodynamic forces can have substantial effect on the distortion, drag, motion and break-up supercooled drizzle droplets.
2. The distortion of the droplets can substantially increase their aerodynamic drag, of intact droplets by a factor two at a Weber number of 8, a factor of three at a Weber number of 16 and a factor of four at a Weber number of 20.
3. These effects on the droplets could have a significant effect on the SLD icing process of aircraft. Further work is required to model the trajectories and motion of drizzle droplet around an aerofoil, taking account of the distortion and resulting drag increase, to evaluate how this would effect the SLD icing process.
4. There are significant scaling issues with respect to the pre-impact droplet trajectories and motion that need to be considered for icing tests with small-scale models, if these are to adequately reproduce the SLD icing conditions for medium to large scale aircraft.
5. The SLD icing process with large aircraft could be significantly different to that for smaller aircraft and test models. If so then this could have important implications for various aspects of the specification, design and operation of aircraft.
6. An effective and efficient semi-empirical model of the drag characteristics of deformable droplets was developed. For droplets greater than 200μm that was consistent with experimental measurements to better than 20%. This model could be extended to smaller droplets with appropriate amendments.
7. The distorted shape of a droplet is primarily determined by the droplet acceleration, as represented by the Bond number. The external aerodynamic pressure, as represented by the Weber number, having only a secondary effect. The aerodynamic pressure distribution primarily determines the drag force and hence the resulting droplet acceleration, which in turn primarily determines the droplet deformation. The droplet deformation then in turn affects the droplet drag force.
8. An approximate analysis showed that the cause of bag break-up was a Rayleigh-Taylor instability of the flattened windward surface of the distorted droplet. This showed that airborne droplets would become unstable and break-up above a sustained Bond number of 13.7. For distilled water droplets free-falling in standard conditions the critical droplet diameter was determined to be 10.1mm, compared to the experimental diameter of 10mm, for which the Weber number was 14.2.
9. In appropriate conditions droplets could survive very severe transient loading, to a Weber number of 30, for short periods relative to their natural response time, as represented by their small perturbation vibration period.
10. It was possible to use a convergent accelerating flow in a low-cost wind tunnel to adequately reproduce the conditions of aerodynamic conditions experienced by droplet in the flow field around an aerofoil. This could only reproduce the linear motion effects, but that was a significant advance in gaining an understanding of the behaviour of drizzle droplets in SLD icing conditions.

11. It was possible to measure the acceleration of distorted droplets with an accuracy of 5%, or better. Knowing the droplet mass and density it was then possible to determine the experimental drag characteristics.
12. The 1D corrected method for analysing flow in a steeply convergent tunnel enabled the required convergent profile to be directly computed to achieve a specified loading profile for the droplets against time or distance.
13. The LED strobe light enabled silhouette images of drizzle droplets to be recorded from a single 50ns flash with the necessary quality and resolution. This also enabled long video sequences to be obtained at the rate of up to 50,000 frames per second. This greatly enhanced the ability to record relevant droplet events compared to the alternative imaging technology available.
14. To obtain improved experimental data for the drag characteristics of droplets it will be necessary to develop an improved droplet generator to produce calibrated droplets with sufficient spacing to prevent droplet coalescence.

Further Work

1. Develop an improved droplet generator to produce calibrated monodispersed droplets with sufficient droplet spacing to minimise aerodynamic interactions and droplet coalescence. It is anticipated that this would use a vibrating nozzle generator followed by electrostatic deflection to remove surplus droplets.
2. Improve the LED flash and imaging capability to achieve better quality images of droplets with improved image resolution. Preferably this would also have the capability of achieving frontal illumination of droplets against a dark background.
3. Develop an experimental facility which would allow simultaneous measurement of velocity, acceleration, size and shape of individual droplets.
4. Improve the facilities of the droplet tunnel to enable better manipulation and positioning of the imaging equipment and instrumentation.
5. Consider the development of a means to simultaneously obtain orthogonal views of the droplets in the tunnel.
6. Carry out further experimental measurements of droplet drag characteristics for a more complete range of conditions and droplet sizes.
7. Construct other transparent convergent working sections for the droplet tunnel which will create transient conditions for the droplets, so that such effects can be experimentally investigated.
8. Develop an effective and efficient transient dynamic model of the droplet distortion. It is anticipated that this may be developed using energy methods and droplet vibration modes with limited degrees of freedom.
9. Evaluate the effect of the drag corrections on the SLD icing process on both full scale and scale model aerofoil using the icing simulation codes.

Chapter 2: Scaling and Transient issues

Droplets in SLD icing are substantially larger than in the more familiar small droplet icing in clouds and fog and have greater inertia in comparison to their aerodynamic drag. It might then be presumed that the aerodynamic forces on droplets in the airflow around an aerofoil have only a minor effect on their velocity and trajectory.

This may, indeed, be the case with small-scale test models, such as may be used in wind tunnel tests to investigate icing, but it may not be the case with full-size aerofoils, such as found on medium to large passenger and freight aircraft.

The purpose of this chapter is to evaluate whether there was likely to be a significance issue with scaling and transient effects, related to droplet behaviour in SLD icing, prior to impact with the aerofoil. The investigation and treatment is approximate, is not exhaustive and is only intended to illustrate the significance of the scaling and transient issue on the pre-impact behaviour of the larger droplets in SLD icing.

A substantial number of references on the scaling of aircraft icing have been identified (Anderson 1994, 95, 95, 96, 96, 98, 99, 2000, 01, 01, 01, 02, 03, 04), (Ruff 1986, 97, 98, 99, 99), (Kind et al 1998, 2001, 01, 02, 03), (Feo 2000), (Papadakis et al 2001), (Armand 1978). Many of these were obtained and reviewed, but virtually all the attention was given to what happened to droplets when and after they struck the aerofoil surface, such as splash, runback and freezing. Almost no consideration was been given to the scaling effects and droplet distortion in the flow field around an aerofoil prior to droplet impact. These issues could significantly affect, or even prevent, the droplet impact in various ways and so have a significant effect on the SLD icing process.

In his publication "Scaling of Icing Tests – A Review of Recent Progress", (Kind 2003), consideration was given to the "recognition that flowfield and droplet-trajectory similarity are necessary", but within the review no consideration was given to the effect that droplet distortion might play in this, presumably because of the assumption that the droplets considered were typically 50µm, or less, in which case droplet distortion was not considered to be a significant issue. Again the focus was on what happened after the droplet contact with the aerofoil surface.

Anderson has provided extensive experimental results on the scaling effects of icing obtained in the NASA Lewis Icing Research Tunnel, with aerofoils and cylinders. It appears that the largest aerofoil tested by Anderson had a chord of 0.914m, and NACA 0012 section with a leading edge radius of about 15mm. The largest cylinder had a radius of 76mm. His tests, however, mostly appeared to be with droplets of around 50µm.

Wright and Potapczuk (AIAA 2004-0412) was the one publication identified which did consider the drag increase due to the distortion of larger droplets in modelling the droplet trajectories, but incorrectly concluded that the drag "at most is 15% higher than the drag of a sphere". This research has, however, shown that for a Weber number of 16 the drag can increase by a factor of three and Wright and Potapczuk calculated that such Weber numbers would readily occur. Hence it was concluded that no other research into SLD icing had sufficiently considered the significance of pre-impact and dynamic response of droplets on the similarity and scaling of the droplet trajectory and velocity.

It was considered possible that the transit of droplets through the flow field around the leading edge of an aerofoil or the upstream side of a cylinder could be sensitive to scaling two ways;

1. Scaling may significantly affect the trajectory and velocity of droplets in the flow field and this could affect the impact velocity, angle and distribution. This may determine whether impact occurs or if it results in aerodynamic break-up of the droplets.
2. Scaling issues may significantly affect the temporal response to aerodynamic loading of droplets. This may determine whether the droplet conditions are transient and produce a dynamic response, or are nearer to quasi-static conditions to which the droplet can respond in a near-steady way.

Scaling effects on droplet motion

The conditions experienced by a droplet will depend on where they enter the flow field of an aerofoil. One option is that they enter the stagnation region near the leading edge, but an alternative is that they enter the accelerating flow over the upper surface of the aerofoil. In either case the size of the flow region will, typically, be proportional to the size of the aerofoil.

The purpose of this evaluation was not to produce an exact solution for the behaviour of the droplets, but to illustrate the nature of the issue, how this is dependent on the scale of the aerofoil and determine what may be relevant scaling parameters.

For the purpose of this evaluation and by way of an example the droplets entering the stagnation region at the leading edge was considered. The flow close to the leading edge will be dominated by the local geometry of the aerofoil, in particular the leading edge radius. This was approximately represented by the inviscid flow upstream of a suitably scaled circular cylinder, which produces an approximately similar flow near the upwind stagnation region. Due to the close proximity to the leading edge, the flow field may typically be considered to have an effective thickness related to the leading edge radius, or another relevant aerofoil dimension.

Static Air Layer Model

For the purpose of simplicity and to identify relevant parameters, initial consideration was given to a the hypothetical situation of a droplet entering a layer of static air at the free-stream velocity. The issue was then whether its motion would be significantly affected after travelling a distance about equal to the leading edge radius, or the radius of a cylinder producing a similar flow near the windward stagnation region.

Given the assumption of a constant drag coefficient, Cd, in stagnant air and no compressibility effects, the equation of motion and force balance is given by;

$$m.dU/dt + Cd.A.(\rho_a.U^2/2) = 0 \quad \text{(acceleration force + drag force = 0)}$$

hence $\rho_w.(\pi.D^3/6).dU/dt + Cd\,(\pi.D^2/4).\rho_a.U^2/2 = 0$

or $dU/dt = -(^3/_4).(Cd / D).(\rho_a/\rho_w).U^2 = U^2 / (t_0\, U_0)$

hence $U_0 .\, dU/ U^2 = dt/t_0$

The solution derived for this simplified situation was;

$$U/U_0 = (1 / (1 + t / t_0)) = Exp(-x/x_0)$$

or $x/x_0 = Log_e(1 + t / t_0) = - Log_e(U/U_0)$

where $t_0 = (^4/_3).(\rho_w / \rho_a).(D / (Cd.U_0)) = U_0/(dU/dt)_0 = U_0 /a_0$

$x_0 = U_0.t_0 = (^4/_3).(\rho_w / \rho_a).(D/Cd) = D.Fr_0 = U_0^2 / a_0$

U_0	initial droplet velocity on entering the stagnation region
a_0	initial droplet deceleration
x	distance travelled in the stagnation region
t	time from entering the stagnation region
U	droplet velocity
ρ_w	density of the droplet
ρ_a	density of the air
D	droplet volume equivalent diameter
Cd	constant drag coefficient
Fr_0	Initial Froude number, $(U_0^2 / a_0.D)$

We can compare the time constant, t_0, with the nominal transit time, t_t, it would take for a droplet to penetrate the flow field at constant velocity at the leading edge of an aero-foil. This is given as;

$$t_t = R / U_0$$

where R is a reference length, such as the radius of the leading edge, or radius of an equivalent cylinder.

Hence the ratio of these two time constants is give as;

$$t_0 / t_t = (^4/_3).(\rho_w / \rho_a).(D / (Cd.U_0)) / (R / U_0)$$

$$= {}^4/_3.Cd.(\rho_w / \rho_a).(D / R)$$

This gives the dimensional parameter group: $\mathbf{(Cd.(\rho_w / \rho_a).(D / R))}$

For the conditions above this gives the result;

$$t_0 / t_t = {}^4/_3 \text{ x } 1.5 \text{ x } (1000 / 1.2).(150\mu m / 45mm) = 5.56$$

For given fluid properties, such as water and air, the density ratio, ρ_w / ρ_a, will, near ground level, be within a reasonably narrow range.

For given droplet conditions, such as represented by the Weber number, the value of Cd will also be within a given range.

Hence, to maintain geometric similarity, it is necessary that the ratio of droplet diameter to the leading edge radius remain within a reasonable range.

We can consider the conditions;

$$U_0 = 80m/s,\ \rho_w = 1000kg/m^3,\ \rho_a = 1.2kg/m^3,\ D = 150\mu m,\ Cd = 0.5$$

$$t_0 = (^4/_3).(1000 / 1.2).(225E\text{-}3 / (0.5 \quad 70.71)) = 3.73ms.$$

$$x_0 = t_0.U_0 = 333mm$$

This gives an initial deceleration of $19200m/s^2$, at a Weber number of 16.

The relationship between velocity, distance and time in shown in Figure 37. The solid line shows the velocity and the dashed line the distance travelled.

In the time $t_0/2$ or 2.1ms, the droplet velocity decreases to 67% of its initial value, and kinetic energy to 44% of its initial value. The distance travelled by the droplet in the time $t_0/2$, from Figure 37, was 135mm. To achieve this could require a cylinder radius of around 250mm, or a leading edge radius of about 150mm. Figure 38 shows the approximate relationship between the airflow near the leading edge and the upwind side of an equivalent cylinder.

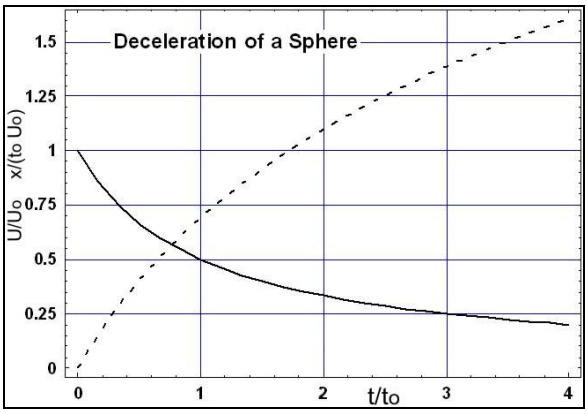

Figure 37: Deceleration of a sphere with a constant drag coefficient, Cd, in still air.

At the initial velocity the droplet would have a nominal Weber number of 16, so this would cause substantial droplet distortion and hence a substantial increase in its drag, as discussed in Chapter 3. Typically for such a condition the drag coefficient would increase by about a factor of 3.3. Hence it would be reasonable to assume a drag coefficient of about 1.5, with respect to the equivalent spherical diameter. This gives a value for $t_0/2$ of 1.4ms, in which time the distance travelled by the droplet would only be about **45mm** for the velocity to decrease to 67% of its initial value.

In Anderson 2002, (AIAA-02-0521), two NACA 0012 scale aerofoils were used to study the scaling effect for SLD icing. One had a chord of 0.914m and leading edge radius of 14.4mm. The other a chord of 0.53m and leading edge radius of 8.42mm.

The nature of the flow around the leading edge of a typical aerofoil is considered later in this Chapter, in Figure 38. This shows that most of the change in the air velocity approaching the leading edge occurs within about twice the leading edge radius, with the mean thickness of the flow field about equal to the leading edge radius. This would, of course, be affected by the incidence and geometry of the aerofoil, but it provide a rough guide of the flow field thickness.

It would thus appear that for the scale models used by Anderson the flow field around the leading edge would not be of sufficient thickness to cause significant deceleration, or deflection, of the droplet size of a150µm considered above.

For an ATR72 wing, the average chord was around 2.5m, with a leading edge radius of around 45mm. This radius was comparable to the distance travelled in stagnant air for a velocity reduction to 62%, with an assumed drag coefficient of 1.5 for a Weber number of 16. In larger aircraft the leading edge radius would be even greater, so an even more significant effect would be expected on the droplet velocity and trajectory.

The preceding approximate evaluation indicated that there could be significant effects on the velocity and trajectory of droplets caused by the flow field around full-size aerofoils, but such effects would be much less with scale models in a wind tunnel.

In Anderson 96 (AIAA-96-0636), icing experiments were also carried out with cylinders up to 76mm radius. This could be equivalent to the leading edge radius of full size aerofoils. Hence in such circumstances significant effects from droplet deceleration and deflection might be expected. In his experiments Anderson compared the ice accretion between a 76mm radius and 38mm radius cylinders for two conditions, with both the

droplet size ratio, relative to cylinder radius, and the Weber number conserved. This resulted in quite reasonable similarity between the ice accretion shapes.

For the 76mm radius the droplet MVD was 40.6μm, with a nominal Weber number of around 4. This was well below the more typical SLD size of 150μm considered above, with a nominal Weber number of 16. With these smaller droplets (Anderson 96) the value of (x_0 / R), or (t_0 / t_t) was about 0.47, compared to a value of about 3 for 150μm droplets with an ATR72 aerofoil. This parameter could have been better matched by using larger droplets. However to maintain the Weber number at a smaller scale might have required an excessive air velocity.

Scaling effects on droplet transient response

Where the aerodynamic conditions change rapidly, in comparison to the dynamic response of the droplets, it can then also be necessary to take into account the transient loading effects on and dynamic response of the droplets.

The transient ramp-up time for the droplet loading will be related to its transit time through the flow field. This will be of the order of $t_t = R/U_0$, where U_0 is the free stream velocity and initial droplet velocity, relative to the aerofoil. The droplet response time will be related to its small amplitude vibration period, t_d, which is given as;

$$t_d = (\pi./4).\sqrt{(\rho.D^3 / \sigma)} \qquad \text{(Lamb 1955 and 1932)}$$

For $d = 150\mu m$ we obtain $t_d = 5.9ms$ for water in ambient conditions

Taking the ratio of these two time parameters we obtain;

$$t_d / t_t = ((\pi./4).\sqrt{(\rho_d.D^3 / \sigma)}) / (R / U)$$

$$= (\pi./4).(D/R).\sqrt{((\rho_d/\rho_a).(\rho_a.U^2.D/\sigma))}$$

$$t_d / t_t = (\pi/4).\mathbf{(D/R).\sqrt{((\rho_d/\rho_a).We_{nom})}}$$

Where We_{nom} is the nominal Weber number, based on the free stream air velocity.

This provided the dimensionless parameter group; $\mathbf{(D / R).\sqrt{((\rho_d/\rho_a).We_{nom})}}$

It is interesting to note that as in the previous group derived for droplet deceleration, $\mathbf{(D / R).(\rho_w / \rho_a).Cd}$, this also included the length ratio, D/R, and the density ratio, ρ_w / ρ_a. The droplet deceleration group included the drag coefficient, Cd, while the transient group included the nominal droplet Weber number. The drag coefficient is, however, a function of the droplet Reynolds number and Weber number. At high Weber numbers, We > 6, the Reynolds number has a reasonably weak effect on drag. For droplets of a given size the relationship between Reynolds number and Weber number is, anyway, fixed so the drag coefficient is then just a function of Weber number.

Hence we see that both parameter groups effectively depend on the scaling ratio, D/R, the density ratio, ρ_w / ρ_a, and Weber number, We.

For low altitude ground testing the density ratio of water and air will remain similar. To reproduce similar results it is necessary to retain similar Weber numbers. Hence to retain similar conditions it is necessary to retain a similar scale ratio of D/R.

Hence, if a reduced-scale aerofoil or cylinder is used, then the droplet size must similarly be reduced in scale. To retain the same Weber number, it is then necessary to increase the air velocity such that;

$$(U_S / U_F) = \sqrt{(R_F / R_S)}$$

where U and R are respectively the free-stream velocity and leading edge radius, for the Scale model relative to the Full size situation.

Hence to obtain a scaling reduction of four to one would require a velocity increase of two to one to retain the Weber number. One consequence could be that compressible effects could become significant, so the conditions would no longer be equivalent.

There can, obviously, be substantial cost benefits in reducing the scale of a test facility. However, as the previous considerations show, there is a limit on how far such scale reduction can reasonably be taken. In reducing the droplet size, to maintain scaling with a scale size aerofoil, this will not maintain similarity of the droplet Laplace number, hence it would not be possible to maintain similarity between the Weber number and Reynolds number. It would seem the only way this could be achieve is with a higher density gas, or pressurised air, which would introduce substantial complications.

For this research the issue was how to adequately replicate the droplet conditions near the leading edge of a large full scale aerofoil using a relatively small and inexpensive test facility. As discussed in Chapter 9 and 10, this was achieved by using a convergent wind tunnel in which the rate of contraction was carefully controlled to reasonably replicate such conditions.

Simulation of droplet dynamic conditions

The preceding evaluation of scaling effects was very approximate. In this it was presumed that the drag coefficient, or Weber number, of the droplet was constant. This could not be so, since the distortion and resulting drag effect on a droplet at high Weber numbers would change as the droplet velocity, and hence Weber number, changed.

It was also assumed that the droplet instantaneously entered completely stagnant air from the free-stream airflow at the free-stream velocity. In practice the transition would be much more gradual, although possibly still quite rapid compared with the droplet response dynamics.

To better evaluate this situation a numerical simulation was run in which the droplet was assumed to be approaching the upstream stagnation region of a cylinder.

In this the flow distribution was assumed to be incompressible and inviscid, so the theoretical solution for irrotational flow around a cylinder could be used, (Panton 1996 & 1984), (Lamb 1995). This was considered to be an adequate approximation for the upstream incompressible flow on the windward side, which was the region of interest.

This gave the velocity distribution as;

$$Ur = U_0.(1 - (R / r)^2).\mathrm{Cos}(\theta)$$

$$U_\theta = U_0.(1 + (R / r)^2).\mathrm{Sin}(\theta)$$

where Ur is radial velocity
U_θ tangential velocity
U_0 free stream velocity
R cylinder radius
r distance from the cylinder axis
θ tangential angle from the stagnation line

Considering a straight trajectory to the stagnation region orthogonal to the cylinder axis for $\theta = 0$ we obtain;

$$Ur = U_0.(1 - (R / r)^2)$$

$$U_\theta = 0$$

Hence the air velocity along this line, towards the cylinder, in terms of the distance **x** from the cylinder surface is given as;

$$U = -U_0.(1-(1/(1 + x/R))^2)$$

The resulting air velocity profile for the cylinder inviscid theoretical model is shown in Figure 38. At a distance of more than the cylinder radius from the surface the air velocity decreased at a relatively slow rate. As an arbitrary reference it was still at 75% of the free-stream velocity one radius from the cylinder surface. It then rapidly decreases to zero velocity at the cylinder surface in the remaining distance of one radius. It can be seen that the average thickness of the flow field is about half the cylinder radius. Hence in the flow field close to the cylinder the droplet would experience a very steep velocity gradient.

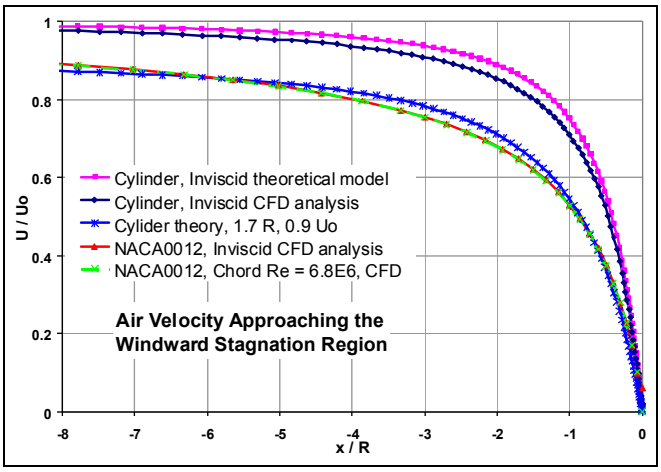

Figure 38: Air velocity approaching the stagnation region of a cylinder and NACA 0012 aerofoil

For comparison some CFD results were provided by a colleague. This included 2D inviscid analysis of a cylinder and also for a NACA0012 aerofoil, as shown in Figure 39. Figure 38 shows that the CFD result for the cylinder was slightly different to the theoretical inviscid result, but no further investigation was made into this discrepancy. The viscid flow for the NACA0012 aerofoil was also provided for a chord Reynolds number of 6.8×10^6, and Figure 38 shows that this was effectively indistinguishable from the inviscid solution.

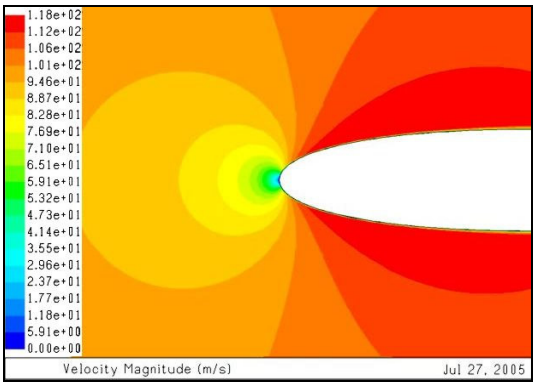

Figure 39: NACA0012 CFD inviscid flow

Also shown in Figure 38 is the effect of assuming the cylinder radius was 1.7 times larger than presumed, with a free stream velocity presumed to be 90% of its correct value. This gave a reasonable approximation to the result for the NACA0012 aerofoil, showing that the flowfield for the aerofoil was about 1.7 time the thickness of that for a cylinder with the same radius as the leading edge.

Using the inviscid velocity profile for cylinders of various sizes, the velocity and Weber number of droplets were computed as they approached the stagnation region. The increased drag, due to droplet distortion, was also included, but as an instantaneous cor-

rection. This used an early version of the drag correction. The later version would have given slightly different results.

In practice it would take about half a vibration cycle for the droplet distortion to respond and that might be with an oscillatory distortion, so producing an oscillatory drag force, (Schmehl 2002). It would, however, seem that net motion of the droplet averages out these fluctuations.

Figure 40 shows the resulting variation of Weber number for various cylinder radii, 200µm droplets and a free-stream velocity of 100m/s. These are plotted against time, in droplet oscillation periods prior to impact with the cylinder surface.

With the smallest cylinder radii, 10mm and 20mm, it can be seen that most of the transient loading occurs in less than half an oscillation period, so the droplet would be likely to strike the surface with little deceleration or distortion at Weber numbers of about 30, which was close to the nominal value based on free-stream velocity.

For the larger radii considered, 200mm and 500mm, it can be seen that the increase in Weber number occurs over many oscillation periods, so would be unlikely to cause oscillation of the droplet, and the distortion would occur in a nearly quasi-static manner. It can be seen that the maximum Weber number, which occurs just prior to impact, is much lower than with the smaller cylinders and for the 500mm cylinder achieves only a maximum value of 12.

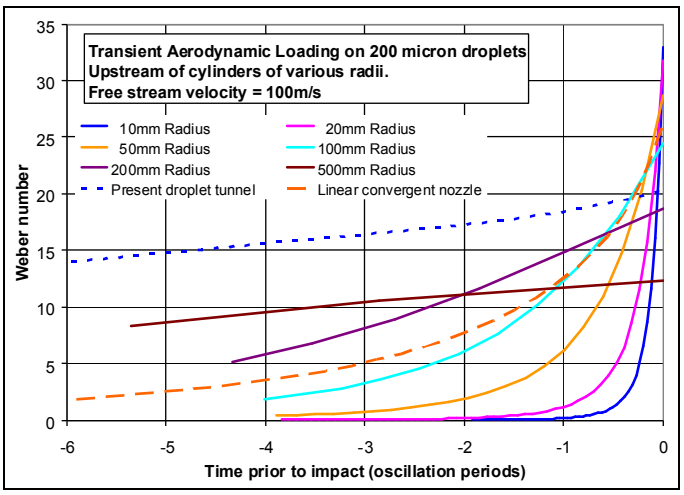

Figure 40: Transient loading on 200µm droplets

The results for the 50mm and 100mm radius gave substantial changes in Weber number in one droplet oscillation period up to Weber numbers of 25, or more. In such circumstances the droplet would be likely to have a substantial dynamic response which could result in break-up prior to impact. This could be of relevance to SLD icing, since this range of cylinder radius would appear to be about equivalent to the leading edge radius of typical medium-to-large aircraft.

Figure 21 shows the distortion of a droplet entering the stagnation region of a splash target in the vertical tunnel, which approximated the leading edge of an aerofoil with a radius of around 30mm to 40mm. The droplet was evaluated to have a Weber number of about 30 and it can be seen that it became increasingly oblate as it approached the target surface.

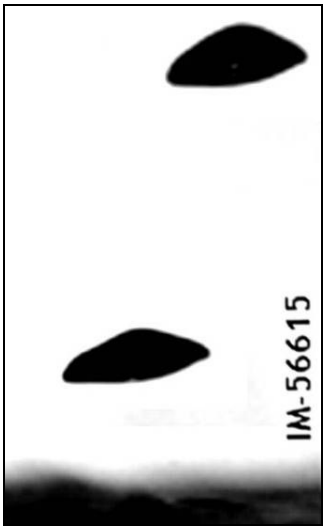

Figure 41: Droplet distortion in the stagnation region

The current version of the convergent tunnel developed for this research, Chapter 9 and 10, was specifically designed to increase the Weber number as slowly as possible and at a near constant rate up to a level sufficient to cause droplet break-up. The upper blue dotted line in Figure 40 shows the simulated variation in Weber number for a 270µm droplet plotted against droplet oscillation periods. For this the Weber number increased from 3.5 to 20 over 17.5 oscillation periods, or a rate of about 0.94 Weber/ period. It can be seen from Figure 40 that this is a much more gentle rate than would be experienced by droplets approaching the leading edge of a typical aerofoil.

The possibility of achieving more typical transient conditions using a more steeply convergent tunnel was also evaluated. The lower brown dashed line in Figure 40 shows the simulated result for a 200µm droplet in a convergent tunnel where the cross section reduced at a constant rate from 120mm square to 30mm square in a length of 90mm. It can be seen that this gives a reasonable approximation to conditions for a 200µm droplet approaching the stagnation region of a 100mm radius cylinder from a free-stream velocity of about 100m/s. This would enable the observation and measurement of droplets subjected to conditions similar to those near the leading edge of a typical aerofoil.

The tunnel convergent profile could readily be designed to more exactly reproduce the transient conditions of droplets approaching the leading edge of an aerofoil of a given size and form.

Conclusions

The evaluation of scaling effects on the pre-impact behaviour of droplets indicated there were two relevant parameter groups, which were;

	$\mathbf{(D / R).(\rho_w / \rho_a).Cd}$	for the droplet motion dynamics
and	$\mathbf{(D / R).\sqrt{((\rho_d/\rho_a).We_{nom})}}$	for transient and dynamic droplet distortion

Since the drag coefficient is primarily determined by the Weber number it was found that there were three primary parameter of relevance, which were;

the length ratio	(D / R)
the density ratio	(ρ_d/ρ_a)
and the Weber number	We_{nom}

Since the Weber number can have a substantial effect on the droplets, it would seem necessary to maintain similarity with this.

For ground tests it is most likely that water and air would be the fluids used, so the density ratio will be fixed within quite narrow limits.

Hence the conclusion was that to maintain similarity between the scaled-down test and the full size situation the size ratio, D/R, would need to be retained.

In order to maintain scale similarity, the air velocity must be increased to maintain Weber number similarity as the scale is reduced. The ability to increase the air velocity could be limited by compressibility effects to retain similarity with the Mach number.

Some parameter groups, such as the Laplace number, cannot be retained as the scale is reduced unless the fluid properties are modified. The main issue would be that of maintaining similarity with the droplet Reynolds number, but this appears to have a weak effect on the drag coefficient. To retain the Laplace number for water drops in air would require either increasing water surface tension or reducing air viscosity, neither of which appears to be practical.

For this investigation of the aerodynamic effects on water droplets, it was found that the most practical option, in terms of resources, cost and time, was to carry out the experiments with full-size droplets and then to replicate the aerodynamic conditions found around the aerofoils of full-size aircraft. This was achieved with the linear airflow in a convergent tunnel which had a carefully designed convergent profile.

The convergent tunnel used so far was deliberately designed to produce a steadily increasing Weber number as slowly as possible, to first allow an evaluation of the near steady-state response of droplets. By increasing the tunnel convergence rate and with other modifications, it would be possible to investigate the transient loading and dynamics response of droplets in conditions very similar to those in the vicinity of a full-size aerofoil.

Chapter 3: Drag Model for Deformable Droplets.

Introduction

For the development of special refrigerated wind tunnels for SLD icing research, and also for the research and modelling of the SLD icing process, it was necessary to have a means of evaluating the distortion and drag properties of small water droplets, between 100μm and 500μm diameter, substantially distorted by strong aerodynamic forces.

Very little directly-applicable data for such drag characteristics was available for such small droplets, where both the distortion and viscous drag effects were significant. To experimentally obtain this data required the design of a special wind tunnel. That could not be designed without an adequate understanding of droplet drag properties, so the possibility of deriving the necessary formulation from available data was investigated.

It was found that high-quality experimental data for free-falling droplets at terminal velocity in ambient air and standard gravity could provide much of the required data, but not at the lower Reynolds numbers and high Weber numbers required. It was concluded that by extrapolating this data, in conjunction with interpolation between the available drag data for spheres and discs, together with droplet distortion models, an effective formulation for drag of distorted droplets was possible. This formulation could then be tested and validated in the resulting droplet wind tunnel.

Definition of Drag

The conventional view of drag is the aerodynamic, or hydrodynamic, retarding force that acts on a body moving through an otherwise stationary fluid. Alternatively it is the component of the aerodynamic, or hydrodynamic, force acting on a body at rest that is acting in the same direction of the free stream velocity of a passing fluid.

In the case of a droplet, or particle, then its velocity and that of the surrounding fluid can each be of any arbitrary magnitude and direction, so the conventional concept of drag needs some clarification. In this case it is the component of the aerodynamic, or hydrodynamic, force vector acting in the direction of the velocity of the surrounding fluid relative to the droplet velocity. Any aerodynamic, or hydrodynamic, lateral force acting perpendicular to the relative velocity is referred to as lift, even though it may have a component acting in the same direction as gravity.

For this research, the assumption made was that the droplet would naturally align its axis of symmetry with the direction of the relative velocity between the droplet and surrounding fluid. Hence this would only resulted a drag force, with no lift force. Such a lift force may occur where the motion of the surrounding flow is sharply curvilinear, as it may be near the leading edge of an aerofoil, so that the direction of the relative velocity between the droplet and fluid can change rapidly before the droplet can realign itself to the relative velocity. This situation was not considered in this research, since only the droplet behaviour in straight-line flow was investigated.

The drag is the result of the differential external surface pressure between the windward and leeward side of the droplets. At very low Reynolds numbers, well below that of interest to this research, the drag due to surface friction can also be significant, but that effect was neglected.

For an ideal inviscid fluid flow around an object there is no surface friction, so the flow follows the contours of the object and results in a symmetry of pressure distribution on

the windward and leeward side of the object, so there is then no drag, or lift, force.

In the case of a normal fluid there will be some surface friction, which may not be sufficient to directly cause significant drag, but which can result in a thin layer of slowly moving fluid at the object surface, known as the boundary layer.

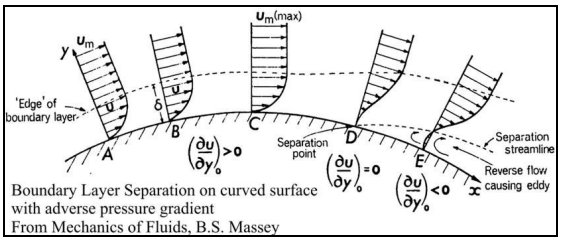

Figure 42: Separation of Boundary Layer

While there is a decreasing pressure gradient in the direction of flow over the surface on the windward side, due to the increasing flow velocity to divert around the object, then the boundary remains stable. However as the boundary layer encounters an increasing pressure gradient in the direction of flow on the leeward side, then the boundary layer can reverse direction, as shown in Figure 42, to cause the flow to separate from the surface.

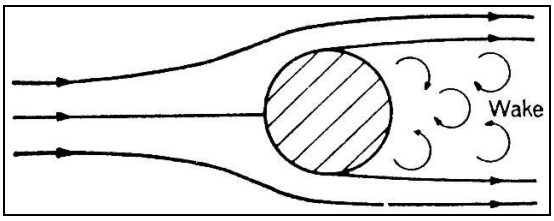

Figure 43: Wake behind an object

As a result of the flow separation the air flow is no longer attached to the surface and forms a wake behind the object, such as shown in Figure 43.

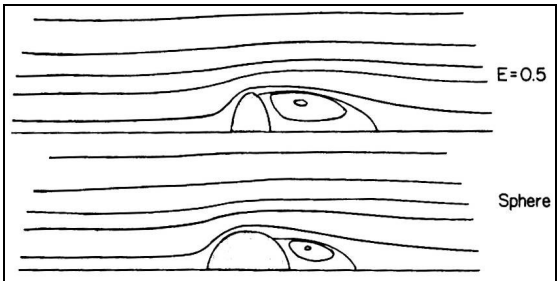

Figure 44: Recirculation in the wake

In the range of conditions relevant to this research, then the wake will tends to contain a toroidal vortex, as shown in Figure 44 for a sphere and ellipsoid, although this is likely to be unsteady and instantaneously non-symmetrical for the conditions of interest.

Figure 45 shows how the average surface pressure distribution is typically affected, so resulting in a higher net pressure on the windward side of the object, compared to the leeward side. This pressure differential between the windward and leeward side of the object then results in the drag force.

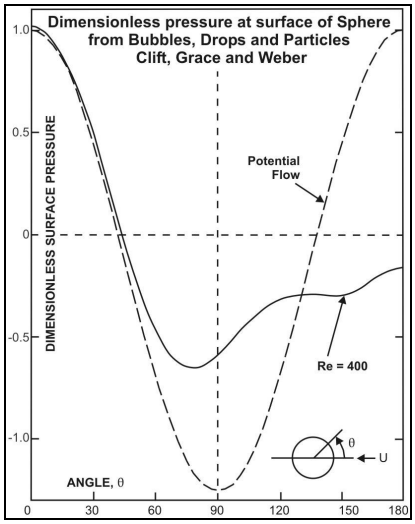

Figure 45: Pressure distribution around a sphere.

Turbulence Length Scale

Both the flow immediately around the droplet and general flow in the surrounding fluid are likely to be turbulent and are likely to interact in some way.

The assumption made was that the droplet dimensions, and the dimensions of any flow disturbances it caused, would be small compared to any other length dimension of disturbances in the flow, or any relevant dimensions of the aerofoil. Hence the droplet would not have any significant effect on the surrounding flow.

Where the surrounding flow was turbulent, then the presumption made was that the length scale of the turbulent disturbances in the surrounding flow were large compared to the dimensions of the droplet. As a result the droplet would not directly "perceive" the general turbulence in the flow, but would "experience" this as a fluctuating variation in the fluid velocity and direction. Hence this would give rise to a drag force on the droplet that is fluctuating in magnitude and direction.

The assumption made was that the period over which these fluctuations occurred would be sufficiently short that they average out with no significant change to the average velocity and trajectory of the droplets. The random fluctuations experienced by each droplet would, however, produce slightly different individual trajectories and velocities, as shown in Figure 46 for droplets in the convergent tunnel travelling right to left. These started as a uniform coherent stream of equispaced monodispersed droplet, Chapter 12.

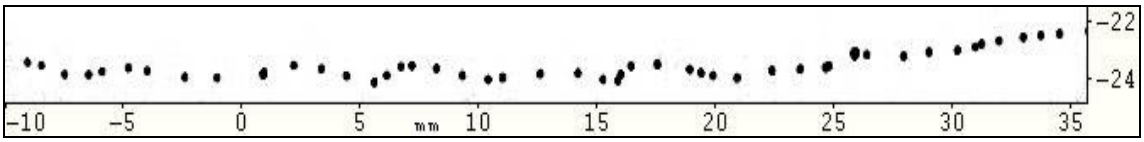

Figure 46: Effect of turbulence on distribution of initially uniformly spaced droplets

It can be seen from Figure 46 that the short term turbulence has a length scale of around 5mm, which is much longer than the droplet size of up to 500µm.

What may be a potential issue is that the time scale of the drag fluctuations may be comparable to that of the droplet resonance. If so then that could result in a significant vibration amplitude of the droplet, which might induce earlier break-up of the droplet. Such issues were, however, beyond the scope of this investigation.

Drag Data for Spherical Droplets

The simplest assumption was that the droplets remained spherical, so available drag data for spheres could be used. This presumed that there was negligible internal flow in the droplets, which is understood to be an acceptable assumption where the drag is dominated by the dynamic pressure force, rather than the viscose shear forces.

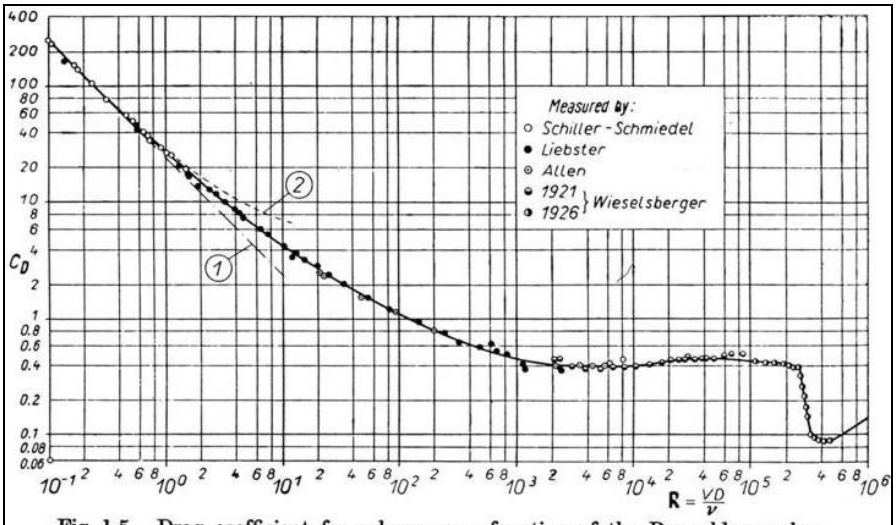

Figure 47: Sphere drag data, from Boundary-Layer Theory, H. Schlichting

In such a case the standard drag curve for a sphere, such as shown in Figure 47 (Schlichting 1979), can be used. Similar data is shown in Figure 48 (Massey 1989) for a reduced range of Reynolds number.

The sphere drag data from these and other sources are compared in Figure 49 for the range of Reynolds numbers relevant to SLD icing.

Apart from the Maybank & Briosi data (1961), considered later, there was a variability of about 10% between the different sources. The preferred sphere drag formulation was that given in Table 2, from Clift, Grace and Weber (1978).

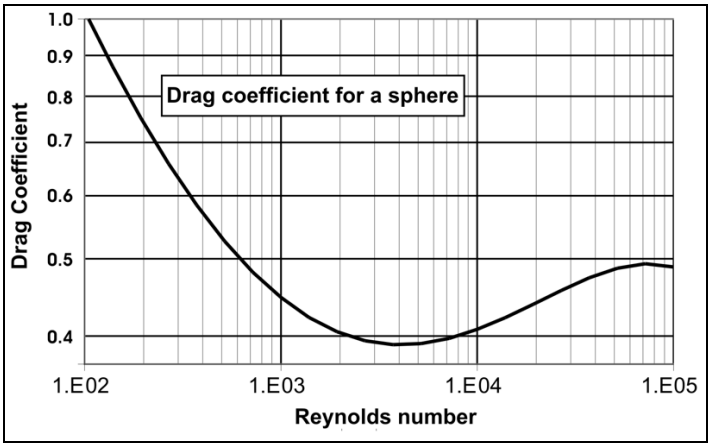

Figure 48: Sphere Drag Data, from Massey 1989, 6th Ed.

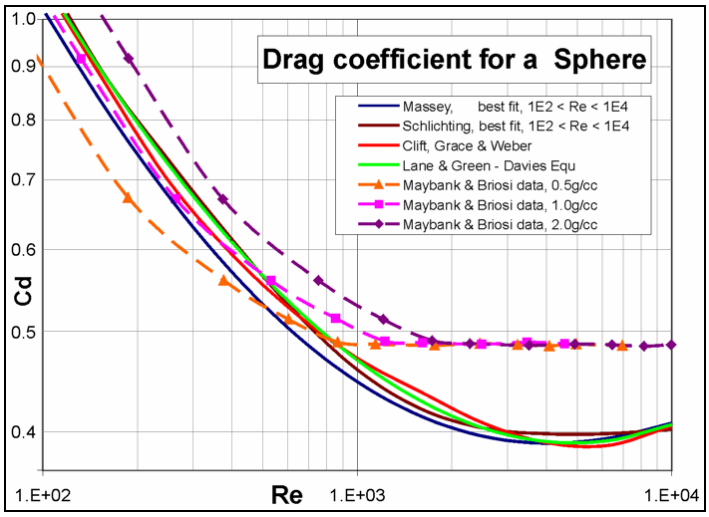

Figure 49: Comparison of various Sphere drag data.

Table 2; Sphere drag formulation; from Clift, Grace and Weber, table 5.2	
x = $Log_{10}(Re)$	
Re <= 0.01:	$Cd = 3/16 + 24/Re$
Re <= 20 :	$Cd = (24/Re).(1 + 0.1315\ Re^{(0.82 - 0.05\ x)})$
Re <= 260 :	$Cd = (24/Re).(1 + 0.1935\ Re^{0.6305})$
Re <= 1500 :	$Cd = 10^{(1.6435 - 1.1242\ x + 0.1558\ x^2)}$
Re <= 12000 :	$Cd = 10^{(-2.4571 + 2.5558\ x - 0.9295\ x^2 + 0.1049\ x^3)}$
Re <= 44000 :	$Cd = 10^{(-1.9181 + 0.637\ x - 0.0636\ x^2)}$
Re <= 338000 :	$Cd = 10^{(-4.339 + 1.5809\ x - 0.1546\ x^2)}$
Re <= 400000:	$Cd = 29.78 - 5.3\ x$
Re <= 1000000:	$Cd = 0.1\ x - 0.49$
Re > 1000000:	$Cd = 0.19 - 80000 / Re$

Drag on a flat circular disk normal to airflow

When a droplet becomes substantially oblate, due to aerodynamic forces whilst still intact, as shown in Figure 50 (Schmehl 2002), its drag characteristics tend to that of a flat circular disk of the same equatorial diameter. Hence a flat circular disk and sphere, with the same equatorial diameter, represents the bounding conditions for an oblate distorted droplet.

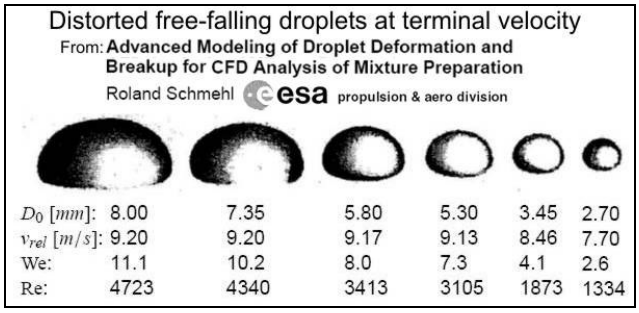

Figure 50: Distortion of free-falling droplets

Most sources of data gave a constant value of 1.1 to 1.2, for Re > 10^3, for the drag coefficient of flat circular disks. Data for lower Reynolds numbers was given by Massey (1989), Nakayama and Boucher (1999) and Streeter (1958). The curves fitted to this data are shown in Figure 51. Data very similar to that from Massey was also given by W.S. Janna (1983).

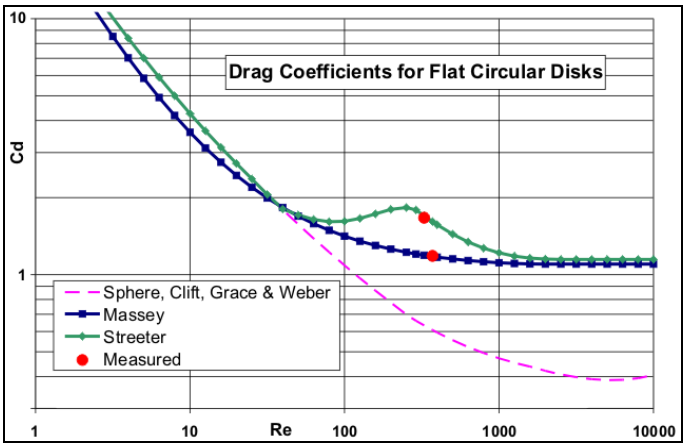

Figure 51: Drag coefficients for Flat Circular Disks.

It can be seen from Figure 51 that there was a substantial difference between the two data sets, by about 40%, at Re = 250. This was a significant issue in developing a drag formulation for distorted droplets. To resolve this either required a more detailed evaluation of the source data or experimental tests. In the time available it was not possible to obtain all the source data, so a simple test was carried out with a free disk sinking through water to determine which set of data might be appropriate.

Figure 52: Test disk for drag measurement

In this test a disk of 15µm thick aluminium foil, on the left in Figure 52, was cut around an 18mm diameter 5p coin. The test disk was then slightly dished, by pressing it against a 50mm diameter sphere, to give it stability while sinking through water. The disk was allowed to sink about 100mm to reach equilibrium and then timed as it sank over the next 100mm. This produced two results, depending on whether the disk sank with a stable motion or while rocking from side to side. The average result of several measurements for each case is shown at the large red circular spots in Figure 51. The upper spot was for stable motion, which was compatible with the data from Nakayama (1999), while the lower spot was for the rocking motion, which was compatible with data from Massey (1989).

Hoerner (1958) indicated that changes in the vortex pattern in the range 200 < Re < 300 were responsible for the peak in the drag coefficient. Figure 53 shows the air flow behind a flat disk at a Reynolds number of 290 (Simmons and Dewey 1930)

FIG. 4. D = 0·3 in., V = 1·8 ft./sec. VD/ν = 290.

Figure 53: Air flow over a flat circular disc for Re = 290

It was initially assumed that for modelling the drag of droplets it would be more appropriate to assume stable motion, with the data from Nakayama, but that was reconsidered in the light of experimental results with droplets. The Nakayama drag data was carefully digitised and using polynomial curve fitting was converted into the function in Table 3.

Table 3: Drag coefficient formulation for a flat disk, data from Nakayama 1961
For Re <= 39 Cd = SphereDragCoeff(Re, 6) ‘ Clift, Grace & Weber equation.
For 39 < Re < 283 $x = Log_{10}(Re)$
$y = -0.61325\ x^5 + 5.01789\ x^4 - 15.87904\ x^3 + 24.40100\ x^2 - 18.50308\ x + 5.98078$
For 283 < Re < 3160 $x = Log_{10}(Re)$ Else For Re >= 3160 $x = Log_{10}(3160)$
$y = 0.10080\ x^5 - 1.64516\ x^4 + 10.54626\ x^3 - 33.00915\ x^2 + 50.00667\ x - 28.83794$
Then $Cd = 10^y$

A similar procedure was applied to the data from Massey, given in Table 4, and these curves are plotted in Figure 51.

Table 4: Formulation for drag coefficient of a flat disk, from Massey, 1989.
For Re < 1: Cd = 24 / Re:
For Re <= 2000 $x = Log_{10}(Re)$ Else For Re > 2000 $x = Log_{10}(2000)$
$y = 0.00507\ x^5 - 0.05161\ x^4 + 0.16082\ x^3 + 0.01987\ x_2 - 0.97385\ x + 1.39573$
Then $Cd = 10^y$

Drag Data for Distorted Droplets

The additional parameter space

The inclusion of droplet distortion introduces an additional factor not encountered with spherical droplets or disks. This is due to the effect of surface tension, which regulates droplet distortion in the presence of unevenly distributed surface pressures, both internal and external. Provided the droplet shape is constant and there is no significant internal flow, then its internal viscosity will have no direct effect on the drag characteristics.

Data on the behaviour and shape of free-falling droplets was given by Schmehl, Figure 50, which shows the distortion of droplets for Weber numbers between 2.6 and 11.1 and Reynolds numbers of 1334 to 4723.

Droplet distortion occurs because of an uneven difference between external aerodynamic and internal hydrostatic pressures at the droplet surface. This difference in pressure has to be balanced by the surface curvature and surface tension. The surface tension force tries to maintain the droplet shape. The ratio of this force to the aerodynamic force, is represented by the Weber number, We;

where $We = \rho.U^2.D/\sigma$

The drag of a distorted droplet is greater for two reasons;

1. The increased frontal area of the droplet.
2. The increased curvature at the equator encouraged earlier flow separation.

The droplet distortion thus requires the one additional parameter group, the Weber number. The droplet density is also relevant in terms of the buoyancy forces and internal pressure distribution, as represented by the Bond number, Bo. This does not, however, require any additional parameter space, since it is related to the Weber number and drag coefficient by the relationship Bo = ¾.We.Cd.

Given the provisos above, the drag properties for Newtonian incompressible flow for a distorting droplet can thus be fully described in terms of the two parameters, Reynolds number and Weber number. A third parameter is then required to represent the resulting drag properties. For a spherical droplet this would normally be the drag coefficient, Cd, but for deformable droplets it is preferable to use the Bond number, Bo.

For various reasons, such as to eliminate a particular variable, when investigating the drag properties different combinations of the Weber, Reynolds and Bond numbers may be used. Typical examples are the Laplace number, La, Rabin number, Ra, Morton number, Mo, drag coefficient, Cd, Froud number, Fr, or other combinations, such as We^2/Bo. Any two of these parameter groups are sufficient to define the droplet conditions. It may then be necessary to determine the Weber number and Reynolds number from these alternative parameter groups. There could be difficulties with such a translation and these issues are considered for a number of circumstances.

Survey of the droplet literature

A survey of the literature produced very little data that was of direct practical use for calculating the drag characteristics of distorted droplets for the conditions of interest. Rabin & Lawhead 1959 and Ingebo 1956 provide some data, but not in a useable form.

To investigate rain ingestion into a Gas Turbine Engine, Kennedy and Roberts (1990) modelled the motion of droplets in a convergent wind tunnel. From their results for the droplet velocity and Weber number along the tunnel axis it was possible to evaluate the drag correction they used, which is shown in Figure 54.

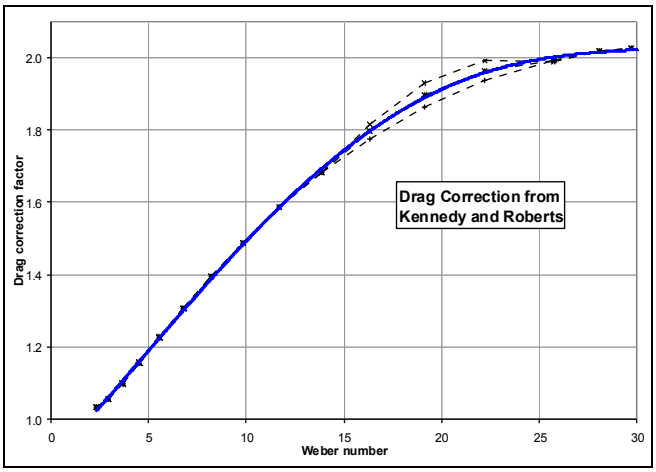

Figure 54: Drag correction derived from Kennedy and Roberts

This shows the proportionate increase in drag, relative to a sphere, for the Weber number. It was later found that they substantially underestimated the correction required. For a Weber number of 16, it was later found that the correction needed to be about 3.3, compared to a value of about 1.8 used by Kennedy and Roberts.

O'Donnell and Helenbrook (2000) investigated "Drag On Ellipsoids at Finite Reynolds Numbers". The numerical study was, however, limited to a maximum Reynolds number of about 200, since beyond this the flow is non-axisymmetric (Johnson & Patel, 1999).

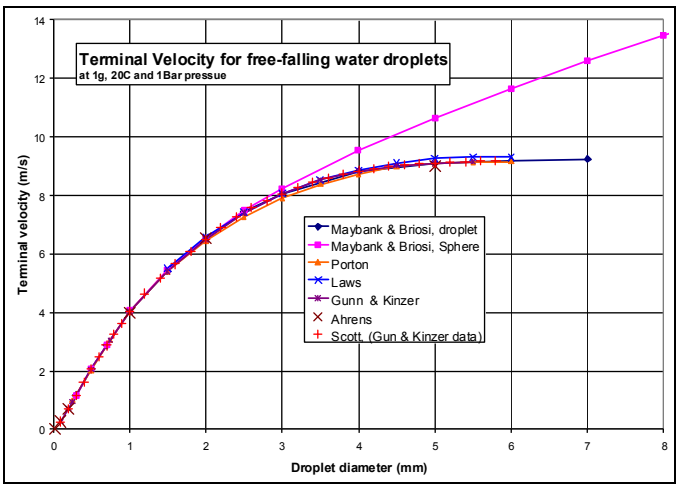

Figure 55: Terminal free-fall velocity of water droplets in ambient air at 1g gravity

The most useful experimental data was that for large water droplets free-falling in ambient air and normal gravity. The best data was from Maybank and Briosi (1956) Scott, Wood & Thurston (1964), Clift, Grace & Weber (1978) and Lane & Green (1956). This data shows that for larger droplets the terminal velocity has an upper limit of about 9m/s, attributed to the greater frontal area and more acute equator curvature of the distorted droplets. The data from these sources is shown in Figure 55.

The preferred data was that from Maybank & Briosi and Scott, Wood & Thurston. The Maybank & Briosi data was, however, found to have a lower variance. It extended to higher Weber numbers and it also gave the terminal velocity for spheres with the same density as water.

Gravity and Acceleration

The objective of the investigation was to the determine the relationship between the drag force of droplets distorted by aerodynamic forces, with respect to the air flow over them, and the resulting free-flight acceleration. The available data was, however, for the terminal velocity of free-falling droplets in ambient air and standard gravity.

In the case of a droplet free-falling at a constant terminal velocity against air resistance, there is no acceleration force. The only body force on the droplet is provided by gravity.

For a small droplet being accelerated in an airflow by the aerodynamic drag the body force is that due to acceleration. While this may also be in conjunction with gravity, it is most likely that gravity will have a negligible effect for the conditions of interest.

To the droplet it makes little difference if the body force is that due to gravity or acceleration. In practice gravity and constant linear acceleration are, experimentally, indistinguishable from each other.

With sufficiently strong gravity, such as on a super-dense planet, it would be possible, in principle, to directly replicate the acceleration of 2000g or more experienced by small droplets in a strongly accelerating airflow. At the surface of the Earth it is, however, not possible to change gravity, so, given water droplets in air at ambient conditions the only variable is droplet size, which requires droplets of several mm diameter. These cannot, however, achieve the required lower Reynolds number for a given Weber number.

The required acceleration could be achieved in a centrifuge, but that would require a rotating frame of reference, so the resulting droplet velocity would introduce Coriolis acceleration. Hence the conditions would not be equivalent to gravity or linear accel-

eration, unless the rate of rotation was sufficiently low. It was assessed that the centrifuge required to achieve this was likely to be impractically large and costly.

Increasing gravity is not practicable, but it is possible to replace gravity with an equivalent accelerating airflow. This was possible with a convergent wind tunnel, discussed in Chapter 9 and 10, that could achieve an airflow acceleration up to 32,000m/s^2, about 3,300 times normal gravity. The resulting acceleration for 250µm droplets was up to 26,000m/s^2, about 2,650g.

The convergent tunnel could have been designed to produce constant acceleration of the airflow along the tunnel axis. In practice it was designed to produce a continuously increasing acceleration. This was so the droplets would experience a steadily increasing acceleration force, over several milliseconds, to cover a range of conditions and avoid causing significant transient effects on, or vibration of, the droplets.

Because of the high acceleration rates, a significant pressure gradient was expected in the compressible air flow, to give a density gradient. Since the droplet drag depends on the air density, it was necessary to keep the density variations and air velocity within acceptable limits and also allow for this in the experimental design and data analysis.

Evaluation of free-falling droplet data.

One difficulty with using the data for free-falling droplets was that the data was only one-dimensional, with droplet size as the only variable. From this a two-dimensional result, for Reynolds number and Weber number, was to be obtained. This required some other information to separate the effects of Reynolds number and Weber number and then combine their effects in an appropriate manner.

The initial method attempted was to determine the increase in drag for a distorted droplet relative to a sphere and then assume this proportion was independent of Reynolds number and only dependent on Weber number (Luxford 2004). This worked reasonably well for Re >1,000. For lower Reynolds numbers, the sensitivity of sphere drag to the Reynolds number is different from that of an oblate droplet, so the ratio of drag due to distortion at a given Weber number could no longer be relied upon. Hence another method of combining the effects of Weber number and Reynolds number was required.

The data obtained from Maybank and Briosi is given is Table 5. This also includes the data for rigid spheres with a density of 0.5, 1.0 and 2.0 g/cc. The data for the rigid sphere is shown in Figure 49 in terms of drag coefficient against Reynolds number.

It can be seen that for turbulent flow, Re > 1E3, the sphere drag for the Maybank and Briosi data was appreciably higher than that from other sources. It was apparent from their paper that appreciable care had been taken in obtaining the data, so it was not clear why there was such a discrepancy. This was a significant issue, since the rigid sphere data provided a reference against which to compare the drag for the oblate droplets.

This raised the question of whether this was an artefact of the method used by Maybank and Briosi. The data was obtained with an upward airflow in a vertical tunnel that exactly balanced the terminal free-fall velocity of the droplet or sphere. The flow pattern was carefully arranged to produce a stable velocity-well at the tunnel centre, so that, if the droplet or sphere were slightly displaced, it would return to the required position.

It was found that droplets were quite stable and adjusted themselves to the slightly fluctuating conditions. In comparison, solid spheres were sometimes quite unstable and

could bounce around and strike the tunnel walls, then return to the stable position.

In discussions with colleagues it was postulated that vortex shedding from the spheres might have resulted in their oscillation in free-fall and that could have modified the drag properties, to give different results from those of other researchers. This may have been due to the low density of the spheres, compared with the more normal use of higher density material, of solid metal, used by others.

Another factor was that there would have been turbulence in the upward flow, which was not present for a free-falling sphere in a stationary fluid. In comparison, the results obtained for free-falling droplets were in very good agreement with those of other researchers, where similar discrepancies might have also been expected. At this distance in time it was not possible to contact the authors to clarify the reasons for any discrepancies.

Table 5: Terminal Velocities for free-falling Drops and Spheres (T = 20C, P = 1Bar), from Maybank and Briosi, 1961.

Diameter	Drop vel	Sphere velocity (m/s)		
(mm)	1g/cc	.5 g/cc	1g/cc	2 g/cc
0.3	1.17	0.84	1.18	1.67
0.5	2.06	1.47	2.08	2.94
0.7	2.87	2.03	2.90	4.10
1.0	4.03	2.86	4.05	5.73
1.5	5.40	3.84	5.43	7.68
2.0	6.49	4.63	6.54	9.26
2.5	7.43	5.31	7.50	10.60
3.0	8.06	5.83	8.23	11.65
4.0	8.83	6.74	9.52	13.48
5.0	9.09	7.52	10.62	15.05
6.0	9.19	8.25	11.65	16.50
7.0	9.24	8.92	12.60	17.85
8.0	--	9.52	13.45	19.05
10.0	--	10.66	15.05	21.30

The Maybank and Briosi results for spheres in laminar flow, with Re < 1,000, having the same density of water, agreed well with other sources. For turbulent flow it was possible to use their results for droplets without reference to their less certain sphere data.

Table 6: Terminal free-fall velocity of water droplets, from Scott 1964
From: Study of Liquid Droplets released from aircraft into vertical and horizontal airstreams;
Data originally from Gunn and Kinzer, 1949

Diam (mm)	Velocity (m/s)	Diam (mm)	Velocity (m/s)	Diam (mm)	Velocity (m/s)	Diam (mm)	Velocity (m/s)	Diam (mm)	Velocity (m/s)
0.10	0.27	0.80	3.27	2.00	6.49	3.40	8.44	4.80	9.07
0.20	0.72	0.90	3.67	2.20	6.90	3.60	8.60	5.00	9.09
0.30	1.17	1.00	4.03	2.40	7.27	3.80	8.72	5.20	9.12
0.40	1.62	1.20	4.64	2.60	7.57	4.00	8.83	5.40	9.14
0.50	2.06	1.40	5.17	2.80	7.82	4.20	8.92	5.60	9.16
0.60	2.47	1.60	5.65	3.00	8.06	4.40	8.98	5.80	9.17
0.70	2.87	1.80	6.09	3.20	8.26	4.60	9.03		

Terminal velocity data for free-falling droplets was also obtained from other sources, as shown in Figure 55. That from Scott, 1964, shown in Table 6, was of particular interest.

The data in Table 6 was originally obtained by Gunn and Kinzer, 1949, with an accuracy of better than 0.7%. It only includes droplets up to 5.8mm diameter but at many intervening droplet sizes down to 0.1mm, whereas Maybank and Briosi used droplets of up to 7mm diameter. This Gunn and Kinzer data agreed very well with that from Maybank and Briosi, although it was found to have slightly greater variability.

Interpretation of data for free-falling droplets

The free-fall data from Maybank and Briosi was analysed in terms of drag coefficient, Reynolds number and Weber number with respect to the equivalent spherical diameter.

The relationship between Drag coefficient and Reynolds number for the spheres and droplets is shown as a Log/Log plot in Figure 56.

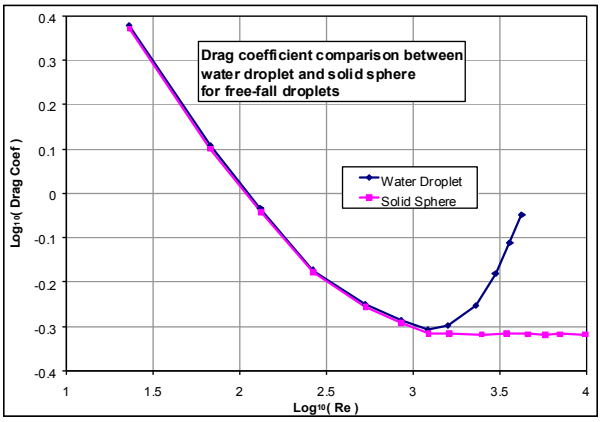

Figure 56: Drag on free-fall droplets against Reynolds number

It can be seen that at a Reynolds number of just over 1,000 the two curves diverged, with that for the sphere remaining near constant, whilst that for the droplet was rapidly increasing.

A similar result was obtained when the drag coefficient was plotted against Weber number, as shown in Figure 57.

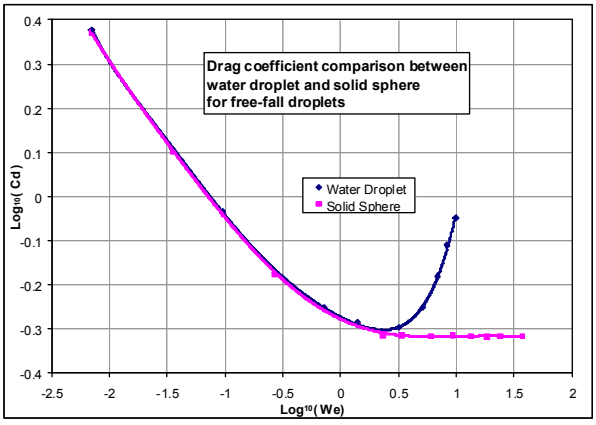

Figure 57: Drag of free-fall droplets against Weber number

This divergence between the curves must have been primarily related to the Weber number, not the Reynolds number, since it was the additional mobility of the droplet's free-surface, hence the resulting droplet deformation, that increased the air drag.

It was fortuitous that, for free-falling droplets in ambient air, the effects of droplet distortion only became significant as the effects of the Reynolds number became weak. For the smaller droplets relevant to SLD icing there was not such a clear distinction. For the same Weber number they had a lower Reynolds number, where the viscosity effects could also be significant, and some further correction was required.

Extrapolation and Representation of the free-fall data.

It was found that, in SLD icing conditions, droplets could experience Weber numbers much greater than 10 without break-up. Since this could be up to a Weber number of 20 or more, it was necessary to have drag data up to this value. Such experimental data was not available, so the question was whether the available data could reasonably be extrapolated to the required Weber numbers.

Data can be extrapolated where;

1. The trend can reasonably be expected to continue
2. The extrapolation method is sufficiently stable over the required interval

Various simple models of distorted droplets were considered, Chapter 6, which indicated that, provided the droplets did not break-up, there would be a stable upper limit to the distortion, as represented by an appropriate parameter.

The data was plotted as Bond number against Weber number, as shown in Figure 58. This curve gives the drag force, F, for a droplet subjected to the body force of gravity, or acceleration, due to aerodynamic drag resulting from the velocity difference between the droplet and the surrounding air.

where $$Bo = \rho_d.a.D^2/\sigma = 6.F / \pi.\sigma.D$$

The Weber number represents the velocity difference, U, between the droplet and air.

where $$We = \rho_a.U^2.D/\sigma,$$

The drag coefficient can be obtained from $Cd = {}^4/_3.Bo/We$.

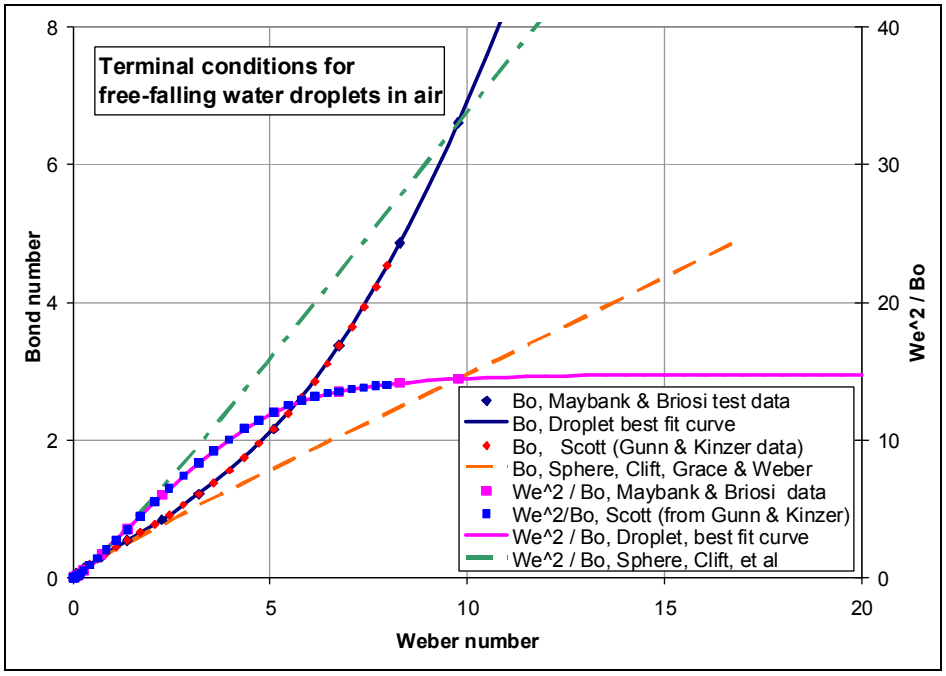

Figure 58: Extrapolation of data for free-falling water droplet in ambient air

Examination of this data showed that, if We^2/Bo was plotted against We, it produced a curve that asymptotically tended to a constant upper limit, as shown in Figure 58,

where $$We^2 / Bo = (\rho_a.U^4 / g.\sigma).(\rho_a / \rho_d)$$

It is interesting to note that this parameter group does not include any length parameter, hence it does not depend on the size, or any other dimension, of the droplet.

It was considered that the curve of We^2/Bo against We may tend to its asymptotic limit with a decaying exponential curve. To investigate this, a graph of $Log_{10}(C - We^2/Bo)$ was plotted against We, as shown in Figure 59, where C is a constant.

For the Maybank and Briosi data it was found that by adjusting the asymptotic value, C, to 14.75, for We >= 3.2, this achieved the straight line, y = 1.435 – 0.1975x, which had the highest correlation coefficient, $R^2 = 0.9999$, or least squares variance of 1.1%.

An evaluation of droplet distortion, Chapter 6, indicated that the dimensionless group We^2/Bo for free-falling distorting droplets would tend to an asymptotic value of around 16 at high Weber and Bond numbers, as $We \rightarrow \infty$, whilst for spherical droplets it would continue to increase indefinitely in a near-linear manner, as shown in Figure 58.

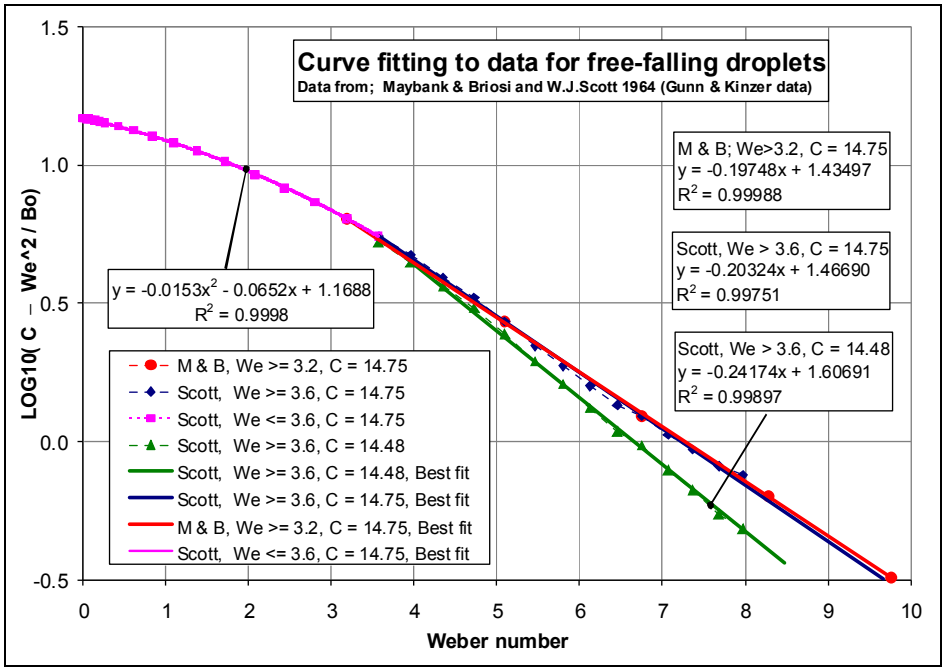

Figure 59: Curve fitting for extrapolation of drag data for free-falling droplets

This procedure was also applied to the Gunn and Kinzer data from Scott (1964) as shown in Figure 59. This gave the line y = 1.6069 – 0.2417 x, with an asymptotic value, C, of 14.48 and a correlation, R^2 = 0.999, or least squares variance of 3.2%. This asymptotic limit was within 2% of that obtained from the Maybank and Briosi data.

When the data from Scott was also plotted with an asymptotic constant, C, of 14.75 this gave the line equation y = 1.4669 – 0.2032 x, which was very similar to the result for Maybank and Briosi, but with a lower correlation, R^2 = 0.9975, and a variance of 5%, compared to 1.1% for the Maybank and Briosi data.

Whilst the Maybank and Briosi data contained many fewer points than that from Scott, it provided a better fit and included a higher Weber number, so this was adopted as the best equation to represent the droplet free-fall results for We > 3.2.

For We < 3.6, the Scott data was plotted for C = 14.75 in Figure 59. The best fit parabolic curve was $y = 1.1688 - 0.0652x - 0.0153x^2$, with a correlation of R^2 = 0.9998, or variance of 1.4%. For We = 0 the intercept was forced to a value of $y_0 = \text{Log}_{10}(14.75)$ = 1.1688. This was because when We = 0, and Re =0, the value of ¾.We/Bo = Cd would have a finite value. Hence We^2/Bo must be zero when We is zero. It was, however, found that for low Weber numbers the parabolic fit in Figure 59 was not effective.

For low values of Weber number it was found to be more effective to fit drag coefficient, Cd, against Weber number, We, using log/log axes, as shown in Figure 60. This also shows the result for the parabolic fit from Figure 59, (Scott, We < 3.6, best fit), and it can be seen that for We < 1 the curve did not fit.

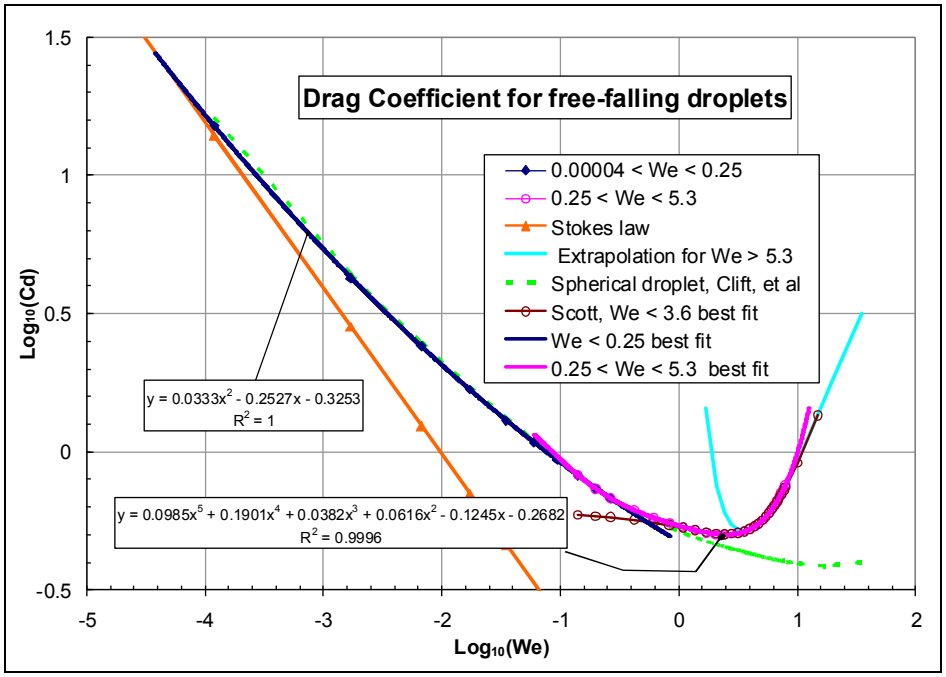

Figure 60: Curve fitting of drag data for free-falling droplets and We < 5.3

For We < 5.3 it was found that the curve could be better represented by the fitted equations given in Table 7.

Table 7: Free-falling droplet drag properties in ambient conditions **P =10^5 Pa, T =20C, g =9.81 m/s^2**
For We < 0.00004; Stokes' law for free-fall droplets, Cd = 24/Re Cd = 24 (Mo / (18 We^3))$^{1/5}$ For 0.00004 < We < 0.25; low Weber number (near spherical droplets) x = Log$_{10}$(We): y = 0.0333 x^2 – 0.2527 x – 0.3253: Cd = 10^y For 0.25 < We < 5.3; intermediate and transition Weber number x = Log$_{10}$(We) and Cd = 10^y where; y = 0.0888 x^5 + 0.1989 x^4 + 0.0423 x^3 + 0.0577 x^2 – 0.1246 x – 0.268 For We > 5.3; high Weber number, use extrapolation curve y = 1.4669 – 0.20324 We ; Scott best fit with C = 14.75 Bo = We^2 / (14.75 – 10^y); where Cd = $^4/_3$ Bo / We

The Bond number can then be obtained from Bo = ¾.Cd.We

Analysis of free-falling spheres

For comparison with the free-falling deformable droplets, it was also necessary to determine the characteristics of free-falling spherical droplets.

For all practical purposes spherical droplets had the same drag properties as smooth rigid spheres. At very low Weber numbers, We < 10^{-3}, and low Reynolds numbers, Re < 10, the drag on a spherical droplet was slightly less than that of a sphere, as can be seen in Figure 60. This small difference was attributed to internal flow within the droplet due to surface viscous friction at the low Reynolds number.

If the droplets were assumed to remain spherical, then surface tension was no longer significant in determining the droplet drag, other than having some small influence on

the internal flow, which had an almost negligible effect. The purpose was, however, to compare the drag properties for droplets with surface tension, where distortion was otherwise prevented, in relation to deformable droplets with the same surface tension.

Originally the sphere free-fall data used was that from Maybank and Briosi, but this was later found to have substantial discrepancies compared to data from other sources, particularly for Re > 1000, as shown in Figure 49. The consequences of this are considered later. As a result it was necessary to use other drag data for spheres, such as that from Clift, Grace and Weber, given in Table 2. One difficulty was that this was in terms of the drag coefficient against Reynolds number, whereas it was required in terms of the Bond number against the Weber number, to enable direct comparison with the data for free-fall deformable droplets.

To derive the required relationship needed some manipulation of the various parameter groups. In this a useful parameter group was the Morton number, Mo, where;

$$Mo = (We^2.Bo)/Re^4 = Bo.(We/Re^2)^2 = Bo/La^2 = g.\mu^4.(\rho_S - \rho_P)/\rho_S^2.\sigma^3$$

The parameter La is the Laplace number, discussed later in this chapter .

The Morton number contains neither velocity nor length and, apart from gravity, or acceleration, only contains fluid properties. Hence for given fluid properties and gravity or acceleration, the parameter can be determined without any knowledge of the droplet size or velocity. For free-falling water droplets in ambient air and 1g gravity this parameter has a value of about $2x10^{-12}$.

This parameter group is used for particles, drops and bubbles, where ρ_S and ρ_P are respectively the densities for the surrounding fluid and the fluid of the bubble, or droplet. The densities difference ($\rho_S - \rho_P$) provide the buoyancy force, whilst the density of the surrounding fluid, ρ_S, is related to drag. For water droplets in air this gives the result;

$$Mo = g.\mu^4.(\rho_a - \rho_w)/\rho_a^2.\sigma^3$$

We notice that, because the density of water is higher than that of air, this results in a negative value. For practical purposes the density of air is almost negligible, compared to water, and also the absolute value of the result is used, which gives;

$$Mo \quad g.\mu^4.\rho_w/\rho_a^2.\sigma^3 = (g.\mu^4/\rho_a.\sigma^3).(\rho_w/\rho_a)$$

It is to be noted that for an air bubble in water, only the water density is required, which provides both buoyancy and drag, to give $Mo = g.\mu^4/\rho_w.\sigma^3$. This is the inverse cube of the Physical Property Group, Npp, where $Mo = 1/Npp^3$ (Middleman, 1995).

It is to be noted that the viscosity, μ, is related to drag, so this needs to be the value for the surrounding fluid, which is that of water for a bubble and for air with a droplet. An important difference with bubbles is that they have negligible internal viscosity, so the internal flow can have a more significant effect on drag at low Reynolds numbers.

To determine the free-fall Bond number from the Weber number for a sphere it was necessary to determine the drag coefficient, Cd. To do this required the Reynolds number. It might be anticipated that this could be obtained using the Laplace number, since $Re = \sqrt{(We.La)}$, however this required the droplet diameter, which might not be known.

Given the Weber number for the conditions of interest, the Morton number can be determined for the free-fall conditions. The resulting equations could not be solved di-

rectly. However the following convergent procedure provides a numerical solution.

1. Mo = $g.\mu_a^4.\rho_d/\rho_a^2.\sigma^3$
2. Cd = 1.0 (initial estimate)
3. Bo = ¾.Cd.We
4. Re = $(Bo.We^2 / Mo)^{1/4}$
5. Cd = SphereDragCoeff(Re) (Table 2)
6. Repeat from 3 until convergence, or iteration count > 20 for non-convergence.

The Morton number depends on the air pressure and temperature and the gravity for the condition at which the free-fall data is defined. These were assumed to be 10^5 Pa, 20C and 9.81 m/s^2. This gave an air density of 1.19kg/m^3, viscosity of 18.2μN.s/m^2, surface tension of 72.7mN/m and Morton number of 1.9×10^{-12}.

The results of this are shown in Figure 58, with the Bond number and We^2/Bo plotted against Weber number for both deformable and spherical droplets.

Drag correction factor in relation to free-falling droplets

The first method used to determine the drag of distorted droplets was to first calculate the drag for a spherical droplet of the same equivalent diameter and then apply a correction factor for the increase in drag due to the droplet distortion at the relevant Weber number.

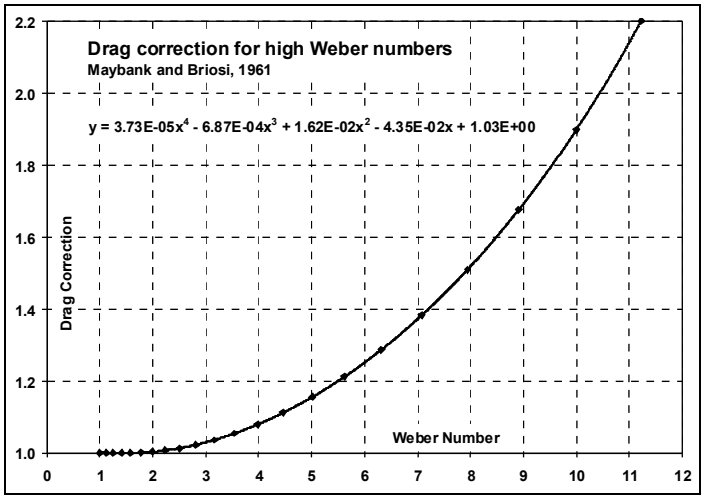

Figure 61: Original drag correction for high Weber no.

The ratio of the drag increase for the distorted droplets was determined from Figure 56 and Figure 57, using the Maybank and Briosi sphere data as the reference. It was not possible to directly make a size to size comparison. As a result it was necessary to use high order curve fitting to represent the curves of Figure 56 and Figure 57, from which the drag correction was determined. The resulting correction is shown in Figure 61.

The data was only available to a Weber number of 10 and because of the high order polynomial fitting any extrapolation much beyond that was uncertain.

Maybank and Briosi found that for Weber numbers greater than 10 the droplets became unstable and disintegrated. It might be concluded that drag data for higher Weber numbers was not relevant, but higher Weber numbers could be possible because;

1. There was lower turbulence or higher internal damping for smaller droplets.
2. The Weber number was increasing sufficiently rapidly that higher values could be achieved before droplet break-up could occur.

Huimin Liu, (1981) indicated that droplets could remain intact for Weber numbers in excess of 20.

It was later discovered that the Maybank and Briosi drag data for spheres with turbulent

flow was about 20% higher than that from other sources, as shown in Figure 49. This meant that the drag correction was likely to be too low for Weber numbers up to 10. For higher Weber numbers the extrapolated correction was uncertain.

There was an issue about the basis on which comparison should be made between deformed droplets and spheres. For a prescribed droplet size this was not an issue, since the relationship between Reynolds number and Weber number was fixed by the Laplace number. With free-falling droplets data the diameter was not constant with respect to the Weber or Reynolds number, so there was no constant relationship between these.

When comparing the drag characteristics of a free-falling distorted droplet to a free-falling spherical droplet, it was necessary to make a specific choice about the criterion for comparison. This was because it was not possible to simultaneously achieve a match between the droplet size, Reynolds number and Weber number.

The droplet size may not be known and the Weber number does not affect the drag of a spherical droplet, so it was assumed that the Reynolds numbers needed to be matched. Hence, for a free falling droplet with a given Weber number, it was first necessary to determine its Reynolds number.

This could not be obtained directly, but it was possible to directly calculate the Bond number from the Weber number for the free-falling droplets, using the best-fit equations, given in Table 7 for the experimental data,.

Hence	Mo	=	$g.\mu^4.\rho_w / \rho_a^2.\sigma^3$
	Bo_{drop}	=	Free-fall BondFunction(We_{drop}) , from Table 7.
	Re	=	$(We_{drop}^2.\ Bo_{drop} / Mo)^{1/4}$
and	Cd_{drop}	=	$^4/_3.Bo_{drop} / We_{drop}$

To calculate the Weber and Bond number for a sphere, we note that the Morton and Reynolds number are the same for a free-falling droplet and sphere. Hence the conditions for the free-falling spherical droplet or sphere can be computed as follows;

	Cd_{sphere}	=	SphereDragCoeff(Re), from Table 2
also	We_{sphere}	=	$(^4/_3.Mo.Re^4 / Cd_{sphere})^{1/3}$
and	Bo_{sphere}	=	$¾.We_{sphere}.Cd_{sphere}$

The preceding analysis gives the drag coefficients for both a free-falling distorted droplet and a free-falling spherical droplet at the same Reynolds number. Hence the ratio of the drag coefficients, Cd_{drop} / Cd_{sphere} , gives the drag correction factor for the given Weber number of the distorted droplet. The drag correction was then assumed to be independent of Reynolds number.

Typical results for this are shown in Figure 62, together with the drag correction from Figure 61 (Luxford 2004) which was obtained by direct comparison with the Maybank and Briosi data for a free-falling sphere. Because of the high-order polynomial curve fitting used for that, the extrapolation was unreliable beyond a Weber number of 11 and was truncated to a maximum value of 5.0.

Figure 62 also shows the revised extrapolation for the same Maybank and Briosi data for spheres and droplets, but using the revised extrapolation for free-falling droplets. This agrees with the original curve for the available data up to a Weber number of 10, but Beyond a Weber number of 11 there was increasing divergence between the curves.

The other curve shown in Figure 62 is the revised drag correction, using the Maybank and Briosi data for the droplet, in relation to the sphere drag given by Clift, Grace & Weber. Up to a Weber number of We = 15 this revised curve gave a significantly higher drag correction than the original curve used for the design of the droplet tunnel.

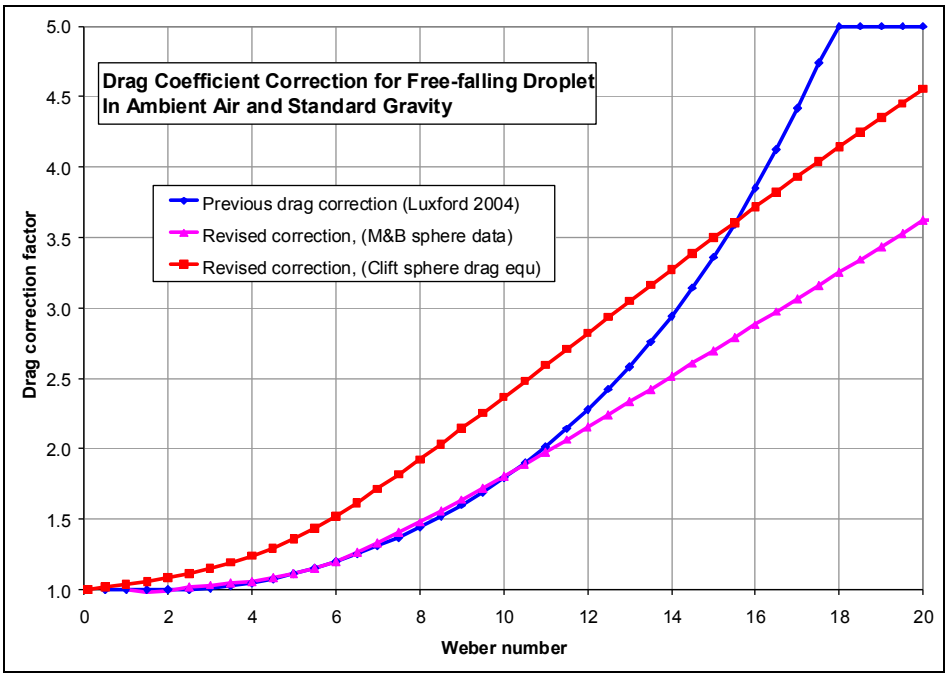

Figure 62: Various droplet drag models using the drag correction method

To calculate the drag for a given droplet size, the Laplace number and Reynolds number will be the same for the sphere and droplet;

where La = $\rho_a.\sigma.D / \mu_a^2$, Laplace number
and Re = $\sqrt{(La.We)}$

The drag coefficient would then be calculated for the equivalent sphere diameter and this would then be multiplied by the revised correction factor.

Issues related to droplet size and Reynolds number

The preceding drag correction, based on the Maybank and Briosi sphere drag data (Luxford 2004), was used to optimise and design the convergent droplet tunnel, since the improved corrections were not then available. Hence, the tunnel characteristics slightly deviated from what was intended, but it was still suitable for the required application.

The drag correction approach was found to have a number of deficiencies, particularly at low Reynolds numbers, Re < 1000, where the distorted and spherical droplets could have had a different sensitivity to Reynolds number.

As a result, a revised method of taking account of both the Weber number and Reynolds number was developed. In this it was necessary to understand how droplet size affected the relationship between Weber number and the Reynolds number, particularly for smaller droplets, where these effects could overlap and interact much more.

For SLD icing, the droplet size range of interest was about 100µm to 500µm. This was about 20 times smaller, and about 8,000 times less mass, than the droplets of 2mm to 8mm diameter considered in free-fall measurements.

The Laplace Number

For this evaluation it was useful to consider the Laplace number, La, which is a parameter group that can be obtained from the Reynolds number, Re, and Weber number, We,

where $La = Re^2/We = (\rho.U.D/\mu)^2 / (\rho.U^2.D/\sigma) = D.(\sigma.\rho/\mu^2)$

The inverse square root of the Laplace number is known as the Ohnesorge number, Oh,

where $Oh = 1/\sqrt{La} = \mu/\sqrt{(\rho.\sigma.D)}$

These parameters included the properties of either the surrounding fluid or the droplet fluid. The convention adopted in this research was to use the Laplace number for the gas, or fluid, flow around the droplet, and the Ohnesorge number for the properties of the droplet fluid, or liquid. The droplet size and surface tension, σ, were common to both, but the values of viscosity, μ, and density, ρ, depended on whether they were related to the gas or liquid phase.

It can be seen that the Laplace number contains only the air, or gas, properties, apart from surface tension and droplet diameter. Hence, for a given fluid and typical conditions the air properties and surface tension will be essentially constant, within a narrow range, so the Laplace number is primarily a droplet size parameter. For a given droplet size the Laplace number is, essentially, fixed, and there is then a fixed relationship between the Reynolds number and Weber number.

The resulting relationship between Reynolds number and Weber number is shown in Figure 63 for typical ambient conditions. Each curve is for a droplet of a given diameter and hence a given Laplace number.

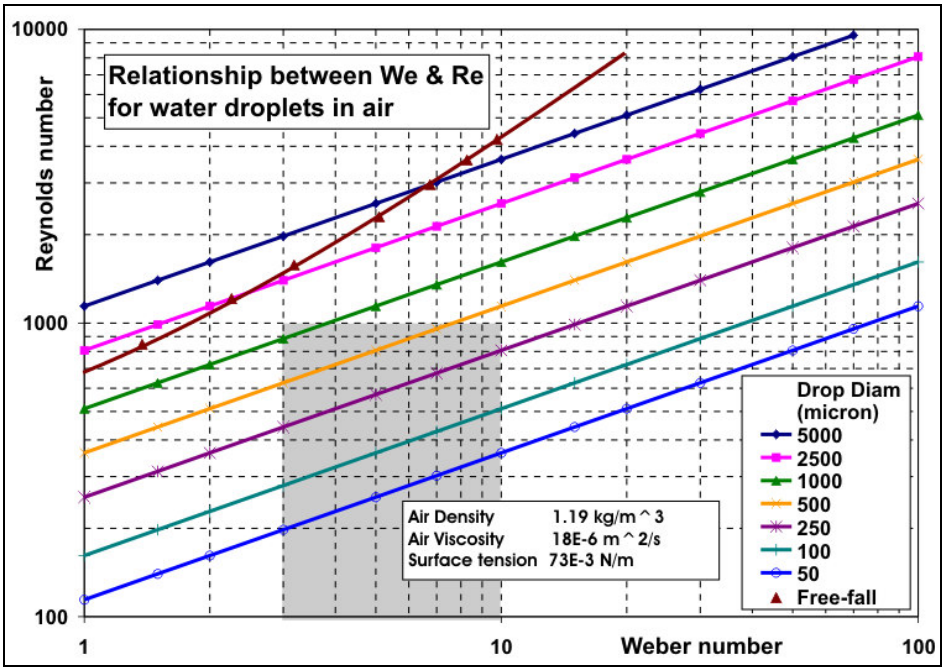

Figure 63: Relationship between Weber number, Reynolds number and droplet size

For typical ambient conditions and a 250μm water droplet in air, the Laplace number was about 65×10^3 and the value was directly proportional to droplet size. As an Ohnesorge number this would be about 3.9×10^{-3} for the air properties.

It is of interest to note that, for 250μm water droplets, $Oh = 7.6 \times 10^{-3}$, which is only a about twice that for air, despite the substantial differences in the fluid properties.

The Ohnesorge number, with respect to drop properties, usefully represents the damping of droplet vibrations. For the 1st vibration mode the damping factor, $\eta \approx (\sqrt{2}).Oh$, giving a vibration-damping factor of about 1% for water (O.A. Basaran, 1992).

It can be seen from the Laplace number, $La = Re^2/We = \sigma.\rho.D/\mu^2$, that for a given Weber number and fluid properties the Reynolds number is proportional to the square-root of droplet size, $Re = \sqrt{(We.La)} = \sqrt{(We.D.(\sigma.\rho/\mu^2))}$. This meant that, for a typical Weber number and a 25 to 1 variation in droplet size, the Reynolds number would only vary by a factor of 5 to 1. For typical SLD conditions, where droplet distortion is a significant issue, this would normally restrict the Reynolds number to a range of about 700 to 6000. For a sphere, the drag coefficient only varies by about 25% within this range of Reynolds number. For a droplet with a given amount of distortion, the variation in the drag coefficient would be no more than for the same range of Reynolds number.

Figure 63 also shows the curve for free-falling droplets in ambient air, where the drop size changes with the Weber number and Reynolds number.

The shaded region of the graph in Figure 63 is between a Weber number of 3 and 10 and below a Reynolds number of 1,000. This shows the region in which there is likely to be significant interaction between the Weber number and Reynolds number in terms of droplet distortion and viscose effects.

Above a Reynolds number of 1,000, the drag is dominated by the dynamic pressure on the droplet surface, and viscous forces have a minimal direct effect. Hence the drag force has much less sensitivity to the Reynolds number.

Below a Weber number of 3, the droplet remains near spherical, such that the flow over it and its drag characteristics are very similar to those for a sphere. The uneven pressure forces on and within the droplet will cause some distortion and a small increase in the equator diameter. This increases the frontal area and hence increases the drag coefficient. The slight flattening of the droplet also reduces the equatorial radius of curvature, so encouraging earlier flow separation, which can further increase the drag. This results in a moderate increase in the drag coefficient, about 15% at We = 3, compared to that for a sphere. Otherwise, the droplet behaves much like a sphere.

Above a Weber number of 10, the droplet is substantially distorted, as shown in Figure 50. In particular, the windward side is flattened, with a much smaller radius of curvature near its outer edge. This is likely to result is well-defined flow separation, so for a given distorted shape the drag is much less sensitive to the Reynolds number.

It can be seen from Figure 63 that the free-falling droplets and droplets greater than 1.3mm diameter are outside of the shaded zone, so the effects of the Reynolds and Weber numbers will only slightly interact.

For droplets less than 1mm diameter and $3 < We < 10$, there is increasing overlap and interaction between the Weber and Reynolds number effects as the droplet gets smaller. For droplets smaller than 100μm the Weber number is likely to be insufficient to cause significant distortion in normal SLD icing, so they could be treated as near-spherical.

The problematic region was for 200 to 300μm droplets and Weber numbers of 3 to 10. For Weber number less than 3, the distortion effects would be small and, above a Weber number of 10, the sensitivity to Reynolds number was likely to be much reduced.

Revised drag model for deformable droplets

Taking the preceding considerations into account, a drag model for distorted droplets could be developed. The purpose was to achieve a plausible, practical and sufficiently-accurate drag model that could be used for engineering and scientific calculations.

To achieve this a number of reasonable assumptions were made. These cannot be proven, but were considered acceptable, given the various considerations and available data. In due course this could be experimentally tested, as discussed in Chapter 1 and 5, which compares the model with preliminary experimental results for 250µm droplets.

The model is derived from the data for free-falling water droplets in ambient air and standard gravity. This provides data for both the terminal velocity and the distorted shape (Maybank and Briosi), (Scott), (Clift Grace and Weber).

An alternative model for droplet distortion was developed from the numerical solution for sessile droplet shape on a horizontal unwettable surface, as discussed in Chapter 6.

The model for droplet drag depends on the following assumptions;

1. The terminal velocity data for free-falling droplets can reasonably be extrapolated to higher Weber numbers, at least to We = 20, so long as the droplet remains intact. This is by assuming the parameter group We^2/Bo exponentially tends to a stable asymptotic value of 14.75, with respect to the Weber number.
2. The droplet distortion primarily depends on the Bond number (Clift, Grace and Weber) as approximated by sessile drops on a horizontal surface (Chapter 6).
3. The drag coefficient, with respect to its equatorial diameter, for an oblate droplet with given distortion would have a value between that for a spherical droplet and a flat circular disk with the same Reynolds number, for the equatorial diameter. The drag coefficient would then be an interpolated combination of the sphere drag coefficient and disk drag coefficient for the same equatorial diameter.
4. For a given amount of droplet distortion, as represented by the ratio of thickness to equatorial diameter, the interpolation ratio for the drag coefficients will be independent of the Reynolds number for the equatorial diameter.
5. The droplet cross-section shape is assumed to be composed of two semi-ellipsoids (Clift, fig 7.10). It is thus assumed that the volume and aspect ratio of these will be equal to an oblate circular ellipsoid of the same thickness and equatorial diameter.

The primary data for this model is that for the free-fall terminal velocity of water droplets in ambient air and standard gravity. Assumption 1 is to enable that data to be extended to higher Weber numbers. The purpose of assumptions 2 to 5 is to enable the free-fall data to be transposed to lower Reynolds numbers that occur with the smaller droplets encountered in SLD icing.

Derivation of the drag interpolation factor

The requirement was to determine the drag force on a droplet, given the air velocity over the droplet. This was most effectively achieved by determining the Bond number from the Weber number for the droplet, based on the equivalent spherical diameter. If required, the drag coefficient was then determined from, $Cd = {}^4/_3.Bo/We$.

The assumption was made that, for a given droplet distortion, as represented by the droplet aspect ratio, the droplet drag could be interpolated between that of a sphere and a disk with the same equatorial diameter and same equatorial Reynolds number.

The issues in this were how to determine the aspect ratio of the droplet and then how to determine the interpolation factor between the sphere and disk.

In principle it was only necessary to determine the required interpolation factor for a given droplet Bond number and distortion ratio at one value of Reynolds number, with the assumption that this interpolation factor was then equally applicable to any other Reynolds number. The drag and distortion data required for this was obtained from free-falling droplet experiments and sessile droplet distortion. This data was used to plot out the drag characteristics of free-fall droplets, with respect to their equatorial diameter, as shown in Figure 64, and plot the drag properties of spheres and disks, together with curves of constant interpolation values of 0.4, 0.6 and 0.8 for comparison.

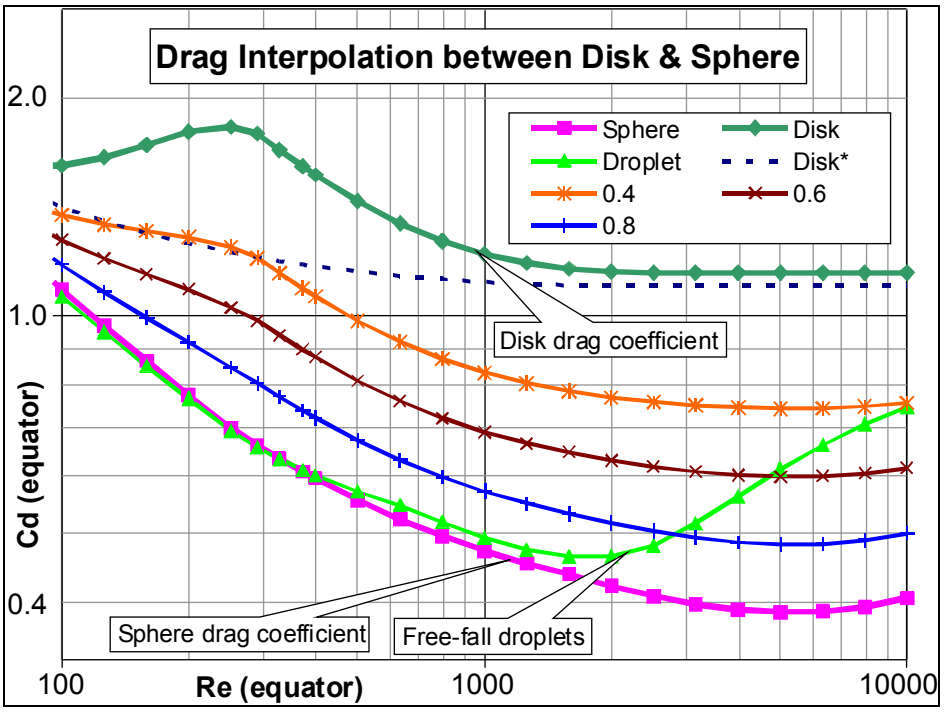

Figure 64: Droplet drag interpolation between spheres and disks

For this, it was first necessary to determine the free-fall Bond number from the Weber number for the droplets of interest. This can be done using the equation given in Table 7. The droplet drag coefficient for the equivalent diameter is then obtained from;

$$Cd = {}^{4}/_{3}.Bo / We.$$

The distorted aspect ratio of the droplet is then calculated from the Bond number, as discussed in Chapter 6. This can either be from data for free-falling droplets (Clift, Grace & Weber, Eq (7-25)) or that of a sessile drop on a horizontal unwettable surface.

By assuming the distorted droplet can be represented by two oblate hemispheroids about a common plane (Clift, Grace and Weber) it was possible to evaluate the equatorial diameter from its equivalent spherical diameter and aspect ratio;

Hence volume $= \pi.De^2.h/6 = \pi.D^3/6$

where De droplet equatorial diameter
h droplet thickness
D equivalent spherical diameter.

However (h/De) is the calculated aspect ratio and from the equivalent spherical diameter, D, we can obtain;

$$De / D = 1 / (h / De)^{1/3}$$

Hence the equatorial diameter of a free-falling droplets can be calculated from the Weber number for the equivalent spherical diameter.

The Reynolds number for the droplet spherical diameter can be calculated from the Laplace number and Weber number, since;

$$Re = \sqrt{(La. We)}$$

The Reynolds number then needs to be adjusted to the equatorial diameter as Rq,

where; $Rq = Re.(De / D)$

This then allowed the drag coefficient for a sphere, Cs, and disk, Cq, with the same equatorial diameter to be calculated for the equatorial Reynolds number, Rq. From this it was then possible to compute the interpolation factor, k.

This gives the proportional combination of the drag coefficients for the sphere and disk which are equivalent to the drag coefficient of the distorted droplet. This can be done as an arithmetic combination;

$$Ci = k . Cs + (1 - k).Cq$$

where k is the interpolation factor
Cs drag coefficient of the sphere
Cq drag coefficient of the flat disk
C_i interpolated drag coefficient

However, because of the substantial range of variation of the drag coefficients, it was considered better to interpret these in logarithmic terms, using geometric interpolation.

Hence $Log(Ci) = k . Log(Cs) + (1 - k).Log(Cq)$

or $Ci = Cs^k . Cq^{(1-k)}$

However $Log(Ci) - Log(Cq) = k.(Log(Cs) - Log(Cq))$

hence $k = (Log(Ci) - Log(Cq)) / (Log(Cs) - Log(Cq))$
$= Log(Ci / Cq) / Log(Cs / Cq)$

Figure 65 shows the interpolation proportion, or factor, and Weber number, with respect to the Bond number. It can be seen that the interpolation factor depended on which distortion model was used. However, providing the same distortion model was used to both determine and apply the interpolation factor, then, in general, it typically introduced less than a 1% difference into the result for We > 2.

Having obtained the interpolation factor, k, for a given droplet distortion for free-fall conditions, the assumption was made that this interpolation factor would apply for any Reynolds number for a droplet with the same Bond number and same aspect ratio.

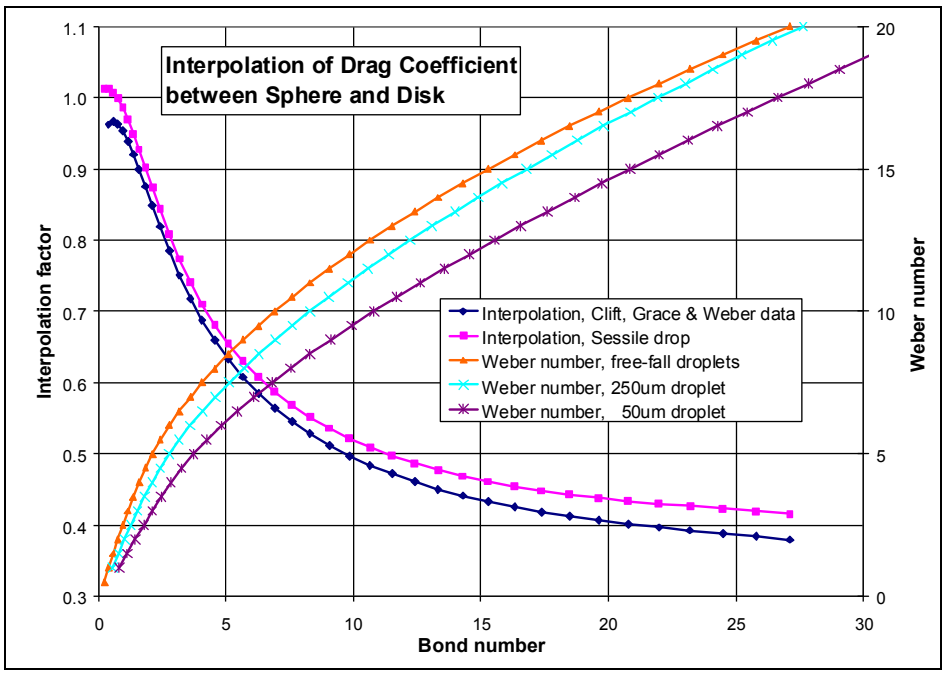

Figure 65: Drag Interpolation between a sphere and disk against Bond number

This assumption seemed reasonable for high Reynolds numbers, where the drag coefficients was reasonably independent of Reynolds number. At lower Reynolds numbers the assumption could be less secure, since the pressure distribution around a disk, or oblate droplet, could depend on Reynolds number in a different way to that for a sphere.

Figure 66 shows the drag coefficient ratio for a disk relative to a sphere for the data from Streeter and Massey. It can be seen from the data of Streeter that, for Re > 300, the ratio is near constant, within 15%, at 2.75. It is unlikely that the drag data for a disk will have any significant effect for Re < 300. In normal conditions droplets less than 100µm are likely to be too small to achieve a high enough Weber number to produce significant distortion. From Figure 63 it can be seen that, for droplets larger than 150µm at Re = 300, the Weber number is too low to produce significant distortion.

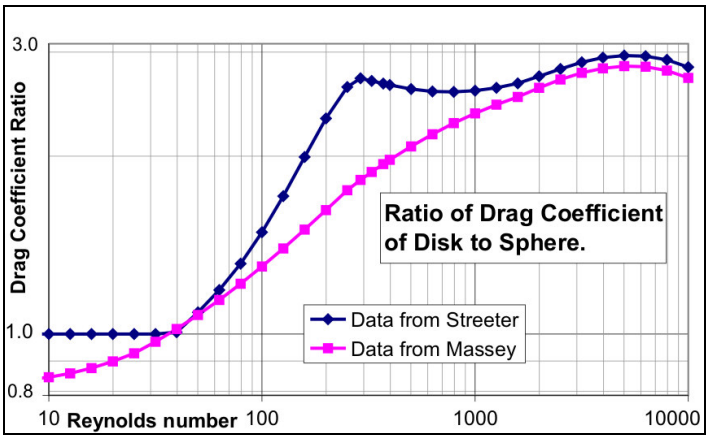

Figure 66: Ratio of Disk drag to Sphere drag coefficients.

The greatest sensitivity in the drag interpolation ratio with respect to Reynolds number is likely to be for an interpolation factor of 50%. If the drag result is to be consistent within 5%, then it requires that the interpolation factor remain constant within about 5% of its range from 0 and 100%. The conjecture is that the flow pattern and pressure distribution around droplets will remain sufficiently similar over the range of interest. As a result, the interpolation ratio should be sufficiently consistent, within the range of the Reynolds numbers of interest, for a given droplet aspect ratio.

Figure 51 shows that the disk drag coefficient, for the Streeter data, substantially decreases between Re = 300 and Re = 1000. This is a slightly greater change than for a sphere over the same range of Reynolds numbers. It can, however, be seen from Figure 63 that for 50µm droplets, at Re = 400, the Weber number will be around 12. This would be sufficient for the disk drag properties to be the greater contributor to the drag. For these conditions the Bond number was about 14.5, for which the interpolation proportion was found to be about 45% sphere drag and 55% disk drag.

To achieve such a Bond number with such a small droplet size of 50µm would require an acceleration, or deceleration, of about 400,000m/s^2 or 41,000g. Such conditions, with We = 12, would require deceleration from around 120m/s in a distance of 18mm. It is doubtful that such conditions could occur with a full-size aerofoil.

These conditions may, however, be possible in a wind tunnel with a scaled-down aerofoil that has a leading edge radius of around 25mm. This indicates that even droplets as small as 50µm can experience substantial distortion in some test conditions. Hence the droplet drag model needs to adequately cope with such conditions. As a result, it would seem necessary to have reliable disk drag data down to a Reynolds number of 300. From Figure 51 this brings it into the region where the difference between the Massey and Streeter data can make a significant difference to the result.

In the case of 250µm droplets at a Weber number of about 12, the Reynolds number will be about 900. It was found that for these conditions the drag coefficient interpolation between disk and sphere would be about equal. For these conditions the effect of the difference between the Massey and the Streeter data appeared to be quite small.

If it was found that the disk drag data from Massey was more appropriate then from Figure 66 the drag ratio for the disk, relative to the sphere, would steadily decrease with Reynolds number below Re = 3000, to about 1.8 at Re = 300. This may indicate that the flow patterns were changing in different ways, which might have resulted in a significant variation in the interpolation ratio for a given droplet shape. The decreasing ratio between the disk and sphere drag meant that any variation in the interpolation ratio would have less effect on the droplet drag as the Reynolds number decreases.

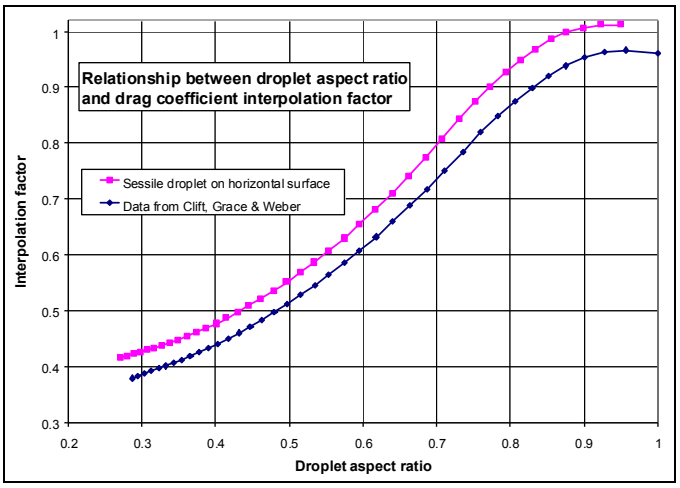

Figure 67: Drag Interpolation against Droplet aspect ratio

At a Reynolds number of 40, the ratio of drag for the disk to the sphere is 1 to 1 for the data from both Massey and Streeter, at which point variations in the interpolation ratio will have no effect. This is, however, well below the range of interest to SLD icing.

Figure 67 shows the relationship between the aspect ratio of the droplet and the interpolation factor. From this it can be seen that for a significant part of the curve the interpolation factor is equal to the aspect ratio. Above an aspect ratio of 0.5 this might be an acceptable approximation.

Computing drag for other droplet sizes

The requirement was to combine the various results to compute the drag of distorted droplets for a given size and given conditions. The primary need was to compute the drag, as represented by the Bond number, from the flow velocity over the droplet, as represented by the Weber number and the Reynolds number.

One difficulty with this was that the calculation for droplet distortion required the Bond number to be known and, if this were so, then the calculation would be unnecessary. This is because the Bond number was found to be the best parameter to use to determine droplet distortion. As a result the two droplet distortion models produced very similar results despite the considerable differences in their derivation. With respect to the Bond number, the aspect ratio of the sessile droplet agreed remarkably well with that for a free-falling droplet, as considered in Chapter 6.

In practice it was found that the drag calculation was quite insensitive to the distortion model used, provided this was based on the Bond number and the same model was used to both derive and apply the interpolation factor between the disk and sphere drag data.

To solve for the Bond number from the Weber number, the procedure has to be iterative, using free-falling droplet data as the initial guess. This required the Laplace number, which could be directly calculated from the fluid properties and droplet size.

Table 8 gives the essential code for the procedure. This is notionally written as an Excel VBA macro in Visual Basic. Anything after single quotes on a line is a comment.

```
Function DropFuncs0(We, La, s%, c%, d%, o%) ' Calculate distorted droplet drag
' s% = distortion model option, 1 Clift, 2 Sessile
' c% = disk drag option,   d% = sphere drag option, 6 for Clift
' o% = output option (not implemented in this sample)
  Re = √(La .We)                        ' sphere Reynolds numb
  Bo = DropFall(We, 0, 2)               ' droplet Bond number (1st guess)
  i    = 0                              ' reset iteration counter
  Do                                    ' Start iteration
    Ds = DropShape(Bo, s%)              ' aspect ratio of droplet, s% shape option
    Dr  = 1 / Ds^(1/3)                  ' equator to sphere diam ratio
    Rq = Dr . Re                        ' equator Reynolds numb
    Cs  = SphereDragCoef(Rq, d%)        ' Sphere drag coef at Rq, (from Table 2)
    Cq  = DiskDragCoef1(Rq, c%)         ' disk drag coef for Rq, Streeter or Massey data
    kk   = DragInterp0(We, Bo, s%, d%, 1)  ' interpolation factor for Bond number
    Ci    = Cs^kk .Cq^(1-kk)            ' logarithmic drag interpolation
    Cd  = Ci .Dr^2                      ' drag coef for spherical droplet at Re
    Bp  = Bo: Bo  = 3/4.Cd.We           ' save current Bond number and revise
    If Abs(Bo / Bp - 1) < 10^-6 Then Exit Do '  Exit iteration if converged
    i = i + 1: If i > 20 Then Stop      ' increment counter, check convergence
  Loop                                  ' end iteration loop
  DropFuncs0 = Cd                       ' return function value
End Function
```

Table 8: Procedure for calculating droplet drag coefficient

There was a difficulty with this in that the interpolation factor also had to be determined from the Bond number, rather than from the Weber number, using the free-fall data. This was because both the droplet of interest and the relevant free-fall droplet data both needed to assume the same Bond number and same distortion for the different Reynolds

numbers. They did not, however, necessarily have the same Weber numbers, as shown in Figure 65. This could be an issue of confusion.

For the free-fall droplet, the Bond number could be directly calculated from the Weber number. To determine the Weber number from the Bond number required an iteration loop. The elements of the necessary procedure are shown in Table 9.

```
Function DragInterp0(We, Bo, s%, c%, d%, o%)
' Determine interpolation factor between Sphere drag coeff and Disk drag coeff
' o%    output option (not implemented in this sample)
  Mo = MortonAmbient(293.1, 1E5, 9.81) ' Morton no., ambient Temp, Press, Grav
  Wf = We: i = 0:                      ' Initial guess for Wf, reset iteration counter
  Do                                   ‘ Start iteration loop
    Re = √(Wf.√(Bo / Mo))              ' Reynolds for sphere diam
    Bf = DropFall(Wf, 0, 2)            ' Bond number, free-fall droplet (from Table 7)
    Wf = √(Re^4.Mo / Bf)               ' Weber number, free-fall droplet
    If Abs(Bo / Bf - 1) < 1E-6 Then Exit Do  ' Iteration convergence
    i = i + 1: If i > 100 Then Stop    ' Increment and check iteration count
  Loop                                 ' End of iteration loop
  Ds = DropShape(Bo, s%)               ' Droplet aspect ratio for Bond number
  Dr = (1 / Ds)^(1/3)                  ' ratio of Equator to Sphere diam
  Rq = Dr . Re                         ' Reynolds for equator diam
  Cs = SphereDragCoef(Rq, d%)          ' Sphere drag coeff for Rq, (using Table 2)
  Cq = DiskDragCoef1(Rq, c%)           ' Disk drag coef for Rq
  Cd = (4 / 3) * Bo / Wf               ' Drag coef for sphere diam
  Ci = Cd / Dr ^ 2                     ' Drag coef for equator diam
  kk = Log(Ci / Cq) / Log(Cs / Cq)     ' Log interpolation factor.
  DragInterp0 = kk                     ‘ Return interpolation value
End Function
```

Table 9: Procedure for determining drag interpolation factor.

The procedure for computing droplet drag was computationally inefficient, since it contained a nested iteration loop and significant redundant calculations. It is anticipated that this could be greatly simplified to a more efficient single iteration loop, but time was not available to develop that.

Results and Sensitivity of the Droplet Drag Model

The predictions from the model are shown in Figure 68 for 250µm and 50µm droplets, using the sphere drag data from Clift, et al, and disk drag data from Streeter. This also shows the result for free-falling droplets.

This indicates a significant deviation between the deformable and spherical droplets for We > 4. By We = 10 the drag on the 250µm deformable droplet is more than double that for the spherical droplet. By a Weber number of We = 20 the increase in drag of the droplet, relative to the sphere, is about a factor of four.

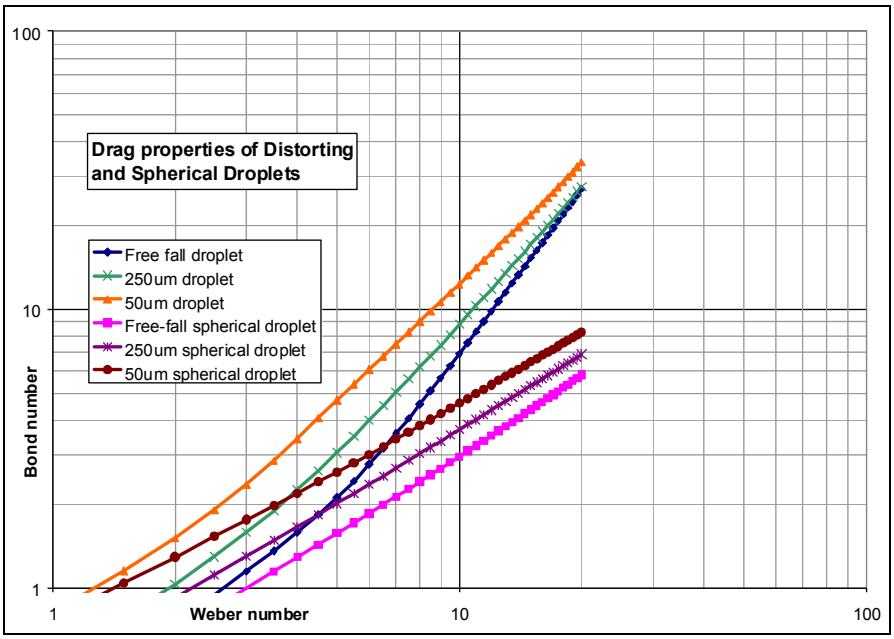

Figure 68: Model results with Streeter disk drag data for 50 & 250µm droplets

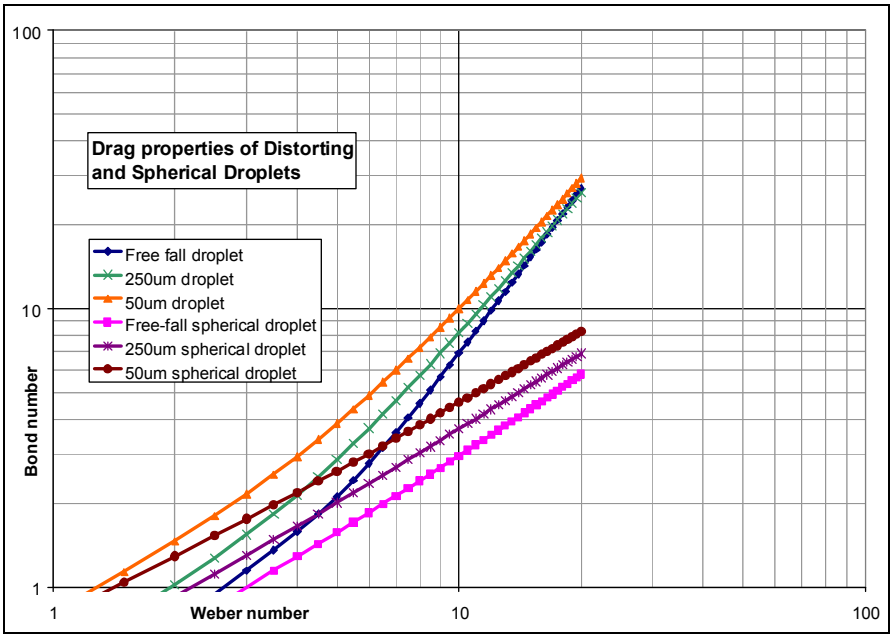

Figure 69: Model results with the Massey disk drag data for 50 & 250µm droplets

Figure 69 shows the result of using the Massey disk drag data. It can be seen that this tends to give significantly less drag than the Streeter data, depending on the conditions..

The difference between using the Massey and Streeter disk drag data is shown in Figure 70. It can be seen that, for 250µm droplets, the maximum difference was about 5%, depending on the distortion model used, and occurred at a Weber number of about 6.5. This difference was sufficiently small for the droplet drag model to be acceptably accurate for droplets larger than 250µm.

For the 50µm droplet the maximum difference was about 20%, depending on the droplet distortion model used, and occurred at a Weber number of about 7 and Bond number of about 6. To achieve these conditions with a 50µm droplet would require a velocity difference with the air of about 90m/s and a droplet acceleration, or deceleration, of about 175,000m/s^2. Such conditions seem unlikely to occur in normal icing conditions with a full-size aerofoil. For this size of droplet it may, however, be possible for such conditions to occur with a scale model of an aerofoil having a leading edge radius of 30mm or less. The resulting distortion of the droplets could then significantly affect their aerodynamic drag, so as to cause a change in the droplet trajectories and hence changing the distribution of the ice accretion. Previously for such test conditions it would have been assumed that such small droplets would remain spherical.

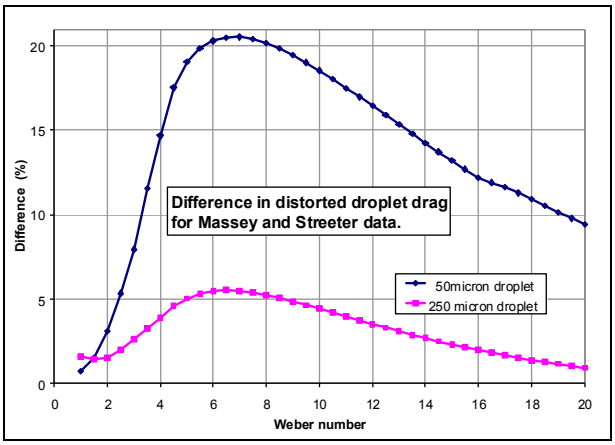

Figure 70: Effect of the Disk Drag Data on the Droplet Drag

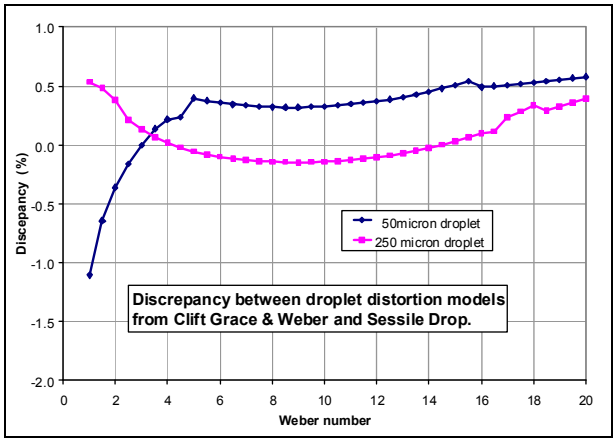

Figure 71: Drag discrepancy between droplet distortion models; Streeter data

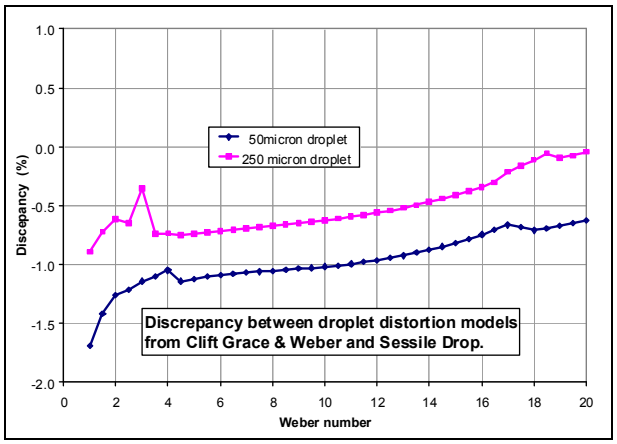

Figure 72: Drag discrepancy between droplet distortion models; Massey data

Achieving such conditions for 50µm droplets in a convergent square section droplet tunnel would, for example, require the tunnel to contract from about 118mm to 76.5mm over a length of about 61mm, with an air exit velocity of about 160m/s. In the convergent droplet tunnel this contraction occurred in about four times that length. The conditions would thus have required a contraction rate and velocity gradient about four times steeper than the droplet tunnel used.

With 50µm droplets the acceleration would still be essentially quasi-static, as the droplet vibration period would be about 33µs, compared to an acceleration period of about 550µs. With this revised tunnel design it would be possible to experimentally validate the drag model for 50µm droplets. This would require the three laser beams, used to measure droplet acceleration, to be much more closely spaced and the instrument would require much more careful design and calibration.

Another issue to be considered was the difference in drag caused by the droplet distortion model. The difference between the drag for the free-fall and sessile droplet distortion models is shown in Figure 71 for the Streeter disk drag data. It can be seen that the choice of the distortion model, in general, made less than 1% difference.

Figure 72 shows a similar comparison using the disk drag data from Massey. For this there was a more significant difference, particularly for the 50μm droplets at lower Weber numbers, but this was less than 1.5%, except for We <1.5.

It was not understood why there should be such a discrepancy at low Weber numbers, where the droplet would be nearly spherical. At low Bond numbers the Sessile droplet distortion model has a very concentrated external pressure distribution, which could have contributed to the difference.

Another approximation which could affect the results was the assumption for the droplet volume. Amendments to the drag model could be made to reduce the difference.

The best method to resolve the uncertainty would be with experimental validation, although this would be unlikely to resolve uncertainties of less than 1%. Since the primary interest with the droplet model was to determine the drag at higher Weber numbers and the time was not available to investigate such small effects for lower Weber numbers, this sensitivity to the droplet distortion model was not investigated any further.

Conclusions

1. The extrapolation of the droplet free-fall data was considered acceptable.
2. Whilst more complicated than the "Correction factor" method, the interpolation method between sphere and disk drag data had adequate computation efficiency, and it was more effective for lower Reynolds numbers and smaller drops.
3. For droplets greater than 250μm the results were consistent within about 6%, irrespective of which model was used for the droplet distortion or disk drag data.
4. For 50μm droplets the drag result could be affected by as much as 20%, at We = 7, depending on the disk drag data used. Hence experimental measurements would be required to select the more suitable options.
5. Further experimental data is required to validate the model and to select the best combination of elements to improve its consistency and accuracy.

Chapter 4: Imaging and Evaluation of Droplets

Introduction

Once experimental measurements of the droplet characteristics had started, it was found that these measurements did not have the consistency expected. It was known from microscope stroboscopic images of the droplets being generated, as shown in Figure 73, that mono-dispersed droplets were being produced. Near the droplet generator these produced consistent signals from the laser beam droplet detector, but with increasing distance from the generator the signals became increasingly erratic.

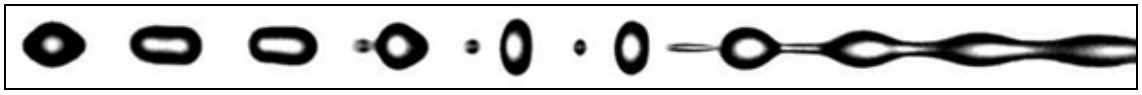

Figure 73: Still Image of Jet Break-up and droplet formation

The simple synchronised strobe system, used for imaging the outlet of the droplet generator, depended on producing the same repeated image many thousands of times from a weak light source of a small LED. This LED could be directly driven from a pulse generator, which was triggered from the signal generator used to drive the piezoelectric elements in the droplet generator.

As the distance from the droplet generator increased, the motion of the droplets became irregular, particularly with a strong turbulent airflow. Hence under strobe lighting this no longer produced a repeatable, or usable, image.

In order to obtain useable images, they had to be obtained with a single flash image. This could be achieved using a camera with a high-speed shutter, or with flashes of short enough duration and sufficient intensity.

The hope was to be able to borrow suitable imaging equipment to observe the droplets. However the relevant equipment was in great demand and never became available.

Development of an Imaging system

It became increasingly necessary to obtain droplet images to determine what was happening, so the development of a suitable imaging system was considered. It was apparent that a camera with the necessary sensitivity and shutter speed would not be available, so development of a suitable flash lamp was considered. This needed to provide sufficient light in one flash to obtain a picture with an available camera and the flash would need to be sufficiently short to keep motion blur within acceptable limits.

It was concluded that 200µm diameter droplets would need to be recorded with a resolution of about 10µm, of which 5µm could be pixilation resolution and 5µm the motion blur. With droplet velocities up to 100m/s this required a flash duration of about 50ns.

The development of a suitable flash unit, using high-power Light Emitting Diodes, or LEDs, is considered in Chapter 15. With this it was possible to achieve a 15A current pulse for 50ns through a high-power LED. This was about 20 to 30 times the maximum steady current for the device. With carefully arranged optics it was possible to achieve the required images with a low-cost digital camera.

Initially an amateur astronomy camera, from Starlight Express, was used. This was directly coupled to the computer with USB and was fitted with a 135mm F2.8 lens with two sets of extension tubes, as shown in Figure 74, to achieve macro imaging.

The astronomy camera had a resolution of about 1.5M pixels in colour, but had no view finder, focusing, or exposure aids. The available computers only had USB1 capability and whilst this was compatible with the camera, it was much slower than the USB2 interface for which the camera had been designed. Hence it took in excess of a minute to transfer and evaluate each image.

Figure 74: Astronomy camera with Extension Tubes and 135mm Lens.

Because of the low light levels, the images were often appreciably underexposed, so before an image could be evaluated, it had to be converted to colour and then subjected to appreciable contrast stretch.

The astronomy camera was designed to obtain images from very low-level light sources. As a result the imaging array was fitted with a Peltier cooling to minimise thermal noise. In addition the image-extraction circuitry was carefully designed to minimise any noise added during this operation, which also made the camera slower.

Figure 75: Wind tunnel test with prototype LED flash and Astronomy camera.

Figure 75 shows the astronomy camera being used with an early version of the LED flash light. Typical pictures obtained with this, for low-speed droplets, are shown in Figure 76. These show the irregularities that developed in the droplet stream, particularly when in an airflow.

The limitation of this system was that the intensity of the illumination was not sufficient; the field of view was too narrow; and the duration of the flash was too long for high-speed droplets.

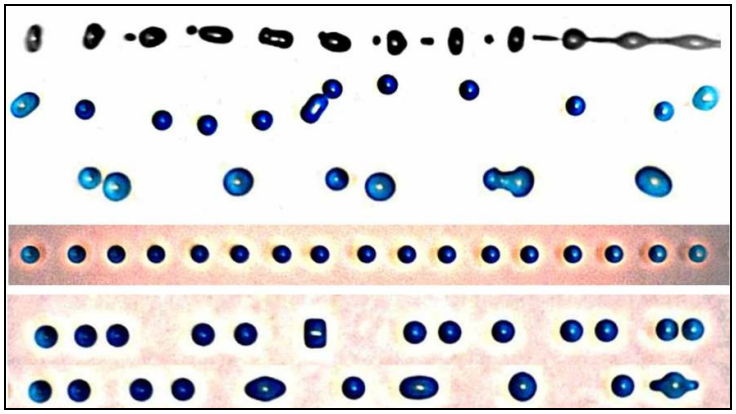

Figure 76: Various Droplet Images from the Astronomical Camera.

The images were, however, sufficient to show that the droplets were not being delivered into the convergent tunnel as a stream of mono-dispersed droplets and that some development of the droplet generator was required, as discussed in Chapter 12.

Application of the Imaging System

The development of the revised flash unit, as discussed in Chapter 15, greatly improved the silhouette illumination. This also enabled the use of a high-speed video camera, as shown in Figure 77, and a standard digital SLR camera, with a 105mm 1 to 1 macro lens, as shown in Figure 78.

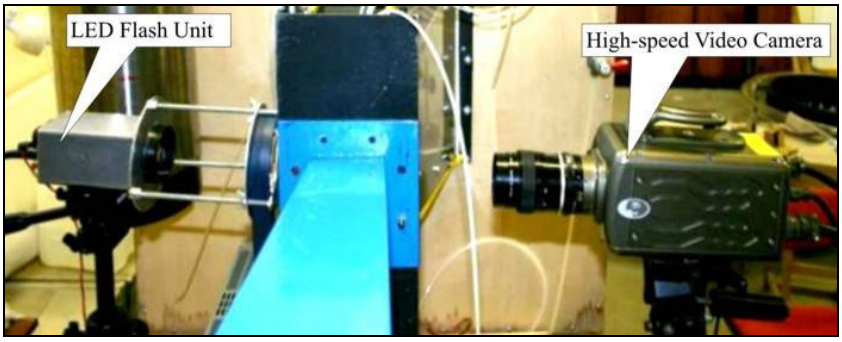

Figure 77: Setup for high-speed video imaging of droplets.

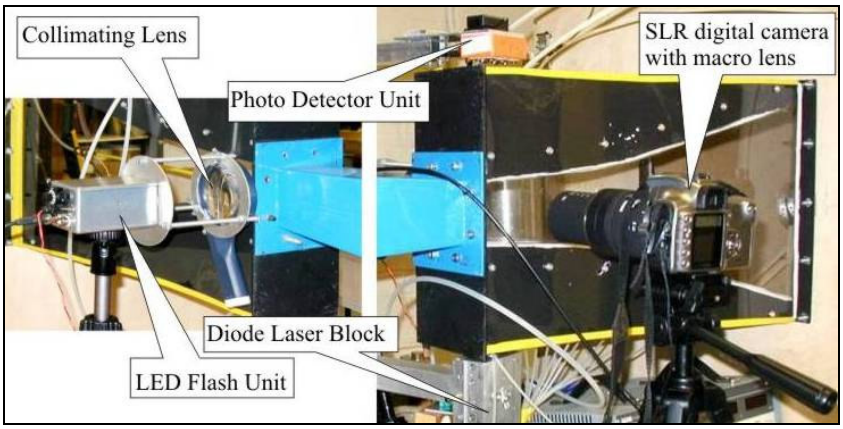

Figure 78: Setup for flash photography of droplets.

Using the high-speed video camera, a Phantom V7, the camera was aligned and focussed and the required frame speed and imaging format was selected. Focusing, calibration and alignment was achieved with a metal grid, with a pitch of 0.6mm, placed at the axis of the tunnel at the required distance from the exit, as shown in Figure 79.

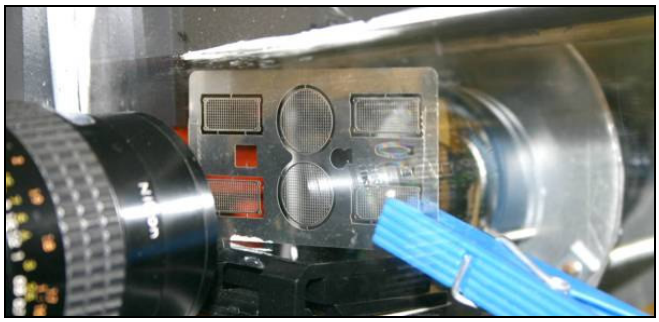

Figure 79: Using calibration grid inside the tunnel

The calibration grid generally used is shown in Figure 80. This had a grid pitch of 0.6mm.

A substantial quantity of high-speed droplet videos and photographs were taken, but regrettably there was not sufficient time to process all of these and only a few samples could be included.

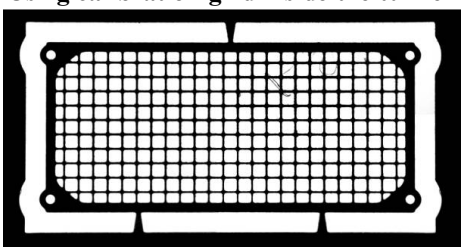

Figure 80: Close-up of 0.6mm pitch calibration grid

Video Image Sequences

The primary purpose of the imaging was to determine whether the droplets were being suitably delivered to the measuring location. Whilst this also provided an opportunity to measure the droplet distortion, this was only done in a few cases due to the limitations of time and image quality.

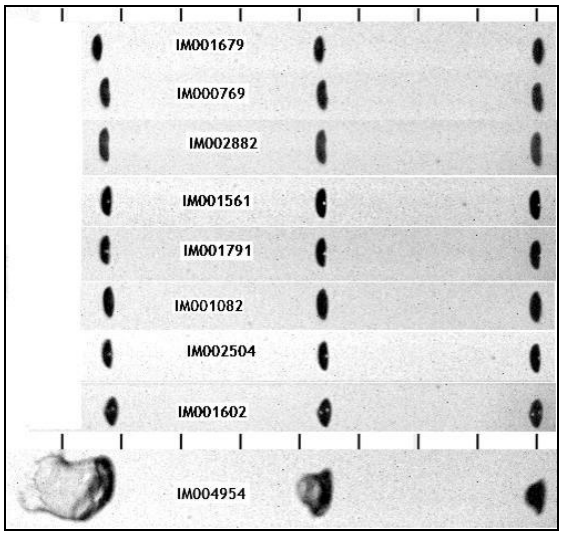

Figure 81: Image sequences of droplets

Figure 81 shows a collection of typical video sequences (ref 04051804). These were taken at a rate of 29400 pictures per second with 512 by 128 pixel resolution, for droplets of 250µm VMD, with an air velocity of 135m/s right to left. From other measurements this was evaluated to give a droplet velocity of 64m/s, with a relative velocity to the air of 71m/s and 21400m/s^2 acceleration, with a Weber number of 16 and Bond number of 18, giving a drag coefficient of 1.5 relative to the VmD.

The conditions appeared to be near those required for droplet break-up, as shown by IM004954 in Figure 81. In this one can see the bag formation and break-up occurring.

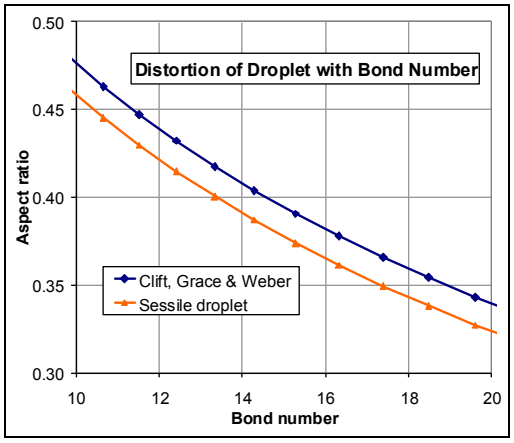

Figure 82: Bond number droplet distortion

With the available image quality it was not possible to accurately determine the droplet distortion. Figure 82 shows the predicted aspect ratio of the droplets with respect to Bond number. That shows an average aspect ratio, for the two distortions models used, of about 0.35 for a Bond number of 18.

To assess whether the observed droplet distortion was reasonably correct, the droplets shown in Figure 81 were elongated by a factor of 1/0.35, or 2.86, as shown in Figure 83. If the aspect ratio of the droplet was 0.35 then the elongated droplets should have had an aspect ratio of 1 to 1. It would seem from Figure 83 that, given the variability, the elongated droplets broadly had the expected aspect ratio.

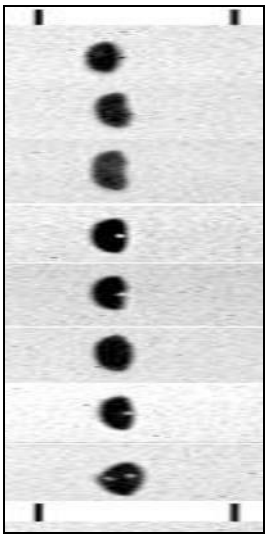

Figure 83: Droplets with 2.86 times elongation

Single Shot photographs

A number of single-shot photographs of droplets were also obtained using the arrangement shown in Figure 78. In this the droplet detector was reoriented to have one laser beam projected vertically across the axis of the tunnel, about 5mm upstream of the imaging location, through two small transparent windows in the upper and lower walls of the tunnel.

Each time a droplet intercepted the laser beam, this produced a slightly delayed triggering of the LED flash, when the droplet was at the imaging location. This ensured the droplet was at the correct distance along the tunnel and on the object focal plane of the camera when the flash occurred.

The arrangement resulted in random LED flashes, typically about 50 per second. The SLR digital camera was then manually triggered, with a shutter speed of around a 50th of a second. This gave a reasonable probability of recording a single droplet. There was also a probability of getting no flash or recording a double exposure, but the unwanted images were deleted and the required images retained.

Figure 84 and Figure 85 show various droplet photographs for the same conditions as Figure 81. The graduations in Figure 84 are about 0.1mm pitch. It can be seen that the droplet shapes were quite variable and some of the droplets were in the process of break-up. The second image from the right in Figure 84 shows the initial formation of a bag, prior to break-up. A particular type of break-up observed is referred to as the "draw handle" mode, in which the droplet separated into two parts joined by a ligament. This ligament would then be extended until break-up, as shown by the two right hand images in Figure 85. The reason for this type of break-up is not understood and it is not known whether it has previously been recorded.

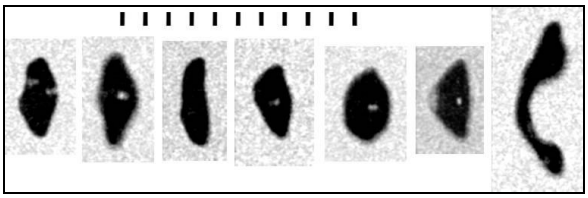

Figure 84: Typical images of distorted droplets

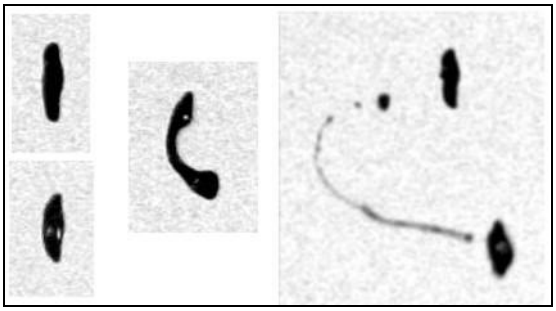

Figure 85: Distortion & break-up of droplets

Many other video sequences and photographs were taken and are archived on CD, but regrettably there was not sufficient time available to carry out the necessary analysis of these. This was not a problem with respect to modelling the droplet drag, since the droplet distortion could be determined by other means, ref Clift et al, and the numerical modelling of sessile droplets, Chapter 6.

Conclusions

1. To resolve what was happening to the mono-dispersed droplets as they were delivered to the measuring location in the wind tunnel, it was necessary to develop a system for imaging the small high-speed droplets.
2. For this it was necessary to develop a low-cost light source with a sufficiently short flash duration and of sufficient intensity, using high-power LEDs.
3. Photographic images were obtained using an amateur astronomy camera and digital SLR camera. These images showed that the droplets were coalescing, and thus resulting in very irregular drop size.
4. It was also possible to obtain high-speed video images of droplets and splashes using the same LED flash unit.
5. With an alternative droplet generator, using a spinning slotted disk, it was then possible to obtain both high-speed video and single-shot images of droplets distorted by the accelerating airflow in the tunnel.
6. At high Weber numbers it was possible to show that the distortion of the droplet was reasonably consistent with the predictions from the distortion models, but that there was also considerable variability in the distorted shapes.
7. The limitations of time and image quality prevented a more detailed study of the many video sequences and photographs of droplets. It would seem that the distortion of droplets was reasonably consistent with that predicted by the distortion model used.

Chapter 5: Measurement and Evaluation of Droplet Velocity and Acceleration.

Introduction

This Chapter of the thesis considers the use of the triple laser beam unit for obtaining experimental measurements of the aerodynamic drag characteristics of droplets distorted by strong aerodynamic forces.

The principles of the method used for this are discussed further in Chapters 13 and 14.

Due to the limitations of time, it was only possible to obtain results for droplets of 250μm diameter VMD. However, this was near the middle of the size range of interest to SLD icing.

Equipment

The experimental facilities used are shown in Figure 86. From right to left are the plenum chamber, with inlet screen to remove unwanted air disturbances, the transparent convergent tunnel, the triple laser beams and photo detectors mounted on a three-axis manipulator, and the air diffuser to the suction fan (not shown). A twin DC regulated power supply was used to drive the laser beams and the motor for the rotating slotted disk droplet generator inside the plenum chamber. A pulse counter determined the rate of droplets intercepting the laser beams, to help with their positioning.

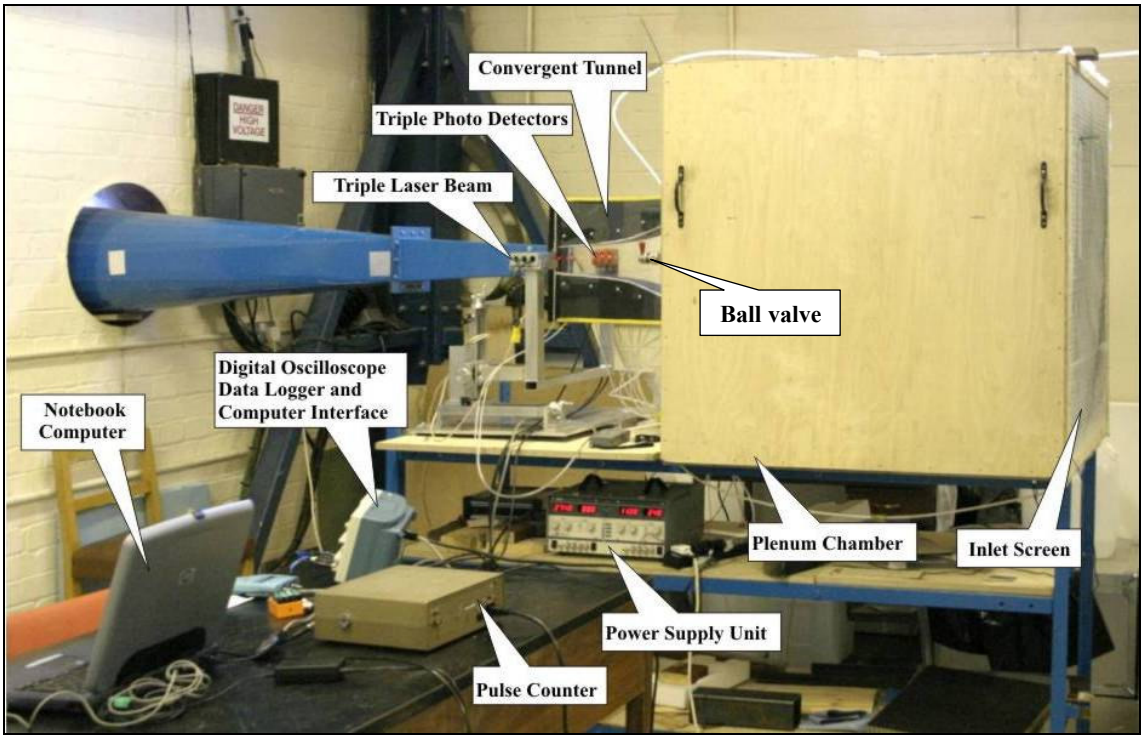

Figure 86: Experimental arrangement for measuring droplet aerodynamic forces

The required data was captured using a four-channel digital oscilloscope with an RS232 computer interface. The data was then recorded onto a notebook computer.

The distilled water for the droplet generator was obtained from a dehumidifier unit. This was held in a stainless steel tank pressurised with compressed nitrogen from a high-pressure cylinder, with a precision pressure regulator to keep the nozzle pressure as sta-

ble as possible. The gas pressure in the tank was measured using a precision digital manometer, shown on the left in Figure 88, and the pressure was set to about 700mB to give a jet velocity of around 10m/s from a 150µm nozzle. To ensure there was no offset on the manometer reading, it was first disconnected to have zero pressure applied to it and the reading was then set to zero.

Figure 87: Close-up view of the laser beam block and photo detectors

A ball valve was incorporated into the water line between the pressurised tank and the droplet generator, shown at the right end of the tunnel in Figure 86. This enabled the water supply to be quickly started and stopped without disturbing the pressure setting.

Figure 88: Precision Manometers

The air velocity in the tunnel was determined using a low-range precision manometer with a resolution of 1Pascal, shown on the right in Figure 87. Before each reading the zero was reset to minimise any offset error. The air velocity in the tunnel was calibrated against fan speed, as considered in Chapter 11.

A mercury thermometer was hung on the outside of the inlet screen to determine the inlet temperature. Air pressure was obtained from a precision digital barometer in the neighbouring laboratory. The fan speed was monitored and controlled by an electronic speed control and digital speed readout to an accuracy of one rev/sec or to 60rpm.

Precision digital scales, with a resolution of 10mg, were used to determine the water flow in the droplet stream by collecting water from the generator over a period of 100secs, as measured with a precision digital stop clock.

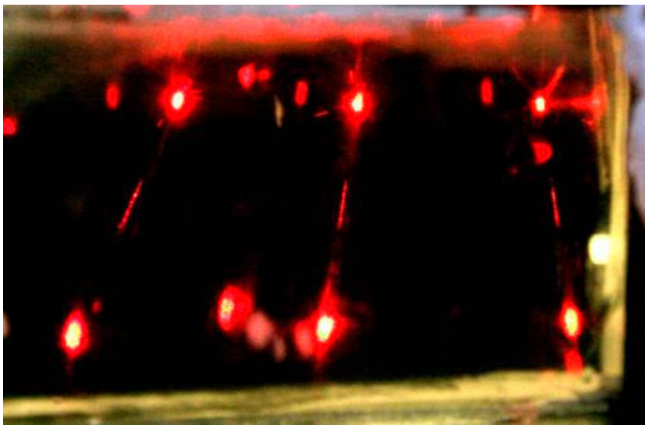

Figure 89: Laser beams intercepting the droplet stream and tunnel walls

The triple-laser beam instrument was located so that the beams were near the mid-plane of the tunnel, with the middle beam 40mm from the exit of the tunnel, or 480mm from

the tunnel entry. The beams were aligned so as to ensure the maximum number of droplets would intercept all three laser beams.

Figure 89 is a photograph taken from the rear side of the tunnel showing the stream of droplets intercepting the laser beams. One can also see where the three laser beams intercepted the transparent sides of the tunnel and various secondary reflections from this.

Method of Measurement

With the tunnel running at the required speed, the stream of droplets was introduced.

The frequency of the droplets was determined from the speed of the slotted disk and the number of slots in the droplet generator. This disk slot frequency had been previously calibrated, using one of the droplet-detector beams and associated photo detector with the oscilloscope, to determine the slot passing frequency. This slot frequency was then related to the voltage supplied to the motor driving the disc and subsequently the same supply voltage was always used.

The flow in the droplet stream was determined by measuring the weight collected over 100 seconds. Because the droplet stream was surrounded by a cloud of fine mist, created by the spinning disk, checks were made by holding the collector in this mist. This was to ensure it did not collect sufficient water to significantly affect the measured weight from the droplet stream.

From the weight of water collected, the time over which it was collected, the frequency of the slots cutting the water jet, and the density of the water, the VMD droplet diameter was determined to be 250μm from the 150μm diameter nozzle used. As discussed in the section on the spinning-disk droplet generator, the droplets were of variable size and it was not possible with the configuration available to determine the individual size and variability of the droplets, as they were measured for their drag characteristics.

Before obtaining measurements, the output from the droplet detectors was observed on the oscilloscope and the droplet detector aligned to optimise the number of occasions on which all three beams were intercepted by the same droplet. It did not follow that all droplet trajectories would be aligned with the beams, since some turbulence in the air flow caused the droplets to take difference paths, with slightly different directions.

A honeycomb flow-straightener screen was available to put over the entry to the screen to further reduce turbulence in the tunnel, but the cells of this became filled with water from the surplus fine spray, so this could not be used.

Adjusting the tilt alignment of the laser beams was achieved by varying the packing thickness under the base of the three-axis manipulator. This could also affect the distance of the laser beams from the tunnel exit. Hence, care was taken to check that the laser beams, in particular the middle beam, were the required distance from the tunnel exit. This was necessary in order to determine air velocity, from the pressure tapping readings, at the measuring location.

It was also necessary to ensure the laser beams were nearly perpendicular to the droplet trajectories, in order to correctly measure the velocity and acceleration of the droplets. It was also advantageous to ensure that the diode lasers were focussed to the minimum spot size in the middle of the droplet stream, since this produced a better signal pulse when the beams were intercepted.

The signals from the droplet detectors were directly recorded by the oscilloscope, but that from the upstream detector was also taken to a threshold detector circuit, which produced square pulses that could then be used to synchronously trigger the oscilloscope time base.

The oscilloscope was then set to single-shot trigger and armed. When this was triggered, by a droplet cutting the first beam, the signals for all three detectors were then inspected to see whether suitable signals had been obtained. If not, the oscilloscope was re-armed for the next triggering.

If suitable signals were obtained then software in the computer, designed for use with the oscilloscope, was used to download the data from the oscilloscope to a computer file. This process could have been automated with the development of a suitable computer program, but in the circumstances this was not considered necessary.

Before saving the data from the oscilloscope, it was inspected on the oscilloscope to ensure it did not contain erroneous and spurious signals from other droplets. The droplet generator had a limitation, in that there were enough droplets that signals from the different detectors could be produced from different droplets. This could produce signals that looked reasonable, but were not from a single drop. Whilst the likelihood of this was low, it did require some judgment about what was an acceptable set of signals.

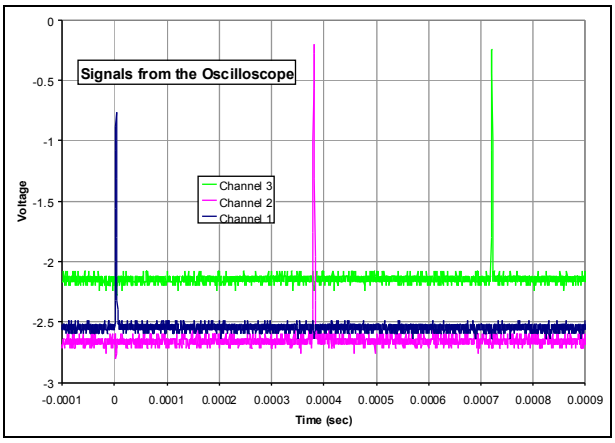

Figure 90: Typical Signals from Oscilloscope

Figure 90 shows typical signals as received from the oscilloscope. Whilst these were of similar amplitude and DC offset, there were significant differences.

The significance of these signals was in the timing of the pulses, not in their amplitude and offset. Hence these signals were normalised to have an offset of zero and amplitude of unity, as shown in Figure 91.

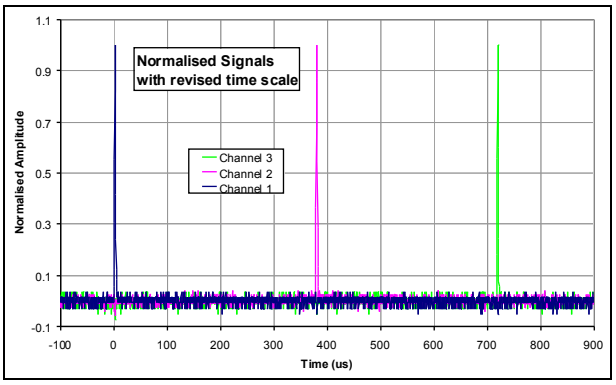

Figure 91: Typical signals after Normalisation

The oscilloscope had only eight-bit resolutions, or 1 part in 256. Hence the signal was electrically quite noisy. To ensure the zero was correctly determined, this was taken as the average of about the first 200 data points, before the first pulse occurred.

The timing of each pulse was taken as midway between the 50% rise and fall time, with linear interpolation between the points. Once the timing had been determined, the pulses could the be aligned with each other and plotted against a stretched time-scale, as shown in Figure 92.

The time intervals between the pulses in Figure 92 were 378.02µs and 339.50µs, an av-

erage of 358.6µs and difference of 38.5µs. From this it was calculated that the droplet velocity was 69.7m/s and the droplet acceleration was 20,915m/s^2.

The number of samples for each channel of the oscilloscope was 2500, which in the example considered gave a sampling interval of 0.4µs, or about 0.11% of the mean time interval. This was, however, about 1% of the difference between the time intervals. Hence, an adverse time error of one sampling interval could make a difference of about 1% to the acceleration result. Using linear interpolation between the sampling intervals it was, however, possible to determine the pulse intervals to an accuracy of 0.1µs, as can be seen from Figure 92.

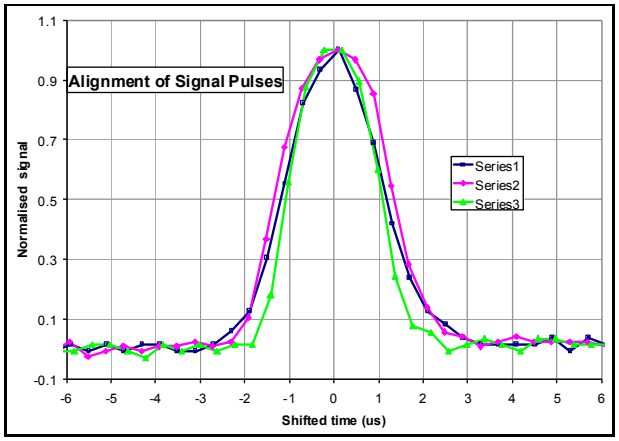

Figure 92: Typical Signals after alignment

It can be seen from Figure 92, the mid-height pulse width was about 2.4µs, giving a droplet thickness of about 167µm. For a distorted droplet this was consistent with the VMD size of about 250µm to 270µm

Evaluation of the Results

Manually analysing the results with Excel was a slow and tedious process, so a computer program was written to process the data files from the detector. This automatically scanned the data to determine the time intervals between the pulses and then determine the velocity and acceleration of the droplets. This included various checks for multiple pulses on the same channel, to asses whether these were acceptably small. From the speed of the fan, the velocity calibration of the tunnel and the known pressure and temperature of the ambient inlet air, it was also possible to determine both the Weber number and Bond number, from which the drag coefficient could also be determined.

Typically 10 or more data points were obtained for each condition. The average results for 250µm droplets are shown in Table 10.

Table 10: Average Experimental Results

Fan rpm	Air Vel	Relative Velocity	Droplet Acceleration	Reynolds number	Weber number	Bond number
1200	66.2	32.04	3244	558.3	4.807	2.788
1500	83.7	40.10	5293	707.8	7.753	4.549
1800	101.2	49.92	9130	823.8	10.565	7.847
2100	118.4	61.16	14982	909.7	12.966	12.877
2400	135.3	71.34	21424	1002.7	15.879	18.414

It can be seen that the relative velocity between the air and the droplet was about half that of the air velocity.

The results obtained are plotted in Figure 92 as Bond number against Weber number. It can be seen that there was appreciable variability in the results, which was attributed to

variability in the droplet size due to the vagaries of the droplet generation method used. To obtain a significant improvement in the consistency of the results it needed a droplet generator that produced droplets of both calibrated consistent diameter and with sufficient spacing to prevent aerodynamics interactions to avoid overlaps between droplets in the measurement.

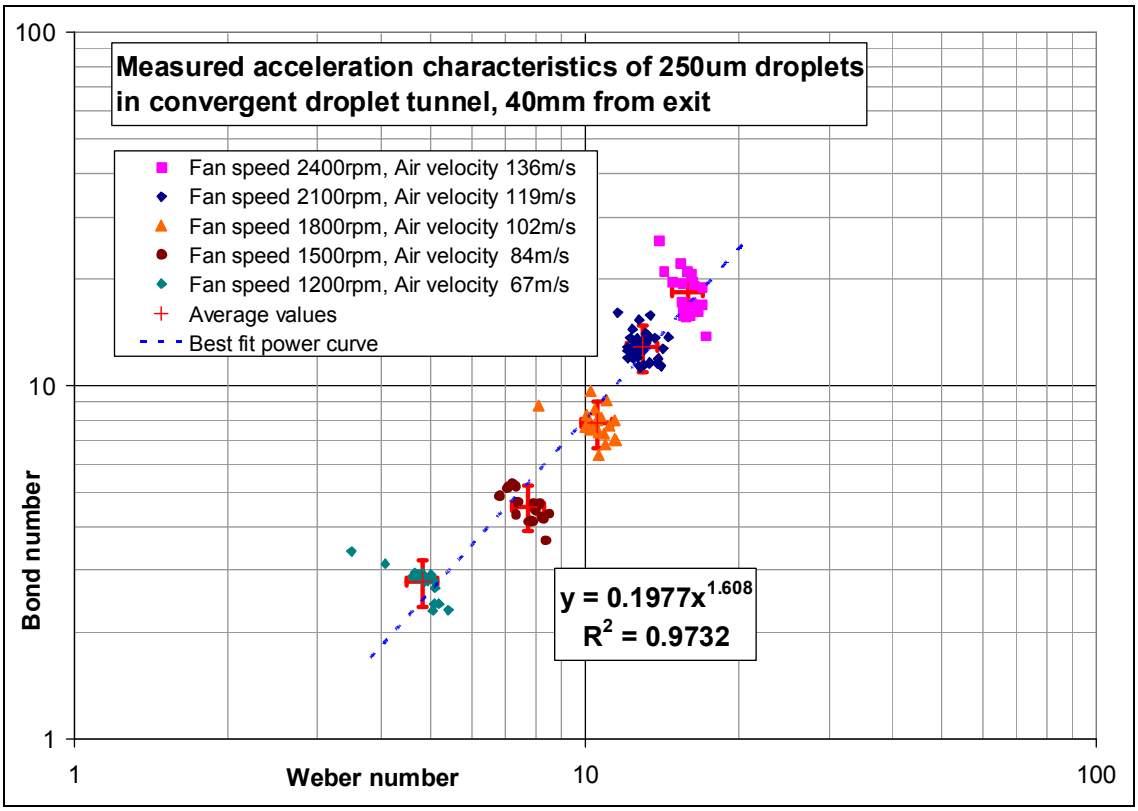

Figure 93: Experimental drag results for 250µm droplets

Conclusions

1. An effective method was developed for measuring the velocity and acceleration of droplets. From these measurements it was possible to experimentally determine the drag characteristics of droplets for the required size and conditions.
2. A range of experimental results was obtained for 250µm droplets which could then be compared with the results predicted by the droplet computer model.

Chapter 6: Droplet Distortion Modelling

The issues

Water droplets naturally tend to a spherical shape, due to surface tension, since this achieves the lowest surface area, and hence the lowest surface energy, for a given droplet volume. They will, however, distort when subjected to uneven surface pressure, either internal or external. External pressure variations would be caused by aerodynamic effects, while internal hydrostatic pressure variations would be caused by the body force of gravity, or acceleration.

If the distributions of internal and external pressure were exactly equal and opposite, then the droplet would remain spherical. Such a situation would occur with a stationary droplet submerged in stagnant immiscible liquid of the same density and subjected to gravitational force, or acceleration. This could result in pressure gradients which might otherwise cause substantial distortion, but the equal pressure gradients in both the external and internal fluids would produce no distortion.

In practice, with an airflow over the droplet, the external pressure gradient would be unlikely to have the necessary equal and opposite pressure distribution to the internal hydrostatic pressure. The resulting imbalance of the external aerodynamic pressure would then produce a net force on the droplet which would to be balanced by a gravitational, or acceleration, force that causes the internal hydrostatic pressure gradient. Hence distortion would occur so that the variation in the curvature of the surface, in conjunction with surface tension, would accommodate the variation in pressure differential across the droplet surface. If this could not be achieved with static equilibrium then some form of dynamic equilibrium might occur, such as vibration or surface ripples. Otherwise an instability might occur that could result in droplet break-up into smaller droplets that could then achieve the necessary stability.

As a droplet distorted, this would change the distributions of external aerodynamic and internal hydrostatic pressure and hence change the resulting distorted shape and in turn the pressure distribution. As a result there would be a complex interaction between the droplet shape and the aerodynamic forces that could be difficult to compute, even with sophisticated CFD methods.

There could, possibly, be circumstances where the external aerodynamic pressure distribution could nearly match the internal hydrostatic pressure distribution due to gravity or acceleration. This might be possible where the flow is lamina or creeping, due to a very low Reynolds number. This combination of circumstances could only be achieved with very small, possibly submicron, droplets for which the gravity, or acceleration, and velocities needed to cause distortion, would be unlikely to occur in SLD icing conditions.

The details of the external pressure distribution could be difficult to compute. Providing there was, however, no significant internal flow, as assumed for this investigation, then, for a constant gravitational force, or steady acceleration, the variation of the internal hydrostatic pressure was quite simple to calculate for a known gravity, or acceleration. The pressure gradient in the direction of gravitational force or acceleration would simply be equal to the fluid density multiplied by gravity or the acceleration rate.

Hence, if the gravity or droplet acceleration was known, then the internal pressure gra-

dient could be computed, from which the droplet distortion could be determined.

One difficulty was that it was the droplet acceleration that was to be determined. Since the distortion could not be computed until the required acceleration was known, it was not possible to directly determine the required acceleration. This situation was, however, resolved by assuming an initial value of acceleration and then an iteration procedure to improve this until the required solution was obtained, as discussed in Chapter 3.

In the acceleration and distortion of a droplets there are three pressures at work which determine the resulting shape of a distorted droplet. These are;

1. The surface tension pressure, $4.\sigma/d$
2. The external aerodynamic pressure, $\rho_a.U^2/2$
3. The internal hydrostatic pressure due to acceleration, $\rho_w.g.d$

where
- σ is surface tension
- d equivalent droplet diameter
- U the air velocity over the droplet.
- ρ_a air density
- ρ_w water density
- g gravitational force, or acceleration

The ratio of aerodynamic pressure to surface tension pressure gives the Weber number;

$$We/8 = \rho.U^2.d / 8.\sigma.$$

If instead we take the ratio of the gravity, or acceleration, pressure to the surface tension pressure, this gives the Bond number;

$$Bo/4 = \rho_w.g.d^2 / 4.\sigma$$

Alternatively, the ratio of aerodynamic pressure to gravity or acceleration pressure gives the Froude number, modified by the density ratio;

$$(\rho_a/\rho_w).Fr / 2 = (\rho_a/\rho_w) . (U^2/g.d) / 2$$

where $Fr = U^2/g.d$

It is also worth noting that;

$$Bo = (\rho_w/\rho_a). We / Fr = \tfrac{3}{4} We.Cd$$

where Cd is the drag coefficient.

Hence $Cd = \tfrac{4}{3} (\rho_w/\rho_a) / Fr$

There are thus two relevant parameters, the Bond number and Weber number, but as has been shown these are not independent of each other, since they have a combined effect on the distorted shape of the droplet. Hence a given droplet shape would have a given value of drag coefficient, Cd, determined by the droplet distortion and Reynolds number. This is in turn would be related to the Weber number via the Laplace number, La, for the given fluid properties and droplet size, as represented by the relationship;

$$La = Re^2 / We = \rho_a.\sigma.d/\mu_a^2$$

Hence for a given value of Laplace number, which for given fluid properties would be determined by the droplet size, there would otherwise be only one independent parame-

ter. The issue was to decide which of the available parameters would be dominant in determining the droplet distortion.

The practicality of the situation was that a distorted droplet shape could be determined by reasonably tractable calculation or by experimental measurements, given the Bond number and a defined external pressure distribution.

In comparison, it was much more difficult to determine the distortion from the Weber number, since this required much more sophisticated analysis, possibly using CFD modelling with a deformable shape, which was much more difficult for Re > 200.

Johnson and Patel (1998) showed that for Re > 200 the flow past a sphere was steady but not symmetric and for Re > 270 the flow was neither symmetric nor steady. Hence CFD analysis would be increasingly difficult, particularly as it required careful design of the CFD mesh to accurately determine the location of the boundary layer separation.

The alternative was to obtain experimental data for droplet distortion, but there were many difficulties with that for all but a few particular conditions.

Sessile droplet model

Given the pressure distribution around a droplet and the acceleration, it was possible to compute the droplet shape, since the curvature of the droplet surface had to be such that in conjunction with the surface tension it accounted for the pressure differential across the droplet surface. For axisymmetric conditions this is described by the following equations (Middleman 1995);

$$\delta P = \sigma (1/R_c + 1/R_m) = P_{internal} - P_{external}$$

or $$\delta P/\sigma = 1/R_t = 1/R_c + 1/R_m$$

thus $$1/R_m = 1/R_t - 1/R_c$$

where δP is the pressure differential across the droplet surface
σ is the surface tension
R_c is the circumferential radius of curvature
R_m is the meridional radius of curvature.
R_t is the combined radius of curvature.

Given that the droplet surface is at angle θ to the droplet axis then it can be shown that;

$$1/R_c = \mathrm{Cos}(\theta) / r$$

$$1/R_m = d\theta/ds$$

where r is the radial distance of the surface from the axis
z is the axial distance
s is the meridional path distance

Hence $$d\theta/ds = (1/R_t - 1/R_c) = \delta P/\sigma - \mathrm{Cos}(\theta)/r$$

and also $$dr/ds = \mathrm{Sin}(\theta)$$

$$dz/ds = \mathrm{Cos}(\theta)$$

$$dv/ds = \pi.r^2.\mathrm{Cos}(\theta)$$

$$dA/ds = 2.\pi.r$$

where v is the droplet volume
A is the droplet surface area

We note that $P_{internal} = P_0 - \rho.g.z$

but $P_{external}$ depend of the aerodynamic pressure distribution.

These equations can be solved by numerical integration. In this investigation the 4th order Runge-Kutta method was used for equal increments of path length. This used the same simulation package used to model the droplet motion dynamics in Chapter 8.

It is to be noted that the equations can become ill conditioned at r = 0. This can be resolved by ensuring that;

$$\mathrm{Cos}(\theta) = 0 \quad \text{and} \quad d\theta/ds = 2.\delta P/\sigma \quad \text{at} \quad r = 0$$

It is possible to change the independent variable from path length 's' to surface angle θ by multiplying the equations through by ds/dθ to obtain

$$ds/d\theta = 1 / (\delta P/\sigma - \mathrm{Cos}(\theta)/r)$$

$$dr/d\theta = \mathrm{Sin}(\theta) / (\delta P/\sigma - \mathrm{Cos}(\theta)/r)$$

$$dz/d\theta = \mathrm{Cos}(\theta) / (\delta P/\sigma - \mathrm{Cos}(\theta)/r)$$

This may be advantageous where the limits for integration can be better defined in terms of surface angle, rather than path distance. It may also be advantageous where the curvature and pressure variations are small, since it can greatly reduce the number of computation points.

In this transformation it is possible for the equations to become ill conditioned and singular when dθ/ds becomes zero or in other words there is no curvature, such as at a point of inflection. Hence such conditions have to be avoided with this formulation. If that is not possible, then the original formulation of the equations can be used.

Where dθ/ds was zero over a short distance, such as at a point of inflection, the original formulation for increments of path length could be used. The solution could then revert the revised version, but the sign for the increments of θ would then have to be changed.

Similar transformations could be made with respect to the radial and axial distances, r and z. The first could be used for evaluating a radial surface with a fixed outer radius and the second could be used when evaluating a cylindrical surface over a given length.

Use of surface equations with CFD analysis

One approach was to determine the external pressure for a given droplet shape and flow conditions either by experiment or with CFD modelling with a prescribed shape.

From this the pressure distribution could then be described, such as a function of the surface angle, θ, from which the revised droplet shape could then be recalculated using numerical integration. This modified shape could then be analysed by CFD analysis or experiment to determine the revised pressure distribution. This procedure could be iteratively repeated until it converged to the required shape.

The advantage of this procedure is that it could use standard CFD analysis for a prescribed shape with a fixed surface. Hence this would avoid the considerable additional complexity and greater stability problems of CFD modelling with free-surfaces. A disadvantage would be that it could only be used for steady conditions.

This method would converge more quickly given an initial shape that was close to the required solution, for which the sessile droplet shape might be appropriate.

CFD free-surface modelling

For this there were two standard methods, the ALE method and the VOF method.

In the ALE (Arbitrary Lagrangian Eulerian) method the boundary of the CFD mesh that represented the droplet surface would be allowed to move to conform to the required pressure distribution across the droplet boundary. In the VOF (Volume Of Fill) method the free-surface boundary would be allowed to move across a fixed mesh.

The ALE method would appear to be more suitable where only moderate amounts of mesh distortion were required and no break-up or joining of surfaces would occur, which is generally the case for modelling droplet distortion.

The VOF method would be more suitable for situation where there were large amounts of surface movement and surface separation and joining were a requirement.

The surface pressure difference would have be computed from the curvature of the surface and this could greatly magnify small errors in the surface representation. With the ALE method the surface boundary would be well defined, so the surface curvature would be readily computed. With the VOF method the surface geometry would be much less well defined and it is understood that this could increase the inaccuracies in the curvature calculation and sometimes cause ambiguity.

Simplified model of droplet shape

Whilst feasible, the CFD methods for determining the droplet shape could be unwieldy, complex and time consuming to develop and use.

It might not be necessary to determine the droplet shape to a high degree of accuracy to obtain acceptable results for droplet drag.

It was simpler to use the assumption of a sessile droplet on a horizontal unwettable surface. For this the external pressure on the free surface was assumed to be constant, whilst the uniform pressure on the base of the droplet was supported at constant z by a flat horizontal surface exerting a higher constant pressure.

At its simplest the pressure from the base could be treated as the aerodynamic stagnation pressure, whilst that on the free surface could be atmospheric pressure.

Assuming that $P_0 = P_{external}$ at $z = 0$, then $\delta P = -\rho.g.z$

The initial conditions for the upper surface of the droplet could be;

$$s = 0$$
$$\theta = -\pi/2 \quad , \quad \text{i.e. } \mathrm{Cos}(\theta) = 0$$
$$r = 0$$
and
$$z = -z_0$$

For the purpose of the evaluation the conditions were normalised to the following;

Gravity	=	4
Density	=	1
Surface tension	=	1

For ambient conditions this would be;

Gravity	=	$9.81 m/s^2$

Density = 10^3 kg/m^3

Surface tension = 73×10^{-3} N/m

By equating the Bond numbers we obtain;

$$D_{normalised} / D_{actual} = \sqrt{((10^3 \times 9.81 / 73 \times 10^{-3}) / (1 \times 4 / 1))}$$

$$= \sqrt{(134.38 \times 10^3 / 4)} = 183.3$$

Hence the calculated size of the droplet needed to be scaled down by a factor of 183.3.

The equivalent size of the droplet was calculated from the droplet volume as;

$$D = \sqrt[3]{(6.v/\pi)}$$

from which the Bond number was calculated.

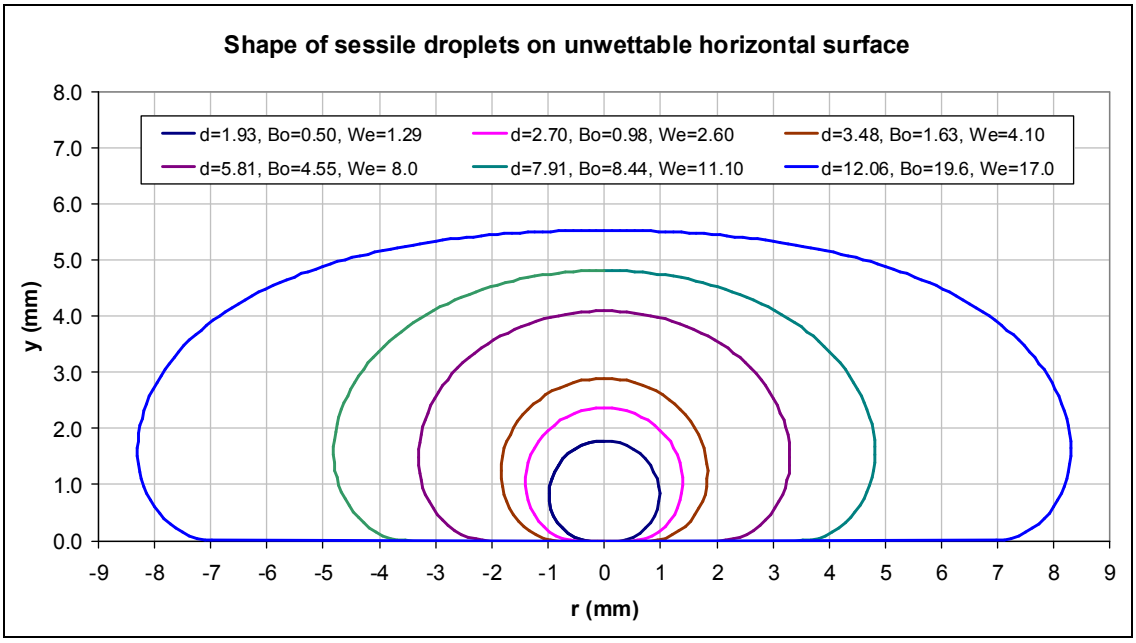

Figure 94: Distorted shape of Sessile Droplets

Varying the value of z_0 gave different amounts of distortion, as shown in Figure 94, where the base of the droplets have been aligned. As z_0 tends to zero, the size of the droplet tends to infinity.

In this analysis the droplet size was adjusted to be the same for available results for free-falling droplets in ambient air and standard gravity, as given by Schmehl (2002).

The resulting droplet diameters obtained were 2.6mm, 3.48mm, 5.81mm and 7.91mm, as compared to 2.7mm, 3.45mm, 5.80mm and 8.00mm given by Schmehl for free-falling droplets, see Chapter 1, section "Sessile Droplet Distortion".

Experimental data for free falling droplets was given by Clift, Grace and Weber as shown in Figure 95.

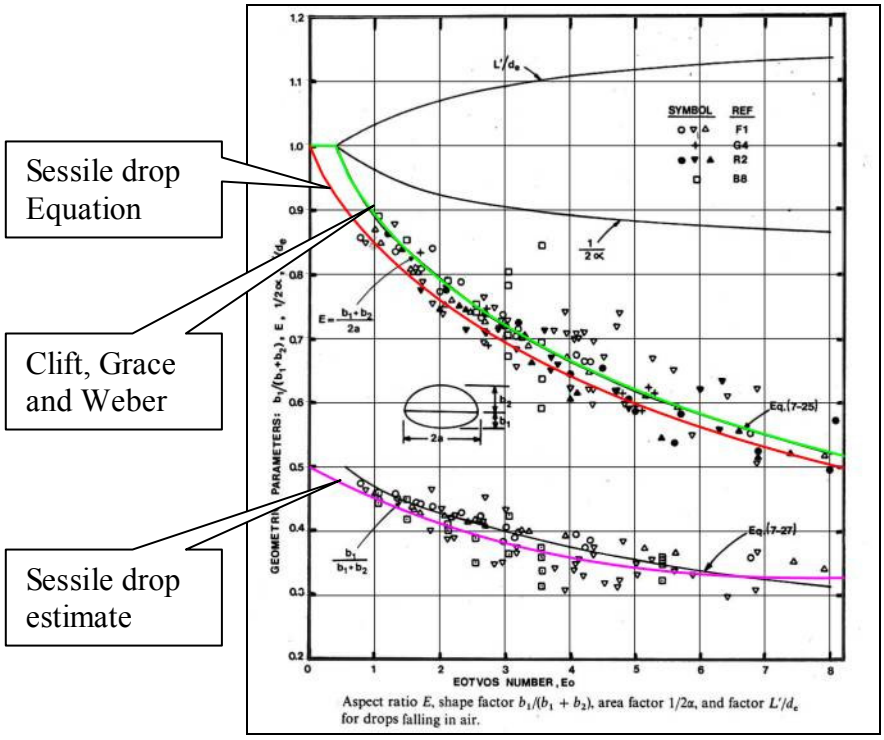

Figure 95: Droplet distortion data, Clift, Grace and Weber

This shows the aspect ratio of the distorted droplet as a function of the Eotvos number, which is equivalent to the Bond number.

The green curve is the equation given by Clift et al,

$$b/a \quad = \quad 1.0 / (1.0 + 0.18 (Bo - 0.4)^{0.8})$$

which are is defined in this Chapter by;

a the equator diameter
b the droplet thickness

This equation can be rewritten in the straight-line form;

$$\log_{10}(a / b - 1.0) = \log_{10}(0.18) + 0.8 \log_{10}(Bo - 0.4)$$

The data from the sessile drop analysis was plotted in the same way in Figure 96, except that it was not found necessary to shift the Bond number by subtracting 0.4. The reason for this being done in the data from Clift et al is not clear, as it did not appear to improve the quality of the fit to the data shown. This may have been done with the assumption that droplets did not distort below a given value of Bond number, but there would seem to be no justification for this. Since, however, the primary interest was at higher Bond numbers this discrepancy was not investigated any further.

The result of the curve fit for the sessile drop was;

$$\log_{10}(a / b - 1.0) = \log_{10}(0.1787) + 0.8209 \log_{10}(Bo) \text{ with a variance of 1.5\%.}$$

or $$b/a = 1 / (1.0 + 0.1787 Bo^{0.8209})$$

This is plotted in Figure 95 as the red curve. It can be seen that this curve also encompasses many of the experimental points, particularly at higher Bond numbers.

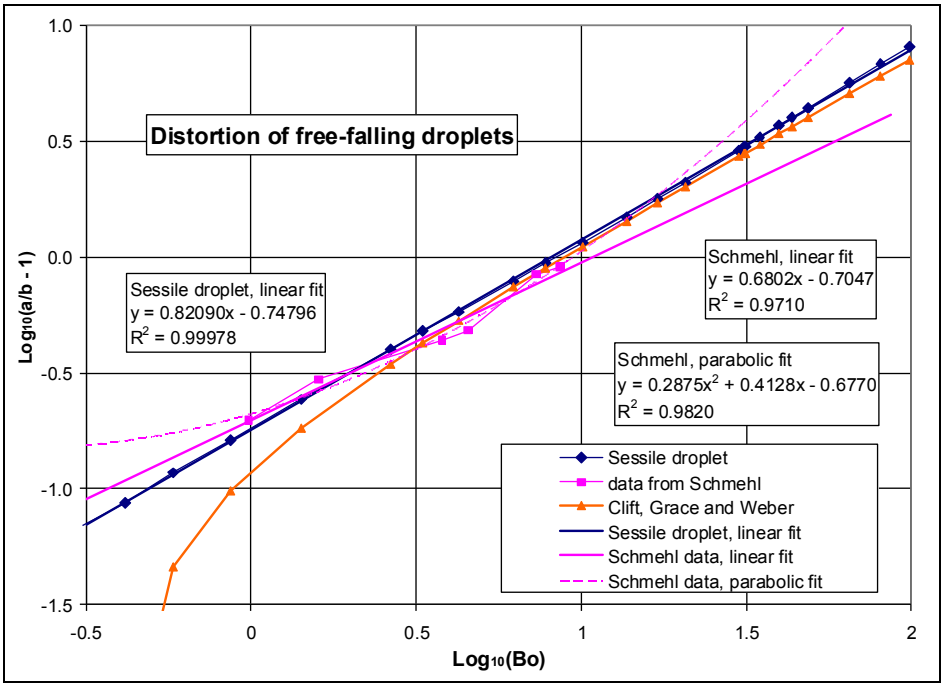

Figure 96: Linearised plot of Droplet Distortion for free-falling Droplets

The estimated proportion of thickness at the equator diameter for a sessile drop is also plotted in Figure 95. This had to be estimated from the numerical analysis, since the model had not been set up to provide this data. The integration steps were larger than ideal for this, so the data obtained was fairly coarse. The curve fitting was directly applied to the data, rather than via the linearised curve with the log/log scales. It can, however, be seen from Figure 95 that the thickness split was very similar to the experimental data for free-falling droplets given by Clift, Grace and Weber.

It is to be noted that in Figure 96 the curve for the equation from Clift et al bends downward at low Bond numbers because the 0.4 shift in Bond number was not applied in this plot. Above a Bond number of about 3 there was good agreement between the Sessile droplet distortion and the data from Clift et al.

Schmehl included pictures from experiments of six droplets in free-fall (see Chapter 1 and 3). These pictures were greatly enlarged and measured to determine their aspect ratio, and this data is also plotted in Figure 96 and fitted with both a linear and parabolic curve. The data quality from this was limited, but between Bond numbers of 1 to 10 the linear fit was in reasonable agreement with that for sessile droplets.

Comparison of Droplet Distortion by Weber number

In calculating the shape of the sessile drop this was matched with the experimental droplet from Schmehl with the same Bond number, for which the Weber numbers would match at the measured free-fall velocity.

The Weber number is defined as; $We = \rho_a.U^2/\sigma = 2.P_d.d / \sigma$

where P_d is the stagnation pressure at the centre of the upstream side of the droplet.

With a free-falling droplet the pressure on the upwind surface would be at the stagnation pressure at the axis and would steadily decrease with increasing distance from the axis. Hence the pressure was averaged out over the frontal surface. On the leeward surface

the pressure was understood to be near uniform and near atmospheric pressure.

For the sessile droplet all of the upstream pressure was concentrated at the contact region, as can be seen in Figure 94. This would have been smaller than the equivalent area over which the dynamic pressure would have been applied for a free-falling droplet, which on average was around 0.4 to 0.5 of the area of the equator diameter for a near-spherical droplet. This was likely to result in greater distortion than for a free-falling droplet at the same Bond number.

As the sessile droplet became more distorted and the frontal loading was spread over more of the frontal area, then the distortion would become more like that of the free-falling droplet. Since the primary interest was with the higher Bond numbers, the distortion errors at low Bond numbers were not of great concern. Even so they introduced no more than a discrepancy of about 1% in the drag calculation for all except the lowest values of Bond number, where the droplets were near-spherical anyway.

It was difficult to ascribe a Weber number to sessile droplets, since they did not have a velocity. This could have been in terms of the stagnation pressure in the contact region, or in terms of the average pressure over the frontal area. For low Bond numbers this either greatly over-estimated, or greatly underestimated, the Weber number, relative to that for a free-falling droplet. As the distortion increased, these two values of Weber number converged towards the free-falling value. In practical terms the sessile droplet was best described in terms of the Bond number and its effective Weber number could then be determined from the data for free-falling droplets with the same Bond number.

Floating Droplets

A more realistic droplet distortion model could be that of a droplet floating on an unwettable liquid of higher density. In this it would be assumed that the surface tension between the droplet and supporting liquid was the same as at the droplet-to-air interface. This would better model the windward side of the droplet and produce a more reasonable pressure distribution at lower Bond numbers than for the sessile droplets. This would not represent the real situation for floating droplets, but would provide a solvable and plausible numerical solution that would better approximate free-falling droplets. This would be more complex to apply, since it would involve two parameters, the Bond number and liquid density ratio. It is not clear how these would be related to each other. Because the sessile droplet gave distortions that adequately represented free-falling droplets, the analysis of floating droplets was not pursued.

Droplet of oval cross-section

A droplet can become sufficiently distorted, such as shown in Figure 97, that its cross-section can be considered as being oval, with two flat and parallel surfaces joined at the edges by a constant radius.

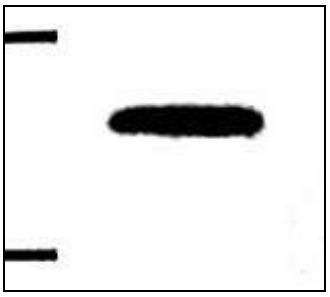

Figure 97: View of distorted droplet

In Figure 97, there are two calibration marks on the left with 0.6mm spacing. In the orientation shown the droplet was being accelerated upward by the airflow in a convergent tunnel. In practice the actual flow was from right to left, but the picture has been rotated clockwise by 90 degrees for comparison with sessile droplets.

The droplet might be viewed as resting on a cushion of upward airflow. In practice this could not be sustained and this image was only achieved because of the rapid increase

in the aerodynamics forces before the droplet would break up.

Asymptotic Limit

The purpose of this evaluation was to determine whether the assumptions made about the extrapolation of the data for free-falling droplets to higher Weber numbers in Chapter 3 was reasonable. In that Chapter, it was argued that the value of We^2/Bo would tend to a stable asymptotic value.

If the droplet in Figure 97 was considered to be resting in a fixed location on a cushion of upward air flow, while subjected to a strong gravitational force, rather than acceleration force, the pressure conditions inside the droplet could be determined.

Because the windward and leeward surfaces were flat, it could be assumed that these would transmit pressure without modification.

If the edges were assumed to be semicircular, with constant radius, it was possible to evaluate the surface tension pressure differential across them.

The distorted droplet was assumed to have the following properties;

a	equator diameter
b	thickness
ρ_w	droplet density
ρ_a	air density
σ	surface tension
U	air velocity
g	gravity

From the gravitational and surface tension forces one could say that the excess pressure, over atmospheric pressure at the droplet's centre, was;

$$P = \rho_w.g.b/2 = \sigma.(2/b + 2/a) = 2.(\sigma/b).(1 + b/a)$$

Hence $\rho_w.g.b^2/\sigma = 4.(1 + b/a) = Bo_b$

where Bo_b is the Bond number for the droplet thickness

The approximate pressure differential across the droplet, due to the aerodynamic forces and the droplet acceleration, could be equated as follows;

$$\rho_a.U^2/2 = \rho_w.g.b = 4.(\sigma/b).(1 + b/a)$$

Hence $\rho_a.U^2.b/\sigma = 8.(1 + b/a) = We_b$

where We_b is the Weber number for the droplet thickness.

Hence $We_b^2/ Bo_b = 64.(1 + b/a)^2 / (4.(1 + b/a)) = 16.(1 + b/a)$

It is to be noticed that this does not relate to any droplet dimension, only to the droplet shape. It is also to be noticed that;

as $b/a \rightarrow 0$, $We^2/Bo \rightarrow 16$

This was also found to be the situation for a sessile droplet on a horizontal unwettable surface.

We notice that, as $b/a \rightarrow 1$, $We^2/Bo \rightarrow 32$, whereas for an actual droplet it tends to zero. This is because the Weber number calculation used for the oval section droplet

model is only reasonably valid when b/a is small.

An alternative method of estimating the Weber number might have given a better approximation to the behaviour of actual droplets, but the primary purpose of this evaluation was to establish that We^2/Bo tends to a finite value of about 16 as We tends to infinity.

With the experimental data from Maybank and Briosi for free-falling droplets, an asymptotic value for We^2/Bo of 14.75 was obtained. It is quite possible that a more careful evaluation of the oval, or sessile, droplet would produce a closer result. However even the very simple model considered was within 8.5% of the measured value.

It was thus argued that, for high Weber numbers with intact droplets, the value of We^2/Bo tended to a constant value of 14.75. This asymptotic value was, in practice, achieved at about We = 13.

Conclusions

1. Droplet distortion is primarily determined by the Bond number.
2. For drag calculations, the distortion of a sessile droplet on a horizontal unwettable surface is an adequate approximation to the distortion caused by gravity or acceleration to a droplet in an airflow.
3. For an intact droplet it was found that We^2/Bo tends to a constant value. For a droplet of oval section, or a sessile droplet, this limit had a value of 16, whilst for free-falling droplets the limiting value was 14.75.

Chapter 7: Approximate Evaluation of Bag Break-up

The primary issue in this investigation was to determine a practical relationship for the drag characteristics of distorted droplets at high Weber numbers, We > 3. This could only be effective up to the break-up of the droplet.

It was thus necessary to have a sufficient understanding about the droplet break-up in order to determine the conditions over which the drag formulation would apply.

Within the literature there appeared to be a variety of opinions about the minimal conditions in which droplet break-up would occur. There was a consensus that for a constant, or slowly increasing, Weber number it would be in the range 12 < We < 24, but this gave a substantial range of uncertainty.

It was known that in transient conditions, with a suddenly applied and sustained aerodynamic pressure, the droplet would break up at a Weber number of about 12 (Wierzba 1990) and the time required for this was about one oscillation period for the droplet's small perturbation vibration.

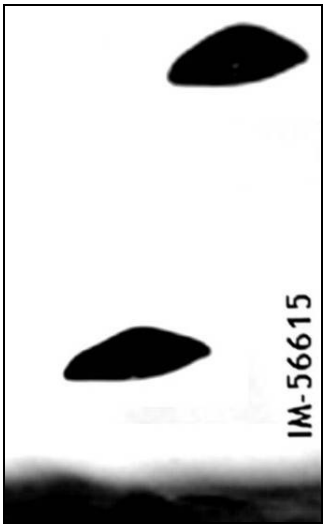

Figure 98: Droplet distortion in the stagnation region

It was also known that droplets could survive at much higher Weber numbers for short periods. Figure 98 shows an intact droplet at a Weber number of about 30, as it entered a stagnation region just prior to impact with a target in the vertical tunnel.

The issue was to determine the minimum break-up conditions for a constant, or slowly increasing, Weber number. In this situation there would appear to be two differing views about causes of droplet break-up.

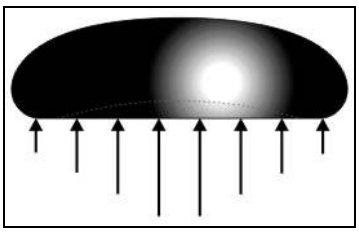

Figure 99: Varying pressure distribution on a droplet

The prevailing view appeared to be that droplet break-up was due to the external aerodynamic forces, as represented by the Weber number, such as expressed by Schmehl, (2002 to 2003, his German thesis and private communications) and Liu (2000). In this view it was argued that the uneven pressure distribution on the windward side of the droplet, as shown in Figure 99, had a higher pressure near the centre which deflected this surface inward to form an internal bubble, or bag, which then expanded and burst.

The Rayleigh-Taylor Instability Model

An alternative view, favoured by the author, was that the droplet distortion and bag break-up was, primarily, dominated by the droplet acceleration or gravity, as represented by the Bond number (Clift, Grace and Weber). In this view the primary contribution of the air drag was to provide the necessary acceleration or to control the free-fall terminal velocity against gravity.

The distorted shape of the droplet would, of course, be affected by the external pressure distribution, but it would seem that the internal hydrostatic pressure variations, due to the fluid density and acceleration or gravity, had the dominant effect, as discussed in Chapter 6. As discussed in that chapter it was found that the deformation of a sessile droplet was quite similar to that of a free-falling droplet at the same Bond number, de-

spite the considerable differences in the external pressure distribution.

For free-falling droplets Clift et al (1978) also gave the distortion of free-falling droplets in terms of the Bond, or Eotvos, number.

The principal mechanism considered for the droplet break-up was the Rayleigh-Taylor instability (Nöbauer1999). This is where a higher density fluid is supported against gravity, or acceleration, by an underlying lower density fluid. In this case the high density water of the droplet and the low density fluid of the surrounding air. Where the interface surface between these had no bounds this situation was shown to be unstable and the higher density liquid would sink into the lower density liquid (G.I. Taylor, 1949).

If the region of the interface was constrained, then for appropriate conditions the water-to-air interface could be stable.

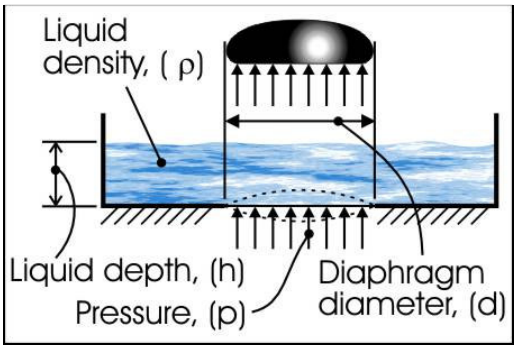

Figure 100: Sessile droplet model of instability

In this case the region of interest was the flattened windward surface of the droplet constrained by the equator diameter, De, shown as (d) in Figure 100. To simplify the evaluation, this was approximated to an inverted water-to-air interface across a circular hole at the bottom of a shallow tank, as shown in the lower diagram in Figure 100. In this a pressure (p) needed to be applied to balance the water head, $\rho_w.g.h$, or $\rho_w.a.h$, where **a** was the droplet acceleration. In the droplet the stagnation pressure, of $\rho_a.U^2/2$, would be applied, at least at the centre of the surface.

With the interface in equilibrium, if this was slightly deflected upward the resulting surface curvature and surface tension would provide a restoring force to return the surface back to its original position. On the other hand, the deformed surface would also experience a lower hydrostatic head, so producing a reduced balancing pressure in the opposite direction to the surface tension, so as to destabilise the liquid interface.

An approximation of the situation is shown in Figure 101, in which vertical movement of the frictionless piston represents deflection of the interface surface and the spring represents the stiffness of the interface due to surface tension.

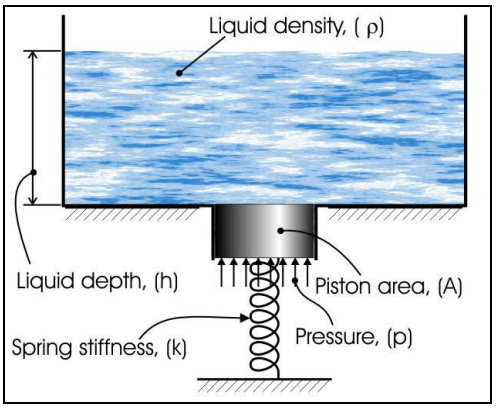

Figure 101: Piston stability in bottom of tank

It can be shown that for neutral equilibrium;

$$k.z = (p - \rho.g.(h - z)).A - (p - \rho.g.h).A$$
$$= \rho.g.A.z$$

or $k = \rho.g.A$

If the spring stiffness was less than this critical value, then the piston would become unstable.

It is noted from this that the stability of the piston does not depend on the depth of water, the applied air pressure, or even the distribution of the pressure.

The axisymmetric solution for the deflection of the water surface is given if Chapter 6 on Droplet Distortion Modelling.

where $d\theta/ds = 1/R_t - 1/R_c = \delta P/\sigma - \mathrm{Cos}(\theta)/r$

$dr/ds = \mathrm{Sin}(\theta)$; $dz/ds = \mathrm{Cos}(\theta)$

For a near flat circular surface, $d\theta/ds$ d^2z/dr^2, s r, $\mathrm{Cos}(\theta)$ dz/dr, $\mathrm{Sin}(\theta)$ 1 this reduces to; $d^2z/dr^2 + (dz/dr)/r - \delta P/\sigma = 0$

or $r^2.d^2z/dr^2 + r.dz/dr - r^2.\delta P/\sigma = 0$

However $\delta P = (p - \rho.g.h) - (p - \rho.g.(h - z)) = -\rho.g.z$

Hence $r^2.d^2z/dr^2 + r.dz/dr + (\rho.g/\sigma).r^2.z = 0$

or $r^2.d^2z/dr^2 + r.dz/dr + ((c.r)^2 + n^2).z = 0$

where $c^2 = \rho.g/\sigma$ and $n = 0$

The solution to this differential equation was the zero order Bessel function of the 1st kind, $J_0(c.r)$, which is shown in Figure 102. The dashed line shows the function $\mathrm{Cos}(\pi.r/De)$.

hence $z = z_0.J_0(c.r)$

where z_0 is an arbitrary constant.

At $r = De/2$, $z = 0$

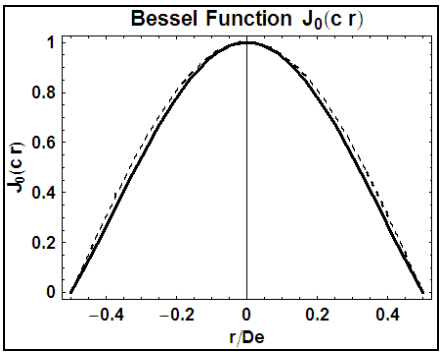

Figure 102: Deflection of water interface

Hence $2.c.r = De.\sqrt{(\rho.g/\sigma)} = 2 \times 2.404826$

or $\rho.g.De^2/\sigma = Bo_E = (2 \times 2.404826)^2$

$= \mathbf{23.133}$

This gives the critical Bond number, Bo_E, for the equator diameter, De.

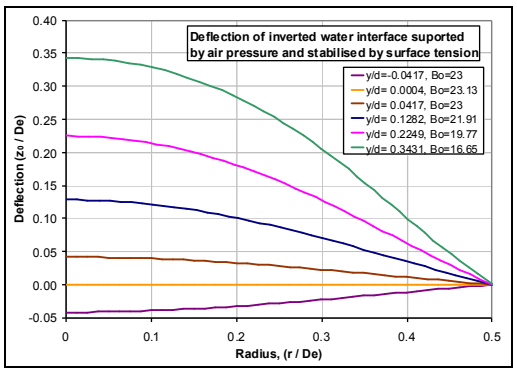

Figure 103: Large deflection of water interface

Numerical Solution

It was not possible to obtain an analytical solution for the large deflections of the non-linear equations;

$d\theta/ds = 1/R_t - 1/R_c = \delta P/\sigma - \mathrm{Cos}(\theta)/r$

$dr/ds = \mathrm{Sin}(\theta)$, $dz/ds = \mathrm{Cos}(\theta)$

These were solved numerically for large deflections, as shown in Figure 103. As the deflection of the interface increased, the stability limit, as represented by the equator Bond number, decreased, as shown in Figure 104.

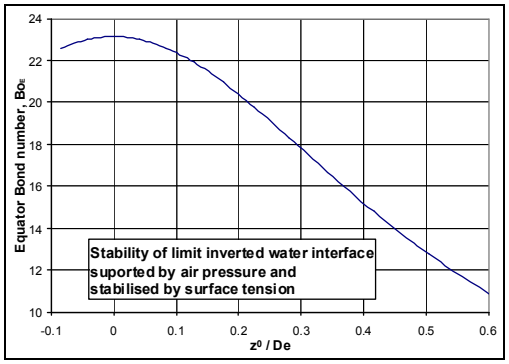

Figure 104: Stability limit against deflection

Once the maximum critical Bond number, $Bo_E > 23.13$, had been exceeded and the upwind surface starts to collapse inward, the critical limit decreases for two reasons;

1. The critical Bond number decreased as the interface deflection increased.

2. As the interface deflected inward, it displaced liquid, which could increase the equator diameter, so further increasing the equator Bond number.

Once the critical limit for the windward surface has been exceeded and it collapsed inward by a significant amount, the instability would then be greatly increased and the full bag instability would quickly develop.

The preceding analysis provides the critical Weber number for the equator diameter, but for practical purposes this needs to be related to the spherical diameter, D, for the same volume. This was achieved with the relationship;

$$Bo_E / Bo = (De / D)^2$$

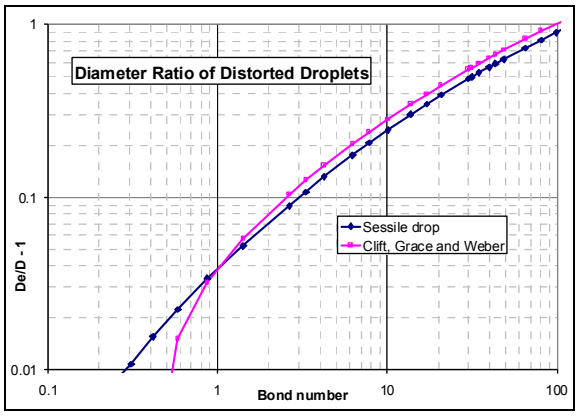

Figure 105: Diameter ratio for distorted droplets

The relationship between these two diameters in shown in Figure 105, both for free-falling droplets (Clift et al 1978) and for sessile drops resting on an unwettable horizontal surface (Chapter 6). In the range of interest the difference in equator diameter for the two relationships was about 3%.

For the sessile drop the ratio of De to D was given by the following equations;

$$x = Log_{10}(Bo) \quad \text{and} \quad De/D = 10^y + 1$$

where $$y = 0.014859\, x^3 - 0.164956\, x^2 + 0.960273\, x - 1.42341$$

Using this relationship the spherical diameter Bond number was adjusted to achieve the critical equator Bond number of 23.13. This occured with a sphere Bond number of 13.69, which for a free-falling water droplet gave a critical Weber number of 14.19.

When the resulting Bond number was evaluated for distilled water and standard ambient conditions, the resulting critical spherical diameter was **10.07mm**.

Hinze (1949) determined the terminal droplet velocity from its size using the data of Merrington and Richardson (1947). Assuming a constant drag coefficient, Cd = 0.7, the break-up free-fall velocity for the critical water droplet size of **10mm** was calculated to be 12.7m/s. This gave a critical Weber number of We = 26.2.

In comparison, Harper, Grube and Chang (1972) developed a model for the break-up of accelerating droplets and determined the lowest critical Bond number to be Bo = 44.9, which was equivalent to a Weber number, We = 25.3, from the extrapolated relationship between We and Bo. This was within 4% of the deduced experimental results of Hinze. Such results seem to have been adopted by some researchers as the lowest critical conditions for droplet break-up.

The results of Hinze could not, however, be correct, as the drag coefficient increases as the droplet velocity increases, due to its distortion. The maximum measured terminal free-fall droplet velocity was 9.24m/s (Schmehl 2002 – 03), (Gunn & Kinzer 1949), (Maybank & Briosi 1961). The absolute limit for distilled water was determined to be 9.29m/s in ambient conditions of 1000mB pressure, at 20C with gravity of 9.81m/s^2.

The critical droplet diameter for distilled water was calculated to be within 0.7% of the

experimental result (Merrington 1947). For Methyl-salicylate it was within 7% and for Glycerine +20% water it was within 4%. For Carbon Tetrachloride the discrepancy was, however, 30%, but that may have been due to experimental errors.

Measurements in the convergent wind tunnel with 250µm droplets, Chapter 5, achieved a Bond number of 18.4 at a Weber number of 15.9. This exceeded the theoretical critical value of 13.7 by 2.2. The related critical Weber number was evaluated to be 13.5, so the measured value exceeded this by 2.4. This was thought possible because of the rapid rate of increase in Weber number the tunnel was designed to achieve. For the 250µm droplets this was at the rate of about one Weber number per droplet oscillation period. Hence the droplets had at least two oscillation periods after exceeding the critical Bond number before breaking up. This would seem reasonable, given that the excess in the Bond number would initially be quite small and it would take time for the droplet dynamics to respond to steadily increasing difference.

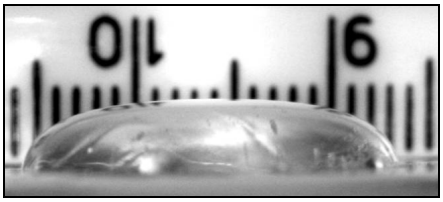

Figure 106: Sessile droplet on PTFE

The reason for terminal free-fall velocity having an upper limit was that, as the droplet size increases, its thickness reaches an asymptotic limit, as shown in Figure 107 for a sessile droplet. This would be observed if a large water droplet were placed on an unwettable horizontal surface, with a contact angle of 180°. Figure 106 shows a water droplet on a PTFE surface. On a truly unwettable surface this would be about 5.6mm thick, for the diameter shown. In practice it was about 3.5mm thick, as the contact angle with the surface was much less than 180°. In free-fall, or in an accelerating airflow, the droplet would be supported by the dynamic air pressure, so there would be no surface contact.

It was noted that the dynamic air pressure of the free-fall velocity had to balance the hydrostatic head of the droplet thickness.

Figure 107 shows the thickness of a sessile water droplet in ambient conditions on an unwettable horizontal surface, with respect to the equivalent spherical diameter.

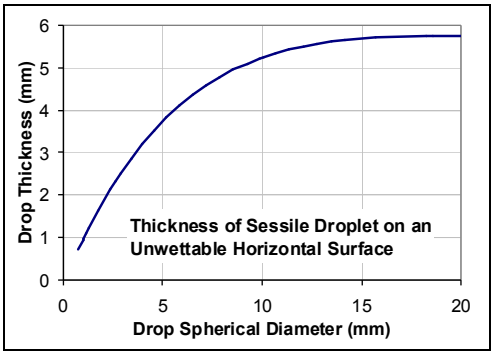

Figure 107: Thickness of Sessile Droplet

It was possible to equate the hydrostatic head for the droplet thickness against the dynamic head for the terminal free-fall velocity in air. This gave the relationship;

$$\rho_w.g.h = \rho_a.U^2/2$$

or $$U = \sqrt{(2.g.h.(\rho_w/\rho_a))}$$

where U is terminal velocity
h droplet thickness
g gravity, or acceleration
ρ_w droplet density
ρ_a air density

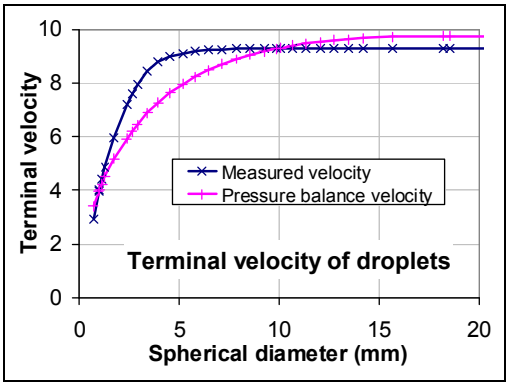

Figure 108: Terminal velocity of droplets

Figure 108 shows the resulting "Pressure balance velocity" against the "measured" ter-

minal velocity, extrapolated for diameters greater than 8mm. These two curves intersect at diameters of 9.84mm and 0.98 mm. It was of interest to note that the larger of these diameters, 9.84mm, was very close to the critical droplet diameter of 10mm, which might have helped to explain why the prediction for the critical diameter was so accurate, since for this size the aerodynamic forces predicted by the sessile drop model happen to equal the actual aerodynamic forces.

Conclusion

1. Bag break-up is the result of the Rayleigh-Taylor instability of the flattened windward surface of the droplet.
2. This gave a critical Bond number, with respect to the equator diameter, of 23.13.
3. Using the distortion model of a sessile droplet, resting on an unwettable horizontal surface, this translated to a critical Bond number of **Bo =13.69**, with respect to a spherical diameter of the same volume.
4. From the Bond number, the critical diameter for a free-falling water droplet was determined to be **10.07mm**, the measured value being 10mm.
5. Extrapolating the available free-fall terminal velocity data for droplets, the critical Weber number for such conditions was determined to be We = 14.19.
6. It was thus concluded that for practical purposes, the limiting conditions for a steady, or steadily increasing, Weber number was **We = 14.2**

Chapter 8: Development of Simulation for Droplet Motion Dynamics

Method of analysis

To help develop the icing wind tunnel facilities and to investigate the effects of droplet distortion in SLD icing, a simulation of droplet motion dynamics was developed. This tracked the Lagrangian motion of droplets in a given airflow, with the assumption that;

1. The droplets did not affect the airflow
2. The droplets did not interact with each other.

The solution was implemented with a general-purpose **NO**nlinear **D**ifferential **E**quation **S**olver (NODES). The development of this was initiated by the author in 1984 for analysis of a pneumatic position servo and a pneumatic percussion hammer. It was further developed in 1990 for an electromagnetic air pump, where the 4th order Runge-Kutta method was implemented (Press et al 1986, Numerical Recipes). After investigating various alternative options, this was found to be the most stable and effective method. This software was subsequently used for various other modelling applications, such as pipeline pressure transients, passenger lift vibrations, 2D transient heat transfer, rocket trajectories, suspension dynamics, ink-jet printer mechanisms and motion dynamics of droplets in ink-jet printers. This last application formed the basis of the model for this investigation. The software was written in Quick Basic 4, under MS DOS 6.1, which could readily be adapted to Visual Basic, under MS Windows, or another language.

Numerical Solution of Equations

The equations to be solved had to be defined as a series of simultaneous 1st order differential equations of the form;

$$
\begin{aligned}
dy_1(y_j) / dy_j &= f_1(x, y_1, y_2, \ldots, y_i, \ldots, y_j \ldots, y_n) \\
dy_2(y_j) / dy_j &= f_2(x, y_1, y_2, \ldots, y_i, \ldots, y_j \ldots, y_n) \\
\ldots\ldots\ldots\ldots & \quad \ldots\ldots\ldots\ldots\ldots\ldots\ldots\ldots\ldots\ldots \\
dy_i(y_j) / dy_j &= f_i(x, y_1, y_2, \ldots, y_i, \ldots, y_j \ldots, y_n) \\
\ldots\ldots\ldots\ldots & \quad \ldots\ldots\ldots\ldots\ldots\ldots\ldots\ldots\ldots\ldots \\
dy_n(y_j) / dy_j &= f_n(x, y_1, y_2, \ldots, y_i, \ldots, y_j \ldots, y_n)
\end{aligned}
$$

where x, y_1, y_2, y_i, y_j and y_n are the system variables.

For the case considered, the solution variables for the droplet were;

1. Time
2. X position
3. Path length
4. Y position
5. Z position
6. X velocity
7. Y velocity
8. Z velocity
9. Droplet temperature.

This gave nine primary system parameters and nine simultaneous differential equations.

Normally time would be the independent parameter of the equations, as represented by

x in the preceding differential equations. The implementation was, however, arranged so that any of the primary parameters could be used as the independent variable, although in practice this was normally time or a distance, such as the X position. Hence time was also included as a dependent variable, even when it was used as the independent variable. This was to provide greater flexibility in the use of the simulation.

It is to be noted that accelerations in the X, Y and Z directions are not included as solution variables in these equations, since these were calculated from the system equations, as discussed later, and thus were among the derived parameters, discussed below.

Some seventeen derived parameters where used, which were not directly required for obtaining a solution, but were of interest in understanding the solution. These included;

1. Path velocity
2. X acceleration
3. Y acceleration
4. Z acceleration
5. Rate of change of droplet temperature
6. Air velocity
7. Air temperature
8. Air pressure
9. Air density
10. Tunnel cross section area
11. Weber Number, We.
12. Reynolds Number, Re
13. Ohnesorge Number, Oh
14. Bond Number, Bo

In this model the equivalent droplet size, volume and mass were assumed to be constant. The droplet distortion, as represented by its aspect ratio, was assumed to be a derived parameter that was instantaneously dependent on the relevant conditions.

It would have been possible for the droplet size and shape to be dependent on differential relationships. That capability could have been implemented, but was not in the version used. The rate of droplet mass loss, or gain, would have depended on the surrounding conditions and droplet properties. The rate of change of droplet shape was likely to depend on the 2nd order vibration dynamics of the droplet. These effects would have added a further three primary solution parameters and three differential equations.

The form of the model used was developed for ink-jet printers, where it was necessary to also consider the electrostatic and aerodynamic interactions between droplets. That required the simultaneous modelling of several droplets, typically four or five, so that each droplet had its own set of simultaneous differential equations. This feature was retained, although to avoid computational difficulties it was not used, and only one droplet was evaluated at a time.

4th order Runge-Kutta solution method

The 4th order Runge-Kutta is a single step method, which computes the parameter changes over an interval **h**. For this;

$$k_1 = h.f'(x, y_n)$$
$$k_2 = h.f'(x + h/2, y_n + k_1 / 2)$$
$$k_3 = h.f'(x + h/2, y_n + k_2 / 2)$$
$$k_4 = h.f'(x + h , y_n + k_3)$$

and $$y_{n+1} = y_n + k_1/6 + k_2/3 + k_3/3 + k_4/6$$

This procedure was implemented in the following code fragment from subprogram rk4 (Press, et al, 1986). The full rk4 subprogram is given at the end of the section.

```
' compute Runge-Kutta increments
  FOR  j = 0 TO 3: rh = INT((j+ 1) / 2) / 2: ht = rh * h
     FOR i= n1 TO n2: yt(i) = yi(i) + rh * kk(i, j-1)
     NEXT: CALL derivs(xi + h, yt(), dydx(), mode)
     FOR i = n1 TO n2: kk(i, j) = h * dydx(i): NEXT i
  NEXT j
' accumulate increments with weights
  FOR i = n1 TO n2: kk = 0
     FOR j = 0 TO 3: wt2 = 1 - ((j=1) + (j=2)): kk = kk + wt2 * kk(i, j) / 6
     NEXT j%: yo(i) = yi(i) + kk
  NEXT i: xo = xi + h
```

The weighting calculation, wt2 = 1-((j=1) + (j=2)), includes the logical equations, (j=1) and (j=2). These return a value of 0 when false and -1 when true. Hence wt2=2 when j=1 or j=2, but otherwise wt2=1.

The parameter **mode** was used to switch the solution between various modes.

To run the analysis it was necessary to;

1. Provide the necessary data. (Sub All Parameters)
2. Select the required outputs and scaling (Sub Select Output)
3. Define the initial conditions (Sub Setup)
4. Define the differential relationships (Sub Derivs)
5. Increment the solution (Sub Solve)

The program had the following primary structure

1. Main Program (SUB Actual Program)
    a. Obtain the necessary data (Sub All Parameters)
    b. Select the output variables (Sub Select Output)
    c. Obtain the solution (Sub Solve)
    d. Output the result (Sub Output Header, Sub Output data)
    e. Exit
2. Obtaining the solution (Sub Solve)
    a. Define the initial conditions (Sub Setup)
    b. Calculate the results for initial conditions (Sub Derivs)
    c. Save the results for initial conditions (Sub Outarray)

d. Repeatedly step through the solution by the required increment
    i. Integrate the equations (Sub rk4)
    ii. Calculate the results for the current increment (Sub Derivs)
    iii. Transfer the result to the output array (Sub Outarray)
    iv. Plot the current conditions to the screen (Sub Graphs)
    v. Carry the results forward to the start of the next solution step.
e. Exit the integration steps
f. Exit the sub program

3. Defining the differential relationships (Sub derivs)
    a. Transfer from the current system parameters into local variables.
    b. Determine the current air velocity at the droplet location (Sub velair)
    c. Determine the local air properties of temperature, pressure, density and viscosity.
    d. Determine the current droplet properties of density, viscosity, surface tension, surface area, volume and mass.
    e. Determine the velocity difference between the air and the droplet.
    f. Compute the drag force from the magnitude of the velocity difference.
    g. Compute the droplet heat transfer and rate of change of temperature.
    h. Determine the orthogonal components of the drag force
    i. Compute the orthogonal components of the droplet acceleration
    j. Compute the other output parameters required
    k. Transfer the results back from local variables into system parameters
    l. Exit the sub program

4. Integrate the differential equations (Sub rk4)
    a. Compute the required Runge-Kutta increments
    b. Obtain the required differential values (Sub Derives)
    c. Accumulate the results for this increment
    d. Exit the sub program

Changing the independent variable

Typically the differential equations were defined in terms of time, such that

$$dy_i / dt = f_i(t, y_1, y_2, \ldots, y_i, \ldots, y_n)$$

such as $dV_x/dt = F_x / m$

and $dx/dt = V_x$

where F_x is the net force applied to the droplet in the X direction
m droplet mass.
V_x droplet velocity
x X coordinate of the droplet

The value of F_x would be determined from the velocity difference between the droplet and air and the drag characteristics of the droplet, as described in Chapter 3.

Such a formulation might not be the most convenient, for example when integrating over a fixed length, such as that of a wind tunnel, or up to the surface of an aerofoil.

Computation at fixed-distance intervals

There could also be circumstances were some differential equations were defined in relation to distance, such as pressure and air velocity gradients in the wind tunnel, while others were defined in terms of time, such as velocity and time, such as droplet acceleration. It was then necessary to convert the equations to a common independent variable.

This could be resolved by dividing through by the common derivative, for example;

$$(dy_i/dt)/(dx/dt) = f_i(x, y_1, y_2, \ldots, y_i, \ldots, y_n) / (dx/dt)$$

where dx/dt is the droplet velocity in the X direction, V_x.

Thus $$dy_i/dx = f_i(x, y_1, y_2, \ldots, y_i, \ldots, y_n) / V_x$$

Hence this enables the solution to be in terms of distance increments over a fixed length interval, rather than time increments for a given time interval. There was a potential difficulty with this if V_x were to become zero, when the equations would become singular. In such circumstances it would be necessary to use an alternative independent variable.

Using distance as the independent variable meant that the solution could, for example, be directly determined at given locations along a wind tunnel, such as at the locations of measuring instruments, so that a direct comparison could then be made between the experimental and predicted results.

One example was the experimental measurement of velocity and acceleration of a droplet, discussed in Chapter 13. In this measurement the time was recorded when a droplet passed three specified locations, as detected by laser beams and photo-detectors. Given the mass and volume of the droplet, it was then possible to determine its drag properties. The methods for determining the velocity and acceleration of a droplet was by differencing the measured time intervals. This, however, introduced differencing errors, which could have been significant, particularly for the acceleration.

If the simulated results were available at given distance intervals, then the experimental method of calculating the droplet velocity and acceleration could be tested by differencing the simulated time intervals at the required location intervals. The advantage of doing this with the simulated results, rather than measured data, was that the data is known to a high degree of precision, with no experimental error, and the "exact" value for the acceleration was also directly available from the simulation. Hence errors due to the differencing method could be directly determined. If required, random errors could be added to the simulated time and location data to see how that affected the differencing results. In this way it was possible to assess the differencing errors that would result from the experimental method for measuring droplet velocity and acceleration, as considered in Chapter 1, "Simulated measuring errors". The measurement system could then be appropriately optimised and designed. A more comprehensive analysis of the differencing method used is given in Chapter 14.

Stability criterion for the numerical solution

For a given set of circumstances there was a maximum increment size for solving the differential equations. It would have been possible to have automatic increment adjustment, but that was unnecessary since each simulation only took a few seconds to run. The increment size could be quickly adjusted manually, if it was necessary to do so.

The general experience with using the simulation method, for many different applications, was that the solution would either be stable and provide an adequately-accurate solution, or be unstable and not provide any solution. Very seldom was it found that the solution was both stable and inaccurate. For these reasons no detailed study of the stability criterion was carried out.

With time as the independent variable, the stability criterion depended on the ratio of the integration time increment to the shortest time constant within the differential equations. This time ratio was similar to the CFL stability criterion, after R. Courant, K. Friedrichs and H. Lewy (Klaus-Jürgen Bathe, 1996).

In the case of the droplet simulation, the shortest time constant was the droplet heat transfer relaxation time. Even with the smallest droplets considered, this was much longer than the time steps used, so the solution stability was not an issue.

In practice the version of the simulation used was very stable and the increments used were much smaller than required for stability and were chosen to obtain sufficient points to adequately describe the solution.

In a potential development of the simulation would be to include the dynamics of the droplet vibration. In this case the shortest time constant would be $1/\omega$, where ω is the angular frequency of the vibration. As a general rule the maximum usable stable time step is about a sixth ($1/2\pi$) of the oscillation period. For 250µm droplets the vibration period is 364µs, giving a maximum time step of 58µs. At an initial velocity of 10m/s the maximum distance increment would be about 0.6mm. Hence for equal distant increments over 520mm this would require about 900 integration steps, which is at least ten times more than required without the droplet vibration. Hence unless the details of the drag due to droplet vibration are important, computational efficiency is much better without this. If necessary the droplet vibration on drag could be evaluated over a short distance, until the vibration decayed, just to asses its likely effect on the droplet motion.

The solution method used was direct and explicit. This required the time steps to be no longer than the shortest time constant in the system, as discussed above. If this was very short compared to the require solution duration, in simulated time, then the number of computational points required could be very large. It was understood that this difficulty could be overcome by using an implicit solution method, but that was beyond the scope of this investigation.

With the simulation procedure used it was not necessary to store the result of every simulation step to achieve the required analysis. Hence the cost of a large number of the integration steps required for small increments would have been in the computational time and effort, not in the data storage required for the results.

Determining the Overall Airflow

The overall airflow could be computed by any acceptable method, since the assumption made was that the airflow would not be affected by the droplets. This is discussed in greater detail in Chapter 10. However there were some general issues related to the droplet simulation which are considered here.

Generally the most accurate method of analysis was CFD modelling, with the resulting velocity, pressure and temperature distribution stored as a look-up array in the simulation. This could then be read and interpolated as required for any given location and, if

necessary, for a given time. A difficulty was that the airflow computation could have been a substantial and complex task that would have required sophisticated computing facilities. The resulting data could have also required substantial storage and a complex interpolation routine.

The accuracy and sophistication of CFD airflow modelling could, however, be of little value if the modelling of the droplet motion dynamics was substantially in error due to the spherical droplet assumption normally made, (Tan 2002). This could be particularly so with significant droplet distortion due to aerodynamic forces, which could substantially change the drag properties, compared to the normally assumed spherical droplets.

For the purpose of this investigation the airflow for the simulation was calculated by simpler means, with corrections applied where necessary and possible (Chapter 10). This was because the primary interest was to investigate the drag properties of distorted droplets, where the accuracy of the airflow analysis was not the primary issue.

For flow in a converging tunnel a modified and corrected 1D adiabatic nozzle flow was assumed. This could adequately describe the three components of velocity and the density, temperature and viscosity for the air at any location within the convergent section.

Only convergent flow was considered, as divergent flow was far more complex due to much greater boundary layer effects and possible flow separation. The tunnel needed a divergent diffuser to reduce energy losses, but a much simpler calculation was used for that, as it was not necessary to fully describe the flow in the diffuser.

For the convergent section the standard equations for one dimensional isentropic compressible flow for a perfect gas were used (Rogers & Mayhew, 1967, 2nd Ed, & 4th Ed). In this the mass flow was assumed constant with time and distance along the tunnel.

From the equation;

$$m/A_2 = p_1 . \sqrt{[2.\gamma/((1 - \gamma).R.T_1).\{(p_2/p_1)^{(\gamma+1)/\gamma} - (p_2/p_1)^{2/\gamma} \}]}$$

where m is the mass flow rate
T_1 Temperature at inlet (location 1)
p_1 pressure at inlet
p_2 pressure at location 2
A_2 tunnel cross section area at location 2
γ Ratio of specific heats, (C_p / C_v)
R Gas constant

It was, in principle, possible to directly compute the pressure at any given location along the tunnel, given the tunnel area at that location and conditions at the tunnel inlet. In practice this required an iterative solution procedure, as discussed in Chapter 10.

Alternative Mode of operation

When designing a convergent profile for a wind tunnel, to achieve particular droplet conditions, the required tunnel shape for this might not be known. In such a case the air velocity for the droplet location, or time, within the tunnel, would have to be defined by some other means, such as a relationship for the velocity difference between the droplet and air with respect to time or distance. For the tunnel used this was required to achieve a constant rate of increase in Weber number with respect to time.

The velocity and other air properties to achieve the required droplet conditions could be computed. From this the convergent cross-section of the tunnel, to achieve the required conditions, could then be directly computed. A limitation of this was that it could result in a very steep rate of convergence for which wall curvature could be impractical to construct. It could also have meant that the tunnel convergence was so steep that the one-dimension flow calculations would no longer have been correct.

Corrections to the airflow errors for the tunnel convergence are discussed in Chapter 10, but this required knowing the tunnel convergent angle to calculate the correction. When the convergence angle was not known this created a potential computational difficulty.

When the small convergent tunnel was being developed, the modelling methods had not been sufficiently developed for such corrections to be applied. As a remedial solution, a maximum limit was put on the tunnel convergence angle. This was equivalent to an included angle of 40° for the equivalent circular cross-section, as discussed in Chapter 10.

This difficulty could have been resolved by writing the gas flow equations in their differential form. This would then have provided an additional differential equation to be solved, together with those for the droplet motion. This would have made available the velocity, temperature and density gradients along the tunnel, from which the convergent angle for the tunnel could then have been computed.

Determining the Droplet Drag force

Computing the motion dynamics of the droplets required a means of calculating the drag force on the droplets for a given velocity of the droplet and air at the same location.

In other simulations the droplet was assumed to be spherical. However, for the condition of interest it was found that such a simplification could introduce substantial errors due to distortion resulting from strong aerodynamic forces. As a result, it was necessary to develop a means to allow for this effect, as discussed in Chapter 3.

The more sophisticated methods for correcting the droplet drag had not been developed, when the small convergent droplet tunnel was developed. Hence it was designed using simpler corrections, which were later found to contain significant errors. This did not, however, prevent the tunnel form being used to obtain the necessary experimental data on the drag properties of distorted droplets, since the relevant tunnel design discrepancies were allowed for in the experimental measurements.

Vertical Tunnel Analysis

With respect to the design of the Vertical Tunnel, for Large Droplet Dynamic Studies, (Tan 2002), a comparison was made in Chapter 10 between the CFD analysis and the corrected 1D flow simulation with the spherical droplet assumption. The discrepancy between these was minor. With the correction for droplet distortion in the simulation there was a moderate increase in droplet velocity, but with the given convergence profile the magnitude of the distortion was not sufficient to achieve a substantial benefit.

With the simulation it would have been possible specify a more demanding acceleration criterion for the droplet acceleration, such as a constant droplet Weber number of 8 after the initial ramp-up period in the first metre. The convergent shape required to achieve this conditions would then have simultaneously been calculated.

It was estimated that this could have reduced the tunnel height by at least 1.5m, which would have greatly simplified installation of the tunnel, by keeping the lower end at floor level, rather than in a sunken pit.

Droplet Heat Transfer

Heat transfer to and from the droplets would occur due to conduction, convection, and evaporation or condensation.

The simulation only included conductive and convective cooling or heating of the droplets using available published data for convective heat transfer for spherical droplets (McAdams, 1954, Fig 10-11). This did not take into account the droplet distortion-effects on heat transfer. This was because heat transfer was only of interest where distortion effects were small.

The resulting effects on the droplets' behaviour could be significant, where the droplet temperature changes were sufficient to have a significant effect on the droplet surface tension, but that was not a major issue.

Principal Subprograms for the droplet simulation program

```
SUB solve (nc%, ns%, nb%, sel(), tyme(), yres())
' solve differential equations
' $INCLUDE: 'minitunl.inc'
  SHARED tint
  CALL empty.key: i% = 0: fv% = 0: mode% = 0: DIM yi(0)
  CALL setup(yi(), tyme, i%)
  nd% = UBOUND(yi): DIM yo(nd%),dyi(nd%),dyo(nd%)
  CALL derivs(ti, yi(), dyi(), mode%) ' initial conditions
  CALL outarray(i%,ti,yi(),sel(),tyme(),yres()) 'trnsfr to outpt
  FOR j% = 1 TO nc%
    FOR k% = 1 TO ns%: c% = c% + 1
      CALL rk4(ti,tf,yi(),yo(),tinc,mode%) ' integrate equatns
      CALL derivs(tf, yo(), dyo(), mode%)  ' current conditions
      CALL outarray(c%,tf,yo(),sel(),tyme(),yres())'trnsfr rslts
      CALL graphs(c%,sel(),tyme(),yres(),nb%,fv%)  ' plot graph
    ' forward results to next step
      FOR i% = 0 TO nd%: yi(i%) = yo(i%): dyi(i%) = dyo(i%):
      NEXT i%: ti = tf
    NEXT k%
  NEXT j%:
END SUB
```

```
DEFDBL A-Z
SUB rk4 (xi, xo, yi(), yo(), h, mode%) STATIC
' advance ordinary differential equations one
' solution step using 4th order Runge-Kutta
' xi    indep vari at intrvl start
' xo    indep vari at intrvl end
' yi()  functs vals at intrvl start
' yo()  functs vals at intrvl end
' h     interval length
  IF (fl = 0) THEN
    n1 = LBOUND(yi): n2 = UBOUND(yi): fl = -1
    DIM yt(n1 TO n2), dydx(n1 TO n2), kk(n1 TO n2, -1 TO 3)
  END IF
' compute Runge-Kutta increments
  FOR j% = 0 TO 3
    rh = INT((j% + 1) / 2) / 2: ht = rh * h
    FOR i% = n1 TO n2: yt(i%) = yi(i%) + rh * kk(i%, j%-1)
    NEXT: CALL derivs(xi + h, yt(), dydx(), mode%)
    FOR i% = n1 TO n2: kk(i%, j%) = h * dydx(i%): NEXT i%
  NEXT j%
' accumulate increments with weights
  FOR i% = n1 TO n2: kk = 0
    FOR j% = 0 TO 3: wt2 = 1 - ((j% = 1) + (j% = 2))
      kk = kk + wt2 * kk(i%, j%) / 6
    NEXT j%: yo(i%) = yi(i%) + kk
  NEXT i%: xo = xi + h
END SUB
```

```
SUB derivs (tyme, y(), dydt(), mode%)
  SHARED tt(),xx(),yy(),zz(),pl(),xv(),yv(),zv(),td()
  SHARED pv(),xa(),ya(),za(),ta(),dt(),dv(),at(),ap()
  SHARED av(),ad(),sa(),wc(),yt(),ra(),re(),oh(),bo()
' $INCLUDE: 'minitunl.inc'
' Compute differential relationships between system parameters
' given dydt(i) = FUNC(y(0), y(1), ... , y(i), ... , y(n))
' NOTE; other parameters passed by the SHARED
  micn = micro * ntn: nant = nano * ntn: picn = pico * ntn:
' dc% = 1  ' with Sperical droplets
  dc% = 2  ' with Maybank and Briosi correction
' dc% = 3  ' with Kennedy and Roberts correction
  n = ndrp:
  REDIM tt(n),xx(n),pl(n),yy(n),zz(n),xv(n),yv(n),zv(n),td(n)
  REDIM pv(n),xa(n),ya(n),za(n),ta(n),dt(n),dv(n),at(n),ap(n)
  REDIM av(n),ad(n),sa(n),wc(n),yt(n),ra(n),re(n),oh(n),bo(n)

' Transfer from state array to local variables
  CALL trans.var(y(), dydt(), tyme, 2, pnt%)

' ================================
' DEFINE DIFFERENTIAL RELATIONSHIPS
  FOR i = 0 TO ndrp
    tt = tt(i): xx = xx(i): pl = pl(i): yy = yy(i): zz = zz(i)
    xv = xv(i): yv = yv(i): zv = zv(i): td = td(i)
    pv = SQR(xv ^ 2 + yv ^ 2 + zv ^ 2)
    SELECT CASE cas%
      CASE 1 ' x0 is start of tunnel contraction
        t% = 7: x0 = 0          ' Current mini tunnel
        CALL velair(t%,x0,xx,yy,zz,yt,zt,ys,zs,vaix,vaiy,vaiz)
        tsct = yt: IF zt <> yt THEN STOP
        tare = 4 * yt * zt
      CASE ELSE: STOP
    END SELECT
    tdif = (vaix^2 - vref^2)/(2*aecp)   ' (V2^2 - V1^2)/2.Cp
    tair = tref - tdif                  ' air temperature
    trat = tair / tref                  ' temperature ratio
    pair = pref * trat ^ (gama / (gama - 1))' air pressure
    dair = pair / (rgcn * tair)             ' air density
    aden = dref * trat ^ (1 / (gama - 1))   ' air density
    mach = vaix / SQR(gama * rgcn * tair)  ' local mach number
    area = mflw / (aden * vaix)         ' section area
    masf = dair * vaix * area           ' mass flow
    sctn = SQR(area)                    ' tunnel section
'   ------------------------------------------------
    avis = air.visc(tair)     ' air viscosity
    sten = watrtens(td)       '  surface tension
    wvis = watrvisc(td)       '  water viscosity
    drpa = pi * drpd ^ 2      ' drop area
    drpv = pi * drpd ^ 3 / 6  ' drop volume
    dmas = drpv * wden        ' drop mass
    dvex = xv-vaix: dvey = yv-vaiy: dvez = zv-vaiz ' vel diffrnc
```

```
    dvel = SQR(dvex^2 + dvey^2 + dvez^2)' relative  velocity
    IF dvel <> 0 THEN
    ' unit velocity vector in X, Y & Z
      epsx = dvex / dvel: epsy = dvey / dvel: epsz = dvez / dvel
    ELSE
      epsx = 1: epsy = 0: epsz = 0
    END IF

    CALL droplt.drag(drpd,dvel,aden,avis,sten,reyn,webc,
                                                  drgg,drag,dc%)
    CALL sphere.heat(drpd,dvel,aden,avis,acon,reyh,nusl,htc.)
    CALL sphere.prop(drpd,dvel,aden,avis,sten,reyd,webr,ohna)
    CALL sphere.prop(drpd,dvel,wden,wvis,sten,dum2,dum3,ohnw)
    wecd = webr * drcf

  ' air drag force in X, Y & Z
    xdfc = -drag*epsx: ydfc = -drag*epsy: zdfc = -drag*epsz
    grfc = drpm * grav   ' gravity forc

  ' acceleration forces in X, Y & Z
    xfrc = xdfc: yfrc = ydfc: zfrc = zdfc - grfc ' gravity in Z
    hflw = htc. * drpa * (tair - td) ' heat flow for drop
    dtdt = hflw / (drpm * spht)   ' temperature rate of change

  ' drop accelerations
    xa(i) = xfrc/drpm: ya(i) = yfrc/drpm: za(i) = zfrc/drpm:
    ta(i) = SQR(xa(i)^2 + ya(i)^2 + za(i)^2) 'total acceleration
    accl = ta(i)
    bond = wden * accl * drpd ^ 2 / sten ' water density
    bona = aden * accl * drpd ^ 2 / sten ' air density

    dt(i) = dtdt: pv(i) = pv
    dv(i) = dvel: av(i) = vaix: at(i) = tair:
    ap(i) = pair: ad(i) = dair:
    sa(i) = area:
    sa(i) = 4 * yt ^ 2:

    wc(i) = webr: re(i) = reyn: oh(i) = ohna: bo(i) = bond
    ra(i) = webr / SQR(reyn)
    yt(i) = 2 * yt ' tunnel section
  NEXT i
' >>>>>>>>>>>>>>>>>>>>>>>>>>>>>>>>
' Transfer from local to state array
  CALL trans.var(y(), dydt(), tyme, 3, pnt%)
END SUB
```

Chapter 9: Design of Droplet Research Tunnel

Introduction

To carry out the experiments required to investigate the distortion and break-up of water droplets from strong aerodynamic forces, a special wind tunnel was developed. Before constructing this, it was necessary to ensure it would have the capability to apply the necessary forces to the droplets in the required way.

To enable the required design analysis, a computer simulation was developed, as discussed in Chapter 8. There was a problem in that the data on the drag properties of distorted droplets, required for the tunnel design, was not available and the reason for constructing the tunnel was to help obtain such data.

It was, however, found that data for free-falling droplets in ambient air and standard gravity could be used to provide adequate data (Chapter 3) to enable the design and construction of the tunnel, so that improved experimental data could then be obtained.

Tunnel Configuration

One of the first considerations was the configuration of the tunnel. In order to keep the costs as low as possible and keep the construction as simple as possible, it was decided to develop a horizontal open-loop suction tunnel using ambient air.

This raised the question of whether the lateral gravitational forces on the droplets in a horizontal tunnel would be an issue. Analysis with the simulation showed that the gravitation effects were negligible. Having a horizontal tunnel made its construction much simpler and if the length of the working section was changed then this could be readily accommodated. It also made observations and measurements in the tunnel much easier.

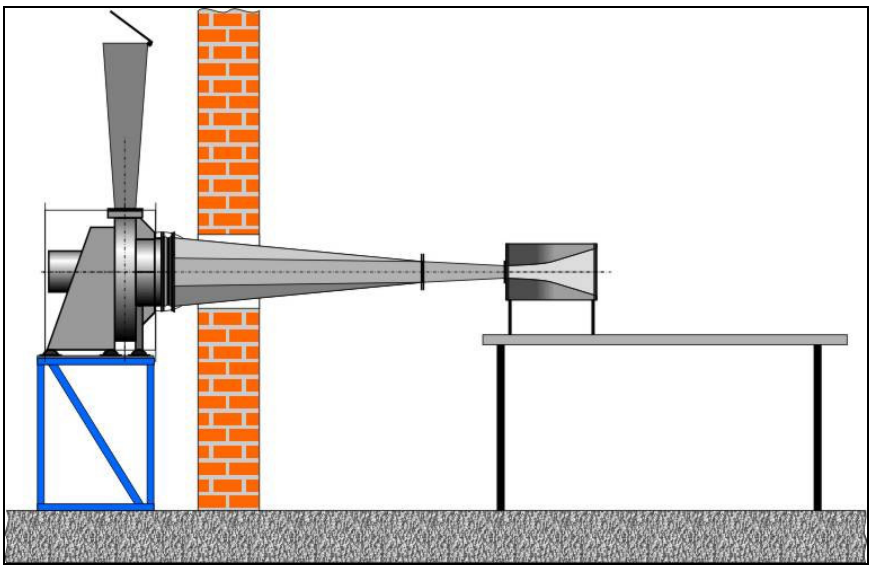

Figure 109: General arrangement of droplet research tunnel

Having an open-loop tunnel using ambient air avoided the cost and complexity of air recirculation ducting, and also avoided the difficulties of heating and turbulence. The fan was used to provide suction, since this reduced turbulence in the tunnel inlet, avoided heat input from the fan and ensured better control of the tunnel pressure.

The suction fan was placed outside the building, open to the weather, to save space and

reduce noise, air disturbance and heat. It exhausted directly to the atmosphere. To save the cost and complexity of housing the fan, a weather-proof version was selected.

A sketch of the tunnel general arrangement is shown in Figure 118 and an annotated photograph in Figure 110. Originally the fan outlet was to have had a diffuser with a weather-proof flap, as shown in Figure 109, but this was not fitted.

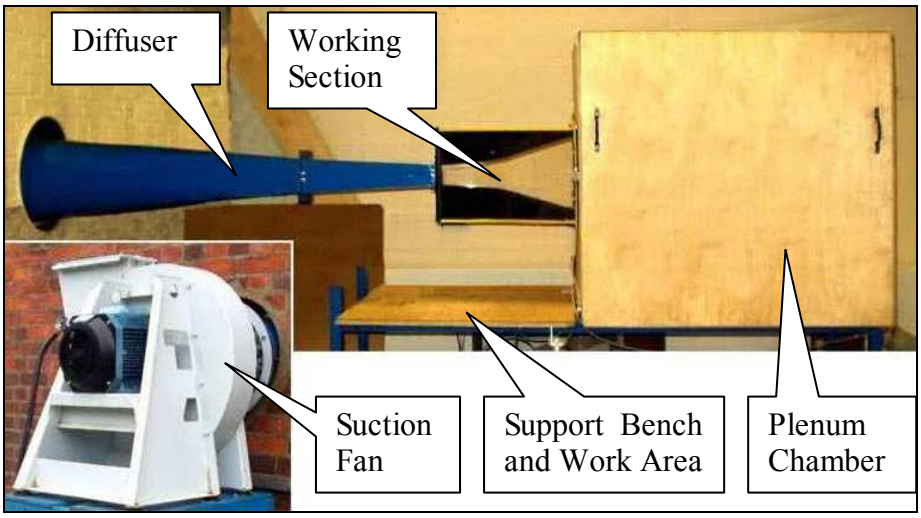

Figure 110: Photograph of droplet research tunnel

The Diffuser

The diffuser was a critical component of the wind tunnel. It was required to recover as much as possible of the kinetic energy in the air from the tunnel exit. This was not so much a matter of efficiency, but more a matter of pressure recovery. A primary factor on the fan selection and cost was its pressure capability.

The pressure capacity of a centrifugal fan was primarily determined by the peripheral velocity of the impeller, which was also a primary factor in determining the stresses in the impeller. Hence, the higher the pressure requirement, the greater the stresses in the impeller, which then required a more robust and sophisticated impeller design and construction and hence a higher cost for the fan.

As a result, the diffuser was optimised for maximum efficiency, within the various performance and dimensional constraints. Since this was a matter of engineering design, rather than scientific investigation, the simpler incompressible flow assumption was used. This was considered reasonable, since the compressible effects were modest, with an air density variation of less than 10%, and accuracy was not critical.

The losses in a circular diffuser are shown in Figure 111 (Massey 1989), (Nakayama 1999). The differences between these was most likely due to digitisation errors from the small data graphs available. From Nakayama & Boucher the minimum head loss was 0.135 occurs at a semi-angle of about 2.75^{O} for a circular diffuser. For a square diffuser the minimum head loss was given as 0.145 at a semi-angle of about 3°.

It was determined that the inlet to the diffuser would be 76.5mm square and the outlet 406mm diameter, with a diffuser length of 2m. The inlet could be converted to an area-equivalent diameter of 86.3mm. This gave a divergent semi-angle of 4.6^{O}, which was well above the optimum angle.

It was, however, found that the diffuser efficiency could be improved, and head loss reduced, if the diffuser was made in two parts. The first part, called the adaptor, was given an exit of 125mm square, with a length of 500mm. Translated into equivalent circular diameters, this had a divergent semi-angle of 3.13^{O}, which was close to that for minimum head loss. The second 1.5m of the diffuser then had an equivalent divergent semi-angle of 5.05^{O}, which was well above the optimum angle.

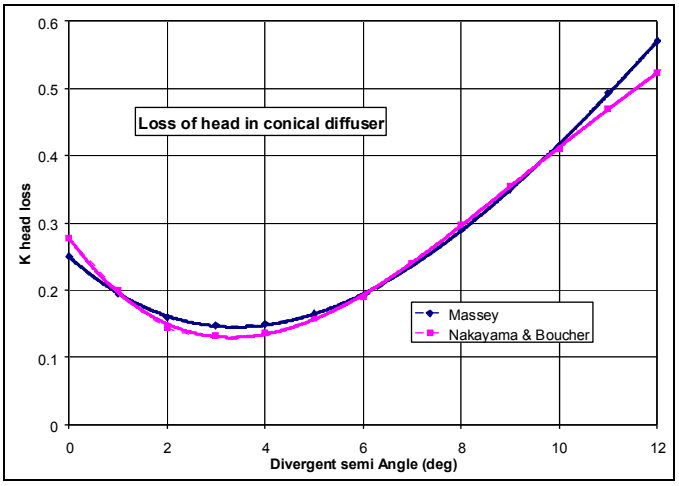

Figure 111: Characteristics of a conical diffuser

The resulting diffuser design is shown in Figure 112. It was found that about 86% of the possible energy recovery was achieved in the first section of the adaptor, so the second section could only recover 14% at most. Hence the reduced efficiency of the second section was more than compensated for by the improved efficiency of the first.

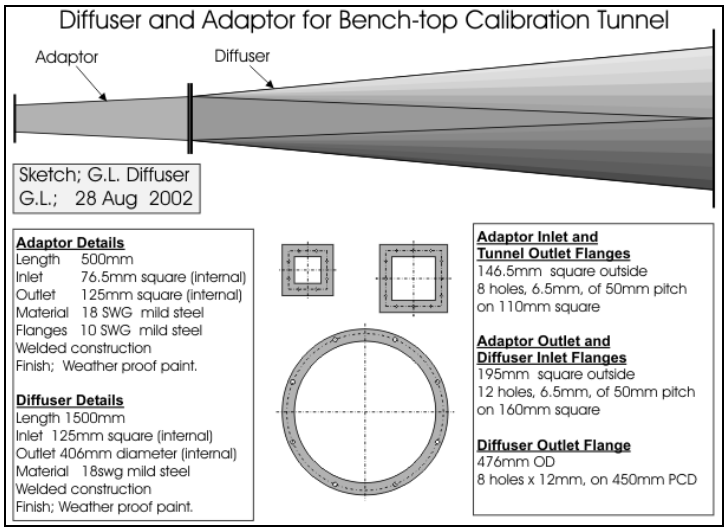

Figure 112: Details of tunnel diffuser design

This evaluation was based on the assumption that the two sections of the diffuser acted independently, but that was unlikely to be the case. It would anyway seem that the performance of a diffuser greatly depends on the airflow conditions at the entry, in particular the boundary layer thickness (Schlichting 1987), which was not explicitly known in this case. It was in any case likely that the boundary layer would increase in thickness in the first section due to the adverse pressure gradient, so the inlet conditions for the second section would be different from those for the first section.

At best the diffuser optimisation was approximate and it was later found, during subsequent commissioning, that there were other important considerations.

Diffuser Flow Stability

When the wind tunnel was commissioned, it was noticed that there were perturbations in the vacuum measured near the tunnel exit. These were interpreted as velocity fluctuations of about 1% to 2%, attributed to flow instabilities in the diffuser, as indicated in Figure 113 (ESDU sheet 87015).

This shows that the flow in the diffuser could have had different modes of boundary

layer conditions. These were Attached flow, Stable separation and Transitory separation. Plotted on this are three points representing the first and second sections and the two combined. It is to be noticed that the first section would have had stable separation, close to the borderline for attached flow. Unfortunately the flow in the second section of the diffuser and combination of both sections was well into the region of transitory flow. Whilst it would seem that the second section contributed only about 14% of the diffuser performance, it would seem that the transitory flow separation in this was sufficient to produce the flow fluctuation in the convergent tunnel.

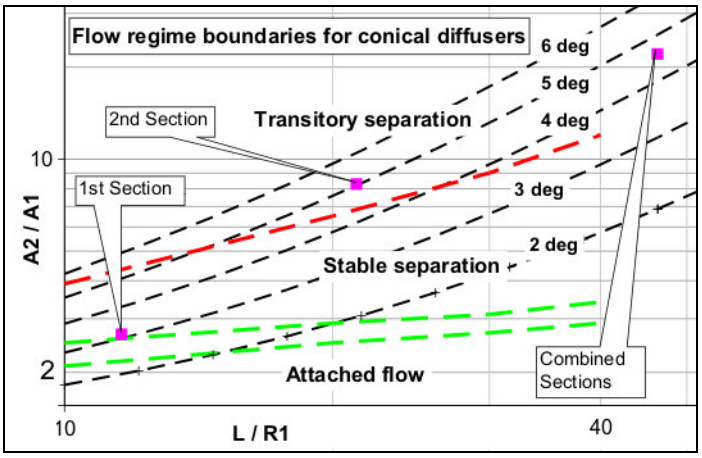

Figure 113: Diffuser flow stability.

Attempts were made to resolve this by splitting the second section into four quadrants with a splitter. The idea was to reduce this to four adjacent diffusers, each with half the divergent angle. However, this proved unsuccessful.

From Figure 111 it would appear that the divergent semi-angle needed to be at least 2^{O} to keep the diffuser efficiency at an acceptable level. Also the area ratio needs to be at least 3.3, if at least 90% of the recoverable kinetic energy was to be achieved. In Figure 113 this would put the diffuser just over the border from attached flow, just into the stable separation region, whilst keeping the head loss to about 15%. Such a diffuser would be about 905mm long. It would then seem necessary to have an abrupt expansion to ensure a stable separation and avoid any transient variations.

It was, however, not possible to remake the diffuser, so the original design had to be used without modification. It was possible that it could have been improved by deliberately inducing flow separation at the end of the first section with a boundary layer trip. This could have been achieved by having the gasket in the joint protruding into the flow, but that possibility was not investigated.

The flow fluctuations were not of significant concern with respect to the droplet experiments, but they made it difficult to accurately measure the vacuum in the tunnel. This was the primary means for determining the pressure ratio, velocity, and other properties of the air in the tunnel.

To achieve high accuracy a digital manometer was used for the vacuum measurement, but it was difficult to read the fluctuating digits. Various attempts were made to smooth the fluctuations, but these were not successful. The most effective solution found was to record about 10 vacuum readings from the readout with a digital camera and then take the average. This also simultaneously recorded the date and time of the readings.

The Fan Requirement

The specially purchased suction fan was a pivotal component of the tunnel. Its characteristics decided the maximum air velocity and size of the tunnel cross-section.

It was determined from the simulation that the maximum tunnel velocity would be about Mach 0.5. This would result in a pressure ratio of about 0.843 and hence a vacuum of about 15.7kPa. If the tunnel exit had had an abrupt expansion, then that would have required a fan with a pressure capability of about 16kPa, but such a fan would have been very much more expensive because of the need for a much stronger impeller.

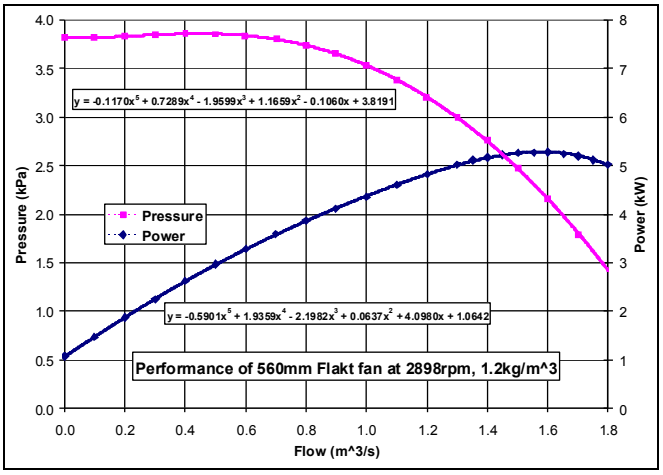

Figure 114: Performance characteristics of the suction

With the diffuser it was possible to reduce the head loss to about 14% of the tunnel vacuum, reducing the fan pressure capability to about 2.2kPa.

With an exit area of 76.5mm square and air velocity of Mach 0.5, this equated to a velocity of 313m/s and air density of 0.755kg/m^3, giving a mass flow of about 1.14kg/s. This translated to a volumetric flow of about 1.16 m^3/s of free air.

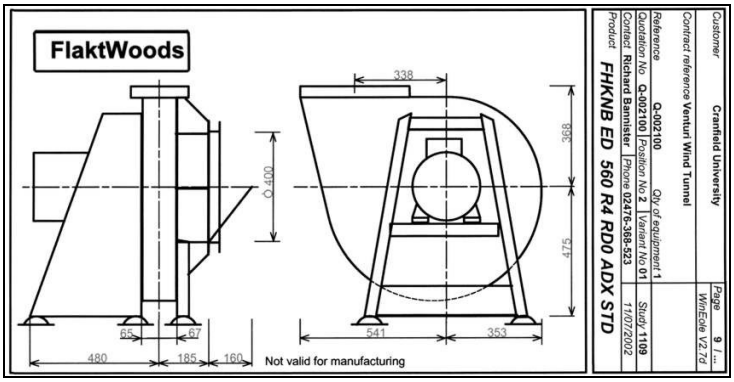

Figure 115: Fan Geometry and Dimensions

Discussion with the fan supplier identified a suitable fan, the characteristics of which are shown in Figure 114. It comfortably achieved the required performance. In practice the fan could be run up to 3000rpm, giving a further 7.2% pressure and 3.5% flow.

The fan was equipped with a digital electronic variable speed drive, so could operate at any speed from zero to 3000rpm.The general arrangement and dimensions of the fan are shown in Figure 115. The full specification is shown at the end of this chapter.

The fan configuration was chosen to have an upward facing exit. This was to direct the exit flow away from anyone in the vicinity. It was anticipated that the fan would later be moved to an internal location, where the exit air would be ducted away, so an upward exit would provide the most adaptable option. The exit was to be covered with a pivoted self-opening weatherproof flap, which was not fitted, so a temporary plastic cover was fitted when the fan was not in use.

Convergent Working Section

The details of the convergent shape of the working section are considered in Chapter 10.

The construction of the tunnel is shown in Figure 116. This was of welded sheet steel construction, with transparent Perspex sheeting bolted to the sides and sealed with silicon rubber to prevent any leakage at the corners and flanges.

A limitation was that optical equipment could only operate through the sides. It was later necessary to have a vertical laser beam across the tunnel, so transparent windows were fitted to the upper and lower surface of the metal walls.

Along one of the metal walls was a series of pressure tappings, used to check the pressure distribution along the tunnel and also to determine the air speed. These were at 40mm intervals, with the last one 20mm from the tunnel exit.

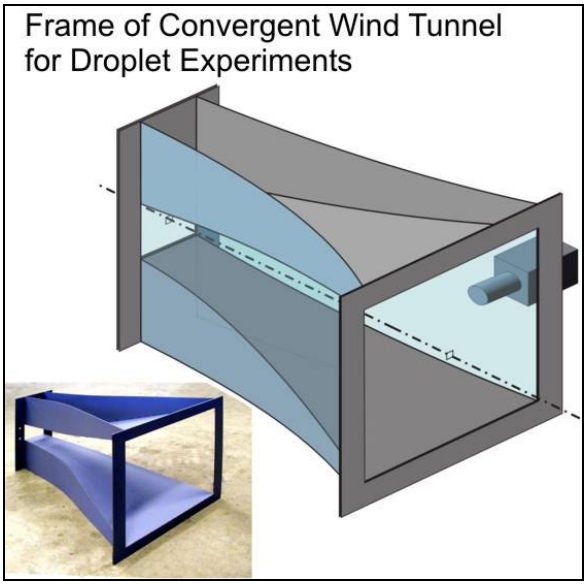

Figure 116: Frame of wind tunnel working section.

Plenum Chamber

It had originally been hoped that the tunnel would operate without a plenum chamber. However, during the commissioning it was found that any air disturbance in the laboratory, such as from heating fans, was greatly magnified within the tunnel and resulted in very erratic flow. This was investigated using a smoke wand to illustrate the flow instability, such as shown in Figure 117.

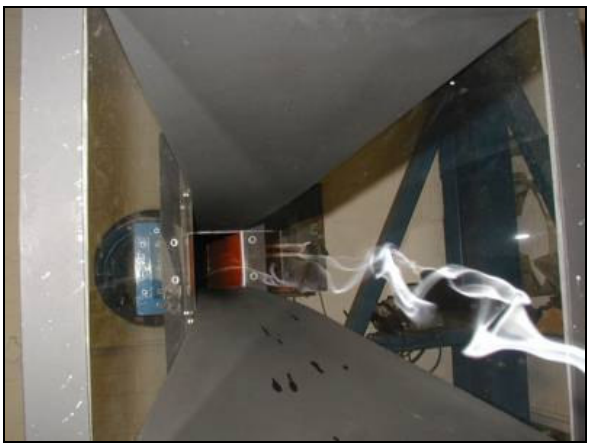

Figure 117: Smoke Test in the convergent tunnel

As a result, a plenum chamber was added, as shown in Figure 110 and Figure 118. This consisted of a box of about 1m cube, with a hole for the tunnel entry at one side and a fibre screen on the opposite side.

The frame was constructed from thin 25mm square steel tube with plastic press-fit corner brackets, known as "Speed Frame", that came from an old bench. The back and top were covered with pressed cardboard, or "Hardboard", and the tunnel's side, bottom and front were covered with plywood. Thicker marine plywood was used for the bottom, to carry equipment inside the plenum chamber and accommodate water spills.

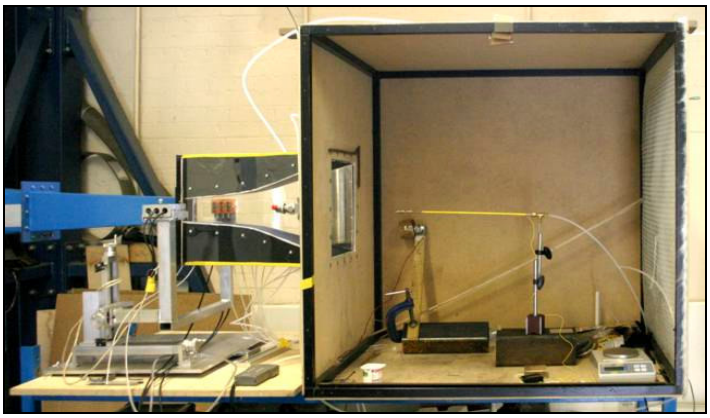

Figure 118: Interior of the Plenum chamber

The front was removable to allow access to the tunnel and equipment in the plenum chamber. The side opposite the tunnel inlet was a screen of four layers of a fibre matting, normally used for air filters, held in place between two layers of wire netting.

It was considered whether all sides of the plenum chamber, apart from that into the tunnel, should be covered with the fibre material to allow better airflow into the tunnel entrance. This was not done for practical reasons, such as the need for a solid base on which to stand equipment and to reduce the amount of fibre matting required. Also the CFD analysis assumed that the inlet flow was only from the opposite side to the tunnel entry and that was found to be satisfactory.

Plenum Chamber Inlet Screen

A critical part of the plenum chamber was the inlet screen, to remove any flow disturbances from the air. A honeycomb flow straightener could have been used in conjunction with the fibre matting, but that was not available for the area required. Hence it was necessary to ensure that the fibre matting alone achieved the required flow stability.

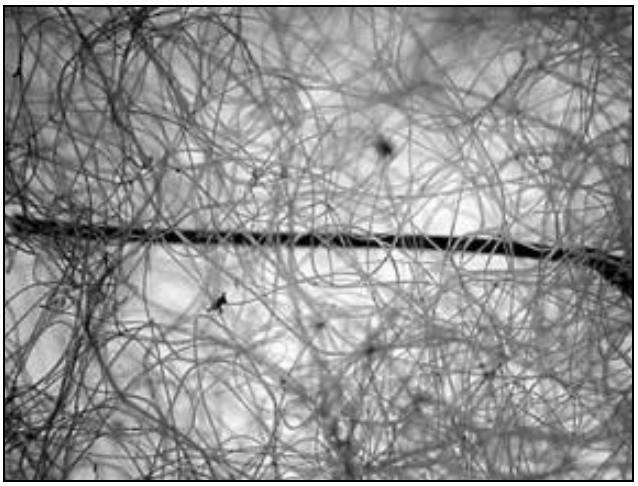

Figure 119: Enlarged view of fibre inlet screen

It was concluded that, if the pressure drop across the fibre matting, due to the plenum chamber inflow, was large compared to the dynamic head of the air velocity through the screen, then any disturbances would have been swamped by this pressure drop across the screen. On the other hand it was important that this pressure drop had a negligible effect on the tunnel operation. These requirements were best met by making the plenum chamber inlet area large enough. The actual area was 0.94m by .84m, or 0.79m^2.

A close-up of the fibre screen is shown in Figure 119. For size reference this includes a piece of 190µm diameter wire.

The tunnel fan was run at various speeds and the vacuum in the plenum chamber and tunnel throat were recorded, as shown in Figure 120. Since the pressure drop across the screen was very much less than that for the tunnel throat, by at least a factor of 100, the effect on the screen pressure drop on the tunnel throat pressure drop was neglected.

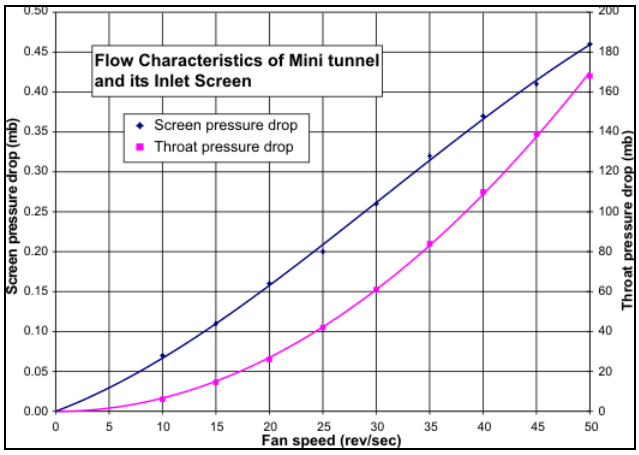

Figure 120: Pressure drop of tunnel and inlet screen

The pressure drop in the tunnel throat was then used to compute the air velocity through the fibre screen using the methods discussed in Chapters 10 and 11, with the results shown in Figure 121. Also shown with this is the dynamic pressure of the airflow, both against the same axis on the left and against the expanded axis on the right. This shows that the pressure drop across the fibre screen was at least 50 times the dynamic head of the air flow through the screen. Hence any disturbances in the inlet flow were swamped and effectively suppressed by the pressure drop across the screen.

Figure 122 illustrates the improvements achieved with the fibre screen in the plenum chamber. This shows two threads in the tunnel, one of wool and one of cotton, attached only to the inlet screen. The lower view shows the situation with the plenum chamber open, where the threads were momentarily crossed due to the resulting flow disturbances in. The upper view was with the plenum chamber closed and the inlet screen in operation, and shows the two threads in a stable flow.

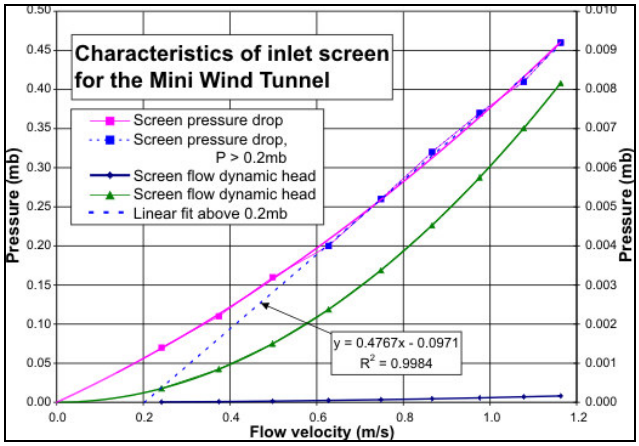

Figure 121: Inlet Screen Pressure loss vs. Flow Velocity

The fibre screen on the inlet to the plenum chamber removed disturbances from the incoming air, but it was also necessary to assess whether it would result in a uniform flow.

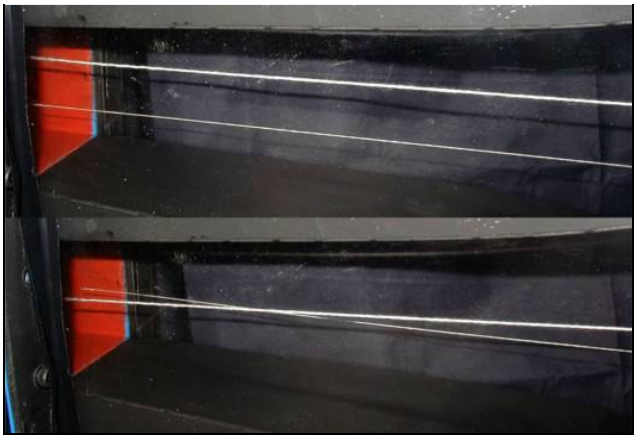

Figure 122: Improvements to tunnel flow stability

Because the strips of fibre matting were not wide enough for the screen, it was necessary to ensure that there were no gaps between the strips and that overlaps between them were minimal. Four layers of fibre matting were used, in which the layers of strips were alternately placed at right angles to each other. Also the overlaps in each of the two layers in the same direction were staggered so that the effects of these were distributed as much as possible.

Another issue of concern was that different parts of the fibre screen were compressed by different amounts, with the possibility that this might affect its uniformity of flow resistance. It was also necessary to determine if the flow through the screen was laminar.

It can be seen that in Figure 121 the relationship between pressure drop across the screen and flow velocity through it appeared to be non-linear, particularly below a pressure difference of 0.2mB. This was, however, less than 0.1% of the full scale range of the digital manometer and probably due to a non-linearity of the instrument at the very low readings. Above 0.2mB the response was linear, at a rate of 0.48mB/(m/s).

From a simple test the fibre was found to be a thermoplastic with a density greater than 1g/cc. From plastics data it was concluded to have a density of 1.2g/cc. Measurements showed the fibres in the screen to be about 35µm diameter.

A sample of the fibre matting, 0.67m by 0.485m by 10mm thick, was found to weigh 37.2 grams. From this it was calculated that the volume of the matting relative to the fibre material was about 104 to 1. Hence the fibre occupied less than 1% of the matting. From this it was deduced that the average spacing between the fibres was between 350µm and 600µm, depending on the assumptions made about the arrangement of the fibres. At this spacing it was concluded that there would be little aerodynamic interac-

tion between the fibres, so the airflow over each fibre could be treated in isolation.

Hence it was concluded that the pressure drop across the matting was primarily due to the drag from the airflow over the fibres. It was calculated that at a velocity of 1m/s the Reynolds number, relative to the fibre diameter, was about 2. Hence the flow over the fibres, and also through the gaps between them, was lamina.

To estimate the pressure drop it was necessary to determine the total length of fibre in the weighed sample of matting. This was found to be about 32km. The drag force perpendicular to this with an airflow of 1m/s was determined, assuming Stokes flow over a cylinder, with the approximate relationship;

$$Cd = 10/Re \quad \text{(for a sphere } Cd=24/Re\text{)}$$
$$= 10/(\rho.U.D/\mu) = 2.F/(\rho.U^2.D.L)$$

Hence $F = 5.\mu.L.U$

where

Re	is Reynolds number	U	air velocity	μ	air viscosity
Cd	drag coefficient	L	fibre length	ρ	air density
F	drag force	D	fibre diameter		

It is to be noticed that the drag force was independent of the air density and fibre diameter and was directly proportional to the air viscosity, fibre length and air velocity.

This gave a drag force of around 3 Newtons, which equated to a pressure loss of about 0.9mb for one layer of fibre matting, or 0.36mb for the four layers of matting used in the screen. At the same velocity the measured pressure drop was about 0.38mb.

There were several potential discrepancies in this evaluation, such as the manometer accuracy and orientation of the fibres. There were also uncertainties about the fibre diameter and density, which affected the calculated fibre length. Even so the result of this very simple pressure-loss model for the screen was in very good agreement with the measured value, which indicates that the assumed model was reasonably correct.

From this evaluation it was concluded that compressing the thickness of the fibre matting would have little effect on its flow resistance and flow uniformity. The pressure drop only depended on the fibre length in a given area of the fibre matting, which would not be affected by compressing the thickness of the fibre matting.

Flow Straightener

A piece of metal honeycomb flow straightener, sufficient to cover the tunnel entry, was freely supplied by Darchem Ltd., as shown in Figure 123, with details shown on the right. This had a hole in the middle so that the droplet injector could be passed through to be inside the tunnel. In practice for this investigation the flow straightener was not used, since it became partially blocked by surplus water spray from the droplet generator used. Fortunately the flow conditioning from the inlet screen proved good enough for the investigation.

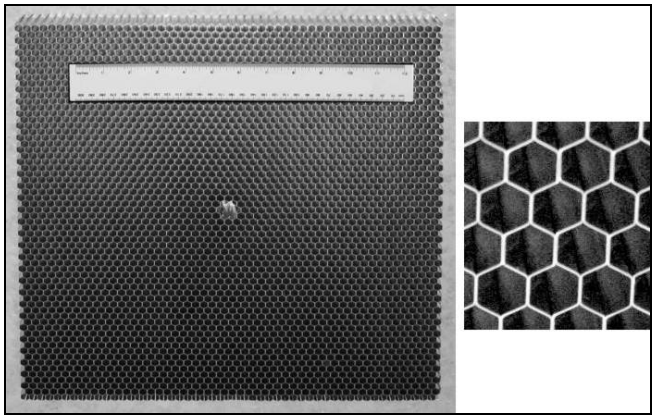

Figure 123: Flow straightener for tunnel entrance

Support Bench

The support bench, as shown in Figure 110, was an angle-iron frame that was available from a previous application. The plenum chamber rested on the right-hand end of this, whilst the left-hand end, under the convergent working section, was used for supporting experimental equipment. The advantage of this arrangement was that it could readily be adapted as circumstances required.

Fan Specification

Customer	Cranfield University			Page 6 / ...
Contract reference	Venturi Wind Tunnel			WinEole V2.7d
Reference	Q-002100		Qty of equipment 1	
Quotation No Q-002100		Position No 2	Variant No 01	Study 1109
Contact	Richard Bannister		Phone 02476-368-523	11/07/2002
Product	**FHKNB ED 560 R4 RD0 ADX STD**			

Requested characteristics

Type of fluid	Air clean			
Temperature of fluid at inlet	20	°C		
Site altitude	0	m		
Density	1.2	kg/m3	at 20	°C
Design temperature	20	°C		
Starting temperature	20	°C		
Intake flowrate	1	m3/s		
Intake pressure	- 0	Pa	at 20	°C
Discharge pressure	+ 3000	Pa	at 20	°C
Static pressure differential	3000	Pa	at 20	°C
Inlet ducted			Discharge free	

Aeraulic characteristics

Flowrate	0.96	m3/s		
Static pressure differential	2845	Pa		
Total pressure differential	2809	Pa		
Power consumption	4.31	kW	at 20	°C
Minimum driving power	4.74	kW		
Efficiency	80.1	%		
Rotation speed	2898	rpm		
Max. rotation speed	4400	rpm		
Impeller diameter	560	mm		
Impeller inertia	0.36	kg.m2		
Start-up time	4	s		

FlaktWoods

Acoustic

Acoustic power level in free field conditions (Intake free - Outlet ducted)

Overall level 92 dB According to standard BS848 Part 2

Acoustic power spectrum in free field conditions

Octave bands	63	125	250	500	1000	2000	4000	8000	Hz
Lw spectrum	57	70	73	84	84	81	80	73	dB(A)

Overall mean acoustic pressure 81 dB(A) at 1 m in free field conditions

Acoustic power level in free field conditions (Inlet ducted - Outlet ducted)

Overall level 87 dB Casing breakout noise

Overall mean acoustic pressure 75 dB(A) at 1 m in free field conditions

Comment: The values for acoustic pressure (or power) levels do not take account of the noise radiation from other sources (motor noise, resonance of walls...)

Tolerances: on overall levels: ± 3 dB
per octave band: ± 5 dB

Chapter 10: Air Flow Calculation for Convergent Droplet Tunnel

Convergent Nozzle Flow Calculations

To determine the airflow in a convergent tunnel this was treated as one-dimensional isentropic compressible perfect gas flow in a convergent nozzle.

The basic formulation for this is;

$$U_2 = m / (\rho_2.A_2)$$

where U_2 is the velocity at the working section
m the specified mass flow rate
ρ_2 the air density at the working section
A_2 the cross section area of the working section

The problem was that ρ_2 was not known, so U_2 could not be solved directly. Once any other air property was known at the required position, then the others could be readily determined. What was known was the values for U_1, T_1 and ρ_1 near the tunnel entry.

The equations used for this evaluation were obtained from "Engineering Thermodynamics Work and Heat Transfer", Rogers & Mayhew, 2nd Ed, Longman 1967, p183, Section 10.2, Adiabatic steady flow-process. For this derivation the specific volume 'v' was replaced by the reciprocal of density, '1/ρ'.

One could start with the equations;

$$U_2^2 - U_1^2 = 2.Cp.(T_1 - T_2)$$

$$T_2 / T_1 = (\rho_2 / \rho_1)^{(\gamma - 1)}$$

and $$p / \rho = R.T$$

where U_1 is velocity at tunnel entry
U_2 velocity at working section
T_1 absolute temperature at tunnel entry
T_2 absolute temperature at working section
ρ_1 air density at tunnel entry
ρ_2 air density at working section
p_1 pressure at tunnel entry
p_2 pressure at working section
Cp specific heat at constant pressure
Cv specific heat at constant volume
R gas constant, $Cp - Cv$,
γ gamma, the ratio of specific heats, Cp / Cv

Hence $$\rho_2/\rho_1 = (1 - (U_2^2 - U_1^2) / (2.Cp.T_1))^{(1 / (\gamma - 1))}$$

In practice U_1 could be small enough to be neglected. Substituting for ρ_2 in,

$$U_2 = m / (\rho_2.A_2)$$

to give, $$U_2 = m / (\rho_1.A_2.(1 - (U_2^2 - U_1^2) / (2.Cp.T_1))^{(1 / (\gamma -1))})$$

in which the only unknown is U_2, provided a solution, but it seems unlikely that this equation could be directly solved for U_2.

It was advantageous to make this equation dimensionless, as this made the implementation more general and more robust. To achieve this required dividing through by an appropriate velocity. One could use the tunnel entry velocity, but that could be zero or indeterminate. A preferred alternative was the entry sonic velocity. This was given as,

$$S_1 = \sqrt{(\gamma.R.T_1)}$$, the velocity of sound at the tunnel entry

This only depended on the known air properties and temperature.

From $Cp - Cv = Cp.(\gamma - 1)/\gamma = R$

this gave $2.Cp.T_1 = 2.S_1^2 / (\gamma - 1)$

and from $\rho_2/\rho_1 = (1 - (U_2^2 - U_1^2) / (2.Cp.T_1))^{(1 / (\gamma - 1))}$

this gave $\rho_2/\rho_1 = (1 - ((U_2 / S_1)^2 - (U_1 / S_1)^2) (\gamma - 1) / 2))^{(1 / (\gamma - 1))}$

For this one could make the substitutions, $M_1 = U_1 / S_1$ and $M_2 = U_2 / S_1$

hence $\rho_2/\rho_1 = (1 - (M_2^2 - M_1^2).(\gamma - 1) / 2))^{(1 / (\gamma - 1))}$

It is to be noted that M_1 is the Mach number for the tunnel entry. M_2, however, was not the Mach number for the working section, as U_2/S_1 was not a ratio of local air velocity with local sonic velocity, but was a ratio with the sonic velocity near the entry.

From $U_2 = m / (\rho_2.A_2)$

gave $U_2/S_1 = M_2 = m / (S_1.A_2.\rho_2)$

Thus $M_2 = m/(S_1.A_2.\rho_1.(1 - (M_2^2 - M_1^2).(\gamma - 1) / 2)^{(1 / (\gamma - 1))})$

Before going further it is worth noting that, given M_2, one could solve for A_2. For this it was worth rearranging the equation to give,

$$m / (A_2.\rho_1.S_1) = M_2 .(1 - (M_2^2 - M_1^2).(\gamma - 1) / 2)^{(1 / (\gamma - 1))}$$

Substituting $F2 = mf / (A_2.W_1.S_1)$

gave $F2 = M_2.(1 - (M_2^2 - M_1^2).(\gamma - 1) / 2)^{(1 / (\gamma - 1))}$

To simplify the calculations a separate function for the density ratio was defined as,

$$\rho_2/\rho_1 = D(M_2, M_1, \gamma)$$
$$= (1 - (M_2^2 - M_1^2).(\gamma - 1) / 2)^{(1 / (\gamma - 1))}$$

Hence $F2 = M_2 . D(M_2, M_1, \gamma) = F2(M_2, M_1, \gamma)$

Figure 124 shows 1/F2, or $A_2/(m/\rho_1.S_1)$, plotted against M_2, or U_2/S_1. Since ρ_1, S_1 and m were constant, for given conditions, this is effectively a graph of tunnel section area against air velocity.

As expected from nozzle theory, there was a minimum section area where the air velocity was at Mach 1. For a given section area greater than the minimum, there were two velocity solutions, one subsonic and one supersonic. The graph was, however, plotted against U_2/S_1, which had a minimum for 1/F2 of 1.728 at $U_2/S_1 = 0.913$.

Figure 124 also shows the density ratio against M_2. This is of interest, since it was preferable that the air density variations were reasonably small, at about 10%, which required a maximum air velocity of Mach 0.464, with $M_2 = U_2/S_1 = 0.454$.

The sonic velocity ratio, S_2/S_1 is also shown in Figure 124. Because the air was cooled as its pressure decreased, it would accelerate and expand, as its sonic velocity decreased. At the operating point of interest, with a density reduction of 10%, the reduction in sonic velocity was only about 2%.

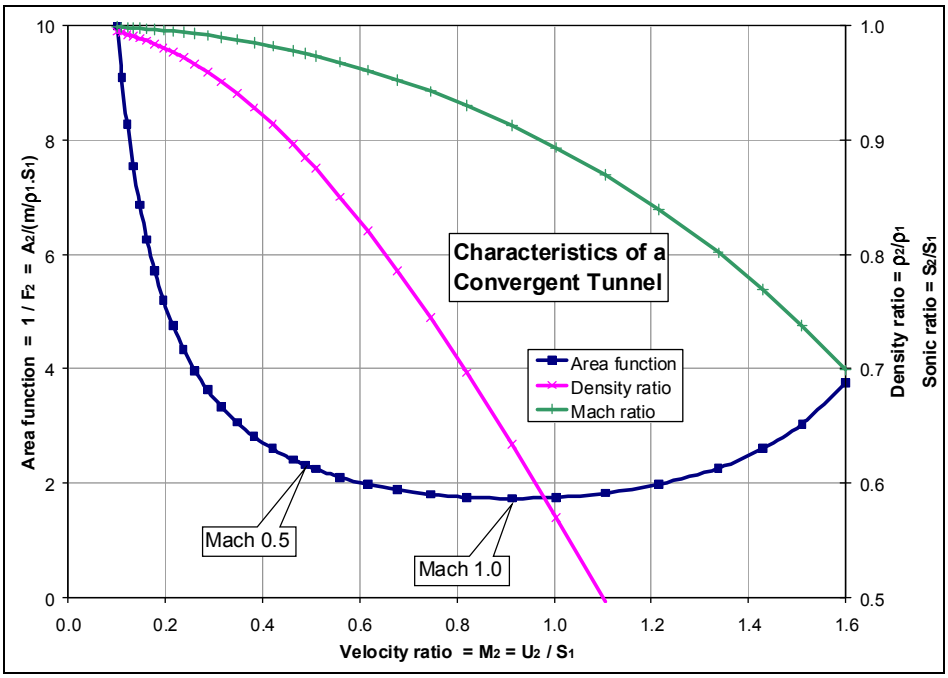

Figure 124: Characteristics of Adiabatic Flow in a Convergent Tunnel

In practice what was also required to calculate the air velocity for a given mass flow and tunnel area. It would seem that this could only be achieved iteratively. This required an initial guess and then a rapidly convergent procedure to obtain a solution.

There were many iterative procedures, with many associated problems. However in this case if the Mach number, 'M', in the working section was not too high, M <= 0.5, there was a simple iterative procedure which reliably converged to the subsonic solution. For this it was first advantageous to have the solution equation in the form,

$$M_2 \quad = \quad m / (S_1.A_2.\ \rho_1.(1 - (M_2^2 - M_1^2).(\gamma - 1)/2)^{(1/(\gamma - 1))})$$

Since 'm', 'A_2', 'ρ_1' and ' S_1' were all known, one could calculate M_2 if an initial guess for this was put into the right hand side of the equation. This gave a revised value which was iteratively substituted back into the right side for recalculation. For moderate Mach numbers, < 0.5, this quickly converged to the solution. For U_2/S_2 >= 1 (Mach 1, or greater) or for M_2 >= 0.913, the iteration could not converge. One could start the procedure with the incompressible solution, M_2 = F2.

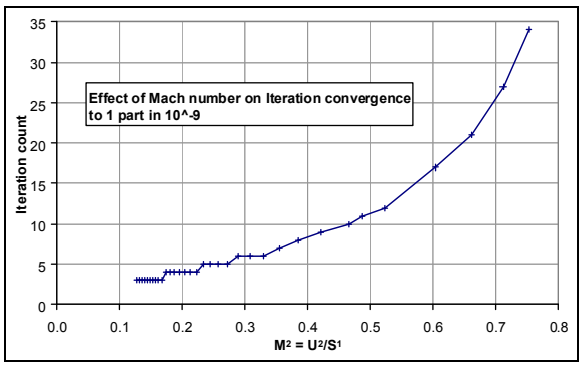

Figure 125: Convergence rate for iteration

The practical upper limit for M_2 was 0.905, or Mach 0.99. Being so close to Mach 1, the convergence rate was much slower, so a convergence limit of 10^{-8}

was used, which required nearly 500 iterations for this condition. Only 11 iterations were required for M_2 = 0.488, or Mach 0.5. Using a convergence limit of 10^{-6} up to Mach 0.5 reduced the iteration count to 8 to converge, which was only a minor benefit.

The relationship between the iteration count and the M_2 is shown in Figure 125 for a convergence limit of 10^{-8}. Up to a value of 0.5 for M_2 only about 11 iterations were required.

Flow Validation

For the small convergent droplet research tunnel, the flow conditions were determined with the nozzle approximation, CFD analysis and pressure tapping measurements.

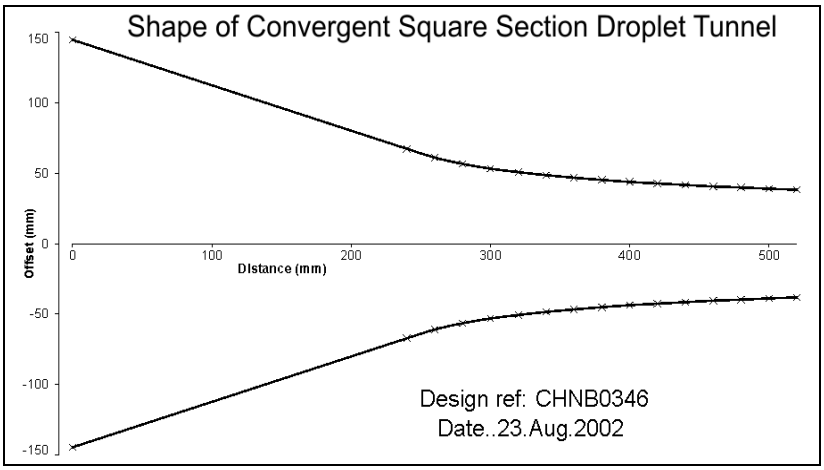

Figure 126: Shape of Convergent Square Section Droplet Tunnel

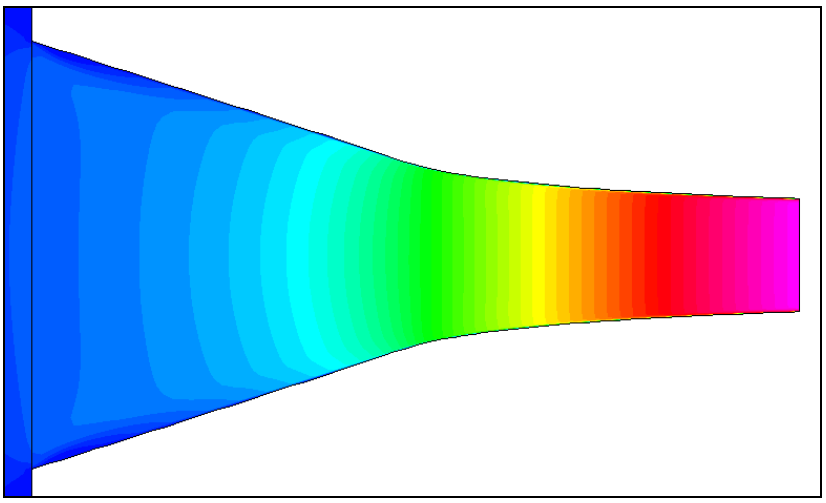

Figure 127: CFD analysis of air velocity in the convergent droplet tunnel.

The shape and size of the square-section tunnel is shown in Figure 126. This was designed with a maximum convergent angle of 20°, each side of the axis, or an included angle of 40°. This was to ensure that the one-dimensional flow calculation was adequately accurate, without any correction for the convergent angle.

The flow in the convergent droplet tunnel was also analysed with CFD modelling, by Joao Amaral Teixeira at Cranfield University, using the CFX package. The resulting velocity distribution is shown in Figure 127.

The velocity and pressure profile along the tunnel axis is shown in Figure 128 for the CFD analysis, convergent nozzle theory and measurements from pressure tapping. This indicates reasonable agreement between the various results.

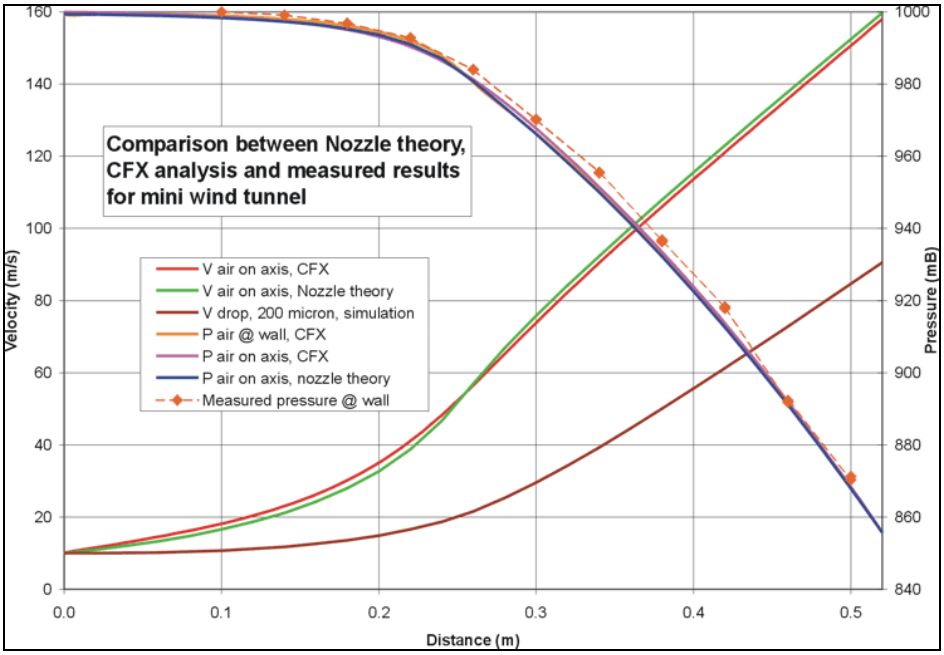

Figure 128: Comparison between Nozzle theory, CFD analysis and measured results

Convergence Correction

Where the convergence angle on each side of the tunnel axis was greater than 20^0, the accuracy of the one-dimensional flow assumption was less certain. For the evaluation of the convergent tunnel development it was necessary to have an effective means to analyse the flow in tunnels with convergent angles up to 90^0 either side of the axis.

The primary interest was to compute the motion of droplets along the axis, but it was also necessary to determine droplet motion off-axis. This was because droplets were introduced away from the axis, and/or with a transverse velocity component, or subjected to transverse forces, such as gravity in a horizontal tunnel. For this it was necessary to describe the flow in at least two dimensions, but preferably in three dimensions.

One answer was to use CFD analysis to calculate the flow, but this was a complex, cumbersome and time-consuming process. It was also much more difficult to integrate this with a simulation of the droplet motion dynamics. CFD analysis was particularly difficult when trying to compute the contraction profile required to achieve particular aerodynamic loading variation on droplets, either with respect to time or distance.

Attempts were made to represent the contractions as a series of sections with conical flow, but this proved to be unsuccessful.

A plausible approximation of the flow distribution was needed. High accuracy was not important, since the highly-convergent section would be a short part of the tunnel length and also the more convergent sections were larger in diameter, where the air had the lowest velocity, and hence the least effect on droplets. The main requirement was that it should sensibly represent the flow, be computationally effective, and not result in any substantial computational irregularities.

Various CFD results were obtained for convergent tunnels, such as shown for the Cranfield 5m tall vertical tunnel in Figure 129, (S.C. Tan, Oct 2002) and Figure 127.

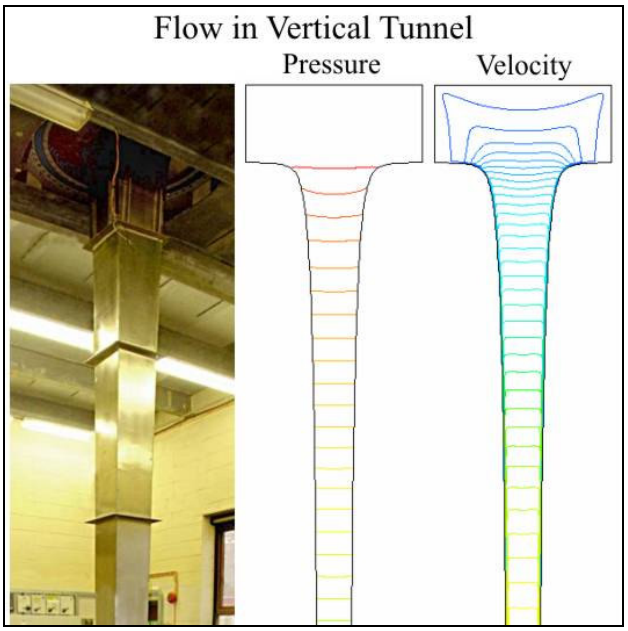

Figure 129: CFD flow analysis of the vertical tunnel

One observation made from this and other CFD results, such as in Figure 127 and Figure 129, was that within the tunnel contraction the contours for pressure and velocity magnitude were reasonably planar, even near a highly convergent entry. It was also noticed that the boundary layer was thin and effectively negligible.

It was also deduced that near the tunnel wall the flow had to be tangential to the wall and that on the axis the flow was along the axis.

Circular cross section

It was more practical to construct a convergent tunnel with a square or rectangular cross section, as shown in Figure 129 for the vertical tunnel. However, initially it was simpler to evaluate the flow in a convergent tunnel of symmetrical circular cross section. The method could then be extended to square and rectangular cross-sections.

The following assumption were made;

1. The was no circumferential flow.
2. The flow was axisymmetric.
3. In a cross-section perpendicular to the axis the velocity magnitude was uniform.
4. Near the wall and at the axis the flow was tangential and parallel to the wall.
5. Between the axis and wall the flow would be at some intermediate angle.

The issue was how to interpolate the angle of the flow between the axis and the wall. Regrettably no plots of the stream functions were available to indicate how this may vary and it was not possible to obtain such a plot.

If it were assumed that the flow was at some angle α to the axis and at a distance **R** from the axis, then a possible assumption was that;

$$\mathrm{Tan}(\alpha) = \mathrm{Tan}(\theta).(R / R_{wall})$$

where θ was the wall angle
R_{wall} the wall radius from the axis

There was a difficulty with this in that, when θ is $\pi/2$, (90^0) to the axis all the flow was radial, with no axial component, except at the axis. Hence this lead to an implausible result as the wall angle approached 90°.

A more plausible approximation was that the flow angle was proportional to the distance from the axis, such that,

$$\alpha = \theta.(R / R_{wall})$$

The axial velocity at any location was then given by;

$$U_z = U_{axis} . Cos(\alpha) = U_{axis} . Cos(R.(\theta / R_{wall}))$$

$$U_r = U_z.Tan(\alpha)$$

Putting $U_z/U_{axis} = y$

and $R/R_{wall} = r$

one obtained $y = Cos(r. \theta)$

Integrating over the cross-sectional area to determine the net flow one obtained;

$$q = y.dA = 2.\pi. \; r.Cos(r. \theta).dr, \quad \text{for } r = 0 \text{ to } r = 1$$

$$= 2.\pi.(\theta.Sin(\theta) + Cos(\theta) - 1)/ \theta^2$$

As θ tends to zero, for uniform flow, one obtained;

$$q = 2.\pi. (\theta^2 + (1 - \theta^2/2) - 1)/ \theta^2$$

or $$q_0 = 2.\pi. (\theta^2/2)/ \theta^2 = \pi$$

Hence the ratio of flow in the convergent tunnel, relative to that in a parallel section with the same velocity at the axis, were given by;

$$q/q_0 = 2.(\theta.Sin(\theta) + Cos(\theta) - 1)/ \theta^2$$

Putting $\theta = \pi/2$, (90°) one obtained;

$$q/q_0 = 2.(\pi/2 - 1)/(\pi/2)^2 = 0.463$$

Alternatively for a given net flow the air velocity along the axis had to be multiplied by the factor,

$$q_0/q = \theta^2/2.(\theta.Sin(\theta) + Cos(\theta) - 1)$$

When $\theta = \pi/2$, the velocity along the axis was then 2.16 times the mean axial velocity.

Rectangular cross-section

The situation with a rectangular section was more difficult, but a plausible assumption was that the flow direction had a compound angle, α and β,

where $\alpha = \theta.(X / X_{wall})$

and $\beta = \phi.(Y / Y_{wall})$

where α was the flow angle with displacement X

θ	wall angle with displacement,	X_{wall}
β	flow angle with displacement,	Y
ϕ	wall angle with displacement,	Y_{wall}

Let $x = X / X_{wall}$

and $y = Y / Y_{wall}$

This results in the velocity components,

$$U_z = U_{axis} / \sqrt{(1 + Tan(x.\theta)^2 + Tan(y.\phi)^2)}$$

$$U_x = U_z . Tan(x.\theta)$$

$$U_y = U_z . Tan(y.\phi)$$

Integrating over the cross-section we obtain,

$$q = \int U_z.dA$$

$$= 4.U_{axis}.\int\int (1/\sqrt{(1 + Tan(x.\theta)^2 + Tan(y.\phi)^2)}).dx.dy;$$

for $x = 0$ to $x = 1$ and $y = 0$ to $y = 1$

There appeared to be no closed form solution for this integral. Even if a solution had existed it was likely to have been so complicated it would have been more effective to use numerical methods. As a result Simpson's-rule of numerical integration was used.

A potential difficulty with the Simpson's rule was that it was intended for line integrals, not area integrals. Fortunately, for a rectangular region this could be resolved with a double integral, by dividing the rectangle into equally spaced rows. The numerical integration was computed along each row and the area integral obtained by numerically integrating across the rows.

The essential parts of the numerical integration procedure are shown in the following fragment of the Excel VBA macro. The full macro is given at the end of the section.

```
Dim u(n), v(n), x(n): h = 1/n
For i = 0 To n: x(i)=i/n: Next` define integration points
  For j = 0 To n: For i = 0 To n
  ` define function to be integrated
    u(i) = 1/√(1 + Tan(θ.x(i))² + Tan(ϕ.y(i))²)
  Next i: v(j)=Simpson(u(), h, n): Next j `integrate rows
Integral = Simpson(v(), h, n) ` integrate columns
```

The results of the calculations are shown in Figure 130. This is for circular and square-section tunnels, but the method was equally effective for rectangular section tunnels. It can be seen that the square and round sections were quite similar, but that the square section had a lower total flow for the same wall angle and same velocity at the axis. This was attributed to the corners of the square section having a steeper convergent angle than the middle of the sides. If the square section was compared with the convergent angle of a circular section of the same cross-section area, then this would account for most of the difference in flow distribution between the circular and square sections.

In Figure 130 the integration for the square tunnel was carried out over a 64 by 64 matrix to minimise any numerical errors. The integral was then re-run with a 2 by 2, 4 by 4 and 8 by 8 matrix. The discrepancy between these and the 64 by 64 matrix are shown. It can be seen that even with the 2 by 2 matrix the maximum discrepancy was less than

0.015%, with a convergent angle of 90°. With an 8 by 8 matrix the maximum discrepancy was only 0.002%, so this integration method was both efficient and accurate.

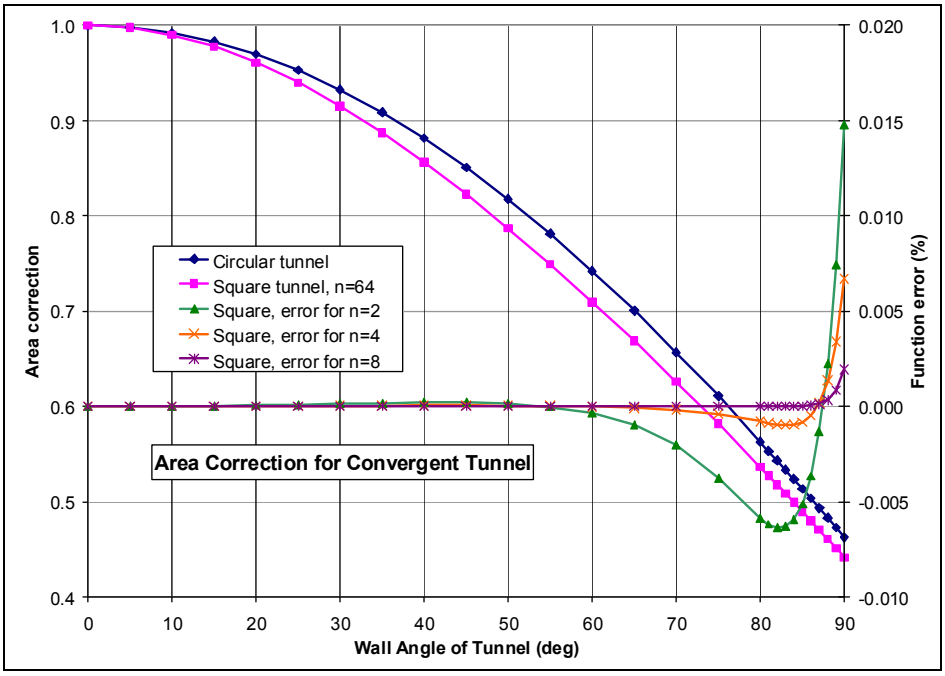

Figure 130: Area Correction for a Steeply-Convergent Tunnel

Verification of the convergent tunnel airflow calculations

To check the validity of the airflow calculations, these were compared against the CFD calculations for the vertical tunnel shown in Figure 129 (S.C. Tan, Oct 2002).

The results of this are given in Figure 131, which shows the velocity distribution along the tunnel axis from the CFD analysis and the nozzle flow approximation, with correction for the flared entry, which started at 0.6m along the axis.

With the flow approximation no flow correction was made for the plenum chamber. It can be seen from the CFD result that the flow velocity actually increased prior to the tunnel entry. On entry to the tunnel the velocity of the approximated flow can be seen to increase to be much closer to the CFD result.

It was found from other simulations that the flow correction only had a significant effect over the first 200mm from the tunnel entry. It would seem that near the tunnel entry there were other unexplained discrepancies between the CFD and the nozzle flow approximation. This might have been due to other complexities of the flow, which the nozzle approximation did not include. Even so, the nozzle approximation with the convergence correction was found to be adequate for the required flow analysis.

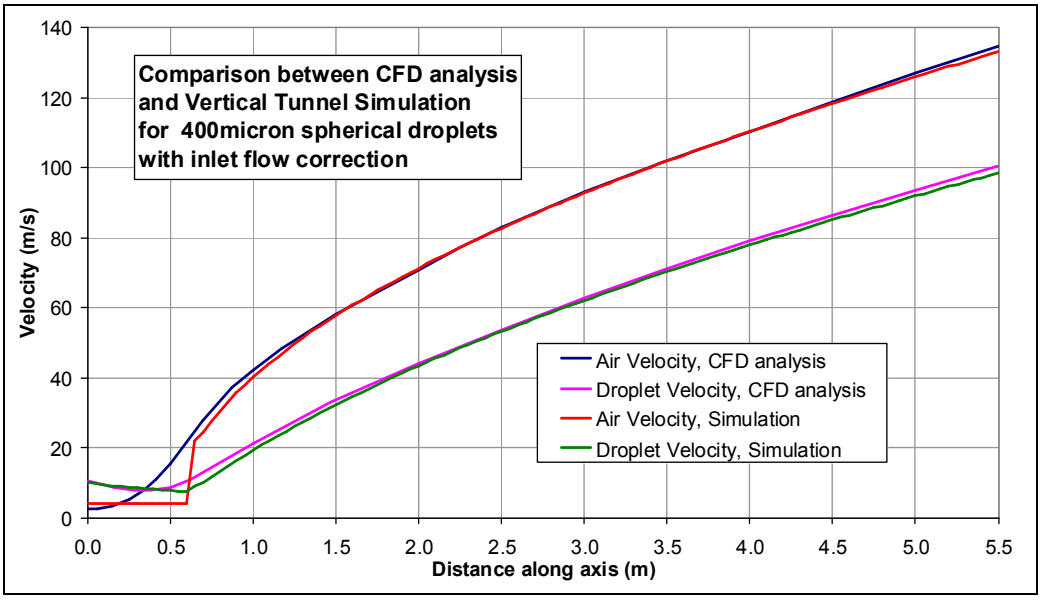

Figure 131: Comparison between CFD analysis and Simulation for Vertical Tunnel

Boundary layer effects

Near to the end of the tunnel, from about 4.5m onward, it can be seen from Figure 131 that the nozzle approximation resulted in a slight underestimate of the flow velocity. This is attributed to development of the boundary layer, which would have slightly reduced the effective cross section of the tunnel and so increased the air velocity. The CFD analysis would have allowed for this effect, but the convergent nozzle approximation had neglected the boundary layer. It would seem, however, that the resulting discrepancy was quite small.

Droplet velocity discrepancies

Figure 131 also shows the predicted velocity for a 400µm spherical droplet, computed using the CFD and Corrected Convergent Nozzle airflow. It can be seen that there was, as expected, some discrepancy near the tunnel entry, but within a metre the discrepancy became reasonably insignificant. In comparison with the errors due to neglecting droplet distortion, the discrepancies in the convergent nozzle airflow were a minor issue.

It is also possible that some of the discrepancies in the calculated droplet velocity were due to the use of different drag formulations in the CFD and Nozzle flow calculations.

The effect of droplet distortion on its velocity were evaluated using the convergent nozzle flow calculations. No such results were available for the CFD flow analysis. In this case the effects were quite small, being comparable to the droplet velocity differences between CFD and Nozzle airflows. This was because the Weber numbers applied to the droplets were quite low, around 7, so the increased drag on the droplets, due to distortion, was only moderate. Even so, it made a significant difference to droplet Weber number, reducing it from 8 for the spherical droplet to about 6.5 for the distorted droplet. This was because of the lower velocity difference between the droplet and air, due to the higher droplet velocity from the increased air drag.

Droplet Tunnel Contraction Profile

Design ref: CHNB0346

Date 23 Aug 2002; Time.11:03

	Distance (mm)	Dev length (mm)	Offset (mm)	Offset (mm)	Size (mm)	Angle (deg)
1	0	0.0	144.7	-144.7	289.5	17.88
2	240	252.2	67.3	-67.3	134.6	17.88
3	260	273.1	61.0	-61.0	122.1	17.39
4	280	293.6	56.5	-56.5	113.1	12.73
5	300	313.9	53.2	-53.2	106.4	9.38
6	320	334.1	50.6	-50.6	101.3	7.38
7	340	354.2	48.5	-48.5	97.0	6.07
8	360	374.3	46.7	-46.7	93.4	5.12
9	380	394.3	45.2	-45.2	90.3	4.41
10	400	414.4	43.8	-43.8	87.6	3.86
11	420	434.4	42.6	-42.6	85.3	3.41
12	440	454.4	41.6	-41.6	83.1	3.04
13	460	474.5	40.6	-40.6	81.2	2.72
14	480	494.5	39.8	-39.8	79.5	2.46
15	500	514.5	39.0	-39.0	78.0	2.22
16	520	534.5	38.3	-38.3	76.5	2.02

Excel VBA macro for Nozzle Calculations

```
'=============================================
Function F(M2, M1, ga)
' Function to determine tunnel area for air velocity
' F = mf / A2.W1.S1
' mf  mass flow rate
' ga  gamma = Cp/Cv, ratio of specific heats
' S1 = Sqr(ga.R.T1), sound velocity at entry
' V1  air velocity at entry
' V2  air velocity at working section
' M1 = V1 / S1, M2 = V2 / S1
' 2.Cp.T1 = 2.S1^2/(ga - 1)
' 1-(V2^2 - V1^2)/2.Cp = 1-(M2^2 - M1^2).(ga-1)/2
  F = M2 * D(M2, M1, ga)
End Function
'=============================================
Function M(F2, M1, ga)
' Air velocity for tunnel area from inverse of F(M2, M1, ga)
  Call Ms(F2, M1, ga, M2, i): M = M2
End Function
'=============================================
Function Mn(F2, M1, ga)
' iteration count for Function M(F2,M1,ga)
  Call Ms(F2, M1, ga, M2, i): Mn = i
End Function
'=============================================
Private Sub Ms(F2, M1, ga, M2, i)
' Find inverse of F(M2, M1, ga)
' F2   required value of F(M2, M1, ga)
' M1 = V1/S1 ' Mach number at entry
' M2 = V2/S1;  i  iteration count
  M2 = F2       ' initial guess
  nc = 500      ' iteration count limit
  er = 10 ^ -8  ' error limit
  For i = 0 To nc: M2 = F2 / D(M2, M1, ga)
    If Abs(1 - F(M2, M1, ga) / F2) < er Then Exit For
  Next i: If (i + 1) >= nc Then M2 = 0.905
End Sub
'=============================================
Private Function D(M2, M1, ga)
' compute density ratio W2/W1
' M1=V1/S1, M2=V2/S1
' W1, W2  density  at 1 & 2
' W2/W1=(1-(M2^2-M1^2).(ga-1)/2)^(1/(ga-1))
  k = 1 - (M2 ^ 2 - M1 ^ 2) * (ga - 1) / 2
  D = k ^ (1 / (ga - 1))
End Function
```

Excel VBA Macro for convergent tunnel flow correction

```
Function entrycorrect(thet, phii, nn)
' calculate entry correction for rectangular convergent tunnel
' thet  is angle of wall in X coordinate
' phi   is angle of wall in Y coordinate
' nn    is the even number of numerical integration points.
  py2 = 2# * Atn(1#):
  If (thet > py2) Or (thet < 0) Then Stop
  If (phii > py2) Or (phii < 0) Then Stop
  If nn <= 0 Then
  ' circular section tunnel
    ec = 1
    If thet > 0 Then
      ec = 2 * (thet * Sin(thet) - (1 - Cos(thet))) / thet ^ 2
    End If
  Else
  ' rectangular section tunnel
    n = -2 * Int(-0.5 - nn / 2)
    ReDim u(n), v(n), x(n): h = 1 / n
    For i = 0 To n: x(i) = i / n: Next i
    For j = 0 To n: For i = 0 To n
      u(i) = zvec(x(i), x(j), thet, phii)
    Next i: v(j) = fullsimp(u(), h, n): Next j
    ec = fullsimp(v(), h, n)
  End If
  entrycorrect = ec
End Function
```

```
Private Function zvec(u, v, tht, phi)
  zvec = 1 / Sqr(1 + Tan(u * tht) ^ 2 + Tan(v * phi) ^ 2)
End Function
```

```
Private Function fullsimp(y(), h, n)
' full simpsons integral
  Sum = 0: If Int(n / 2) <> n / 2 Then Stop
  For i = 2 To n Step 2
    ya = (y(i - 2) + y(i)) / 2: yc = y(i - 1)
    Sum = Sum + 2 * (ya + (yc - ya) * 2 / 3) * h
  Next i: fullsimp = Sum
End Function
```

Chapter 11: Calibration of Convergent Droplet Tunnel

To determine the drag characteristics of deformable droplets in the convergent tunnel it was necessary to determine the velocity of the droplets relative to the airflow velocity.

The droplet velocity was determined with the triple laser beam instruments, see chapter 13, but some other means was required for determining the airflow velocity.

The normal means of determining the air velocity in such circumstances is with a Pitot-static tube, but there were various difficulties and uncertainties with obtaining, installing and using these.

It was anyway deduced that the pitot pressure on the axis of the tunnel would be the total pressure and, with a thin boundary layer, this pressure would essentially be the same static pressure as in the plenum chamber. Hence the Pitot pressure reading could more easily be obtained by measuring the static pressure of the plenum chamber.

To obtain the static pressure on the axis of the tunnel would, in any case, require some intrusion into the airflow, which itself would affect the reading obtained. Since it was found from CFD modelling that the pressure distribution was adequately uniform over the cross section, as shown if Figure 132, it was concluded that it would be acceptable to take the static pressure readings for the tunnel via wall tappings.

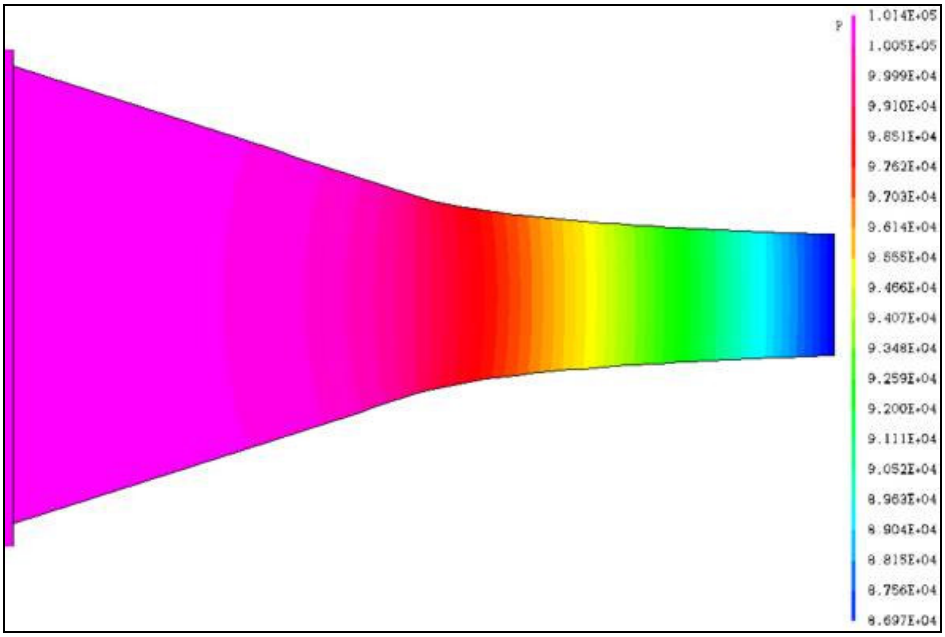

Figure 132: Pressure distribution in convergent tunnel from CFD analysis.

Figure 133 shows the comparison between the measured pressure at the wall tappings in comparison with the 1D nozzle flow prediction and CFD results for the axis and wall. From this it was concluded that the wall pressure tappings were an adequate measure of the static pressure at the tunnel axis. When combined with the static pressure in the plenum chamber, this could be used to determine the tunnel air velocity near the axis.

Because of the good agreement between the pressure tapping measurements and the CFD modelling it was concluded that there was no need to measure the flow distribution across the tunnel section.

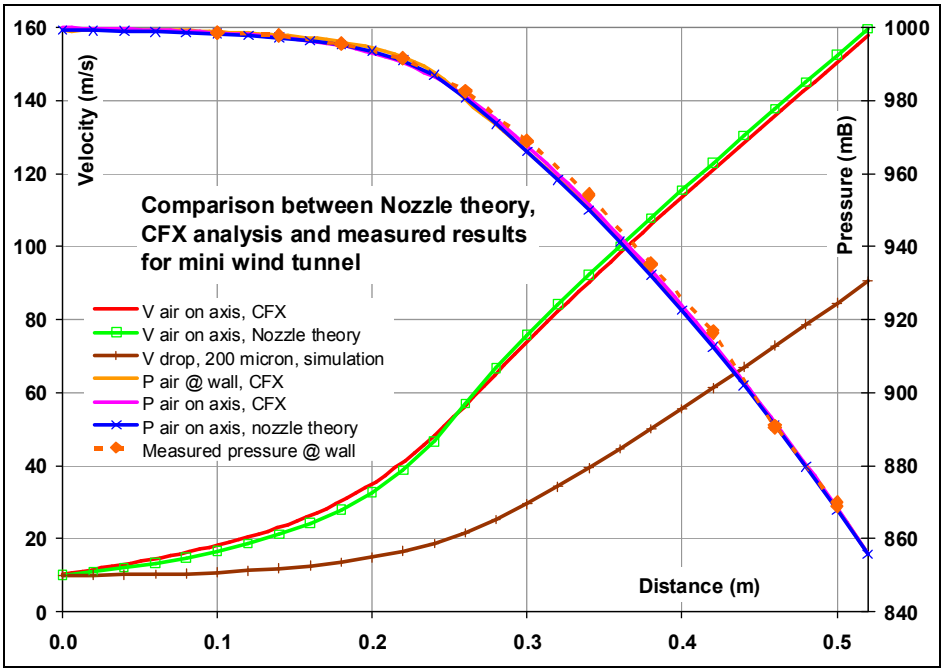

Figure 133: Comparison between the model predictions and pressure tappings

The pressure tappings were at 100mm from the tunnel entry, then every 40mm up to 500mm from the tunnel entry, with the tunnel 520mm long.

Most of the measurements and observation of droplets were made at 480mm from the entrance, or 40mm from the exit, midway between the last two pressure tappings. It is to be noticed in Figure 133 that the readings from these two tappings were in very good agreement with the model predictions.

There was no pressure tapping at the location required, 40mm from the exit, and it was neither necessary, nor practical, to have an additional tapping installed. Figure 133 shows that in the latter half of the tunnel the velocity increases at a constant rate, with respect to distance, so it was quite acceptable to take the average of the two velocities obtained from the pressure tappings at 60mm and 20mm from the tunnel exit.

Using the velocities derived from the two pressure tappings is was possible to determine the airflow velocity gradient. From the droplet drag coefficient, determined from the measurements, it would then be possible to determine the droplet rate of change of acceleration, or jerk, to make any necessary corrections to the measured droplet velocity and acceleration. From simulation at the measuring location the errors caused by jerk were less than 0.3% for acceleration and 0.15% for the velocity, which were neglected.

Determination of Air Velocity

The air velocity at the pressure tappings was determined with the following equation, (Rogers and Mayhew, 1992 or 1967, Equ.(18.17), 2nd, 4th Edition.)

$$U_2 = [((2.\gamma/(1-\gamma)).R.T_1.\{(p_2/p_1)^{(\gamma-1)/\gamma} - 1\}]^{1/2}$$

Where T_1 and p_1 are the temperature and pressure in the plenum chamber.

U_2 and p_2 are the velocity and pressure the pressure tapping.

In this, p_1 is the ambient atmospheric pressure, from a nearby precision digital barome-

ter, apart from a minor pressure drop across the inlet screen. The value of $p_1 - p_2$ is the pressure difference, or measured vacuum, between the plenum chamber and the pressure tapping using a precision digital manometer.

The tunnel was run at fan speed increments of 5rev/s, or 300rpm, up to 50rev/s, or 3000rpm. For each fan speed the two pressure tappings results are given in Table 11.

The results were interpreted in terms of air velocity against fan speed, rather than tunnel pressure against fan speed, so that any small variations in ambient air density would have a minimal effect on the calibration. At the time of any droplet measurements the density of the air at the droplet location was determined from the calibrated air velocity and ambient air density.

For each fan speed about ten readings were taken to average out fluctuations in the tunnel pressure, believed to be caused by small flow instabilities in the diffuser. The precision digital manometer had a resolution of 1Pa, but with the jittering digital display was difficult to read. To overcome this the display was photographed with a digital camera to capture the instantaneous readings. From these the average, standard deviation and variance of the vacuum was calculated for each fan speed.

Table 11: Tunnel condition 20mm from exit

Rev/S	Vacuum	Std Dev	Variance	x	U / (rev/s)
5	132.18	6.3	4.7%	0.1	2.96
5	135.33	9.4	7.0%	0.1	3.00
10	559.25	7.6	1.4%	0.2	3.05
15	1322.9	19.2	1.4%	0.3	3.13
20	2378.8	31.7	1.3%	0.4	3.16
25	3825.1	40.1	1.0%	0.5	3.21
30	5578.5	49.0	0.9%	0.6	3.24
35	7523.5	51.1	0.7%	0.7	3.24
40	9593.4	88.5	0.9%	0.8	3.21
45	11938.	76.2	0.6%	0.9	3.20
50	14505.	101.0	0.7%	1	3.19
Tunnel condition 60mm from exit					
5	152.50	6.4	4.2%	0.1	3.18
5	149.67	7.2	4.8%	0.1	3.15
10	651.36	12.6	1.9%	0.2	3.29
15	1552.3	25.6	1.6%	0.3	3.39
20	2817.1	41.4	1.5%	0.4	3.44
25	4476.8	64.0	1.4%	0.5	3.48
30	6564.1	61.0	0.9%	0.6	3.52
35	8990.7	131.8	1.5%	0.7	3.55
40	11539.	113.0	1.0%	0.8	3.53
45	14511.	137.6	0.9%	0.9	3.54
50	17497.	170.3	1.0%	1	3.52

The results from this are shown in Table 11, in terms of tunnel vacuum in Pascals, relative to the plenum chamber, again fan speed in revs per second.

It can be seen from Table 11 that at low speeds there was appreciable variance (standard deviation divided by the mean), typically about 5% at 300rpm. However this would reducd to about 2.5% variance in the air velocity. In practice the minimum speed used for measurements was 1200rpm, or 20 rev/s, where the variance in the vacuum was typically about 1.5%, or 0.75% of the mean air velocity.

The resulting air speed, in m/s, is plotted against the fan speed, in rpm, in Figure 134. At maximum fan speed and 20mm from the tunnel this gives an air speed of 176m/s, or about Mach 0.53. At 60mm from the exit this gave 159m/s, or Mach 0.48. At 40mm from the tunnel exit, where most of the measurements and imaging were taken, this would give a maximum velocity of about 168m/s, or about Mach 0.5.

It was of interest to note that the fan rotor was 0.56m diameter, with a peripheral velocity of 88m/s at 3000rpm. Hence the air velocity 40mm from the tunnel exit had a velocity of approximately 1.9 times the peripheral velocity of the fan rotor.

In practice measurements could not normally be taken at the full fan speed at 40mm from the tunnel exit, since this would result in excessive aerodynamic forces and cause the droplets to break-up. For 250µm droplets the maximum speed normally used was 40rev/s, or 2400rpm, with an air velocity of about 135m/s, or about Mach 0.4. It was considered important to keep air compressibility within reasonable limit and at Mach 0.4 the reduction in air density was about 7.6%, which was considered acceptable. The limit set for a maximum reduction in density was 10%, which occurs at Mach 0.46, or a fan speed of about 2753rpm.

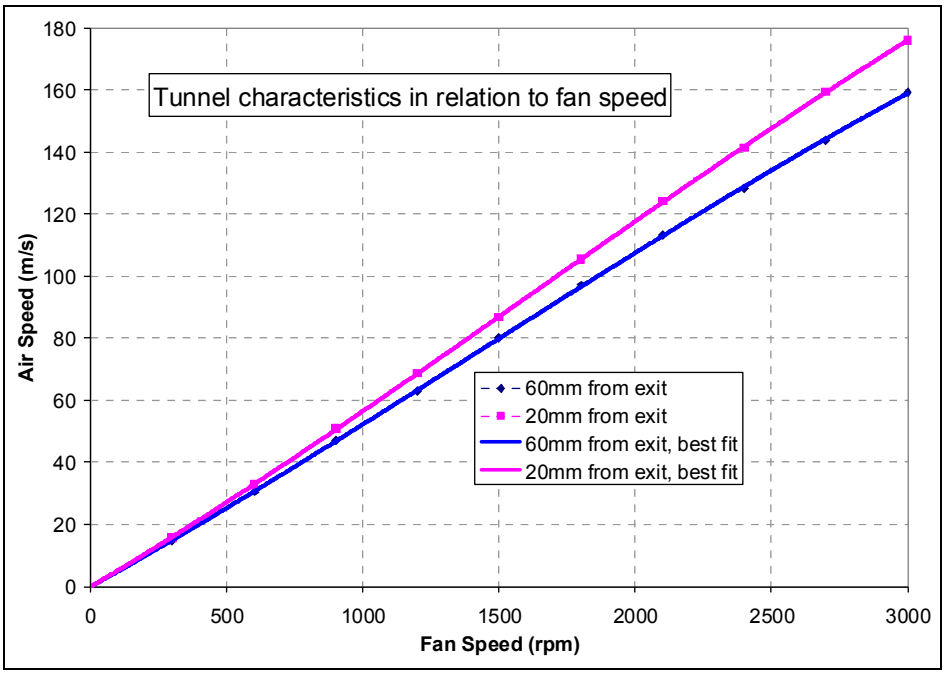

Figure 134: Direct plot of Air speed against Fan speed.

While the curves in Figure 134 appear to be reasonably linear, in practice they deviate significantly from a straight line. Cubic, or quartic, curve fitting could be used, preferably with a zero intercept, but the quality of the fit was likely to be poor for lower values. Also because the X axis covers such a large range this could result in difficulties with the curve fitting in Excel. For the pressure tapping at 20mm from the exit this gave;

$$y = 1.48 \times 10^{-13} x^4 - 2.10 \times 10^{-09} x^3 + 7.52 \times 10^{-06} x^2 + 5.11 \times 10^{-02} x$$

where x = N (rpm) and y = U (m/s). In practice 3 decimal places were used.

Another issue was the great range of the coefficients, more than eleven orders of magnitude, which could cause computational problems.

If however this is plotted with;

x = N / 3000 rpm and y = Air velocity (m/s) / N (rev/sec)

as shown in Figure 135, this reduces the X axis to a range of unity, with the result;

$y = 0.5007 x^3 - 1.6090 x^2 + 1.6104 x + 3.0254$ at 20mm from the exit

and $y = 0.2164 x^3 - 1.0469 x^2 + 1.1424 x + 2.8688$ at 60mm from the exit

In this the coefficients were all of a similar magnitude and were all within an order of magnitude of unity, so the curve fitting is well conditioned. This curve fitting also gave similar weighting, in terms of fractional errors, to the low speed readings, so the fitting errors were better distributed. Hence, although this did not look such a good curve fit, it gave a more reliable result, particularly for the lower speeds.

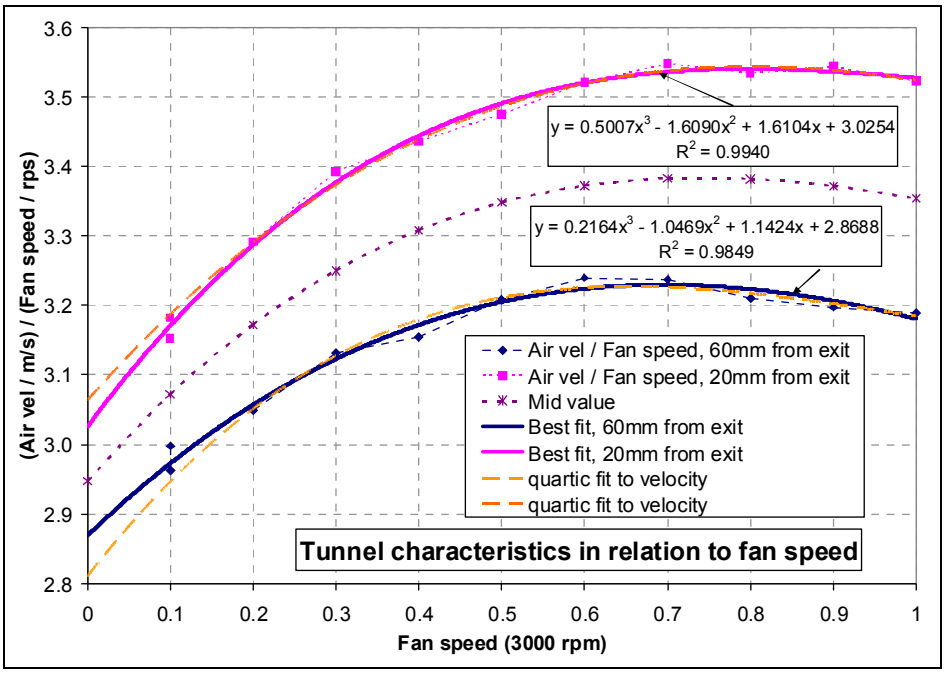

Figure 135: Tunnel velocity calibration against fan speed.

Figure 135 shows the resulting errors due to directly fitting the velocity to the fan speed, from Figure 134, shown as the orange dashed lines. These start to diverge for speeds less than 600 rpm.

Figure 135 also shows the significant non-linearity between the air velocity and fan speed, which would have otherwise given curves with a constant value. The reason for the departure from a linear relationship, between air velocity and fan speed, was attributed to the Reynolds number, boundary layer and Mach number compressibility effects.

Other potential errors

The tunnel was open loop, in that it took in air from the laboratory and expelled it externally. This air then had to be replaced by air entering the laboratory from outside.

There were no ventilation grills to the laboratory, so the air had to find its way in via any inadvertent gaps, such as that around the diffuser between the tunnel and the fan.

The effect of this could be to reduce the pressure in the laboratory to less than the atmospheric pressure given by the digital barometer, which was in a neighbouring laboratory. When the tunnel was run, particularly at high speed, it was normal to open the exterior door of the laboratory to allow for the necessary air flow from the exterior. The velocity of the flow through the door would have been less than 1m/s at the maximum fan speed, so the error due to this would have been negligible.

Another source of error could have been the pressure drop across the inlet screen to the plenum chamber. This was made of four layers of fibre matting, normally used for air filters. The pressure drop across this was measured and is discussed in Chapter 9 about the tunnel design. This needed to produce a pressure drop sufficient to swamp any extraneous air disturbance in the laboratory, such as from heating fans, but not sufficient to have a significant effect on the air density in the plenum chamber.

At maximum speed the pressure drop across the screen was less than 0.5mb, or 50Pascals. Because the flow through the inlet screen was laminar, due to the low velocity, and fine fibre mesh, the pressure drop across this was proportional to the air velocity through it. Hence the pressure drop across the inlet screen was, approximately, 1Pascal per rev/sec of the fan speed.

Because the vacuum in the tunnel was approximately proportional to the square of the air flow, the pressure drop error of the inlet screen would be a more significant proportion at lower speeds. At a fan speed of 50rev/s, 300rpm, the inlet screen pressure drop was about 5Pascal, although the digital manometer only recorded about 3Pascal due to the instrument nonlinearity at the bottom of its measuring range. For this the screen pressure drop would be about 3.3% of the tunnel vacuum, which could result in about a 1.6% flow error at the lowest fan speed.

Conclusions

1. It was possible to derive effective polynomial functions for the tunnel air velocity at the two pressure tappings nearest the tunnel exit, which were 20mm and 60mm from the exit. These functions would appear to give results within 1% of the average measured values.
2. For other locations along the tunnel the velocity could be determined from the corrected 1D adiabatic compressible flow model for flow, given in Chapter 10.
3. Between the two pressure tappings the velocity gradient was near constant, as determined by the flow model, so the velocity at 40mm from the exit, the location for imaging and measuring the droplets, could be taken as the average velocity for the two tappings.
4. The velocity difference between the tappings could be used to determine the velocity gradient where the droplet measurements were made.
5. The effect of pressure losses through the inlet screen was negligible for all but the very lowest speed, which was not used for any measurements.

Chapter 12: Development of Droplet Generator

Introduction

To carry out research into the behaviour of droplets it was necessary to produce a stream of droplets having calibrated size and velocity.

The method used was to eject a water jet from a fine nozzle that was vibrating at the frequency required to produce a stable break-up of the jet. The theory behind this is well established (Middleman, 1995).

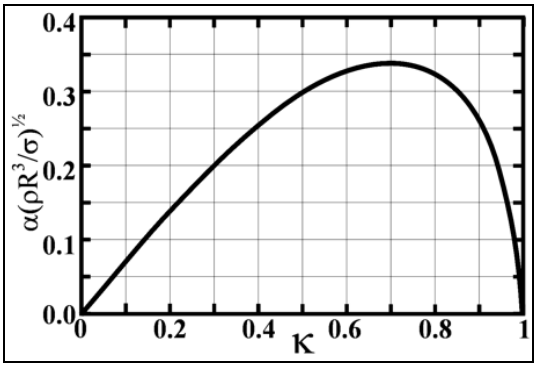

Figure 136: Growth rate of surface ripples on a laminar jet

Principles of operation

A laminar jet of water has a natural tendency to form unstable and growing ripples along its length due to surface tension forces. The rate of growth of the ripples depends on the their wavelength, as shown in Figure 136.

Where $\kappa = \pi.d / \lambda = 2.\pi.R / \lambda$

κ	is the wave number
α	wave growth rate
λ	wave length
ρ	fluid density
σ	surface tension
d	jet diameter (d = 2.R)

A good approximation to this curve is given by the parametric equation;

$$\kappa = 1.8z - 0.8z^2$$

$$\alpha.(\rho.R^3/\sigma)^{1/2} = 1.35(z - z^2) \qquad \text{for} \qquad 0 < z < 1$$

We see that the surface wave grows most rapidly at a wave number of 0.7, but has a significant growth rate for a wave number range between 0.4 and 0.9.

The principle of the generator was to introduce a disturbance into the jet at the optimum frequency to initiate wave development at the required wavelength. Since this wave-length then had an initial start over other wavelengths and could grow more rapidly to become the dominant wavelength.

When the wave amplitude becomes comparable to the jet radius, it would grow no further and the jet would breaks to form a liquid droplet, which would then become spherical. Figure 137 shows examples of the wave development and droplet formation.

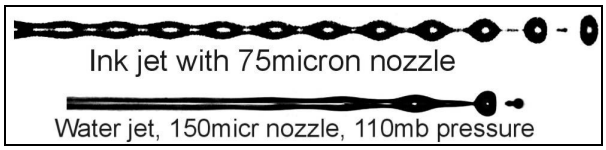

Figure 137: Development of surface wave and droplet formation

If no initial disturbance was applied, then background vibrations and flow irregularities would initiate random surface disturbances. Those nearest to the preferred wavelength would selectively grow and result in droplets. This delayed, but did not prevent, droplet formation, as shown in Figure 138, where the 150µm water jet took 27mm to form droplets. This then resulted in much more irregular droplets, as shown in Figure 139.

The disturbance normally applied to the liquid jet to introduce some fluctuation in jet velocity at the required wavelength. Since the jet had a forward velocity, this required that the disturbance be applied at a given frequency, such that;

Figure 138: Delay of droplet formation without nozzle vibration

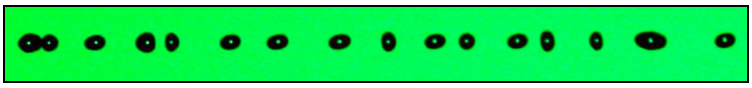

Figure 139: Irregular droplets formed without nozzle vibration

$$f = U / \lambda$$

where $U = \sqrt{(2.\zeta.P / \rho)}$

- f is the applied vibration frequency
- U jet velocity
- ζ jet efficiency
- P applied pressure to the nozzle

The velocity disturbance, or modulation, of the jet could be achieved by directly vibrating the nozzle, known as direct modulation, or by introducing a pressure fluctuation in the fluid behind the nozzle, known as indirect modulation. In this investigation direct modulation of the nozzle was used.

A difficulty could arise if the wavelength was made too long to increase the size and spacing of droplets. If this reduced the wave number, κ, much below 0.4 then harmonics could create high frequency shorter wavelengths that might be closer to the optimum wave number than for the fundamental frequency. This could be due to harmonics from the signal generator, or nonlinearities in the equipment and droplet formation process.

While the wave from the harmonic may be smaller, it could grow much more quickly and overtake the wave produced by the fundamental frequency. This could result in multiple droplets per cycle of the fundamental wave. In some cases it could result in unstable, or chaotic, droplet generation.

Because of the issues previously discussed, if accurately repeatable and calibrated droplets were to be produced, then the droplet generator needed to operate with a wave number of around 0.7. From this it was possible to determine the resulting droplet size for a given jet diameter. This was achieved by equating the volume of one wavelength of jet to that of the droplet, hence;

$$\pi.\lambda.d^2/4 = \pi.D^3 / 6$$

where D is the droplet diameter.

d is the jet diameter

hence $\lambda/(\pi.d) = 1/\kappa = (2/(3.\pi)).(D/d)^3$

or $D/d = ({}^3/_2\, \pi / \kappa)^{1/3}$

also $\lambda/d = {}^2/_3\, (D / d)^3 = \pi / \kappa$

$D/\lambda = {}^3/_2\, (d / D)^2 = {}^3/_2\, ({}^2/_3\, \kappa / \pi)^{2/3} = 1.1447\, (\kappa / \pi)^{2/3}$

for $\kappa = 0.7$, $D/d = 1.89$, $\lambda/d = 4.49$, $D/\lambda = 0.421$

and for $\kappa = 0.4$, $D/d = 2.28$, $\lambda/d = 7.85$, $D/\lambda = 0.29$

Hardware Implementation

The practical implementation of the droplet generator is shown in Figure 140. The left shows a diagram of the components and the right is a photograph of an actual unit. The diameter of the left-hand end of the droplet generator was 10mm diameter.

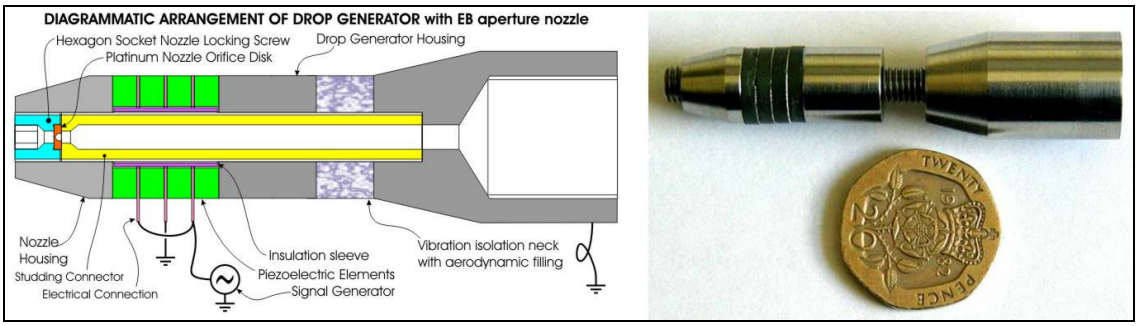

Figure 140: Droplet Generator, construction and appearance

The principle is that an alternating voltage of the required frequency is applied to the piezoelectric elements. These were arranged so that they all expanded in thickness for one polarity of voltage and contracted with the opposite polarity of voltage.

The piezoelectric elements were firmly clamped between two stainless steel masses, one being the Nozzle Housing and the other the Drop Generator housing. This latter item was to provide some mass for the piezoelectric elements to push against to vibrate the Nozzle housing. The Studding-connector through the middle of the droplet generator holds the unit together and carried the liquid supply to the nozzle, but also provided vibration isolation from the fixing and pipe adaptor on the right-hand end.

The droplet generator was designed to be used in a wind tunnel, although for development it was provided with a bulky pipe adaptor. The original configuration used is shown in the top of Figure 141, but with a bulky fitting that could disturb the airflow over the droplet generator. This was revised with a more streamlined connector, shown in the middle and bottom of Figure 141.

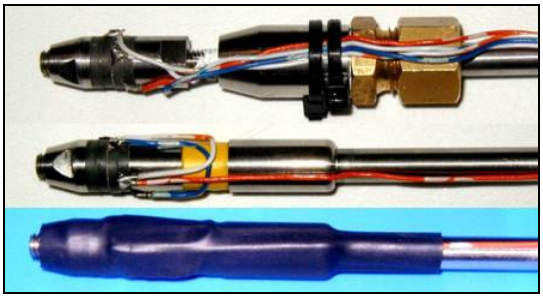

Figure 141: Implementations of the droplet generator

Figure 142 shows that after the droplets were formed they initially vibrated until this was damped by the liquid viscosity. This then resulted in a stream of droplets of uniform diameter, spacing and velocity, as shown in Figure 143.

Figure 142: Droplets being formed

Figure 143: Uniform droplet stream after becoming spherical.

Droplet Coalescence

One issue with the droplets from a vibrating nozzle droplet generator was that to produce consistent droplets the spacing between the droplets could be no more than one, or perhaps two, diameters. This was much less than the length of the wake disturbance behind a droplet, which resulted in an aerodynamic interaction between the droplet.

When the droplets were equally spaced and subjected to a retarding, or accelerating airflow, then the aerodynamic force was the same for all the droplets in the stream.

If due to some disturbance a droplet were to move slightly in the downwind direction in the stream, then it would experience a slightly greater aerodynamic force and would slightly reduce the aerodynamic force on the droplet downwind of it. Hence these two droplets would be encouraged to move closer together. The result would be to cause the droplets to become unevenly spaced, as in Figure 144, often as pairs, or triplets. It can be seen that the 3rd and 4th droplets from the left are nearly in contact with each other.

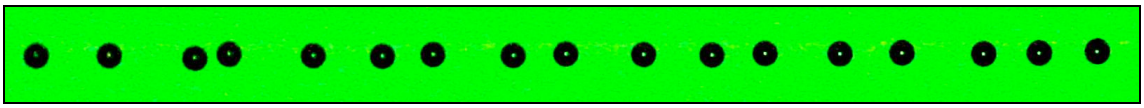

Figure 144: Displacement of droplets due to airflow along the droplet stream.

The reason for this was that the upwind droplet reduced the aerodynamic force on the adjacent downwind droplet. Figure 145 shows the interaction between two disks, or cylinders, (Hoerner 1958) and Figure 146 shows how the drag on droplets decrease as the space between the droplets is reduced, (Lars Reichelt 2004). In this the key translations are that Widerstandsbeiwert is the drag coefficient and Renolds-Zahl the Reynolds number.

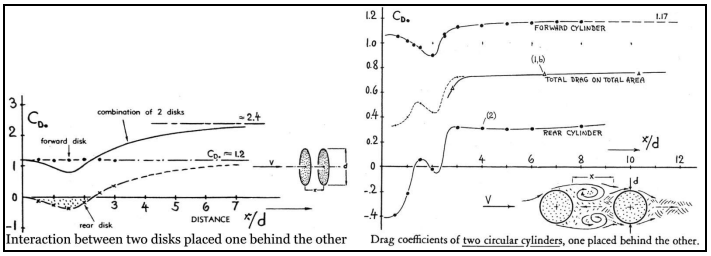

Figure 145: Drag Interactions between Discs and Cylinders

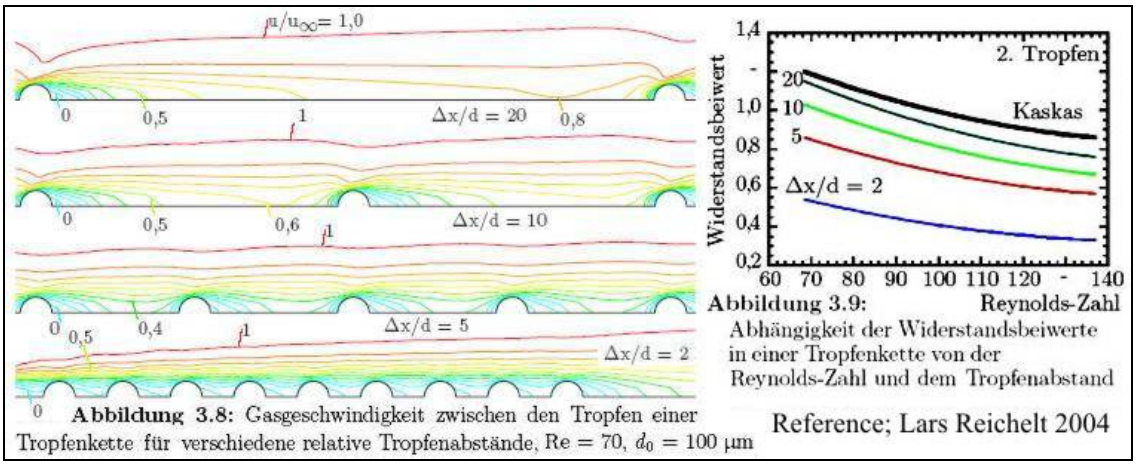

Figure 146: Effect of droplet spacing and Reynolds number on the drag coefficient.

It can be seen that the effect extends for many diameters, particularly for the disks and spheres. Over a distance of two diameters there could be negative drag on the down wind disk. In a stream of spherical droplets the interactions could be complex where they are unevenly spread and misaligned and no data was found for that situation.

The conclusion reached was that the droplets would need to be at least ten to fifteen diameters apart to reduce this effect to an acceptable level.

Inevitably some droplets were brought into contact and Figure 147 shows a video sequence obtained for the coalescence of two 270µm droplets, taken at 50,000 pictures per second.

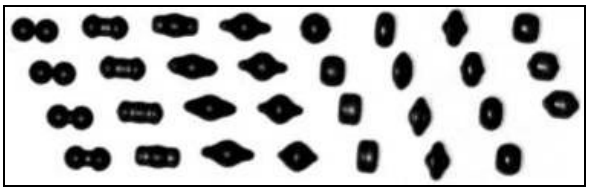

Figure 147: Image sequence of droplet coalescence

The result is a stream of droplets of irregular size and spacing, as shown in Figure 148.

The larger droplets tended to break-up again as the aerodynamic forces increased, which then resulted in even more irregular droplet sizes.

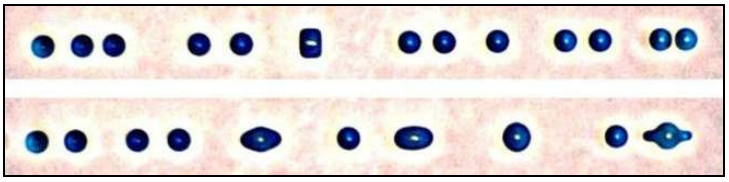

Figure 148: Irregular droplets due to aerodynamic interactions

The close spacing of the droplets and the irregular droplet sizes, due to droplet coalescence, made it difficult to carry out the imaging and measurements required. This required some improvement to the method of generating the droplets.

Electrostatic Removal of Surplus Droplets

The preferred option would have been to use the vibrating nozzle droplet generator, but remove the surplus droplets. This would have been possible using the electrostatic deflection method, but the available time and resourses precluded this.

The principle of the method was that used in continuous ink-jet printers, as shown in Figure 149. In this the droplet to be deflected was electrostatically charged by the charge electrode as it is formed and detached from the jet. These charged droplets would then be deflected as they pass through the electrostatic field between the deflection plates.

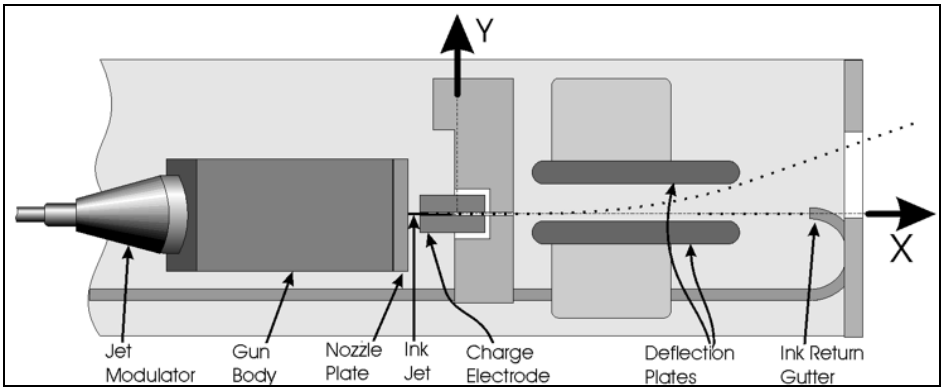

Figure 149: Typical arrangement for droplet deflection used in an ink-jet printer.

For the droplet investigations at least nine-tenths of the droplets would be charged and deflected into a catcher. The required uncharged droplet would then continue on without deflection for the experimental investigation.

Alternative Droplet Generator

To produce droplets with the necessary spacing the possibility of using a slotted spin-

ning disc was considered. Initially the idea was to generate the droplets and then use the disk to only allow through the required droplets. A typical slotted disk is shown on the left of Figure 150, which was made by etching stainless steel shim. This did not work effectively because of the need to accurately synchronise the slots with the droplets.

An alternative approach was to have a uniform jet, without any nozzle vibration, impinging directly onto the spinning disc, as shown in the centre of Figure 149. As a slot passed in front of the jet this would allow through a particle of fluid that would subsequently form into a droplet. as shown on the right of Figure 150.

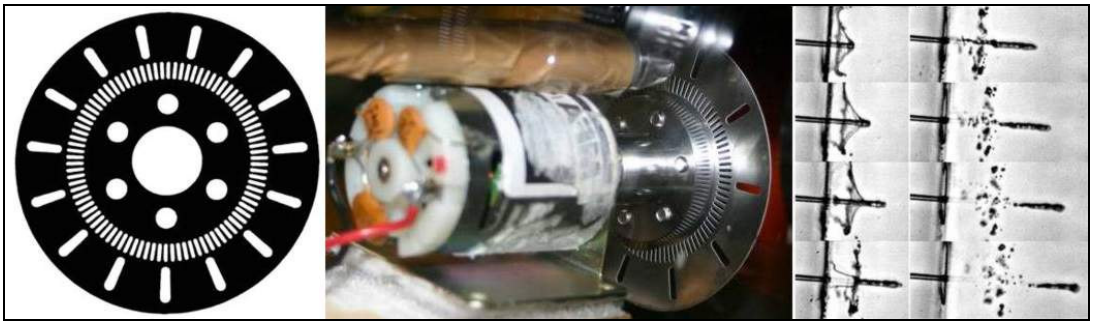

Figure 150: Spinning disc droplet generator.

Figure 151 shows the slotted disc generator under test. The stream of droplets can be seen in the lower right corner. Since only a small proportion of the water produced the required droplets, the rest of it was spun off as a spray. A guard was later added to catch most of this spray.

Images of the droplets produced by this method are shown in Figure 152. It can be seen that these were quite variable.

Figure 151: Testing of spinning disc droplet generator.

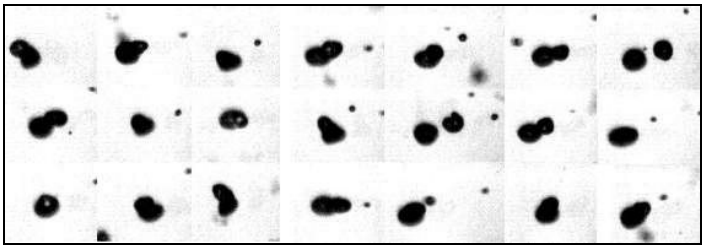

Figure 152: Droplets formed from the spinning slotted disc.

The droplet produced by the spinning slotted disc then provided a stream of spherical droplets, as shown in Figure 153.

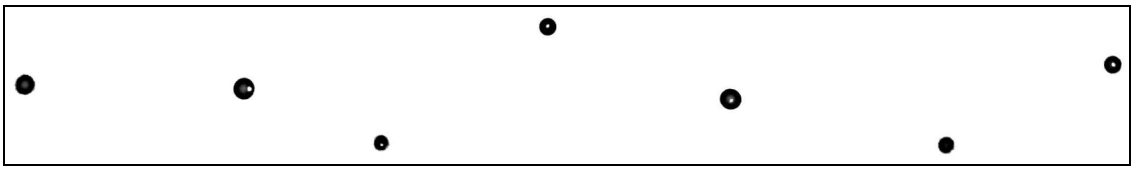

Figure 153: Stream of droplets produced by the spinning slotted disc.

It can be seen that this achieved the required increased spacing between the droplets, but at the expense of the uniformity of droplet size, which was an important requirement for determining the drag forces on the droplet. This was achieved from measuring the droplet acceleration, but the method used for this could not simultaneously measure the

droplet size and depended on having consistent size droplets from the droplet generator.

The average mass and volume of the droplets could, however, be determined by collecting and weighing the droplet produced over a given time. Since the droplets were produced at a known frequency, determined by the slots on the disc and speed of the motor, the droplet Volume Mean Diameter (VMD) could be determined, so the average mass and volume of the droplets were known.

This enabled the required measurements to be made, but due to the variability of the droplet size this produced a similar and unwanted variability in the experimental results.

Since time and resources did not allow for any further development of the droplet generator, the spinning disc method was adopted to provide the experimental validation of the predicted drag forces on the distorted droplets.

Improving the droplet generation, using the electrostatic method to remove surplus droplets, was seen as a primary issue for any future droplet research.

Using the spinning disk droplet generator

The droplet generator was mounted inside the plenum chamber in front of the tunnel entry, as shown Figure 154, to inject the stream of droplets into the entrance of the wind tunnel.

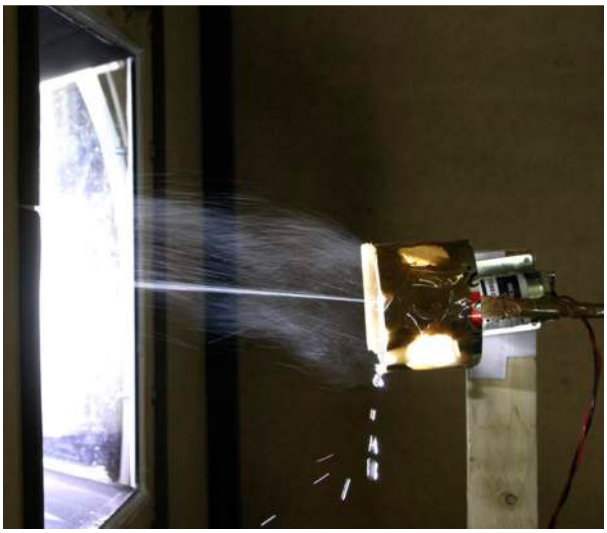

Figure 154: Spinning slotted disc droplet generator

Most of the surplus spray was caught by the guard around the slotted disk and drained into a receptacle below. There was, however, a lot of fine spray carried into the wind tunnel by the airflow. Fortunately most of this did not interfere with the main stream of droplets and was generally too fine to affect the experimental measurements.

The droplet generator did represent an appreciable disturbance to the airflow entering the tunnel. It was, however, not possible to use the honeycomb flow straightener over the tunnel entry, since the droplet stream and fine spray accumulated on this, and blocked many of the honeycomb cells, so producing a more significant disturbance to the airflow. Hence the disturbance from the droplet generator was tolerated, but the main effect of this was just to increase the dispersion of the droplet stream, due to the additional turbulence.

Chapter 13: Instrumentation to measure Droplet Velocity and Acceleration

Introduction

A primary objective of the research was to experimentally determine the drag properties of distorted droplets. The method adopted was to measure the speed and acceleration of droplets with calibrated size and mass, from which the acceleration force and hence drag coefficient could be determined.

There were a number of established ways of measuring droplet velocity, all of which, in some way, depended on determining the time and related distance travelled by a droplet. It appeared to be much more difficult to determine the acceleration, since this required determining the change in velocity over some time or distance. Since the velocity would only change by a small amount in the available time or distance, it was potentially difficult to resolve the acceleration with a satisfactory level of accuracy.

In order to measure acceleration this required knowing the time and location of the droplet for at least three points. For this research three points were arranged to be in a straight line, so that only linear acceleration, or deceleration, needed to be considered.

The mathematical analysis for this and the likely errors are discussed in Chapter 14. That is for both constant acceleration and a constant rate of change of acceleration, or jerk. The method could not determine the jerk, unless at least four points in time and space were determined. It was, however, possible to determine the jerk by other means, such as from the simulation or the air velocity gradient, so that the resulting acceleration errors due to the jerk could be assessed. This error was typically about 0.3%.

This chapter considers the practicalities of the instrumentation hardware and how the measurements were made.

The Methods used

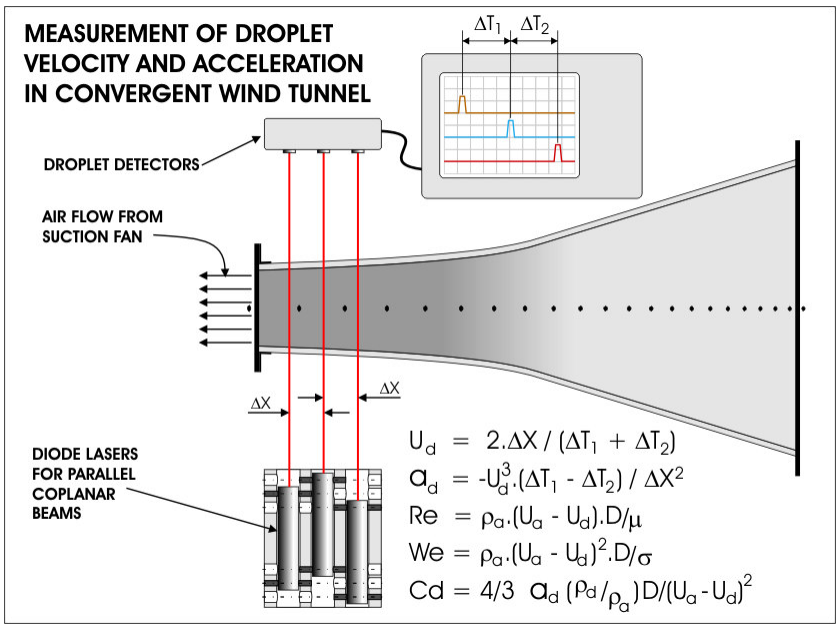

Figure 155: Arrangement for measurement of droplet velocity and acceleration

The method used in this research to determine the time and location of droplets was to

record when the droplets intercepted three parallel coplanar laser beams. The arrangement for this is shown in Figure 155. As a droplet cut each of the three beams in turn, this produced three electrical pulses from the photo detectors which were recorded on a data logger. In this case a digital oscilloscope was used, which could then transfer the signals to a computer for subsequent analysis.

The Diode Laser Unit

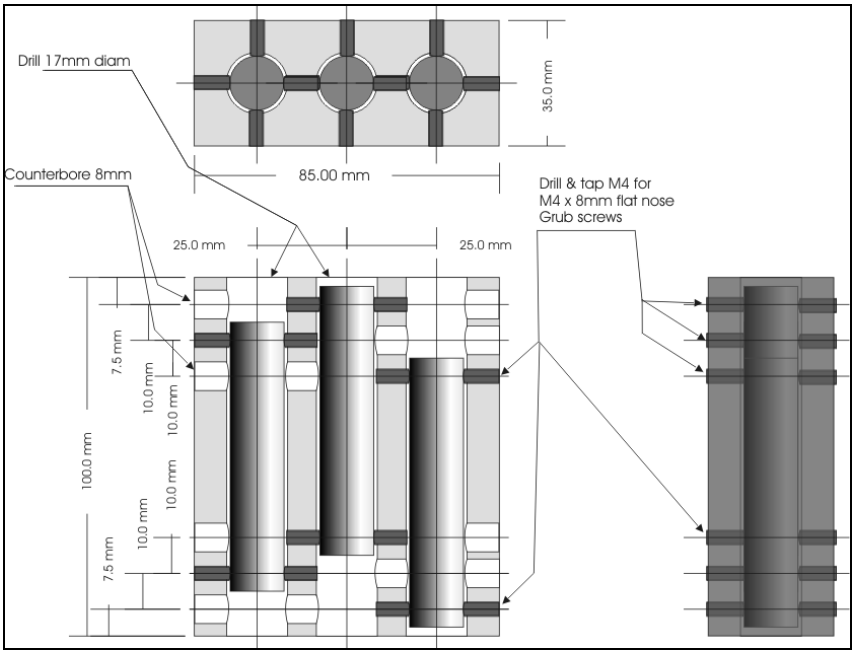

Figure 156: Triple laser mounting block

The three diode lasers were mounted in a solid metal block, as shown in Figure 156. Each end of the lasers was supported by four flat-point grub screws, to allow fine adjustment of the laser position and direction. Figure 157 shows the dimensions and a photograph for one of the 1mW diode lasers used.

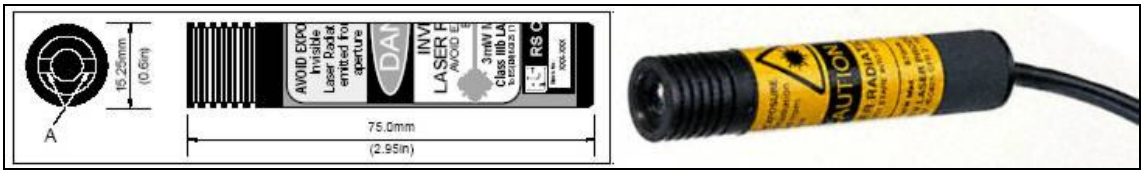

Figure 157: Dimensions and photograph of 1mW diode laser units

The Laser characteristics were;

Output power	1 mW
Beam colour	Red (670nm)
Minimum beam diameter	100µm
Supply volts	8V
Length and diameter	75mm by 15mm

A critical issue was the symmetry of the spacing between the laser beams, which required careful alignment of the beams. For this the laser measuring unit was fixed to the bed of a digital milling machine, as shown in Figure 158. After focussing the beams mid way between the lasers and photo detectors, they were shone across the corner of a target plate, shown clamped in the drill chuck, lower right inset of Figure 158.

Figure 158: Alignment of diode lasers on milling machine bed

The machine bed was then adjusted for each beam in turn to determine and adjust the spacing and alignment of the beams with the use of the digital readout of the milling machine. In this the beam was shone across the horizontal, or vertical, edge of the target corner, to achieve vertical and horizontal alignment. When the output voltage from the photo detectors was mid range, it was assumed that the centre of the laser beam was on the edge of the target. The beams were adjusted to have a spacing of 25mm, to pass through a straight line and come to focus at about 100μm diameter, half way between the laser block and the photo detectors.

The alignment could only be achieved to within about 10μm. Analysis of discrepancies in the laser beam alignment is discussed in Chapter 14, however when the acceleration, **a**, is near constant, the result is given as;

$$\mathbf{a} = (2.x/t^2).\beta.(1 - \alpha/\beta) / (1 - \beta^2)$$

where

α	=	$(x_1 - x_2) / (x_1 + x_2)$	asymmetry of beam spacing
β	=	$(t_1 - t_2) / (t_1 + t_2)$	asymmetry of the time intervals
x	=	$(x_1 + x_2)/2$	average spacing between the laser beams
t	=	$(t_1 + t_2)/2$	average time interval between detections

Typically β was found to be around 0.05, or 5% to 7%. Hence if the acceleration was to be determined to an accuracy of 2%, without being affected by the beam asymmetry, then α had to be less than 0.1%. Given a beam spacing of 25mm this required a difference between the beam spacing of less than 50μm. Hence the middle beam had to be no more than 25μm off-centre. This requirement was readily met with the alignment.

Figure 159: Arrangement for supporting and inverting the diode laser block.

As a further precaution, the laser beam block was made invertible, as shown in Figure

159. Hence any errors caused by indeterminate beam spacing asymmetry with the diode block in the normal orientation, shown left if Figure 159, would be cancelled by repeating measurements, for the same conditions, with the laser block inverted, shown centre.

To ensure that the laser block could be accurately aligned, repeatedly inverted and quickly relocated to exactly to same position, it was kinematically constrained against 6 location points, 5 of which were adjustable screws, as shown right in Figure 159.

Photo Detector unit

The laser beam photo detector unit consisted of three photo diodes on the front of the mounting box, as shown left in Figure 160. The fixing of these allowed the position of each photo detector to be moved a few mm in either direction and then clamped in place. The circuitry, shown in the centre, just consisted of a load resistor in series with the photo detector, followed by an integrated high-frequency buffer amplifier.

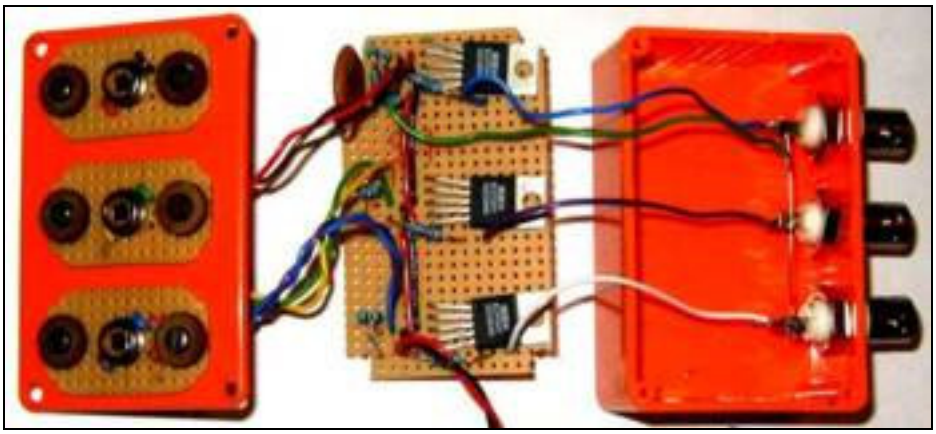

Figure 160: Photograph of interior of photo detector unit.

To obtain a predictable and repeatable condition approximating to droplet interception of the laser beam the photo detectors were evaluated on a test rig, shown left in Figure 161, in which a whirling wire attached to a motor shaft represented the passing droplets.

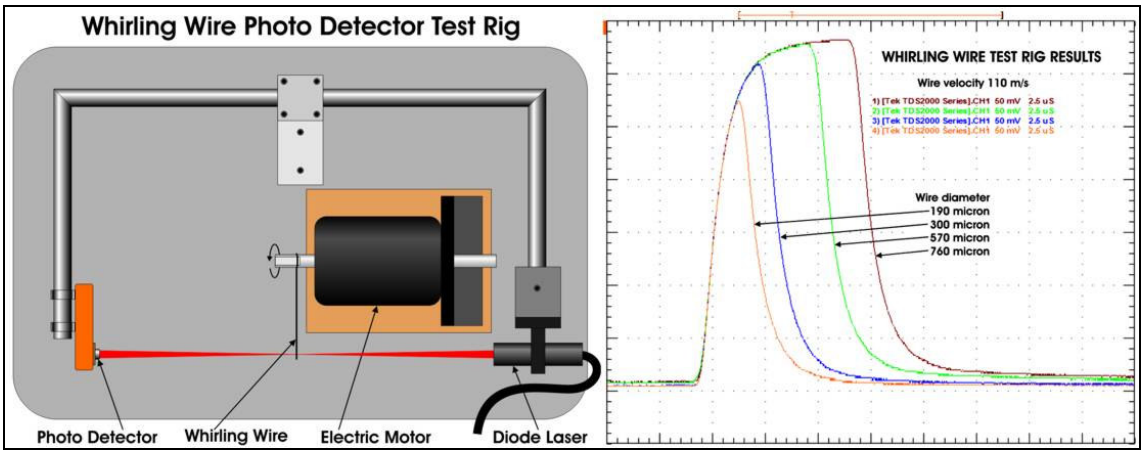

Figure 161: Diagram and results of the Whirling Wire test rig

The speed of the motor was adjusted so that the wire intercepted the laser beam at a velocity of 110m/s. Four wire sizes were used, 190, 300 570 and 760µm. The results of these are shown right in Figure 161, with a time scale of 2.5µs/div. It can be seen that all the wire produced measurable signals, with a rise/fall time of around 1µs. For the test

conditions the occlusion time for the 100µm diameter beam was about 1µs.

More elaborate photo detector circuits were considered, to achieve a faster rise/fall time, but, since the rise time was in any case limited to 1µs by the occlusion time of the laser beam at a wire velocity of 100m/s, there was no advantage in further improvements to the circuit response, so that was not pursued further. In practice the droplet velocities being measured were well below 100m/s, which further increased the occlusion time.

Example Measurement Results

Figure 162 show a typical result from the laser beam instrument. The left shows the original signal after normalisation to a zero origin and unity amplitude. There was a significant reduction in the time intervals between the pulses due to droplet acceleration.

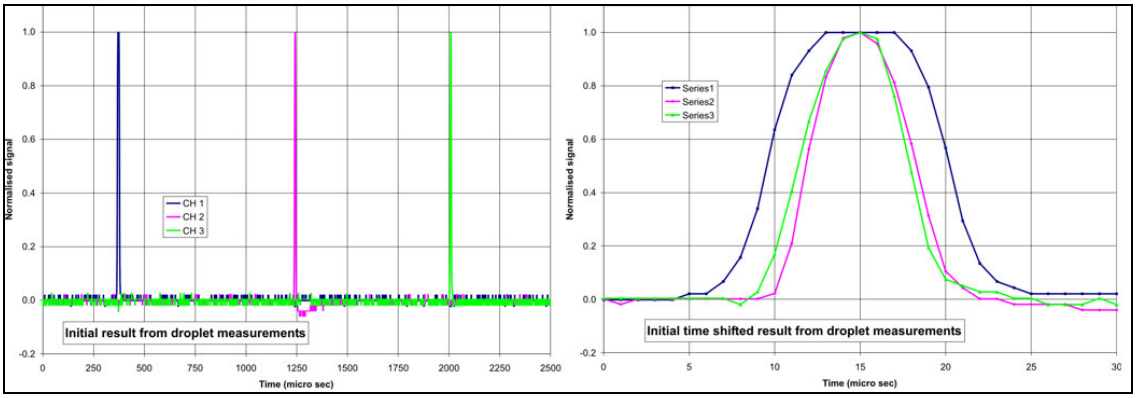

Figure 162: Typical signals from the droplet measurement

The right of Figure 162 shows the pulses against an expanded time scale after they are superimposed on each other. It is worth noting that the first pulse was significantly wider than the other two, which was believed to be due to the droplet intercepting the laser beam more completely than the other two beams.

The time at which the pulse occurred was taken as the average of the time the leading edge and trailing edge of the pulse were at 50% of the pulse height. Typically this could determine the pulse timing to 0.1µs. During the measurements the data recorded with the digital oscilloscope was manually selected to ensure it was an adequately clean recording of a single droplet. It was possible for the pulses to be produced by different droplets, but the chances of this producing just the three clean pulses with the anticipated spacing was remote. Each measurement was in any case repeated many times to ensure the measured values were consistent. In practice the primary difficultly was the variability of droplet size, which is considered in Chapter 12.

Each set of data from the oscilloscope was manually downloaded to files in the computer using software supplied with the oscilloscope. A computer program was written to analyse the data from the oscilloscope.

For Figure 162 the time increment between the 1st and 2nd pulses was 870µs and that between the 2nd and 3rd pulses was 767µs. This gave an average time interval of 818.5ms over 25mm and value for β of 6.29%.

The results from this were;

$$U = (x/t).(1 + \beta^2) / (1 - \beta^2)$$
$$= 25\text{mm} / 818.5\mu\text{s} \times 1.008 = 1.008 \times 30.54 \text{ m/s}$$

$= \mathbf{30.79\ m/s}$

$a = (2.\beta.x/t^2) / (1-\beta^2)$
$= (2 \times .0629 \times 25mm/818.5\mu s^2)/0.996$
$= 1.004 \times 4695.9\ m/s^2$
$= \mathbf{4714.8\ m/s^2 = 480.6g}$

Figure 163 shows another typical result obtained during the measurements. The resulting data file generated is given at the end of this chapter, with the data points up to 15µs either side of the pulse centre. This also used the data for the fan speed to determine the air speed and calculate the conditions for the droplet, such as Reynolds, Weber and Bond number, together with the drag coefficient. The result of this was;

Re = 580.1, We = 5.18, Bo = 2.41, Cd = 0.620

An interesting issue with this particular data was that the second pulse was much wider than the other two. From this result the droplet velocity was determined to be 30.7m/s and the 2nd pulse was 11.9µs, giving a droplet width of 365µm, which was more than the anticipated droplet size of 250µm. This and the flat top of the pulse indicate that two droplets were simultaneously recorded by the 2nd pulse. At the time no filters were included in the data analysis to detect and possibly reject such recordings, which was a limitation of the analysis, so they were included in the data set. It is estimated that in this particular case this could have introduced up to a 2µs timing error, for the 2nd pulse which could have introduce about a 6% acceleration error into this particular result.

In practice the main source of discrepancy was the indeterminate variation in droplet size and the overlap of droplets passing through the detector which could give false readings. As a result the measurement of droplet velocity and acceleration were not able to achieve the intended accuracy, but they did provide sufficient accuracy to resolve the principal effects of interest, as discussed in Chapters 1 and 5.

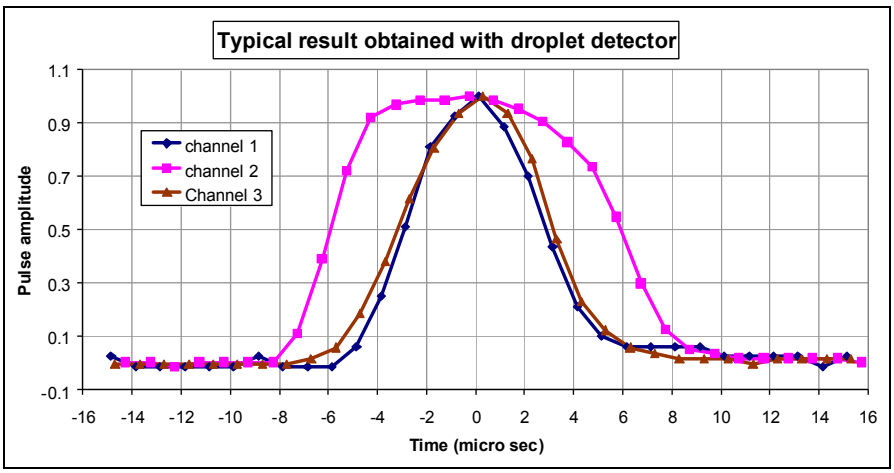

Figure 163: Typical result obtained with droplet detector.

A further example of the results is given in Figure 164. This was obtained with double the fan speed of Figure 163. This gave an air velocity of 136m/s, droplet velocity of 73.7 m/s and droplet acceleration of 20,293 m/s^2, or 2069g.

The resulting droplet conditions were;

Re = 966, We = 14.7, Bo = 17.4, Cd = 1.58

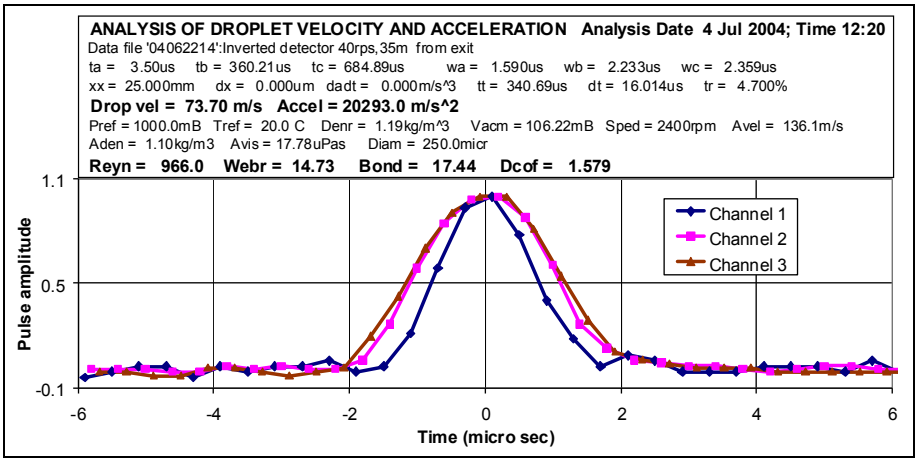

Figure 164: Measured droplet characteristics at high velocity.

Figure 165 also shows results for similar conditions to those in Figure 164.

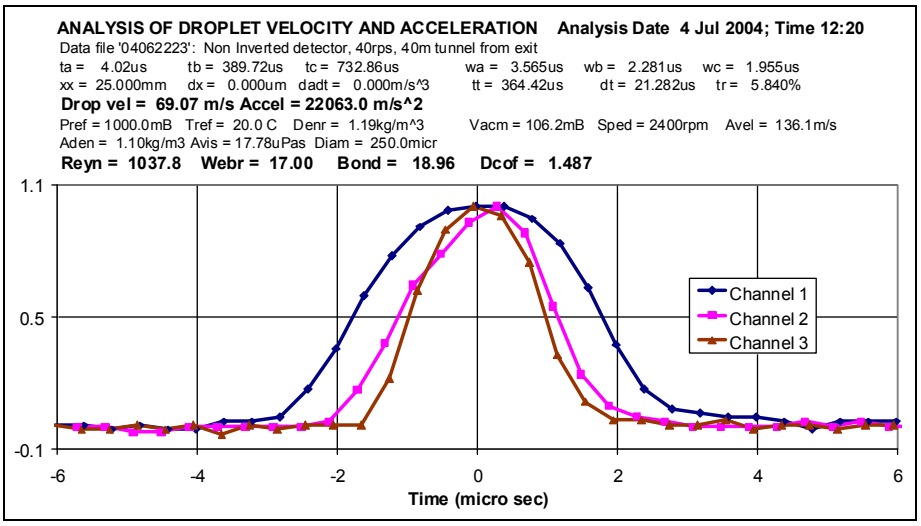

Figure 165: Further result at high droplet velocity

Typical result file from the droplet measurement

```
ANALYSIS OF DROPLET VELOCITY AND ACCELERATION
Analysis Date  6 Jul 2004; Time 22:47
Data file '04070660':Inverted N=20rps X=40mm from exit
  T=23C Pa=1009.2 Trig Ch 1 slotted disk drop generator

ta =   -0.14us     tb =  847.26us     tc = 1633.70us
wa =   5.810us     wb =  11.865us     wc =   6.375us
xx =  25.000mm     dx =   0.000um   dadt =   0.000m/s^3
tt =  816.92us     dt =  30.484us     tr =   3.732%

Drop vel =  30.69 m/s Accel =  2799.7 m/s^2

Pref = 1000.0mB   Tref =  20.0 C    Denr =  1.19kg/m^3
Vacm =  26.19mB   Sped = 1200rpm    Avel =   66.5m/s
Aden =  1.17kg/m3 Avis = 18.10uPas  Diam =  250.0micr

Reyn =   580.1    Webr =   5.18     Bond =    2.41
We^2/Bo = 11.14   Dcof =   0.620
```

	Channel 1		Channel 2		Channel 3	
	Relative Time/us	Normlsd Signal	Relative Time/us	Normlsd Signal	Relative Time/us	Normlsd Signal
0	-14.857	0.0251	-14.261	0.0031	-14.698	-0.0047
1	-13.857	-0.0124	-13.261	0.0031	-13.697	-0.0047
2	-12.857	-0.0124	-12.261	-0.0125	-12.698	-0.0047
3	-11.857	-0.0124	-11.261	0.0031	-11.697	-0.0047
4	-10.857	-0.0124	-10.261	0.0031	-10.698	-0.0047
5	-9.857	-0.0124	-9.261	0.0031	-9.698	-0.0047
6	-8.857	0.0251	-8.261	0.0031	-8.698	-0.0047
7	-7.857	-0.0124	-7.261	0.1121	-7.698	-0.0047
8	-6.857	-0.0124	-6.261	0.3925	-6.698	0.0167
9	-5.857	-0.0124	-5.261	0.7196	-5.698	0.0594
10	-4.857	0.0626	-4.261	0.9221	-4.698	0.1877
11	-3.857	0.2501	-3.261	0.9688	-3.698	0.3801
12	-2.857	0.5126	-2.261	0.9844	-2.698	0.6152
13	-1.857	0.8125	-1.261	0.9844	-1.698	0.8076
14	-0.857	0.9250	-0.261	1.0000	-0.698	0.9359
15	0.143	1.0000	0.739	0.9844	0.302	1.0000
16	1.143	0.8875	1.739	0.9533	1.302	0.9359
17	2.143	0.7000	2.739	0.9065	2.302	0.7649
18	3.143	0.4376	3.739	0.8287	3.302	0.4656
19	4.143	0.2126	4.739	0.7352	4.302	0.2304
20	5.143	0.1001	5.739	0.5483	5.302	0.1236
21	6.143	0.0626	6.739	0.2991	6.302	0.0594
22	7.143	0.0626	7.739	0.1277	7.303	0.0381
23	8.143	0.0626	8.739	0.0498	8.302	0.0167
24	9.143	0.0626	9.739	0.0343	9.302	0.0167
25	10.143	0.0251	10.739	0.0187	10.302	0.0167
26	11.143	0.0251	11.739	0.0187	11.302	-0.0047
27	12.143	0.0251	12.739	0.0187	12.302	0.0167
28	13.143	0.0251	13.739	0.0187	13.302	0.0167
29	14.143	-0.0124	14.739	0.0187	14.302	0.0167
30	15.143	0.0251	15.739	0.0031	15.302	0.0167

Chapter 14: Derivation for Determining Droplet Velocity and Acceleration

To experimentally determine the drag characteristics of a droplet in free-flight it was necessary to know its velocity, relative to the surrounding air, and its acceleration. Then knowing the size, mass and surface tension of the droplet and properties of the surrounding air, the drag parameters for the droplet could be determined.

The average droplet velocity over an interval can be readily determined by measuring the distance travelled in a given time, or the time to travel a given distance. This can be achieved by various methods, but the one used in this investigation was to measure the time at which the droplet interrupted parallel coplanar laser beams, perpendicular to the droplet path, in this case with a spacing of 25mm.

At its simplest the average velocity between two points is the distance between them divided by the time to travel between them. If the distance between the points is 'x' and the transit time is 't', then the average velocity, 'U', is given as; $\mathbf{U = x / t}$

With 25mm spacing to an accuracy of 0.1mm and a timing accuracy of 2µs, for 50m/s, this would achieve an accuracy of better than 1%.

Where the velocity remains reasonably constant during the measuring interval these requirements can readily be met with two parallel laser beams that are perpendicular to, and intercept the path of, the droplets. Electronic signals from photo detectors for the laser beams then provide the timing measurement to determine the droplet velocity.

Where the velocity of the droplet varied significantly within the measuring interval, then it was necessary to be more specific about the location within the interval to which the measurement applies and then determine any corrections that may be necessary.

Droplet Acceleration Measurement

The measurement of droplet acceleration was much more difficult and this was believed to be one of the main reasons why there was so little good data on the drag characteristics of small distorted droplets. The only situation in which the body force was easy to determine accurately was for free-falling droplets at terminal velocity in 1g gravity, which required the use of much larger droplets.

The acceleration of a droplet could be determined by knowing its location at three moments in time. In this the change in velocity between the first and second point and the second and third point could be used to compute the acceleration.

If measurements were taken at three equally spaced time intervals along a straight line, such as obtained from video images, then a simple central differencing method of the distance 'x' could be used to obtain the velocity and acceleration.

Velocity	U_0	=	$dx/dt = (X_3 - X_1) / 2.\Delta T$
Acceleration	a	=	$d_2x/dt^2 = (((X_3 - X_2) - (X_2 - X_1)) / \Delta T^2$
where	ΔT	=	$(T_3 - T_1) / 2 = T_3 - T_2 = T_2 - T_1$

and X_1, X_2 & X_3 are the positions of the droplets at the recorded times of T_1, T_2 & T_3.

To simplify the algebra, the following substitutions were made;

$$x_1 = X_2 - X_1 = x + \Delta x = x.(1 + \alpha)$$
$$x_2 = X_3 - X_2 = x - \Delta x = x.(1 - \alpha)$$

$$t_1 = T_2 - T_1 = t + \Delta t = t.(1 + \beta)$$
$$t_2 = T_3 - T_2 = t - \Delta t = t.(1 - \beta)$$

Hence $x = (x_1 + x_2) / 2 = (X_3 - X_1) / 2$

and $t = (t_1 + t_2) / 2 = (T_3 - T_1) / 2$

$$\alpha = (x_1 - x_2) / 2.x = ((X_2 - X_1) - (X_3 - X_2))/(X_3 - X_1)$$
$$= -(X_3 - 2.X_2 + X_1) / (X_3 - X_1) \quad (1)$$
$$\beta = (t_1 - t_2) / 2.t = ((T_2 - T_1) - (T_3 - T_2))/(T_3 - T_1)$$
$$= -(T_3 - 2.T_2 + T_1) / (T_3 - T_1) \quad (2)$$

If $x_1 = x_2$, $\alpha = 0$

If $t_1 = t_2$, $\beta = 0$

For equal time intervals, with $\beta = 0$, we obtain;

$$\mathbf{U_0 = x / t} \quad (3)$$
$$\mathbf{a = -2.\ \alpha.x/t^2} \quad (4)$$

In practice it was simpler to have two equal distance intervals, $\alpha = 0$, over which to measure the time intervals. From this one could directly determine the second derivative of time with respect to distance

Hence $d_2t/dx^2 = ((T_3 - T_2) - (T_2 - T_1)) / X^2$
$$= (t_2 - t_1)/x^2$$
$$= \mathbf{-2.\ \beta.t/x^2} \quad (5)$$

However $a = d_2x/dt^2$ (acceleration)
$$= d/dt.(dx/dt) = d/dx.((dt/dx)^{-1}).(dx/dt)$$
$$= -d_2t/dx^2\ ((dt/dx)^{-2}).(dx/dt)$$
$$= -d_2t/dx^2\ .(dx/dt)^3 = -d_2t/dx^2.U_0^3$$
$$\mathbf{a = 2.U_0^3.\beta.t/x^2} \quad (6)$$
$$= 2.(x/t)^3.\beta.t/x^2$$

Thus $\mathbf{a = 2.\beta.x/t^2}$ (7)

The preceding simple analysis determined the droplet velocity and acceleration either with constant time increments, $\beta = 0$, or constant distant intervals, $\alpha = 0$.

If the values of β was small, < 10%, it could be shown that the two results above could be combined to give the acceleration, with an error of less than 1%, providing the acceleration was constant over the measuring interval.

Thus $\mathbf{a = 2.(\beta - \alpha).x/t^2}$ (8)
$$= 2.\beta.(1 - \alpha/\beta).x/t^2$$

This allowed for both the time intervals and the distance interval to be unequal. We see from this, however, that if the effect of unequal distance intervals was to be negligible, < 1%, this required α to be less than 1% of β, or $\alpha/\beta < 0.01$.

More detailed acceleration analysis

The preceding simplified analysis provides a basic method of computing the droplet velocity and acceleration from measuring the time intervals to travel between three nearly equispaced points along the straight path of a droplet.

That analysis neglected two intrinsic sources of error;

1. That due to large differences between the two measured distance and time intervals
2. That due to a significant change in acceleration in the measuring interval.

The diagram below, Figure 166, shows a curve of droplet velocity against time. Hence the area under the curve is the distance travelled by the droplet.

Two situations are considered;

1. The linear curve for constant acceleration
2. The parabolic curve for a constant rate of increase in acceleration, or constant jerk.

In either case the area x_1 under the left-hand-side of the curve give the distance between the 1st and 2nd laser beams, while the area under the right-hand-side of the curve is the distance between the 2nd and 3rd laser beam. The mid location is that at which the velocity U_0, shown as V_0 in the diagram, is to be determined.

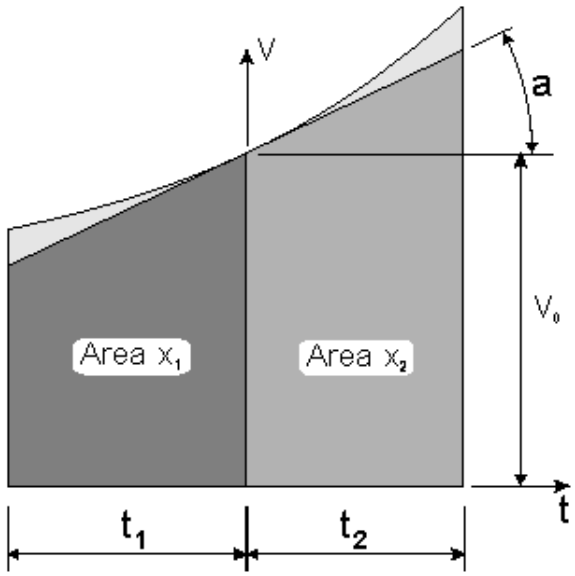

Figure 166: Velocity vs. Time diagram for droplet

Constant Acceleration

For constant acceleration with time, from Figure 166 we obtain;

$$\mathbf{x_1 = U_0.t_1 - \tfrac{1}{2}.a.t_1^2} \qquad (9)$$

$$\mathbf{x_2 = U_0.t_2 + \tfrac{1}{2}.a.t_2^2} \qquad (10)$$

As before, let

$$x_1 = x + \Delta x = x.(1 + \alpha)$$
$$x_2 = x - \Delta x = x.(1 - \alpha)$$
$$t_1 = t + \Delta t = t.(1 + \beta)$$
$$t_2 = t - \Delta t = t.(1 - \beta)$$

where $\alpha = \Delta x/x$ and $\beta = \Delta t/t$

Hence
$$x_1+x_2 = x.(1+\alpha) + x.(1-\alpha) = 2.x$$
$$x_1-x_2 = x.(1+\alpha) - x.(1-\alpha) = 2.x.\alpha$$

Thus
$$\alpha = (x_1 - x_2) / (x_1 + x_2)$$
$$t_1+t_2 = t.(1+\beta) + t.(1-\beta) = 2.t$$
$$t_1-t_2 = t.(1+\beta) - t.(1-\beta) = 2.t.\beta$$

Hence
$$\beta = (t_1 - t_2) / (t_1 + t_2) \qquad (11)$$
$$t_1^2+t_2^2 = t^2.(1+2.\beta+\beta^2) + t^2(1-2.\beta+\beta^2) = 2.t^2.(1+\beta^2)$$
$$t_1^2-t_2^2 = t^2.(1+2.\beta+\beta^2) - t^2(1-2.\beta+\beta^2) = 4.t^2.\beta$$
$$x_1+x_2 = U_0.(t_1+t_2) - ½.a.(t_1^2 - t_2^2)$$
$$2.x = 2.U_0.t - 2.a.t^2.\beta$$

Hence
$$\boxed{\mathbf{U_0 = x/t + a.t.\beta}} \qquad (12)$$

Thus the droplet velocity calculated also depends on the droplet acceleration.

Also
$$x_1-x_2 = U_0.(t_1 - t_2) - ½.a.(t_1^2 + t_2^2)$$
$$2.x.\alpha = 2.U_0.t.\beta - a.t^2.(1+\beta^2)$$
$$a.t^2.(1+\beta^2) = 2.U_0.t.\beta - 2.x.\alpha$$
$$\mathbf{a = 2.(U_0.t.\beta - x.\alpha) / (t^2.(1+\beta^2))} \qquad (13)$$

but
$$a.t^2.(1+\beta^2) = 2.(x/t + a.t.\beta).t.\beta - 2.x.\alpha$$
$$= 2.x.\beta + 2.a.t^2.\beta^2 - 2.x.\alpha$$
$$a.t^2.((1+\beta^2) - 2.\beta^2) = 2.x.(\beta - \alpha)$$
$$a.t^2.(1-\beta^2) = 2.x.(\beta - \alpha)$$
$$\boxed{\mathbf{a = (2.x/t^2).(\beta - \alpha) / (1-\beta^2)}} \qquad (14)$$

We notice that this introduces a correction to the acceleration of $(1-\beta^2)$. Hence providing β is less than 10%, then the correction will be less than 1%.

Equating equations (13) and (14);
$$2.(U_0.t.\beta - x.\alpha) / (t^2.(1+\beta^2)) = (2.x/t^2).(\beta - \alpha) / (1-\beta^2) \qquad (15)$$
$$(U_0.t.\beta - x.\alpha) / (1+\beta^2) = x.(\beta - \alpha) / (1-\beta^2)$$
$$(U_0.t.\beta - x.\alpha).(1-\beta^2) = x.(\beta - \alpha).(1+\beta^2)$$
$$U_0.t.\beta.(1-\beta^2) - x.\alpha + x.\alpha.\beta^2 = x.\beta + x.\beta^3 - x.\alpha - x.\alpha.\beta^2$$
$$U_0.t.\beta.(1-\beta^2) = x.\beta + x.\beta^3 - x.\alpha.\beta^2 - x.\alpha.\beta^2$$
$$U_0.t.(1-\beta^2) = x.(1+\beta^2 - 2.\alpha.\beta)$$
$$\boxed{\mathbf{U_0 = (x/t).(1+\beta.(\beta - 2.\alpha))/(1-\beta^2)}} \qquad (16)$$

This introduces a correction to the droplet velocity of $(1+\beta^2.(1-2.\alpha/\beta))/(1-\beta^2)$. In practice the laser beams are constructed so that $\alpha/\beta < 0.01$, so the correction can be simplified to $(1+\beta^2)/(1-\beta^2)$. Hence for $\beta = 10\%$ introduces a velocity error of 2% if

the correction is not applied.

Constant rate of change of acceleration with time

In the preceding analysis it was assumed that the acceleration remained constant over the measuring interval.

In practice the droplet acceleration was not constant, but was increasing against time and distance. The question was how much the rate of change of acceleration affected the measured velocity and acceleration.

For constant rate of change of acceleration with time, or constant jerk, '**b**', from Figure 166 we obtain;

$$x_1 = U_0.t_1 - \tfrac{1}{2}.a.t_1^2 + {}^1/_6.b.t_1^3 \qquad (17)$$

$$x_2 = U_0.t_2 + \tfrac{1}{2}.a.t_2^2 + {}^1/_6.b.t_1^3 \qquad (18)$$

$$t_1^3 = t^3.(1 + 3.\beta + 3.\beta^2 + \beta^3)$$

$$t_2^3 = t^3.(1 - 3.\beta + 3.\beta^2 - \beta^3)$$

$$t_1^3+t_2^3 = 2.t^3.(1 + 3.\beta^2)$$

$$t_1^3-t_2^3 = 6.t^3.\beta(1 + {}^1/_3.\beta^2)$$

$$x_1+x_2 = U_0.(t_1 + t_2) - \tfrac{1}{2}.a.(t_1^2 - t_2^2) + {}^1/_6.b.(t_1^3 + t_1^3)$$

$$2.x = 2.U_0.t - 2.a.t^2.\beta + {}^2/_6.b.t^3.(1 + 3.(\beta^2)$$

Hence $U_0 = x/t + a.t.\beta - {}^1/_6.b.t^2.(1 + 3.\beta^2)$

$$\boxed{\mathbf{U_0 = x/t + a.t.\beta - {}^1/_6.b.t^2.(1 + 3.\beta^2)}} \qquad (19)$$

$$x_1-x_2 = U_0.(t_1 - t_2) - \tfrac{1}{2}.a.(t_1^2 + t_2^2) + {}^1/_6.b.(t_1^3 - t_1^3)$$

$$2.x.\alpha = 2.U_0.t.\beta - a.t^2.(1 + \beta^2) + b.t^3.\beta.(1 + {}^1/_3.\beta^2)$$

$$a.t^2.(1 + \beta^2) = 2.U_0.t.\beta - 2.t.x.\alpha + b.t^3.\beta.(1 + {}^1/_3.\beta^2)$$

$$a = 2.((U_0.t.\beta - x.\alpha)/t^2).(1+\beta^2)) + b.t.\beta.(1 + {}^1/_3.\beta^2)/(1 + \beta^2) \qquad (20)$$

$$a.t^2.(1 + \beta^2) = 2.(x/t + a.t.\beta - {}^1/_6.b.t^2.(1+3.\beta^2)).t.\beta - 2.\Delta x + b.t^2.t.\beta.(1+{}^1/_3.\beta^2)$$

$$a.t^2.(1 + \beta^2) = 2.(x/t + a.t.\beta).t.\beta - 2.x.\alpha + b.t^2.t.\beta.((1+{}^1/_3.\beta^2) - {}^1/_3.(1+ 3.\beta^2)$$

$$a.t^2.(1 + \beta^2 - 2.\beta^2) = 2.(x/t).t.\beta - 2.x.\alpha + {}^2/_3.b.t^3.\beta.(1- \beta^2)$$

$$a.t^2.(1 - \beta^2) = 2.x.(\beta - \alpha) + {}^2/_3.b.t^3.\beta.(1- \beta^2)$$

$$\boxed{\mathbf{a = (2.x/t^2).(\beta - \alpha)/(1- \beta^2) + 2.b.t.\beta/3}} \qquad (21)$$

The preceding analysis provides a direct solution for acceleration, **a,** which is calculated using equation (21). This value can then substituted into equation (19) to obtain $\mathbf{U_0}$.

Using a computer Mathematical package it was, however, shown that $\mathbf{U_0}$ could be directly calculated from:

$$\boxed{\mathbf{U_0 = (x/t).(1 + \beta.(\beta - 2.\alpha))/(1 - \beta^2) - b.t^2.(1 - \beta^2)/6}} \qquad (22)$$

We notice from (22) that if the effect of $\boldsymbol{\alpha}$, the offset of the central laser beam, is to be acceptably small, then $\boldsymbol{\alpha}$ must be much smaller than $\boldsymbol{\beta}$, since the result depends on $(\beta - 2.\alpha)$. Otherwise the value of $\boldsymbol{\alpha}$ must be known from calibration, which may be difficult to determine accurately.

Typically $\boldsymbol{\beta}$ will have a value of around 7%, so for 2% accuracy $\boldsymbol{\alpha}$ will need to have a value of less than 0.14%. In practice a value for $\boldsymbol{\alpha}$ of less than 0.1% was achieved.

The values of x_1 and x_2 could be interchanged, by inverting the block carrying the laser beams, so that the offset error would be cancelled out with the average of measurements for the normal orientation and then the inverted orientation for the same conditions.

The value of the rate of change of acceleration, **b**, cannot be determined from the timing measurements, so, if necessary, had to be obtained by some other means.

Given the drag coefficient for the droplet, the rate of change of velocity, or acceleration, of the air, and the acceleration of the droplet, then the rate of change of the acceleration could be evaluated. This would require an iterative loop, since the calculation of **b** would slightly change the computed drag and acceleration by a small amount.

The air acceleration could be determined from the air velocity at two points either side of the measuring position, or from the air velocity and the tunnel contraction rate.

Alternatively an adequate value for the rate of change of droplet acceleration could be obtained from the computer simulation for the droplet motion. In practice the simulation did not calculate this directly, but it could be adequately obtained by differencing adjacent values of droplet acceleration.

Typically $\boldsymbol{\beta}$ was less than 10%, so that $\boldsymbol{\beta^2}$ was less than 1%, hence the factor $\mathbf{(1-\beta^2)}$ would introduce less than 1% error.

Making the approximation $\mathbf{(1-\beta^2) = 1}$, we obtain;

$$\boxed{\mathbf{U_0 = x/t - b.t^2/6}} \qquad (23)$$

or

$$U_0 = x/t.(1 - b.t^3/6.x). \qquad (24)$$

$$\boxed{a = 2.\beta.((x/t^2).(1 - \alpha/\beta) + b.t/3)} \qquad (25)$$

If $\boldsymbol{\alpha << \beta}$, which it was likely to be, then;

$$a = 2.\beta.(x/t^2 + b.t/3) \qquad (26)$$

$$\mathbf{a = 2.\beta.x/t^2.(1 + b.t^3/3.x)} \qquad (27)$$

Hence the fractional acceleration error, $\boldsymbol{\varepsilon}$, due to the rate of change of acceleration is;

$$\varepsilon = b.t^3 / 3.x = b.t^2 / 3.U_0$$

For $\boldsymbol{\varepsilon} << 1$ $\quad U_0 = x/t$, or $t = x / U_0$

Hence $\quad \mathbf{\varepsilon = b.x^2 / 3.U_0^3}$ (28)

thus $\quad \mathbf{a = 2.\beta.x/t^2.(1 + \varepsilon)}$ (29)

and $\quad \mathbf{U_0 = x/t.(1 - \varepsilon/2)}$ (30)

Hence the correction for the droplet velocity due to the rate of change of acceleration, or jerk, would be half that required for the acceleration and in the opposite direction.

Chapter 15: Development of the Strobe Flash Light

Introduction

To understand the behaviour of the small droplets when distorted by strong aerodynamic forces it was necessary to obtain photographs and videos of this process.

Because of the small size of the droplets, down to 200µm, and their possible high velocity, up to 100m/s, it was necessary that the exposure time should be very short to keep motion blur to an acceptable level. The acceptable motion blur needed, however, to be balanced against the resolution of the imaging system, since there was no value in achieving a motion blur much less than the image resolution.

Greater resolution could be achieved by increasing the magnification of the imaging system, but that required more light, which was likely to require a longer flash. Hence there was a trade-off between image resolution and motion blur. The best compromise was considered to be when the motion blur was about equal to the image resolution.

The best resolution from the available camera and optical systems was about 5µm. Hence to achieve the equivalent motion blur at 100m/s required a flash duration of 50ns.

This could be achieved with a pulsed laser system, at least for a single-shot photograph, however such a lighting system was not obtainable because of its high cost.

It was known from experience with developing ink-jet printers that Light Emitting Diodes, or LEDs, were capable of very short flashes, down to a fraction of 1µs, but the issue was whether an LED could produce sufficient light from a single flash.

Where the event to be observed was precisely repetitive and could be back illuminated in silhouette then repeated weak flashes from a low-power LED could provide sufficient light over a small field of view, which could be viewed and photographed through a low power microscope, such as shown in Figure 167.

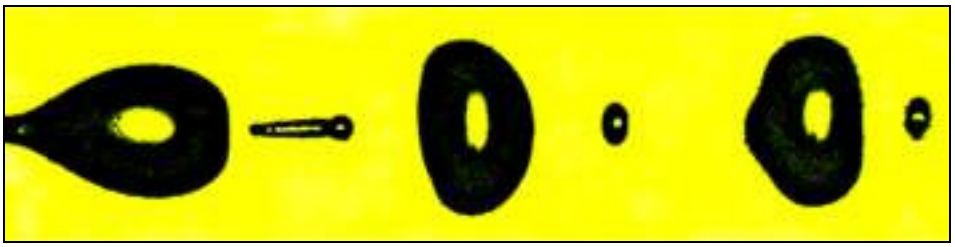

Figure 167: Droplet image obtained from strobe illumination with low-power LED

For this synchronizing pulses, from the signal generator used to drive the piezoelectric elements in the droplet generator, were use to trigger a pulse generator which then directly sent very short duration current pulses, < 1µs, through the LED.

The water droplets were transparent, however the light passing through the droplets was refracted away from the camera, so providing black droplets in silhouette against an illuminated background. Where, however, the opposite sides of the droplet were near parallel the light passed through the droplet to the camera to produce a bright spot.

This method worked well for droplets produced from a vibrating nozzle where the droplets were exactly repeatable with the flash synchronised with the nozzle vibration.

Images from a Single Flash

When viewing distorted high-velocity droplets in a wind tunnel the events were not repeatable because of turbulence, hence it was necessary to obtain each image with a single flash. The issue was whether enough illumination could be obtained and if the flash could be short enough to avoid motion blur.

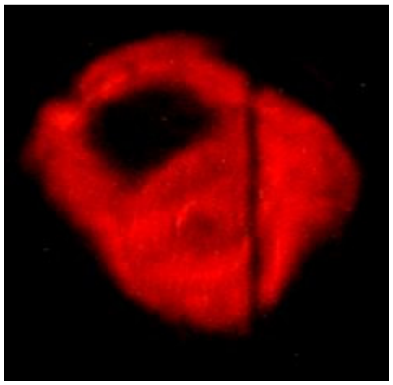

Figure 168: Initial wire image from a single LED flash

To determine if enough light could be produced, 100ns pulses were applied to a low-power LED via a high-frequency buffer amplifier. A wire of about 200µm diameter was placed in front of the LED and a compact digital camera was used to photograph this with a single flash, as shown in Figure 168. In this the wire can be seen from top to bottom, slightly right of centre. Hence this demonstrated that an LED could produce a recordable image from a single flash.

To determine if the flash could be short enough, the test arrangement on the left in Figure 169 was set up. In this a fine wire, about 200µm, was attached to the shaft of the small DC motor.

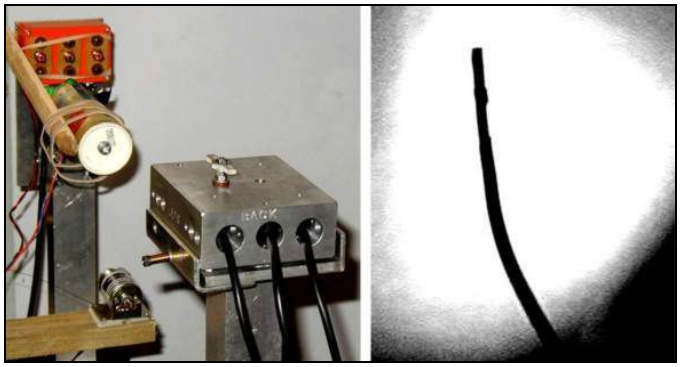

Figure 169: Test for evaluating LED response speed.

When the motor was running the wire had a tip velocity of about 100m/s. On each revolution this interrupted a laser beam and the resulting signal from the associated photo detector triggered a slightly delayed flash from the LED. Again using a standard compact digital camera the image on the right of Figure 169 was obtained from multiples flashes. This showed that the image of the wire travelling at 100m/s could be frozen.

These two tests demonstrated that the required flash duration and intensity from an LED were feasible given a suitable LED and a suitable electronic circuit to drive it.

To improve the light output and speed a high-power high-frequency MOSFET transistor was used as a current switch for a high-power LED. To enable the rapid supply of current these were closely connected to a 1µf capacitor, shown on the left in Figure 170.

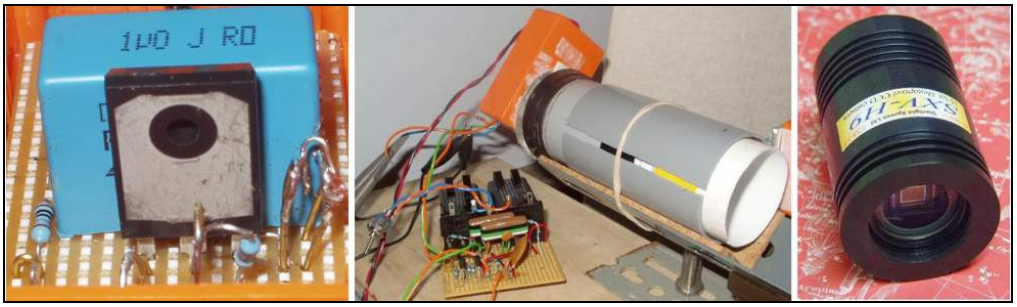

Figure 170: Prototype LED flash unit and Starlight Express astronomy camera

This circuit was driven from a high-frequency buffer amplifier and the LED was provided with a collimating lens, as shown in the centre of Figure 170.

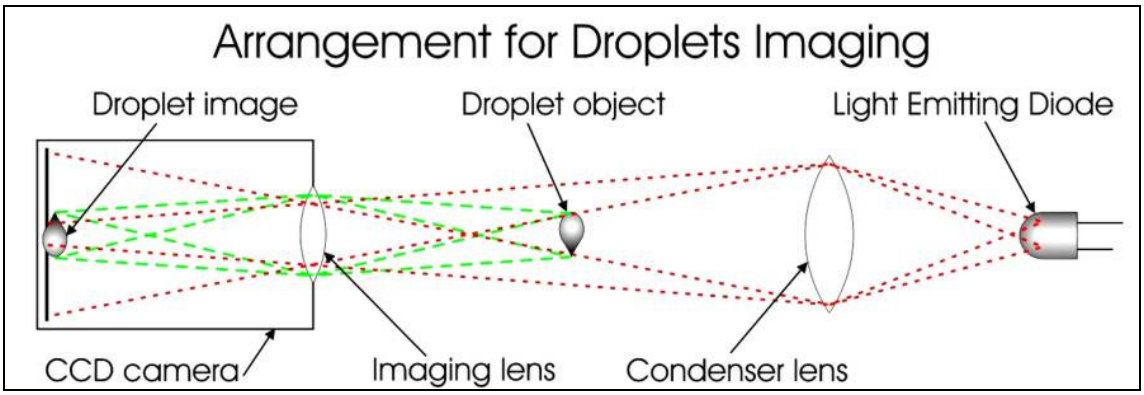

Figure 171: Optical arrangement of Droplet Imaging

To capture the maximum amount of light from the LED system and achieve uniform illumination, it was necessary to improve the optical system for the flash unit. The arrangement developed is shown in Figure 171. In this the image of the LED was focused onto the imaging lens of the camera. The smaller this image could be, the greater the depth of field. If the LED image was larger than the aperture of the imaging lens, then this would reduce the available illumination.

The image of the droplets was then focused onto the imaging sensor of the CCD camera. This was typically achieved with a 1 to 1 macro lens of around 105mm to 135mm focal length, with a maximum aperture ratio of F2.8, given a maximum imaging aperture of around 43mm.

The right of Figure 170 shows the astronomy camera, from Starlight Express, used for the imaging and the 1.6Mb imaging sensor array can be seen at the front of the camera.

The camera and flash unit were directly aligned with each other, as shown on the left in Figure 172. The camera was fitted with a 135mm F2.8 lens. As before, a wire of around 250µm was attached to the shaft of a small motor, top left of Figure 172 left, so that it passed between the camera and flash unit at a speed of 100m/s.

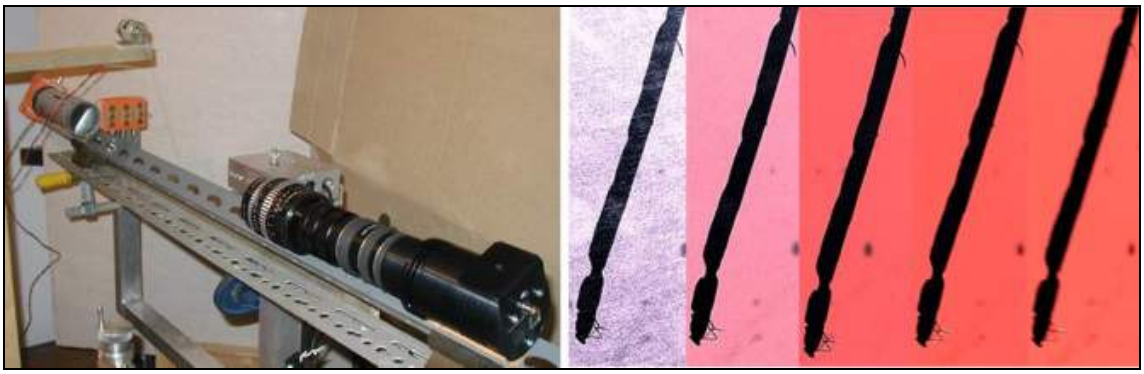

Figure 172: Test of LED flash unit and camera with resulting images at 100m/s.

On each revolution this wire interrupted a laser beam to trigger a slightly delayed flash from the LED.

In this case the camera exposure time was set so that only one flash was used to record each image and the results of this are shown on the right of Figure 172.

The images of the test wire in Figure 172 were, from left to right, for a flash duration of 50ns, 100ns, 200ns, 500ns and 1000ns. It can be seen that at 50ns the available light was only just enough to achieve an image, whilst at 500ns and 1000ns there was ample light, but also noticeable motion blur. The best images were obtained with 100ns and 200ns flashes, depending on the compromise between exposure and motion blur.

Improved LED Driver

The test circuits discussed above were sufficient to prove the principles, but were not a practical implementation. With the support of NASA an electronics engineer developed the circuit shown in Figure 173. This included the pulse generator, U1:B, and the pre-amplifier for the MOSFET switch, consisting of Q2, Q3 and Q4. A gating timer was also included, U1:A, to enable bursts of flash for a given period.

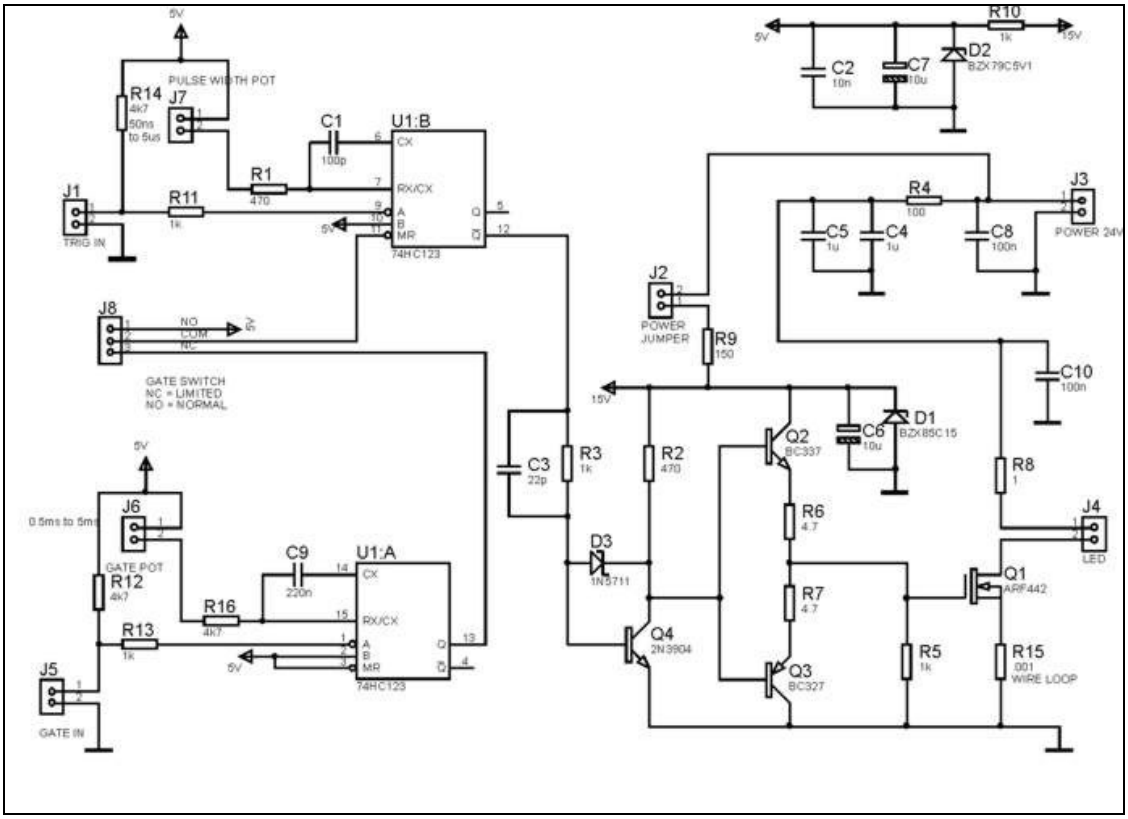

Figure 173: Circuit diagram for LED flash unit

The requirement was to achieve a current pulse of up to 15A with a rise and fall time of 25ns. With these criteria even a tiny inductance was a significant issue. A single loop of 0.6mm diameter wire 8cm long around a 20mm square has an inductance of 7nH/cm, or 55nH in total. To overcome this inductance required 33V, which required up to a 60V DC supply. Hence it was important to keep the wires of the current pulse loop, through the MOSFET, discharge capacitor, load resistor and LED, as short as possible.

Figure 174 shows the actual layout of the circuit and Figure 175 gives the physical position of the components and the practical interconnections.

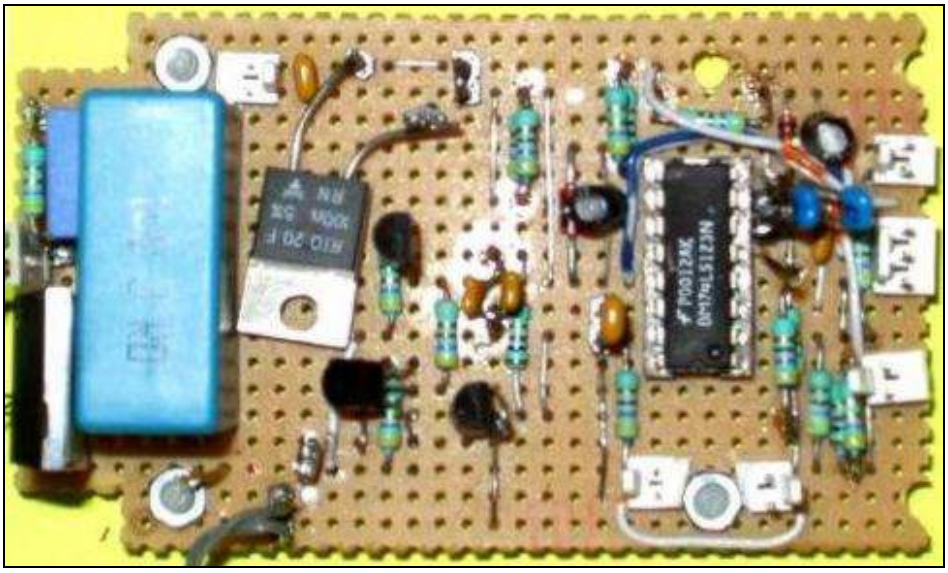

Figure 174: Circuit board layout

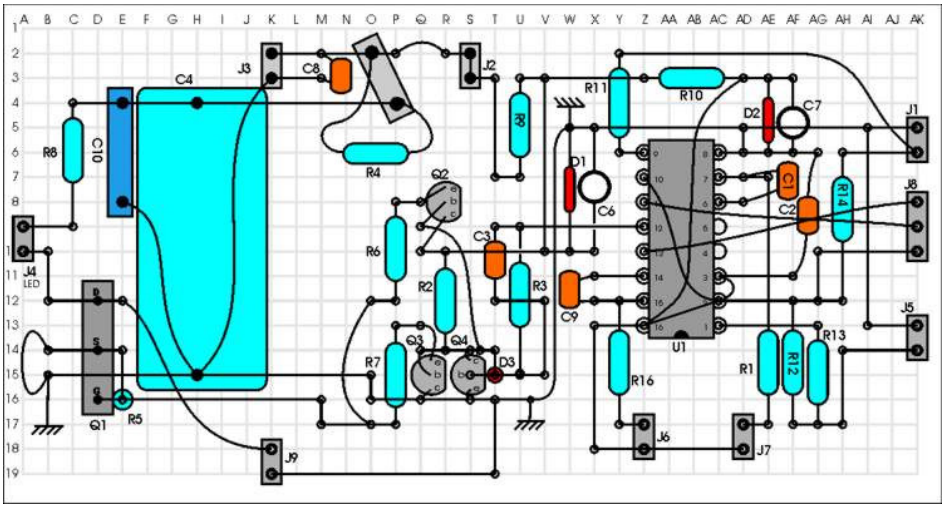

Figure 175: Component arrangement.

The left of Figure 176 shows the controls of the flash unit and the inputs required.

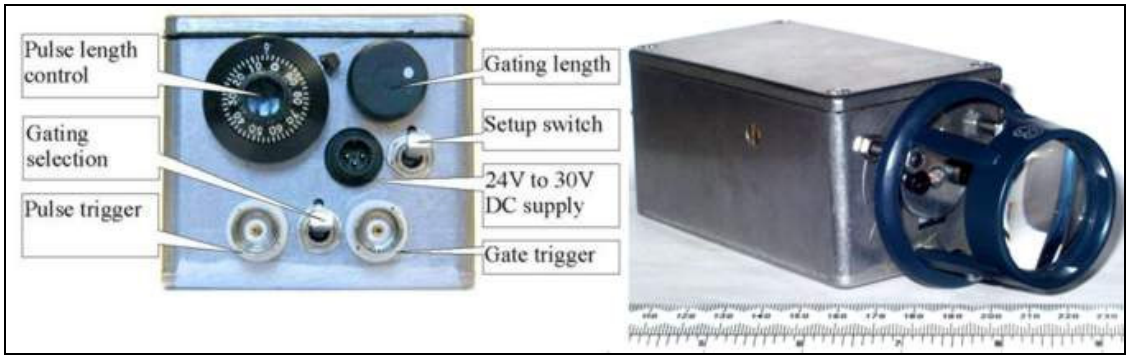

Figure 176: LED Flash unit, showing controls and collimation lens

The right of Figure 176 shows the unit fitted with a collimating lens. This was 35mm diameter by 35mm focal length. For this a high quality aspheric lens was used to achieve a large aperture ratio with uniform illumination.

The electronic performance of the circuit was measured using a high-frequency digital oscilloscope. The results of this are shown in Figure 177 for pulse durations of nominally 50ns, 100ns, 200ns and 400ns. The upper traces for the voltages across the LED were typically 18V to 20V. The lower traces show the voltages across a 2.2Ω resistor in series with the LED, with a peak current of up to 9Amps. Subsequently peak currents of up to 15Amps were achieved, with a 1Ω resistor in series with the LED and a 60V DC supply. This improved the quality of the 50ns pulses and enabled clear photographs to be obtained with a 50ns flash.

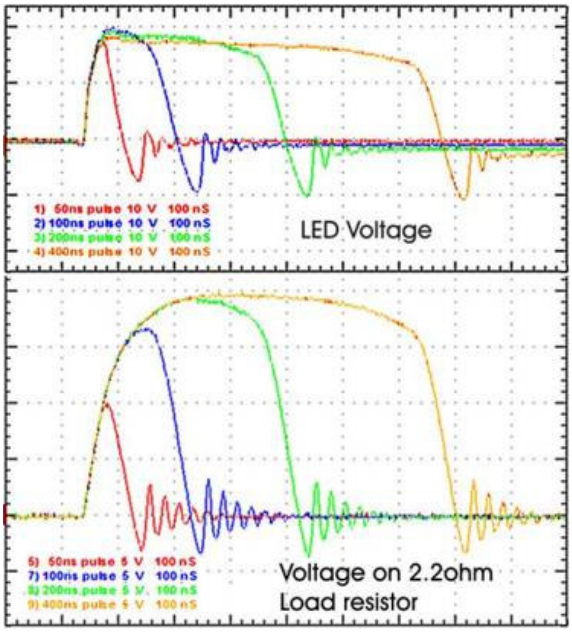

Figure 177: Response of LED driver circuit

To test the revised LED driver the whirling wire tests were repeated, as shown in Figure 178. It can be seen that this gave full illumination for all the time flash durations, down to 50ns. Some motion blur was noticed for a flash duration of 200ns and longer and was particularly noticeable of 500ns an longer.

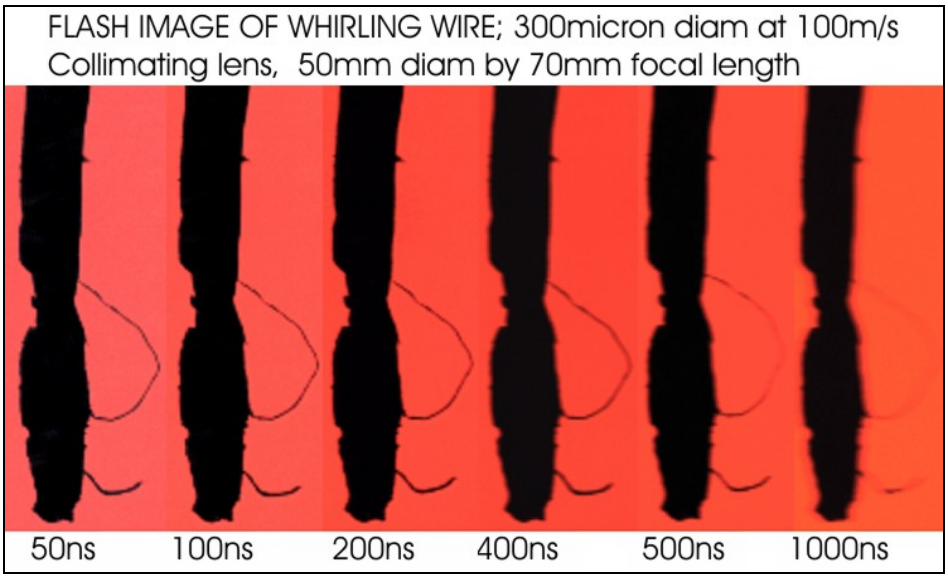

Figure 178: Whirling wire test at 100m/s with revised LED flash unit.

To achieve a larger field of view the flash unit was fitted with an aspheric lens of 80mm diameter by 80mm focal length, as shown in Figure 179.

This provided a larger field of view, but with a reduced light intensity.

Figure 179: LED flash unit with Collimating Lens

Use of LED flash unit with high-speed Video

An advantage of the LED flash unit was that, with appropriate design, it could be repeatedly flashed at a high frequency. The great advantage of this, compared to a continuous light source, was that it could be used to freeze motion and also, for a given power limit, the light intensity could be much higher for the short duration for which it was required.

For use with a high-speed video imaging the flashes had to be accurately synchronised with the camera. Providing the camera could output a suitable synchronisation pulses this was not a problem. One advantage of the LED light source was that it could respond almost instantaneously, within 50ns, compared to some other flash sources.

The LED flash unit was designed to operate up to 100kHz, although to achieve this required a reduction of the peak current through the LED and hence a reduction in the peak brightness of the flash.

A typical example of a high-speed video sequence, obtained with the LED flash and a Phantom 7 video camera, is shown in Figure 180. The incoming droplet was around 400μm and the frame rate was understood to be around 30,000 pictures per second.

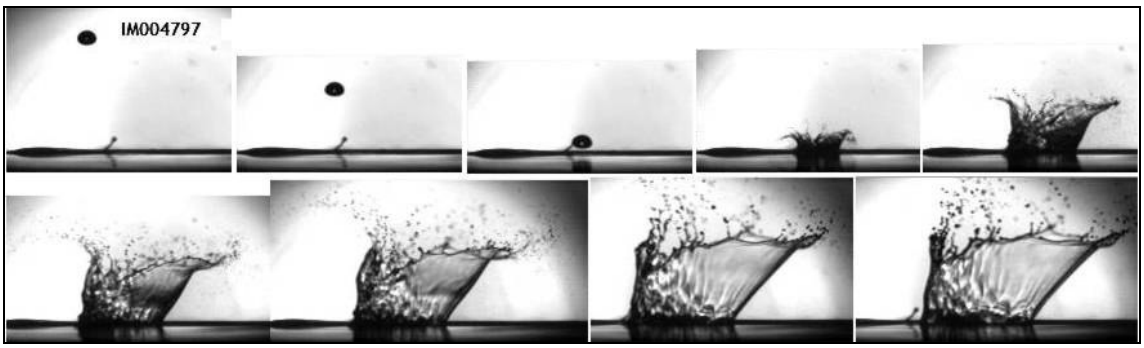

Figure 180: Example of high-speed video imaging with the LED strobe flash unit.

References, Bibliography and Literature

** - available, B - book, *B - have the book, B* - have extract of book, * - have seen or have extract, T-Thesis

1. ** **2005** **G. Luxford, PhD thesis, Cranfield University, "Experimental and modelling investigation of the deformation, drag and break-up of drizzle droplets subjected to strong aerodynamic forces".**
2. * 2005 R.E. Kregger, W.B. Wright, "The influence of Viscous Effects on Ice Accretion Prediction and Aerofoil Performance Predictions", AIAA-05-1373
3. * 2005 W.B. Wright, "Validation Results for LEWICE 3.0", AIAA-2005-1243
4. * 2005 M.G. Potapczuk, Dean Miller, R. Ide, J. Oldenburg, "Simulation of a Bimodal Large Droplet Icing Cloud in the NASA Icing Research Tunnel", AIAA-2005-0076
5. * 2005 Dean Miller, M.G. Potapczuk, "Preliminary Investigation of Ice Shape Sensitivity to Parameter Variation", AIAA-2005-0073
6. ** **Jan05** **G. Luxford, D. Hammond, P. Ivey, "Modelling, Imaging and Measurement of Distortion, Drag and Break-up of Aircraft-icing Droplets.", AIAA05-0071**
7. ** **Jan 05** **D. W. Hammond, M. Quero, P. Ivey, D. Miller, R. Purvis, O. McGregor, J. Tan, "Analysis and experimental aspects of the impact of supercooled water droplets into thin water films" AIAA-2005-0077**
8.
9.

---

10. Process Associates of America, "Dimensionless Numbers", http://www.processassociates.com/process/dimen/dn_all.htm
11. Wikipepia, "The free encyclopedia.", Dimensionless numbers, http://en.wikipedia.org/wiki/Dimensionless_number
12. Everthing2, "Dimensionless numbers", http://www.everything2.com/index.pl?node_id=772468
13. ** Jul 04 M. Wu, T. Cubaud, C-M Ho, "Scaling law in liquid drop coalescence driven by surface tension", Phys. Fluids, v16, n7, p L5
14. ** Jan 04 M.P. Fard, N. Ashgriz, J. Mostaghimi, "A Numerical Model for Flow Simulation in Spray Nozzles", AIAA 2004-1156
15. ** Jan 04 R. Domann, Y. Hardalupas, "Break-up Model for Accelerating Liquid Jets", AIAA 2004-1155
16. ** Jan 04 C. Aalburg, K.A. Sallam, G.M. Faeth, "Properties of Non-turbulent Round Liquid Jets in Uniform Cross flows", AIAA 2004-0969
17. ** Jan 04 C.J. Li, T.N. Dinh, T.G. Theofanous, "An Experimental Study of Droplet Break-up in Supersonic Flow: The Effect of Long-Range Interactions", AIAA 2004-968
18. ** Jan 04 K.W. Gwinn, K.E. Metzinger, "Analyses of Foam Impact onto the Columbia Shuttle Wing Leading Edge Panels using Pronto3D/SPH", AIAA 2004-942
19. ** Jan 04 R.J. Flemming, P. Alldridge, R. Doeppner, "Artificial Icing Tests of the S-92A Helicopter in the McKinley Climate Laboratory", AIAA 2004-0737.
20. ** Jan 04 J.D. Bell, "Icing at the McKinley Climate Laboratory: An update of the new icing capability project (end of FY03)", AIAA 2004-0735
21. ** Jan 04 E.F. Emery, Dean Miller, S.R. Plaskon, W. Strapp, L. Lillie, "Ice Particle Impact on Cloud Water Content Instrumentation", AIAA 2004-0731
22. ** Jan 04 C-S. Tan, M. Papadakis, S. Muthuswamy, "Development of a Total Water Content Probe", AIAA 2004-0730
23. ** Jan 04 L.C. Castro Santos, L.T. Neto, R. Papa, G.L. Oliveira, A.B. Jesus, S. Wirogo, " Gridd Sensitivity Effects in Collection Efficiency Computation", AIAA 2004-566
24. ** Jan 04 M. Papadakis, A. Rachman, S-C Wong, H-W Yeong, K. Hung, C. Bidwell, "Water Impingement Experiments on a NACA 23012 Airfoil with Simulated Glace Ice Shapes", AIAA 2004-0565
25. ** Jan 04 C. Bhargava, E. Loth, M. Potapczuk, "Numerical Simulation of Icing Clouds in the NASA Glenn Icing Research Tunnel", AIAA 2004-0563
26. ** Jan 04 R. Purvis, F.T. Smith, "Large Droplet Impact on Water Layers", AIAA 2004-0414
27. ** Jan 04 J-C Tsao, D.N. Anderson, "Additional Study of MVD Effects on Ice Shapes", AIAA 2004-0413
28. ** Jan 04 W.B. Wright, M.G. Potapczuk, "Semi-Empirical Modelling of SLD Physics", AIAA 2004-0412

29. ** **Jan 04** **G. Luxford, D.W. Hammond, P. Ivey, "Role of Droplet Distortion and Break-up in Large Droplet Aircraft Icing", AIAA 2004-0411**
30. ** Jan 04 C-S. Tan, "A Tentative Mass Loss Model for Simulating Water Droplet Splash", AIAA 2004-0410
31. ** Jan 04 D.R. Miller, C.J. Lynch, P.A. Tate, "Overview of High-Speed Close-Up Imaging in an Icing Environment", AIAA 2004-0407
32. ** Jan 04 C.C. Ryerson, R.A.Melloh, G.G. Koenig, "Method of Characterising Cloud Drop Spectra Spatial Variation", AIAA 2004-0230
33. ** Jan 04 A. Brown, A. Nazarov, G. Vertigan, M. Hoog, A. Lenton, "In-Flight Icing Data; Comparison of Tasmania and British Isles/Central France Air Operations Icing Encounters", AIAA 2004-0229
34. ** Jan 04 M. Fregeau, Saed, Paraschivoiu, "Surface Heat Transfer Study for Ice Accretion and Anti-Icing Prediction in Three Dimensions", AIAA 2004-0063
35. ** Jan 04 W.B. Wright, "An Evaluation of Jet Impingement Heat Transfer Correlation for Piccolo Tube Applications", AIAA 2004-0062
36. ** Jan 04 E. Ogretim, W. Huebsch, J. Narramore, "The Effect of Leading-Edge Ice Roughness on Downstream Frost Formation", AIAA 2004-0059
37. ** Jan 04 B.D. Matheis, Rothermayer, "Impact of Surface Roughness on Local Aerodynamics using a Three-Dimensional Navier-Stokes Solver", AIAA 2004-0058
38. ** Jan 04 A.P. Rothmayer, J.A. Krakos, "Residual Droplet Impacts and Thin Film Dynamics", AIAA 2004-0057.
39. ** May 04 P.R. Neal, "Dimensionless Numbers". http://www.ceic.unsw.edu.au/users/peter_neal/downloads/research/nom_dimlessnos.pdf
40. T** Apr 04 Lars Reichelt, "Aerodynamisher Tropfenzerfall bei dieselmortorischen Umgebungsbedingungen", Dissertation, D82(Diss. RWTH Aachen)
41. ** 2004 L. Xu, W. Zhang, S.R. Nagel, "Drop splashing on a dry smooth surface", The James Frank Inst. and Dept of Phys., Uni. of Chicago., SRNagel@uchicago.edu
(1) ** 2004 T. Wriedt, "Piezodropper, Computer controlled Piezoelectric Droplet Generator" 22 July 2004, University of Bremen
42. ** 2004 S.D. Howison, Ockendon, Oliver, Purvis, F. Smith, "Droplet impact on a thin fluid layer", Oxford Univ, Univ Nottingham, Univ College London.
43. ** 2004 M. Hase, Weigand, "Transient heat transfer of deforming droplets at high Reynolds numbers", Int., J. Num. Methods for Heat & Fluid Flow, v14, n1.
44. ** 03-04 L. Reichelt, Renz, "Experimental and num. investigation of the aerodynamic break-up of liquid droplets at diesel engine conditions", Aachen Univ.
45. ** 03-04 T. Berg, J. Deppe, T. Schucht, H. Voges, "Mass Flux Imaging in Sprays", LaVision GmbH, Göttingen, Germany, Info@LaVision.de
46. ** Oct 03 R Schmehl, "Droplet deformation and break-up in technical mixture preparation process", Dept Mech Eng, University of Karlsruche, presentation
47. T** Oct 03 R Schmehl, "Tropfendeformation und Nachzerfall bei der technischen Gemischaufbereitung" , Dept Mech Eng, Univ of Karlsruche, Dissertation
48. ** Jan 03 F. Morency, H. Beaugendre, W.G. Habashi, "Fensap-Ice: A Study of the Effect of Ice Shapes on Droplet Impingement", AIAA 2003-1223.
49. ** Jan 03 R.J. Kind, "Scaling of Icing Tests – A Review of Recent Progress", AIAA 2003-1216
50. ** Jan 03 B. Lu, M.B. Bragg, "Aerofoil Drag Measurement with Simulated Leading-Edge Ice Using the Wake Survey Method", AIAA 2003-1094
51. ** Jan 03 K. Al-Khalil & E. Irani, "Mixed icing simulation and testing at the Cox Icing Wind Tunnel", AIAA 2003-903
52. ** Jan 03 David W. Hammod & Geoffrey Luxford, The Cranfield University Icing Tunnel", AIAA 2003-901
53. ** Jan 03 J. Pan, E. Loth, M.B. Bragg, "RANS Simulation of Airfoils with Ice Shapes", AIAA 2003-729
54. ** Jan 03 A.P. Broeren, M.B. Bragg, "Effect of Airfoil Geometry on Performance with Simulated Intercycle Ice Accretion", AIAA 2003-728
55. ** Jan 03 C. Bernstein, et al, "An inferred climatology of supercooled large droplet icing conditions for North America"., AIAA 2003-563
56. ** Jan 03 M.K. Politovich, Zhang, Vivekanandan, Williams, "Characteristics of clouds containing SLD relevant to icing remote sensing", AIAA 2003-562
57. ** Jan 03 S.C. Tan & M. Papadakis, "General effects of large droplets dynamics on ice accretion modelling", AIAA 2003-392.
58. ** Jan 03 S.C. Tan & P.G. Bartlett, "An experimental study of droplet break-up using a wind tunnel", AIAA 2003-391
59. ** Jan 03 D.N. Anderson & J.C. Tsao, "Additional results of ice-accretion scaling at SLD conditions", AIAA 2003-390

60. ** Jan 03 R.W. Gent, Ford, Moser and Miller "Results from super-cooled large droplet mass loss tests in the ACT Luton Icing Wind tunnel", AIAA 2003-389
61. ** Jan 03 A. Rutkowski, W.B. Wright & Mark Potapczuk, "Numerical study of droplet splashing and re-impingement", AIAA 2003-388
62. ** Jan 03 Thomas H. Bond, Dean Miller, Mark G. Potapczuk, "Overview of SLD engineering tools development", AIAA 2003-386
63. ** Jan 03 T.N. Dinh, G.J. Li & T.G. Theofanous, "An investigation of droplet break-up in a high mach, low Weber number regime", AIAA 2003-317
64. ** 2003 R.S. Subramanian, "Drag on spherical particles and steady settling velocities", http://www.clarkson.edu/subramanian/ch301/notes/dragsphere.pdf
65. ** 2003 J. Keffler, A. Ortega, B. Bouldin, "Experimental Measurements of Boundary Layer Flow with Suction into a Honeycomb Panel", ASME IMECE2003-43336
66. ** 2003 M Cross, T.N. Croft, G. Djambazov, K. Pericleous, " Computational Modelling of Bubbles, Droplets and Particles in Metals Reduction and Refining", 3rd Int Conf on CFD in Minerals and Process Industry, CSIRO, Melbourne, Australia, 10-12 Dec 2003

67. ** 02-03 R Schmehl, "Modelling droplet break-up in complex two-phase flow", Roland.Schmehl@ESA.int, European Space Agency, Noordwijk, Netherlands
68. ** 02-03 S. Markus, U. Fritsching, "Modelling Secondary Break-up of Melts in Sprays"", University Bremen, SFB 372 "Spray Forming", Badgasteiner Straße, 3, 28359 Bremen, Germany.
69. ** 02-03 B. Lehmann, Nobach, Tropea, "Acceleration Measurement Using the Laser Doppler Tech.", Institut für Antriebstechnick, Abteilung Turbulenzforschung, Müller-Breslau-Straße 8, 10623 Berlin.
70. ** 02-03 J. Lacoste, D. Kennaird, S. Begg, M.R. Heikal, "Phase Doppler anemometry measurements of a diesel spray". School of Eng., Uni. Brighton, http://www.sussex.ac.uk/automotive/tvt2002/16_lacoste.pdf
71. ** 02-03 B.J. O'Donnell, B.T. Helenbrook, "Drag On Ellipsoids at Finite Reynolds Numbers", Dept. Mech. & Aero. Eng., Clarkson Univ. Potsdam, NY 13699 http://www.clarkson.edu/mae/faculty/helenbrook.html , Atomization and Sprays, in press, 2004.
72. ** 02-03 M. Dai, H. Wang, J.B. Perot, D.P. Schmidt, "Direct Interface Tracking of Droplet Deformation", Uni. Massachusetts, Dept. Mech Eng.
73. ** 02-03 M. Burger, R. Schmehl, O. Schäfer, R. Koch, S. Wittig, "Numerical study of Strouhal instabilities in two-phase flows", Institut für Thermische Strömungsmaschinen, Universität Karlsruhe.

74. ** Oct 02 S.C. Tan; "Design of a Vertical Tunnel for Large Droplet Dynamic Studies", Nat Inst for Aviation Research report for Cranfield University
75. ** Sep 02 R. Schmehl, "Advanced modelling of droplet deformation and break-up for CFD analysis of mixture preparation.", ILASS-Europe 2002, Saragossa, 9-11 Sep 2002, Roland.Schmehl@ESA.int , http://www.its.uni-karlsruhe.de/~schmehl/presentations/ilass2002_present.pdf
76. Sep 02 Kind, Oleskiw, "Recent Dev. in Scaln. Meths. for Icing Wind Tunl. Test. at Reduced Scale", ICAS 2002-7.3.1, Proc. Int. Cong. Aero. Sci., Toronto
77. ** Aug 02 N. Ross, S.G. Bradley, "Model for optical forward scattering", Applied Optics, v41, n24, p5130-5141
78. Jul 02 M. Nagaoka, "Nonlinear spheroidal oscillating model of a single droplet with aerodynamic force", Jap Soc Mech Eng, Trans B, V66, n647, p271-277
79. ** Jul 02 M. Hase, B. Weigand, "Direct Numerical Simulation of Flow and Heat Trans. of Drop with Transient Deformation due to ... Gas Stream", 5th World Congress on Comp. Mech., Jul 02, Vienna.
80. ** Jul 02 T.J. Kwon & S.D. Heister, "Modelling droplet impact on dry and wet walls", AIAA 2002-4178
81. ** Jun 02 M. Milanez, Naterer, Venn, Richardson, "Eulerian formulatn. for droplet tracking in dispersed phase of turbulent multiphase flow", AIAA 2002-3182
82. ** Jun 02 A.A. Dafa'Alla, "Ice effect on the Aerodynamic Characteristics of Aerofoils", AIAA 2002-3050.
83. ** Jun 02 G.F. Naterer, Popplewell, Barrett, Anderson, Faraci, McCartney, Lehmann, "Experimental Facilities for New Hybrid Ice/Spray Flow Tunnel with Laser Based Drop. Meas.", AIAA 2002-2867
84. *T May 02 Anni Vuorenski, (Cranfield Univ), Simulation of fuel droplet behaviour in and intake manifold. (MSc thesis)
85. jt Apr 02 M. Sommerfeld, "Theoretical and Experimental modelling of particulate flow – Overview and fundamental", lecture series 2000-6, Von Karman Inst.

86. T** Jan 02 Frank Schmelz, “Tropfenzerfall in beshleunigten Gasströmungen”, Dissertation D290, University of Dortmund, 22 January 2002
87. ** Jan 02 C. Presser, J.F. Widmann, P.E. Desjardin, L.A. Gritzo, “Measurement and Numerical Prediction of Homogeneous Turbulent Flow over a Cylinder: A Baseline for Droplet-Laden Flow Studies”, AIAA-2002-0905.
88. ** Jan 02 A.V. Korolev, G.A. Isaac, J.W. Strapp, S.G. Cober, “Observation of drizzle at temperatures below -20C”, AIAA 2002-0678
89. ** Jan 02 B.D. Matheis & A.P. Rothmayer, “Numerical simulation of Thins Air Driven Films”, AIAA 2002-0525
90. ** Jan 02 D.N. Anderson, A. Feo, “Ice-Accretion Scaling using Water-Film Thickness Parameters”, AIAA-2002-0522
91. ** Jan 02 D.N. Anderson, “Preliminary study of Ice-Accretion scaling for SLD conditions”, AIAA 2002-0521
92. ** Jan 02 C. Croce, Beaugendre, Habashi, “FENSAP-Ice Conjugate Heat Transfer Computations with Droplet Impingement and Runback”, AIAA 2002-0386
93. ** Jan 02 J.T. Riley, McDowall, Hughes, Flemming, “A Quantitative Method for Assessing Agreement between Experimental and Calculated Ice Shapes”, AIAA 2002-0384
94. ** Jan 02 C. Aalburg, G.M. Faeth, B. van Leer, “Deformation and Drag Properties of Round Drops Subjected to Shock Wave Disturbances”, AIAA 2002-0341
95. Jan 02 S. Sikalo, et al, “Analysis of impact of droplets on horizontal surfaces”, AIAA, Experimental Thermal and Fluid Science, V25, N7, Jan 02, p503-510.
96. ** 2002 F.J Montes, Galán, Cerro, “Comparison of Theoretical and Experimental Characteristics of Oscillating Bubbles”, Ind. Eng. Chem. Res., v41, p 6235.
97. ** 2002 R. Miller, V.B. Fainerman, A.V. Makievski, M Ferrari, G. Loglio, “Measuring Dynamic Surface Tensions”, Handbook of Applied Surfaces and Colloid Chemistry”, Vol 2, Wiley 2002
98. *B 2002 P.K. Kundu, I.M. Cohen, “Fluid Mechanics”, Academic Press, 2nd edition.
99. * 2002 K. Holmberg, “Handbook of Applied Surface Colloidal Chemistry, Vol 2”, Wiley, Chap 12 measuring Dynamic Surface Tensions
100.** 2002 B.T. Helenbrook, C.F. Edwards, “Quasi-steady deformation and drag of uncontaminated liquid drops”, Int. J. Multiphase Flow, v28, p 1631-1657

101.** Dec 01 X. Li, J.L. Gaddis, T. Wang, “Modelling of Heat Transfer in a Mist/Steam Impinging Jet”, J Heat Trans, V 123, Dec 2001, P 1086
102.** 2001 FLUENT, “Collection Efficiency for Icing Analysis”, Application Brief EX156
103.** Nov 01 FLUENT, “19.4.4 Dynamic Drag Model”, http://www.mech.ed.ac.uk/~george/fluent_docs/fluent6/help/html/ug/node622.htm
104.** Nov 01 FLUENT, “19.4.3 Spray Break-up Models” http://www.mech.ed.ac.uk/~george/fluent_docs/fluent6/help/html/ug/node621.htm
105.** Nov 01 FLUENT, “19.4.2 Droplet Collision Model”, http://www.mech.ed.ac.uk/~george/fluent_docs/fluent6/help/html/ug/node620.htm
106.** Nov 01 FLUENT, “User Guide Bibliography”, http://www.mech.ed.ac.uk/~george/fluent_docs/fluent6/help/html/ug/node1177.htm
107.** Aug 01 F.G. Gregorio, et al, “PIV Investigation on Airfoil with Ice Accretion and Resulting Performance Degradation”, 19th Int Congress of ICIASF 2001, Cleveland USA
108. Jun 01 J. Han & G. Tryggvason, “Secondary break-up of axisymmetric liquid drops: II Impulsive acceleration”, Physics of fluids, v13, n6, AIP, p1554-1565
109.** Jun 01 D.N. Anderson, G.C. Botura, A.P. Broeren, “A study of Scaling for Inter-cycle Ice Accretion Tests”, AIAA-2001-0834
110.** Mar 01 D.R. Secker, P. H. Kaye, “Real-time observation of the change in light scattering for droplets with increasing deformity”, v8, n6, Optics Express 290
111.** Jan 01 F. Morency, G.S. Baruzzi, W.G. Habashi, “FENSAP-ICE: A Comprehensive 3D simulation system for in-flight icing”, AIAA 2001-2566
112. ** Jan 01 R.J. Kind, M.M. Oleskiw, “Experimental Assessment of a Water-Film-Thickness Weber Number for Scaling of Glaze Icing,” AIAA-2001-0836
113. ** Jan 01 R.J. Kind, “Assessment of Importance of Water-Film Parameters for Scaling of Glaze Icing,” AIAA-2001-0835
114. ** Jan 01 D.N. Anderson, G.C. Botura, A.P. Broeren, “A Study of Scaling for Inter-cycle Ice Accretion Tests”, AIAA-2001-0834
115. ** Jan 01 M. Papadakis, B.E.G. Laflin, G.M. Youssef, T.P. Ratvasky, “Aerodynamic Scaling Experiments with Simulated Ice Accretion”, AIAA-2001-0833
116. ** Jan 01 D.N. Anderson, “Acceptable Tolerances for Matching Icing Similarity Parameters in Scaling Applications”, AIAA-2001-0832

117.** Jan 01 D.G. Jackson, Cronin, Severson, Owens, "Ludlam limit considerations of Cyl. Ice Accretion: Aerodynamic and Thermodynamic", AIAA-2001-0679

118.** Jan 01 D. Pokhariyal, M.B. Bragg, T. Hutchingson, J. Merret, "Aircraft Flight Dynamics with Simulated Ice Accretion", AIAA-2001-0541

119.* Jan 01 M.G. Giridharan, D.S. Crocker, J. Widmann, C. Presser, "Issues Related to Spray Combustion Modelling Validation", AIAA 2001-0363

120.** Jan 01 M. M. Oleskiw, F.H. Hyde, P.J. Penna, "In flight icing simulation capabilities of NRC's altitude icing wind tunnel", AIAA 2001-0094

121. Jan 01 C.H. Lee, Reitz, "Effect of Liquid Properties on the Break-up Mechanism of High-Speed Liquid Drops", Atomization and Sprays, V 11, no 1, P 1-19

122.** 2001 S. Hou, D.P. Schmidt, "Modelling Droplet Collision With Adaptive Meshing and Updated Outcomes", Soc Auto Eng.

123.** 2001 C. Braun, U.K. Krieger, "Two-dimensional angular light-scattering in aqueous NaCl single aerosol particles during deliquescence and efflorescence", V8, N6, Optics Express, p314, 12 March 2001.

124.** Dec 00 S. Butson, C. Hadley & S Pratt, "A systematic study of splashes", Instructor Dr Winters. http://courses.ncssm.edu/hsi/class2000/SPLASHES

125.** Jul 00 T. Suzuki, Mitachi, "Experimental Study on Aerodynamic Break-up of Liquid Droplets in Time Dependent Rel. Vel. fields", 8th Int. Conf. Liquid Atomisation and Spray Systems, Pasadena

126.** Jul 00 R. Schmehl, G. Maier & S. Wittig, "CFD analysis of fuel atomization, secondary droplet break-up and spray dispersion in the premix duct of a LPP combustor", 8th Int Conf on Liquid Atomization and Spray Systems, Pasadena, CA.

127.** Jan 00 D.N. Anderson, "Effect of Velocity in Ice Scaling Tests," AIAA-2000-0236

128.** Jan 00 M.R. Archambault, Edwards, "Computation of spray dynamics by direct solution of moment transport equations", AIAA 2000-0197.

129.** Jan 00 M. Gorokhovski, "Stochastic spectral relaxation model of drops break-up in liquid spray computations", AIAA 2000-0193.

130.* Jan 00 P. Hancir, A. Anderson, E. Loth, "Computations of Droplet Distributions in the NASA Icing Research Tunnel", AIAA 2000-0101

131.* Jan 00 M. Papadakis, Hung, Yeong, Bidwell, Breer, "Experimntl. Investigtn. of Water Imping. on Single & Multi-Element Aerofoils", AIAA 2000-0100

132.* Jan 00 S. Lee, H.S. Kim, M.B. Bragg, "Investigation of Factors that Influence Iced-Aerofoil Aerodynamics", AIAA 2000-0099

133.* Jan 00 M. Papadakis, Alansatan, Wong, "Aerodynamic Characteristics of a Symmetric NACA Section with Simulated Ice Shapes", AIAA 2000-0098

134.** 2000 H. Voges, T. Berg, D.Weide, T. Muller, V. Beushausen, S. Kruger, G. Grunefeld, "Spray Imaging System for Quantitative Spray Analysis", 5th ILASS-ASIA, http://www.lavision.de/download/papers/Spray/voges_ilassasia_2000.pdf

135.** 2000 **F. Risso, "The Mechanism of Deformation and Break-up of Drops and Bubbles"**, Multiphase Sci & Tech (0276-1459), v12, p1-50

136.** 2000 M. Rieber, Graf, Hase, Roth, Weigand, "Numerical Simulations of Moving Spherical and Strongly Deformed Droplets", ILASS-Europe 2000

137.** 2000 G. Poots, "Introductory Remarks – Physical aspects of ice and snow accretion on structures", Phil. Trans. R. Soc. A, v358, p 2803-2810

138. 2000 M. Papadakis, K.E. Hung & H.W. Yeong, "Experimental investigation of water impingement on single and multi-element airfoils", AIAA 2000-0100

139.** 2000 L. Makkonen, "Models for the growth of rime, glaze, icicles and wet snow on structures", Phil Trans. R. Soc. Lond. A (2000), v358, p 2913-2939

140.*B 2000 **H. Liu, "Science and Engineering of Droplets – fundamentals and applications"**, www.spraysoft.com, Noyes Publications.

141. 2000 C.H. Lee, Reitz, "An experimental study of the effect of density on the distortion and break-up .. of drops in … gas stream", Int J Multiphase Flow, v26, p229

142. 2000 S. Kumar & E. Loth, "Aerodynamic simulation of airfoils with upper-surface ice shapes." J Aircraft, v38 n2, p285-295.

143.** 2000 T. Gemci, J. Hom, N. Chigier, "Experimental Study of Evaporating Full-Cone Spray by Determining Droplet Temperature with Rainbow Refractometry and Comparing with Numerical Simulation", 8th Int. Conf. on Liquid Atomisation and Spray Systems, Pasadena, CA, USA, July 2000

144.*B 2000 A Frohn & N Roth, "Dynamics of Droplets", Springer-Verlag.

145. 2000 A. Feo, "Icing Scaling with Surface Film Thickness Similarity, for High LWC Conditions" AE/PRO/4420/184/INTA/00, Técnica Aerospatiale, Oct

146.** 2000 Z. Feng, E. Michaelides, "Drag coefficient of viscous drops", Proc IMECE, Nov 5-11, Orlando, Florida, http://www.me.tulane.edu/Faculty/Michaelides/Courses/MCEN632/ASME-paper.doc

147. 2000 Chung, Reehorst, Yung, Potapczuk, Slater, "Navier-Stokes analysis of flowfield characteristics of an ice-contaminated aircraft wing", J Aircraft, 37(6), P 947-959

148. 2000 R.T Bonecaze & W.S. Ryoo, "Deformation of a 3-Dimensional Rising Bubbles", May 4., ChE 385M Surface Phenomena, Dep. Chem. Eng., University Texas http://willson.cm.utexas.edu/Research/Sub_Files/Surface_Phenomena/Spring%202000/DEFORMATION_OF_A_3-DIMENSIONAL_RISING_BUBBLE.pdf

149.** 2000 C.L. Bartley, Martinez, Baron, Secker, Hirst, "Droplet Distortion in Accelerating Flow", J. Aerosol Sci. v31, n12, p1447-1460 (PDF file)

150. 2000 S.K. Aggarwal, G.S. Zhu, "Quasi-Steady High –Pressure Droplet Model for Diesel Sprays", SAE Technical Paper 2000-01-0588.

151. Sep 99 A.A. Fuentes, Bayazitoglu, "Effect of non-spherical shape on oscillatns of levitated droplets", AIAA, J Thermo-phys. & Heat Trans, V13, N3, P384.

152.** Jul 99 C. Crowe, "Modelling fluid-particle flows: Current status and future directions", AIAA 99-3690, 30th Fluid Dynamics Conf, Norfolk VA

153.** Jul 99 F. Schmelz, P. Walzel, "Break-up of Liquid Droplets in Accelerated Gas Flows", ILASS-Europe, Toulouse, July 1999.

154.** Jan 99 G.A. Ruff, "Automated comparison of ice accretion shapes", AIAA-99-0625

155.** Jan 99 K.E. Yeoman, "Shortcomings of the ATR-72 Accident Investigation and disposition of the case", AIAA 99-0495, 37th Aerospace Sci Meet, Reno NV

156.** Jan 99 S.G. Cober, et al, "Measurements of aircraft icing environments which include Supercooled Large Drops (SLD)" , AIAA 99-0494, 37th

157.** Jan 99 G.A. Isaac, Cober, Korolev, Stapp, Tremblay & Marcotte, "Canadian Freezing Drizzle Experiment", AIAA 99-0492

158. ** Jan 99 D.N. Anderson, G.A. Ruff, "Evaluation of Methods to Select Scale Velocities in Icing Scaling Tests", AIAA-99-0244

159. 1999 Z. Zapryanov and S. Tabakova, "Dynamics of bubbles, drops and rigid particles", Kluwer Academic Publishers

160.*B 1999 **W.A. Sirignano, "Fluid Dynamics and Transport of Droplets and Sprays"**, Cambridge University Press.

161.** 1999 W. Samenfink, Elsäßer, Dullenkopf, Wittig, "Droplet interaction with shear-driven liquid films: analysis of deposition and 2ndary droplet characteristics", Int. J. Heat & Fluid Flow, v20, p462

162.T** 1999 G.T. Nöbauer, "Droplet Motion and Break-up", University of Oxford, Keble College Maths Inst, MSc Dissertation.

163.***B 1999** **Y. Nakayama, R.F. Boucher, "Introduction to Fluid Mechanics", Arnold.**

164. 1999 T.G. Myers & D.W. Hammond, "Ice and water film growth from incoming supercooled droplets", Int J Heat Transfer, v42, p2233-2242

165.** 1999 M.R. Maxey, "Examples of fluid-particle interactions in dispersed two-phase flow", AIAA 99-3691, 30th AIAA Fluid Dyn Conf, June-July 99

166. 1999 D.D. Joseph, J. Belanger & G.S. Beavers, "Break-up of a liquid suddenly exposed to a high-speed airstream", In J Multiphase Flow, v25, p1263-1303

167. ** 1999 T.A. Johnson, Patel, "Flow past a sphere up to a Reynolds number of 300", J. Fluid Mech, v378, p 19-70, Printed by Cambridge University Press.

168.** 1999 J. Han, Tryggvason, "Secondary break-up of axisymmetric liquid drops: I Acceleration by constant body force", Physics of Fluids, v11, p3650-3668.

169. 1999 A.A. Dafa'Alla, "Evaluation of AIRUNS2D for high Re flows", Tech rep, BAe Airbus Wing Engr (B61) report B61R/R&D/991002

170. 1999 A.A. Dafa'Alla, "Validation of the unstructured Navier Stokes 2D code, AIRUNS2D, for low speed flows", Tech Rep, BAe Airbus wing Eng (B61) rep B61R/R&D/990563, 1999

171.B 1998 **C.T. Crowe, M. Sommerfield and Y. Tsuji, "Multiphase flows with droplets and particles",** Boca Raton, FL: CRC Press (532.6)

172. 1998 G. Ramachandran, Sreenath, Vincent, "Towards a new method for experimental determination of aerosol sampler aspiration efficiency in small wind tunnels", J Aerosol Sci, v29, n7, p875-891

173. 1998 S.H. Zaidi, Altunbas, Azzopardi, "Study of aerodynamic break-up of liquid drops using laser diffraction", 14th Ann Conf ILASS-Europe, p 60-65

174.** 1998 G.A. Ruff, D.N. Anderson, "Quantification of ice accretion for icing scaling evaluations", AIAA-98-0195, Jan 98, Reno, Nevada.

175. ** 1998 R.J. Kind, M.G. Potapczuk, A. Feo, C. Golia, A.D. Shah, "Experimental and computational simulation of in-flight icing phenomena.". Progress in Aerospace Science, v34 (1998), p 257-345.

176.* 1998 R.W. Johnson, "The Handbook of Fluid Dynamics", Boca Raton: CRC Press, Section 37 Phase Doppler Particle Analyzer.

177. 1998 D. Hammond, "CFD investigation into the influence of simplifying predicted ice-shapes-BAe contribution the 3E's icing harmonisation programme, Task 5", Tech report, BAe Airbus, Systems Eng Rep SDF/B81/A/108/4299_01.

178.** 97-98 K. Su, C.Q. Zhou, "Numerical Study of Spray Parametric effects on Gas Turbine Combustion Performance", Purdue University, Calumet Hammond.

179.** 97-98 W.H. Mason, "Applied Computational Aerodynamics Text/Notes", PDF files CAtxt*.pdf , http://www.aoe.vt.edu/~mason/Mason_f/CAtxtTop.html

180.** 97-98 Q. Liu, Huang, Orme, "Mutual Electrostatic Interactions between Closely Spaced Charged Solder Droplets", Dept. Mech. Eng., Uni. California.

181.** 97 Applied Computational Aerodynamics, CAtxt, Chapter 3. Computer, Codes, and Engineering

182.** 98 Applied Computational Aerodynamics, CAtxt, Chapter 4, Incompressible Potential Flow Using Panel Methods

183.** Jan 97 W.A. Cooper, W.R. Sand, "Threshold Conditions for Ice Accretion", AIAA 97-0307, 35th Aerospace Sci Meet, Reno NV

184.** Jan 97 M.T. Brahimi, Tran, Chocron, Tezok, Paraschivoiu, "Effect of Supercooled Large Droplets on Ice Accretion Characteristics", AIAA 97-0306, 35th Aero. Sci Meet.

185.** Jan 97 R. Ashenden & J. Marwitz, "Turboprop Aircraft Performance Response to various environmental conditions", AIAA 97-0305, 35th A.S.M. Reno NV.

186.** Jan 97 D.E. Cook, "Unusual natural icing encounters during Boeing 777 flight tests", AIAA 97-0304, 35th A.S.M. Reno NV.

187.** Jan 97 G. Mingione, et al, "Ice accretion prediction on multi-element airfoils", AIAA 97-0177, 35th A.S.M. Reno NV

188.** Jan 97 Y. Bourgault, et al, "An Eulerian approach to Supercooled Droplet (SLD) impingement calculations", AIAA 97-0176, 35th A.S.M. Reno NV

189.** Jan 97 W.B. Wright & M.G. Potapczuk, "Comparison of LEWICE 1.6 and LEICE/NS with IRT experimental data from modern airfoil tests", AIAA 97-0175, 35th A.S.M.

190. 1997 S.C. Tan & P.G. Bartlett, "Droplet dynamics, ICECREMO project task 1.3", Contractor report, ICECREMO/TR/CRAN1/JT970531/1

191. *B 1997 **S.S. Sadhal, P.S. Ayyaswamy, J.N. Chung, "Transport Phenomena with Drops and Bubbles"**, Springer-Verlag , New York.

192. 1997 Z. Liu & R.D. Reitz, "An analysis of the distortion and break-up mechanisms of high-speed liquid drops", Int J Multiphase Flow, v23, p631-650

193. 1997 J Hengst, Gent, Hammond, Subert, B. Wagner, "Ice accretion and its effects on aircraft", in "Ice accretion simulation", AGARD Advisory Rep344 of Fluid Dynamics Panel Working Group 20.

194.** 1997 FAA, "FAA In-flight Aircraft Icing Plan", U.S. Dept. of Transportation Federal Aviation Admin. April 1997.

195. 1997 W.H. Chou, Hsiang, Faeth, "Temporal properties of drop break-up in the shear break-up regime", Int J. Multiphase Flow, V23, P 651-669.

196.** 1997 J.D. Bernardin, et al, "Mapping of impact and heat transfer regimes of water drops impinging on a polished surface", J Heat Trans, V40, N2, P247

197. 1997 S. Ainley, et al, "Modelling particle motion in a turbulent air flow", FEDSM 97, ASME, June 22-26.

198. 1997 AGARD, "Ice Accretion Simulation", AGARD-AR-344

199.** 96 - 97 W.B. Wright & M.G. Potapczuk, "Computational Simulation of Large Droplet Icing". NASA Lewis Research Centre

200.** Jul 96 NTSB, "In-Flight Icing Encounter and Loss of Control, Simmons Airlines, d.b.a. American Eagle Flight 4184 Avions de Transport Regional (ATR) Model 72-212, N401AM, Roselawn, Indiana, October 31, 1994; Vol. 1: Safety Board Report AAR-96/01; Vol. II: Draft Response of Bureau Enquetes-Accidents to Safety Board's

201.** Jun 96 S.W.D. Wolfe, Laub; "Low-Disturbance Flow Meas. in the NASA-Ames Laminar Supersonic Wind Tunnel". 19th AIAA Advanced Measurement and Ground Test. Tech. Conf.

202.** Jan 96 D.R. Miller, H.E. Addy Jr, R.F. Ide, "A study of Large Droplet icing accretions in the NASA-Lewis IRT at near-freezing conditions", AIAA 96-0934

203.** Jan 96 M.B. Bragg, "Aircraft aerodynamic effects due to large droplet ice accretions", AIAA 96-0932, 34th A.S.M. Reno NV

204. Jan 96 J. Marwitz, "A forecast and verification experiment for Supercooled Large Drops (SLD)", AIAA 96-0931, 34th A.S.M. Reno NV
205. ** Jan 96 D.C. Anderson, "Evaluation of Constant-Weber-Number Scaling for Icing Tests", AIAA-96-0636
206. ** Jan 96 D.C. Anderson, "Further Evaluation of Traditional Icing Scaling Methods", AIAA-96-0633
207. Jan 96 G.F. Mitchell & Y. Bayazitoglu, "Viscosity measurement of acoustically levitated droplets in air", AIAA-96-0236, 34th A.S.M. Reno NV
208.B* Jan 96 R.L. Panton, "Incompressible Flow", Wiley 2nd Ed.
209. 1996 Z. Zhao, Poulikakis & Fukai, "Heat transfer on fluid dynamics during the collision of a liquid droplet on a substrate ...", Int J Heat Mass Transfer, v39, p2771-2789
210. 1996 T.G. Wang, A.V. Anilkumar & C.P.Lee, "Oscillations of liquid drops: results from USML-1 experiments in space.", J Fluid Mech, V308, P 1-14.
211.** 1996 Maureen L. Tan, "Aircraft Icing", From Engineering Outlook, Fall 1996. Re. Prof Michael Bragg, Dept. Aeronautical Eng., http://www.engr.uiuc.edu
212. 1996 A. Press, "Final report: Icing research", Tech Rep, BAe, SRC Rep JS13633.
213.B 1996 E.J. Lavernia & Y Wu, "Spray Atomization and Deposition", J Wiley, New York
214. 1996 T.A. Kowalewski, "On the separation of droplets from a liquid jet", Fluid Dynamics Res, v17(3), p121-145
215. 1996 S.R. Harris, et al, "Quantitative measurement of internal circulation in droplets using flow tagging velocimetry", AIAA J, v34, p449-454
216. 1996 B.E. Gelfand, "Droplet break-up phenomena in flows with velocity lag", Progress in Energy and Combustion Science, v22, p201-265
217. 1996 J.B. Edson, et al, "Spray Droplet Modelling 2. An interactive Eulerian-Lagrangian model of evaporating spray droplets", J Geophys Res, v101(C1), p1279-1293
218. 1996 G. Brenn, Durst, Tropea, " Monodispersed Sprays for various Purposes – There production and Characteristics", Part. Part. Syst, Charact., v13, p179-185
219.*B 1996 Klaus-Jürgen Bathe, "Finite Element Procedures", Prentice Hall. (P 816)
220.** Sep 95 "Recommended Practice for the Assessment of the Effects of Atmospheric Water .. on .. Performance .. of Gas Turbine Engines", AGARD-AR-332.
221. May 95 W.D. Warnica; "Aerodynamic drag of droplets in turbulent flow fields", Heat & Mass Transfer, vol 21, no 3, pp 266, Elsevier
222. Jan 95 D.N. Anderson, "Methods for Scaling Icing Test Conditions", AIAA-95-0540
223. Jan 95 A.J. Bilanin & D.N. Anderson, "Ice accretion with varying surface tension", AIAA-95-0538, Aerospace Science Meeting & Exhib, 33rd Reno NV
224. 1995 A.L. Yarin & Weiss, "Impact of drops on solid surfaces: self similarity capillary waves and splashing … kinematic discontinuity", J Fluid Mech, v283, p141-173
225. ** 1995 C. Mundo, Somerfeld, Tropea, "Droplet wall collisions: Experimental studies of the deformation and break-up process", In J Multiphase Flow, v21(2), p151-173
226.*B 1995 **S. Middleman, "Modelling Axisymmetric Flows – Dynamics of Films, Jets and Drops"**, Academic Press
227. 1995 P.M. Lovalenti, Brady, "Force on a body in response to an abrupt change in velocity at small but finite Reynolds number", J Fluid Mech, v293, p35
228.*B 1995 **H. Lamb, "Hydrodynamics"**, Cambridge Univ Press 6th Ed. (First published 1879)
229.*B 1995 G.E. Kaye, T.H. Laby, "Table of Physical and Chemical Constants", Longman 16th Edition.
230. 1995 S.C. Kong, Han, Reitz, "The dev. and application of a diesel ignition and combustion model for multidimensional engine simultn", SAE 872089
231.T 1995 S. Jain, "Three-dimensional simulation of turbulent particle dispersion", PhD thesis, University of Utah, Utah, 1995
232. 1995 N. Isshiki, "Theoretical and experimental study on atomization of liquid drop in high-speed gas", Rep. Transportation Tech. Res. Inst. Jpn, No. 35.
233. 1995 S.S. Hwang, Reitz, "A photographic study of the break-up of high-speed vaporizing drops", Proc Int Conf on Liquids Atomization and Spray Systems, ILASS Toy, Michigan, USA, p164-188
234. 1995 L.P. Hsiang & G.M. Faeth, "Drop deformation and break-up due to shock wave and steady disturbances.", Int J Multiphase Flow, v21, n4, p 545-560
235. 1995 J.O. Hinze, "Fundamentals of the hydrodynamic mechanism of splitting in dispersion processes", J.A.I. Chem. E J, v1, n3, p289-295

236. 1995 G.M. Faeth, Hsiang & P-K Wu, "Structure and break-up properties of sprays", Int J Multiphase Flow, v21, suppl issue (1995), p99-127, p545-560 ?

237. *B 1995 E.O. Doebelin, "Engineering Experimentation; planning, execution, reporting", McGraw-Hill

238.** Jun 94 E.H. Trinh, K. Ohsaka, "Measurement of Density, Sound Velocity, Surface Tension, and Viscosity of Freely Suspended Supercooled Liquids", 12th Symp Thermo-phys. Properties, Boulder.

239.** Jun 94 P. Trichet, Lavergne & Biscos, "Amplitude and temporal response of droplets in a turbulent flow field", AIAA 94-3279, 30th AIAA/ASME/SAE/ASEE Conf

240.** Jan 94 M.R,H. Nobari & G. Tryggvason, "Numerical simulations of drop collisions", AIAA 94-0835, 32nd Aerospace Sciences Meeting (A.S.M.) Reno NV

241.** Jan 94 Q. Shi & H. Haj-Hariri, "The effect of convection on the motion of deformable drops", AIAA 94-0834, 32nd A.S.M. Reno NV

242. Jan 94 S.P. Lin, "The break-up of a liquid jet at microgravity", AIAA 94-0833, 32nd Aerospace Sciences Meeting (A.S.M.) Reno NV.

243. ** Jan 94 D.N. Anderson, "Rime-, Mixed-, and Glaze- Ice Evaluation of Three Scaling Laws", AIAA-94-0718

244. 1994 R.D. Cohen, "Effect of viscosity on drop break-up", Int. J. Multiphase Flow, v20, P 211-216

245. 1994 W.D. Warnica, Renksizbulut & Strong "Drag coefficient of spherical liquid droplets, Pt2, Turbulent gaseous fields", Exp Fluids, v18, p265-276

246. * 1994 W. Samenfink, "Secondary break-up of liquid droplets", ICLASS 1994, Rouen, France.

247. 1994 H.A. Stone, "Dynamics of drop deformation and break-up in viscous fluids", Ann Rev Fluid Mech, v26, p65-102

248. 1994 U. Shavit & N. Chigier, "Fractal geometry of liquid jets under break-up", Fractals, v2(2), p277-281

249. 1994 N. Roth, K. Anders & A. Frohn, "Determination of size, evaporation rate and freezing of water droplets using light scattering and radiation pressure", Part Syst Charact, v11, p207-211

250.** 1994 R. Mei, "Flow due to an oscillating sphere and an expression for unsteady drag on the sphere at finite Reynolds no.", J fluid Mech, v270, p133-174

251. 1994 E.E. Michaelides & Feng, "Heat transfer from a rigid sphere in a nonuniform flow and temperature field", Int J Heat Mass Transfer, v37, p2069-2076

252. 1994 R. Mei, "Flow due to and oscillating sphere and an expression for unsteady drag on the sphere at finite Re number", J Fluid Mech, V270, P 110-119

253. 1994 T.A. Kowalewski, D. Bruhn, "Nonlinear Oscillations of Viscous Droplets.", In IPPT PAN, Warszawa 1994, Akiyama, Kleiber, editor, Proc of Japanese-Center. European Workshop of Adv. Comp. in Eng.' Pultusk, pages 63-68

254. 1994 R.J. Haywood, et al, "Transient deformation and evaporation of droplets at intermediate Re numbers", Int J Heat Mass Transfer, v37, n9, p1401-1409

255. 1994 J.B. Edson, et al, "Spray droplet modelling 1. Lagrangian model simulation of turbulent transport of evaporating droplets" J Geophys Res, v101(C1), p1279-1293

256. 1994 J.P. Delplanque, Sirignano, "Boundary layer stripping effects on droplets transcritical convective vaporisation.", Atomization Sprays, V4, P325-349

257. 1994 E.J. Chang, Maxey, "Accelerated Motion of Rigid Spheres in Unsteady Flow at Low to Moderate Re No., Pt 1, Oscillatory", J Fluid Mech, V27

258. 1994 E. Becker, W.J. Hiller & T.A. Kowalewski, " Nonlinear dynamics of viscous droplets.", J Fluid Mech, V 258, P 191-216

259. 1994 S.K. Aslanov & Shamshev, "Theory of drop atomisation in a spray", Phys Doklady, v39(6), p444-446

260.** 93 - 94 S. Eberhardt, Ok, "Aircraft Icing Predictions Using and Efficient Incompressible Navier-Stokes Solver", Dept. Aeronautics, Univ. of Washington.

261.** Jan 93 L.P. Hsiang & G.M. Faeth, "Deformation and secondary break-up of drops", AIAA 93-0814, 31st Aerospace Sciences Meeting, Jan 93, Reno NV

262.** Jan 93 C. Presser & A.K. Gupta, "Behaviour of droplets in pressure-atomized fuel spray", AIAA 93-0132, 31st Aerospace Sciences Meeting, Reno NV

263. 1993 A. Tarnogrodzki, "Theoretical prediction of the critical Weber number", Int. J. Multiphase Flow, v19, n2, p 329-336

264. 1993 W.A. Sirignano, "Fluid dynamics of sprays – 1992 Freeman Scholar Lecture", J Fluid Eng, v115, p345-378

265.*B 1993 J.A. Schetz, "Boundary Layer Analysis", Prentice Hall

266. 1993 N. Roth, Anders, Frohn, "Size and evaporation rate meas. of optically levitated droplets", Proc 3rd Int Congr on Optical Particle Sizing, p371-377
267. 1993 M. Rein, "Phenomena of liquid drop impact on soled and liquid surfaces", Fluid Dyn Res, v12, p61-93
268. 1993 M.R. Maxey, "The equation of motion for a small rigid sphere in a nonuniform or unsteady flow", ASME/FED, Gas-Solid flows, V 166, P 57-62
269.** 1993 M.R. Maxey, "Characteristics of small droplet motion in turbulence", AIAA 93-1877, 29th Joint Propulsion Conf, June 93, Monterey CA.
270. 1993 A.B. Liu, D. Mather & R.D. Reitz, "Modelling the effects of drop drag and break-up on fuel sprays", SAE Tech Paper 930072, SAE 1993
271. 1993 J.M.H. Janssen & Meijer, "Droplet break-up mechanisms: stepwise equilibrium vs. transient dispersion", J Rheology, v37940, p597-608
272. 1993 E.A. Ibrahim, et al, "Modelling of spray droplets deformation and break-up", AIAA J Propul Power, v9, p651-654
273. 1993 L.P. Hsiang & G.M. Faeth, "Drop properties after secondary break-up.", Int J Multiphase Flow, v19, p721-735.
274. 1993 S.P. Fisenko, "Mathematical modelling of heat and mass transfer in transpiration cooling of water droplets ….", J Eng Phys Thermophys, v64(2), p119-123
275. 1993 C.H. Chiang & W.A. Sirignano, "Axisymmetric calculations of three droplet interactions.", Atomization Sprays, V3, P91-107.
276. 1993 S.C. Caruso, "Lewice droplet trajectory calculations on a parallel computer", AIAA-1993-0172 (available at Cranfield)
277. 1993 G. Brenn & A. Frohn, "An experimental method for the investigation of droplet oscillations in a gaseous medium.", Exp Fluids, V 15, P 85-90
278. 1993 L. Bayvel & Zorzechowski, "Liquid Atomization", Taylor & Francis: Washington D.C.
279. fl 1993 L.L. Baxter & J.P. Smith, "Turbulent Dispersion of Particles: The STP Model", Energy and Fuels, v7, p852-859
280.** Jan 92 E. Daniel, Larini, Loraud, Porterie, "A numerical simulation of injection of droplets in a compressible flow", AIAA 92-2929, 31st Aerospace Sciences Meeting.
281. Jan 92 S.R. Mohler, "Comparison of two-dimensional and three-dimensional droplet trajectory calculations in the vicinity of finite wings", AIAA-92-0645
282.** Jan 92 I. Kim, S. Elghobashi & W.A. Sirignano, "Three-dimensional flow computation for two interacting, moving droplets", AIAA 92-0343, 30th Aerospace Sci Meet.
283.** **Feb 92 O.A. Basaran, "Nonlinear Oscillations of Viscous Liquid Drops", J. Fluid Mech. (1992). vol 241, pp 169-198.**
284.T 1992 W.D. Warnica, "Aerodynamics drag of droplets in turbulent flow fields [PhD thesis]", AIAA Technical Lib, Univ Microfilm No. DANN75827. ISBN 0315758279
285.*B 1992 G.F.C. Rogers & Y.R. Mayhew, "Engineering Thermodynamics, Work and Heat Transfer", Longman 4th Edition.
286. 1992 A.M. Podvyotski, Dubrovski, "Experimental study of time-varying aerodynamics break-up of liquid drops …..", Fluid Mech Res, v21(5), p34-38
287. 1992 W.L. Olbricht , Kung, "The deformation and break-up of liquid drops in low Re number flow through a capillary", Phys Fluids A, v4(7), p1347-1354
288. 1992 Q.V. Nguyen & Dunn-Rankin, "Experiments examining drag in linear droplet packets", Exp Fluids, v12, p157-165
289. 1992 R. Mei, Adrian, "Flow past a sphere with an oscillation in the free-stream and unsteady drag at finite Re number", J Fluid Mech, V237, P323-341
290. 1992 I. Kim, Elghobashi, Sirignano, "Three-dimensional flow computation for 2 interacting, moving droplets.", Preprint AIAA 92-0343,
291. 1992 S.K. Mitra, J Brinkman & H.R. Pruppacher, "A wind tunnel study on the drop-to-particle conversion", J Aerosol Sci, v23, n3, p245-256
292. 1992b J.M. MacInnes & F.V. Bracco, "A Stochastic model of turbulent drop dispersion in dilute sprays", ILASS-Europe Conf, Amsterdam.
293. 1992a J.M. MacInnes & F.V. Bracco, "Stochastic Particle Dispersion Modelling and the Tracer-Particle Limit", Phys Fluids A, V4, P2809-2824
294. 1992 A. Li, Ahmadi, "Dispersion and deposition of spherical particles from point sources in turbulent channel flow", Aerosol Science and Tech, v16, p209
295. 1992 H. Hirahara, Kawahashi, " Experimental investig. of viscous effects upon a break-up of drops in high-speed air flow", AIAA Exp Fluids V13, P423.
296. 1992 L.P. Hsiang & G.M. Faeth, "Near-limit deformation and secondary break-up.", Int J Multiphase Flow, v18, n5, p635-652.
297. 1992 Z.T. Deng & S.M. Jeng, "Numerical simulation of droplet deformation in convective flows", AIAA J, v30, n5, p1290-1296
298.*B 1992 R.P. Chhabra & D. De Kee, "Transport processes in bubbles, drops and particles", Hemisphere publishing Corp.

299.* Jun 91 Z.T. Deng & S.M. Jeng, "Numerical Simulation of Non-spherical Droplet Evaporation in Convective Flows", AIAA 27th Joint Prop Conf,

300.** 1991 W.D. Warnica, Van Reenen, Renksizbulut, Strong, "A piezoelectric droplet generator for use in wind tunnels", Dept Mech Eng, Univ Waterloo, Ontario http://scitation.aip.org/getabs/servlet/GetabsServlet?prog=normal&id=RSINAK000062000012003037000001&idtype=cvips&gifs=yes

301. 1991 P.K. Wu, G.A. Ruff, G.M. Faeth, "Primary break-up in liquid/gas mixing layers", Atomisation Sprays, v1, p 421-440

302.*B 1991 F.M. White, "Viscous Fluid Flow", McGraw Hill, New York

303. 1991 A.G. Tomboulides, Orszag & Karniadakis, "Three-dimensional simulation of flow past a sphere", ISOPE Proc, Edinburgh 1991

304. 1991 T.W. Patzek, R.E. Benner, O.A. Basaran & L.E. Scriven, "Nonlinear oscillations of Inviscid free drops.", J Comp Phys, V 97, P 489-515.

305. 1991 R. Mei, Lawrence & Adrian, "Unsteady drag on a sphere at finite Reynolds number with small fluctuations in the free-stream velocity", J Fluid Mech, v233, p613

306. 1991 G.T. Linteris, P.A. Libby & F.A. Williams, "Droplet dynamics in a non-uniform field.", Combust Sci Tech, v80, p319-335

307. 1991 R.J. Lichford & S.M. Jeng, "Efficient statistical transport model for turbulent particle dispersion in sprays", AIAA, J, v29, p1443

308. 1991 N. Chigier, "Optical imaging of sprays", Proc Energy Combust Sci, v17, p211-2662

309. 1991 S. Chandra & Avedisian, "On the collision of a droplet with a solid surface", Proc R Soc Lond A, v432, p13-41.

310. 1991 M.B. Brag & Mohler, "Predicting droplet impingement of yawed wings", J. Aircraft, v29, p964-968

311.** 1991 E. Becker, Hiller & Kowalewski, "Experimental and Theoretical Investigation of Large-Amplitude Oscillations of Liquid Droplets", J Fluid Mech, V231, P189

312. 1991 R.J. Adrian, "Particle imaging techniques for experimental fluid mechanics", Ann Rev Fluid Mechm v23, p261-304

313.* Jul 90 Z.T. Deng & S.M. Jeng, "Numerical Simulation of Droplet Deformation in Convective Flows", AIAA 26th Joint Prop Conf, Orlando. (AIAA-90/2309)

314.** May 90 J.B. Kennedy & Roberts, "Rain Ingestion in a Gas Turbine Engine", P 164, ILASS-Americas, Inst of Liquid Atomisation & Sprays, 4th An Conf, Hartford USA

315.** Apr 90 A. Wierzba, "Deformation and break-up of liquid drops in a gas stream at nearly critical Weber numbers", Exp in Fluids 9, 59-64 (1990)

316. 1990 K. Tsurutani, et al, "Numerical analysis of the deformation process of a droplet impinging upon a wall", JSME Int J, II v33(3), p555-561

317.** 1990 H.A. Stone & L.G. Leal, "The effect of surfactants on drop deformation and break-up", J Fluid Mech, V 220, P 161-186

318.** 1990 E. Hasegawa & M. Saikai, "On the Trajectories of a Small Particle Passing Through a Narrow Curved Channel", JSME, Ser II, Vol 33, No 2

319. 1990 A. Berlemont, Desjonqueres & Gouesbet, "Particle Lagrangian Simulation in Turbulent Flows.", Int J Multiphase Flow, V 16(1), P 19-34

320.B* 1990 A.W. Adamson, "Physical Chemistry of Surfaces", Wiley-Interscience 5th Ed

321.* Jan 89 J. Beck, Lefebvre & Koblish, "Airblast Atomisation at Conditions of Low Air Velocity", AIAA 89-0217, 27th Aerospace Science Meeting.

322. 1989 H.A. Stone & L.G. Leal, "Relaxation and break-up of an initially extended drop in an otherwise quiescent fluid", J Fluid Mech, v198, p399-427

323. 1989 H.A. Stone & Leal, "The influence of initial deformation on drop break-up in subcritical time- dependent flows at low Re no.", J Fluid Mech, v198, p223-263

324.T 1989 M.G. Potapczuk, "Navier Stokes analysis of airfoil with leading edge ice accretion", PhD Dissertation, Univ Arkon, Ohio.

325.*B 1989 B.S. Massey, "Mechanics of Fluids", Chapman Hall 6th Ed, also Van Nostrand (1970) 2nd Ed.

326.*B 1989 **A. H. Lefebvre, "Atomization and Sprays",** Hemisphere Publishing Corp, ISBN: 0891166033,

327. 1989 J. Kitscha & G. Kocamustafaogullari, "Break-up criteria for fluid particles", Int J Multiphase Flow, V15, P573-588

328. 1989 A. Haider & O. Levenspiel, "Drag coefficient and terminal velocity of spherical and nonspherical particles", Powder Technology, v58, p63-70

329.** 1989 D. Dress, "Drag Measurements on a Modified Prolate Spheroid Using a Magnetic Suspension and Balance System", AIAA 1989-0648

330.T fl 1989 L.L. Baxter, "Turbulent Transport of Particles", PhD thesis, Brigham Young University, Provo, Utah.

331.	1989	B. Abramzon, W.A. Sirignano, "Droplet Valorisation Model for Spray Combustion Calculations", Int. J. Mass Transfer, v32(9), p 1605-1618
332.	Sep 88	T.G. Wang (Ed), "Drop and bubbles": Proc 3rd Int Colloquium of Drops and Bubbles, Monterey, California, Conf Proc.
333.**	Jun 88	P.Y.Lian, Eastes & Gharakhari, "Computer Simulation of Drop Deformation and Drop Break-up", AIAA 24th Joint Propulsion Conf, Boston
334.	1988	M. Renksizbulut & R.J. Haywood, "Transient droplet evaporation with variable properties and internal circulation …..", Int J Multiphase Flow, v14, p189-202
335.	1988	A. Wierzba & K. Takayama, "Experimental investigation of the aerodynamic break-up of liquid drops", AIAA J 26, 1328-1335
336.*	1988	H.n. Oguz & S.S. Sadhal, "Effects of soluble and insoluble surfactants on the motion of drops", J Fluid Mech (1988), V 194, P 563-579
337.	1988	J.A. Mulholland, Srivastava & Wendt, "Influence of droplet spacing on drag coefficient in non-evaporating, monodispersed streams", AIAA J, v26,n10, p1231
338.**	1988	M. Strani & F. Sabetta, "Viscous oscillations of a supported drop in and immiscible fluid", J. Fluid Mech (1988) V 189, P 397-421
339.	1988	T.S. Lundgren & N.N. Mansour, "Oscillations of drops in zero gravity with weak viscous effects.", J Fluid Mech, V194, P479-510.
340.	1988	M.M. Clark, "Drop break-up in a turbulent flow – Conception and modelling considerations", Chem Eng Sci, v43, n3, p617-679
341.**	Sep 87	ESDU, "Performance Improvements of Axial Diffusers for Incompressible Flow", ESDU data sheet 87015
342.	1987	J.A. Wesselingh, "The velocity of particles, drops and bubbles", Chem. Eng. Process., v21, p 9-14
343.B*	1987	Hermann Schlichting, "Boundary-Layer Theory", McGraw-Hill, 3rd English Edition, 6th edition of the book, reprint of 1968 edition.
344.	1987	R.D. Reitz, "Mechanisms of atomization processes in high-pressure vaporizing sprays", Atomization & Sprays Technology, v3, p309-337
345.	1987	P.J. O'Rouke, Amsden, "The TAB method of numerical calculation of spray droplet break-up", Soc Automotive Engr (SAE), tech paper 87-2089
346.	1987	D.L. Oliver & J.N. Chung, "Flow about a fluid sphere at low to moderate Reynolds numbers", J Fluid Mech, v 177, p 1-18
347.	1987	M. Pilch, Erdman, "Use of break-up time data and velocity history data to predict the maximum size of stable fragments for acceleration-induced break-up of a liquid drop." Int J Multiphase Flow, V13, n6, P 741-757
348.	1987	R. Natarajan & R.A. Brown, "Third-order resonance effects and the nonlinear stability of drop oscillations.", J Fluid Mech, V 183, P 95-121
349.**	1987	D.E. Fyfe, Oran & Fritts, "Numerical simulation of droplet oscillation, break-up and distortion", 25th Aerospace Sci. Meeting, Reno, AIAA-87-0539
350.**	1987	K.V. Beard, C. Chuang, "A New Model for the Equilibrium Shape of Raindrops", American Metrology Soc., 1 June 1987, p 1509.
351.	1987	B. Abramzon, W.A. Sirignano, "Approximate Theory of a Single Droplet Vaporization in a Convective Field: Effects of Variable Properties, Stefan Flow and Transient Liquid Heating", Proc 2nd ASME, Thermal Eng. Joint Conf., v1.
352.**	Jan 86	S. Malloggi, Tognotti, Zanelli, "An Experimental Study on the Mechanism of Jet Break-up", Proc on sprays and their applications, Dep Energetica-Politecnico
353.	1986	H.A. Stone, Bentley & L.G. Leal, "An experimental study of transient effects in the break-up of viscous drops", J Fluid Mech, v173, p131-158
354.	1986	G.A. Ruff, "Analysis and Verification of the Icing Scaling Equations", AEDC-TR-85-30, v1 (rev), Mar 1986
355.	1986	R.D. Reitz, "Mechanism of break-up of round liquid jets", The Encyclopaedia of Fluid Mech, ed N. Cheremisnoff, v2, p223-249
356.*B	1986	W.H. Press, Flannery, Teukolsky, Vertterling, "Numerical Recipes, The Art of Scientific Computing", Cambridge University Press. 1988 reprint.
357.	1986	R. Natarajan, Brown, "Quadratic resonance in the three-dimensional oscillations of Inviscid drops with surface tension.", Phys Fluids, V29, P 2788.
358.	1986	S.E. Fielding, "Experimental study of water droplets at high speeds and low incidence", RAE report C2450/FR
359.	1986	N.P. Cheremisinoff, "Gas-Liquid flows", in "The Encyclopaedia of Fluid Mechanics", Gulf Publishing, Houston, TX, USA, V3.
360.	1986	B.J. Bentley, Leal, "An experimental investigation of drop deformation and break-up in steady 2D linear flows", J Fluid Mech, v167, p241-283
361.	1985	A. Wierzba, "Break-up of liquid drops in a gas stream", Rep. Inst. Aviation, n 37, Warsaw (Polish).

362.**B*** **1985** **V.L. Streeter, E.B. Wylie, "Fluid Mechanics", McGraw-Hill (Fig 6.11, drag coeffs for spheres and circular disks)**
363.B 1985 R.W. Shellens & Brzustowski, "A prediction of the drop size distribution in a spray from 1st principles", Atomization and Spray Technol, v1, p89-102
364. 1985 J.B. Kennedy, "High Weber number SMD correlations for pressure atomizers", ASME Paper 85-GT-37
365. 1985 A. Ferrenberg, Hunt & Duesberg, "Atomization and Mixing Study", Tech report RI/RD85-312, NAS8-34504, Rocketdyne, Conoga Park, CA.
366.** Jun 84 **R.W. Gent, "Calculation of Water Droplet Trajectories about an Aerofoil in Steady Two-Dimensional Compressible Flow"**, RAE TR 84060
367.* 1984 R.L. Panton, "Incompressible Flow", Wiley-Interscience 1st Ed. Chapter 18, Ideal Flows in a Plane
368.** Jan 83 J.T. Cansdale & R.W. Gent, "Ice Accretion on Aerofoils in Two-Dimensional Compressible Flow – A Theoretical Model", RAE Tech Rep 82128
369.** 1983 J.T. Tsamopoulos & R.A. Brown, "Nonlinear oscillations of Inviscid drops and bubbles", J Fluid Mech, V 127, P 519-537
370.B* 1983 W.S. Janna, "Introduction to Fluid Mechanics", Brook/Cole Engineering Division, (6.3 Drag of Various Three-Dimensional Bodies)
371. 1983 P.H. Gillaspy and T.E. Hoffer, "Experimental measurements of the effect of viscosity on drag for liquid drops", v29, p 229-236
372.** 1982 E. Trinh & T.G. Wang, "Large-amplitude free and driven drop-shape oscillations: experimental observations", J Fluid Mech, V 122, P 315-338
373.** 1982 S. Temkin, H.K. Mehta, "Droplet drag in an accelerating and decelerating flow", J. Fluid Mech, v 116, p 297-313
374. 1982 R.D. Reits & F.V. Bracco, "Mechanism of atomization of a Liquid Jet", Phys Fluids, v26, n10, p1730-1742
375. B 1982 G. Hastroni, "Handbook of multiphase systems", Hemisphere Publishing Corp, McGraw Hill, USA.
376.*B 1982 M. van Dyke, "An Album of Fluid Motion", Parabolic Press.
377. 1982 J.N. Chung, "The motion of particles inside a droplet.", J Heat Trans, V 104, P 438-445.
378. 1982 P.O. Brunn, "Heat and Mass Transfer from Single Spheres in Low Reynolds Number Flow.", Int J Eng Sci, V20, P817-822.
379. * 1982 M.B. Bragg, "A Similarity Analysis of the Droplet Trajectory Equation", AIAA82-4285, v 20, n 12, Dec 1982
380. 1982 M.B. Bragg, "Rime ice accretion and its effect on airfoil performance: final report", NASA/CR-165599
381. 1981 C.D. Stow & Hadfield, "An experimental investigation of fluid flow resulting from the impact of a water drop with .. surface", Proc R Soc Lon A, v373, p419-441
382. 1981 J.M. Rallison, "A numerical study of the deformation and burst of a viscous drop in general shear flows", J Fluid Mech, v109, p465-482
383.T 1981 P.J. O'Rourke, "Collective drop effects on vaporizing liquid sprays", PhD thesis, Princeton, New Jersey.
384.** 1981 M.O. McKinney & J. Scheiman, "Evaluation of Turbulence Reduction Devices for the Langley 8-Foot Transonic Pressure Tunnel", NASA Tech Memo 81792
385. jt 1981 C.W. Hirt & B.D. Nicholls, "Volume of Fluid method for dynamic free boundary", J Comput Phys, v39, 1981.
386. 1981 A. Borisov, B. Gel'fand, M. Natanzon & O. Kossor, "Droplet break-up regimes and criteria for their existence", J Engrg Phys, v40(1), p44-49, AIAA-90-2309
387.** 1980 S. Temkin, S.S. Kim, "Droplet motion induced by weak shock waves", J. Fluid Mech. v96, n1, p 138-157
388. 1980 J.M. Rallison, "Note on the time-dependent deformation of a viscous drop which is almost spherical", J Fluid Mech, v98, p625-633
389. 1980 A. Prosperetti, "Normal-mode for the oscillations of a viscous liquid drop in a immiscible liquid.", J Mech, V19, P149-182
390. 1980 A. Prosperetti, "Free oscillations of drops and bubbles: the initial value problem.", J Fluid Mech, V 100, P 333-347.
391. 1980 P.L. Marston, "Shape oscillation and static deformation of drops and bubbles driven by modulated radiation stress – theory.", J Acoust Am, V 67, P 15-26
392. 1980 P.L. Marston & Apfel, "Quadrupole resonance of drops driven by modulated acoustic radiation pressure: experimental properties.", J Acoust Soc Am, V67, P27-37
393. 1980 S.A. Krzeczkowski, "Measurement of liquid droplet disintegration mechanism.", Int J. Multiphase Flow, v6, p227-239
394. *B 1980 H.G.Jerrard, D.B. McNeil, "A Dictionary of Scientific Units, including dimensionless numbers and scales.", Chapman Hall 4th edition.

395. 1980 L.S. Christensen & S.L. Steely, "Monodispersed atomizers for agricultural aviation applications", NASA CR 159777

396. 1979 S.E. Hinkle, "Water drop kinetic energy and momentum measurement considerations", Appl Eng Agric, v5, p386-391

397. 1978 S.K. Karanfilian & T.J. Kotas, "Drag on a sphere in unsteady motion in a liquid at rest", J Fluid Mech, v87, p88-96

398.*B 1978 **R. Clift & J.R. Grace, M.E. Weber "Bubbles, Drops and Particles", Technical report, Academic Press, New York, 1978 (532.6)**

399. 1978 J.R. Grace, Wairegi, Brophy, "Break-up of drops in stagnant media.", Canadian J Ch Engng, V56, P3-8.

400. 1978 C. Armand, F. Charpin, G. Fasso, G. Leclere, "Techniques and Facilities at ONERA Modane Centre for Icing Tests", Appendix to Paper No. 6 in AGARD Advisory Report No. 127, Nov. 1978. (flowfield and droplet-trajectory similarity – scaling)

401. 1977 C.D. Stow & Stainer, "The physical products of a splashing water drop", J Meteorol Soc Jpn, v55, p518-532

402. 1977 M.P. Anisimova & Stekol'shchikov, "Deformational break-up of drops in a gas stream", Power-Eng, Academy of Sciences of the USSR, Vol 15, No 3, p 126-133

403. 1976 S.C. Yao & Schrock, "Heat and mass transfer from freely falling drop", Trans ASMW J Heat Transfer, v98(1), p120-126

404. 1976 V.Y. Rivkind & G.M. Ryskin, "Flow structure in motion of a spherical drop in a fluid medium at intermediate Re no." Proc Acad Sci USSR Mech Fluid, v11, p5

405.** Jun 74 ESDU, "Performance in Incompressible Flow of Plane-Walled Diffusers with Single-Plane Expansion", ESDU data sheet 74015.

406.* Mar 74 J.A. Albers & E.J. Feldman, "Boundary-Layer Analysis of Subsonic Inlet Diffuser Geometries for Engine Nacelles", NASA TN D-7520.

407. *B 1974 E.S. Taylor, "Dimensional analysis for engineers", Clarendon Press, Oxford.

408. ** 1974 M.S. Plesset, C.G. Whipple, "Viscous effects in Rayleigh-Taylor instability.", Phys Fluids, v17, n1, p1, Jan 1974.

409. 1974 H.K. Hendriksen, Ostergaard, "On the mechanism of break-up of large bubbles in liquids in three-phase fluidized beds.", Chem Engng, V29, P 626

410. 1974 B.D. Fishburn, "Boundary layer stripping of liquid drops fragmented by Taylor instability", Acta Astronautica, v1, p1267-1284

411. 1974 R. Clift, J.R. Grace & M.E. Weber, "Stability of bubbles in fluidised beds", Ind Engng Chem Fumd, V 13, P 45-51.

412. 1974 C.T. Alonso, "The dynamics of colliding and oscillating drops.", Proc Int Colloq on drops and bubbles, V1, P139, Jet propulsion lab, Pasadena, CA.

413. 1973 M.N. Topp, "Ultrasonic atomization – a photographic study of the mechanism of disintegration", J. Aerosol Sci, v4(1), p17-25

414. 1973 M. Sevik & S.H. Park, "The splitting of drops and bubbles by turbulent fluid flow", J Fluid Eng, v95, p53-60

415. 1973 G.B. Foote, "A numerical method for studying simple drop behaviour: simple oscillation.", J Comp Phys

416. 1973 R. Clift & J.R. Grace, "The mechanisms of bubble break-up in fluidized beds.", Ind Engng Chem Fumd, V27, P2309-2310

417. 1973 D. Bradley, "On the atomization of liquids by high-velocity gases", J Phys D, Appl Phys, v6, p1724-1736

418. * Oct 72 M.J. Green, Nachtsheim, "Numerical Meth. for the Solution of Large Systems of Diff. Equations of the Boundary Layer Type", NASA TN D-7068

419. ** Oct 72 P.G. Simpkins & E.L. Bales, "Water-drop response to sudden accelerations", J Fluid Mech, vol 55, n4, p629-639

420. ** 1972 S.A. Morsi & A.J. Alexander; "An investigation of particle trajectories in two-phase flow systems", J Fluid Mech , V55, n2, P193-208

421. ** 1972 E.Y. Harper, G.W. Grube, I-Dee Chang, "On the break-up of accelerating liquid drops.", J. Fluid Mech. (1972), v52, pt 3, p 565-591.

422. 1972 B.P. Le Clair, Hamielec, "A theoretical and experiment. study of the internal circulation in water drops falling …. in air", J Atmos Sci, v29, n2, p728

423. 1971 P.G. Simpkins, "On the distortion and break-up of suddenly accelerated droplets", AIAA paper, AIAA-71/325.

424. ** 1971 P.G. Simpkins, "Non-Linear Response of Deforming Drops", Nature Physical Science , v 233, 13 Sept 1971

425. 1971 Z. Levin, Hobbs, "Splashing of water drops on solid and wetted surfaces: Hydrodynamics and charge separation", Phil Trans R Soc Lond A, v269, p555-585

426. 1971 J.D. Klett, "On the break-up of water drops in air", J Atmos Sci, V 28,, P 646-647

427.*B	1971	B.J. Brinkworth, “An Introduction to Experimentation”, The English University Press
428.	1970	H.R. Pruppacher & K.V. Beard, “A wind tunnel investigation of the internal circulation and shape of water drops falling at terminal velocity in air”, Quart J Royal Meteor Soc, v 96, p247-256, 1970
429.	1969	A.A. Ranger & J.A. Nicholls, “Aerodynamic shattering of liquid drops.”, AIAA J. V7(2), p71-97, or p285-290.
430.*	1969	“SAE Aerospace Applied Thermodynamics Manual”, 2nd Ed, By SAE Committee AC-9, Aircraft Environmental Systems. From Soc of Automotive Eng, Inc.
431. jt	1969	G.J. Parker & E. Bruen, “The collision of drops with dry and wet surfaces in air atmosphere”, Proc Inst Mech Eng (Lond), v184, paper 23, p1969-
432.**	1968	J.H. Neilson, Gilchrist, “An analysis and experimental investigation of the velocities of particles entrained by the gas flow in nozzles”, J. Fluid Mech, v33, n1, p131
433.	1968	J.F. Harpel & D.W. More, “The motion of a spherical liquid drop at high Reynolds number.”, J Fluid Mech, v32, n2, p367-391
434.	1968	V.G. Fornes, “A literature review and discussion of liquid particle break-up in gas streams.”, Tech Rep NWC-TP-4589, Naval Weapons Center, China Lake, CA
435.	1968	C. Miller & L.E. Scriven, “The oscillations of a fluid droplet immersed in another fluid.”, J Fluid Mech, V32, P417-435
436.*B	1967	G.F.C. Rogers & Y.R. Mayhew, “Engineering Thermodynamics, Work and Heat Transfer”, Longman 2nd Ed.
437.	1967	F.H. Harlow & J.P. Shannon, “The splash of a liquid drop”, J Appl Phys, v38(10), p3855-3866
438.	1967	C.T. Crowe, “Drag coefficient of particles in a rocket nozzle”, AIAA J, v5, p1021-1022
439.	1967	W.R. Cotton & N.R. Gokhale, “Collision, coalescence and break-up of large water drops in a vertical wind tunnel”, J Geophys, v72, n16, p4041-4049
440.B	1967	R.A. Brodkey, “The phenomena of fluid motions”, Addison-Wesley, Reading, MMA, USA
441.**	Jun 66,	R.A. Dickerson & T.A. Coultas, “Break-up of Droplets in an Acceleration Gas Flow”, AIAA 2nd Propulsion Conf.
442.	1966	G. Vali & E.J. Stanburg, “Time-dependant characteristics of the heterogeneous nucleation of ice”, Can J Phys, v44, p477-502
443.	1965	R.S. Valentine, N.F. Sather & W.J. Heideger, “The motion of drops in viscous media”, Chem Engng Sci, v20, p719-728
444. jt	1965	F.H. Harlow, Welch, “Numerical calculation of time-dependent viscous incompressible flows of fluid with free surface”, Phys Fluids, v8, p2182
445.**	May 64,	D.C. Jenkins & J.D. Booker, “The Time Required for High Speed Airstreams to Disintegrate Water Drops”, RAE Technical Note Mech. 401
446.**	Apr 64	H.E. Wolfe, Anderson, “Kinetic Mechanism and … Droplet Sizes of Aerodynamic Break-up of Liquid Drops”, US Army Chem. Centre, Rep. 0395-04(18)SP, AD-437340, Aerojet report
447.**	1964	W.J. Scott, “Studies of liquid droplets released from aircraft into vertical and horizontal airstreams”, Nat. Research Labs (Can) Rep LR-415, Nov 64
448.	1964	F. Odar & W.S. Hamilton, “Forces on a sphere accelerating in a viscous fluid”, J Fluid Mech, v18, p302-314
449.	1964	M. Komabayashi, Gonda & Isono, “Life time of water drops before breaking and size distribution of fragments droplets.”, J Met Soc Japan, V 42, P 330-340
450.	1964	F.C. Haas, “Stability of droplets suddenly exposed to a high velocity gas stream.”, AIChE J, v10, p920-924
451.B*	1964	N.A. Fuchs, R.E. Daisley, M. Fuchs, C.N. Davies, “The Mechanics of Aerosols”, Pergamon Press 1964, Revised and Enlarged Edition.
452.	1964	D.J. Carlson & Hoglund, “Particle drag and heat transfer in rocket nozzles”, AIAA J 2, 1980-1984
453.	1964	A.A. Buzukov, “The break-up of drops and a fluid stream by air shock wave”, Tech Rep FTD-TT-63-839, AD-435996, J Appl Mech Tech Phys, Rus.
454.	1964	R.C. Amsden, “Factors affecting the application of low-volume sprays”, J Roy Aeronautical Soc, v68, n 644, p535-539, Aug 64
455.*B	1963	A.M. Worthington, “A study of splashes”, Macmillan, New York
456.*B	1963	L. Rosenhead (Editor), “Laminar Boundary Layers”, Dover Publications.
457.	1963	G.I. Taylor, “The shape and acceleration of a drop in a high-speed airstream”, The Scientific Paper of G.I. Taylor, ed G.K. Batchelor, Vol III, Camb Univ Press.

458. ** 1963 A.R. Hanson, E.G. Domich & H.S. Adams, "Shock-tube investigation of break-up of drops by air blasts.", Phys Fluids, v6, n8, p1070-1080.

459. 1962 C.A. Sleicher, "Maximum drop size in turbulent flow", AIChE J, v8, p471-477

460.***B 1961 V.L. Streeter, "Handbook of Fluid Dynamics", McGraw-Hill, 1st edition.**

461.** **Dec 61, J. Maybank & G.K. Briosi, "A Vertical Wind Tunnel", Suffield Technical Paper No. 202, DRB project no.D52-95-10-07**

462. Mar 60 E.A. Rabin, Schallenmuller & Lawhead, "Displacement and shattering of propellant droplets, final report", Washington DC, US Air force Office of Scientific Research, AFOSR TR 60-75

463.*B 1960 D.C. Ipsen, "Units, Dimensions and Dimensionless Numbers", McGraw-Hill

464. 1960 W.A. Reid, "The oscillation of a viscous liquid drop", Quart Appl Math, v18, p86-89.

465.** Mar 59 E. Rabin & R. Lawhead, "The Motion and Shattering of Burning and Non-Burning Propellant Droplets", Rocketdyne report R-1503.

466. 1959 P. Krishna, et al., "Fall of liquid drop in water, drag coefficients, peak velocities and maximum drop sizes.", J Chem Engng Data, V 4, P 340-343.

467. 1959 D.G. Gordon, "Mechanism and speed of break-up of drops", J Appl Phys, v30, n11, p1759

468.*B 1959 H. Glauert, "Elements of Aerofoil and Airscrew Theory", Camb Univ Press, 2nd Ed.

469. 1959 S. Chandrasekhar, "The oscillations of a viscous liquid globe.", Proc Lond Math Soc, V 9, P141-149.

470.*B 1959 I.H. Abbott & A. E. von Doenhoff, "Theory of Wing Sections", Dover Publications

471.B* 1958 S.F. Hoerner, "Fluid-Dynamic Drag, practical information on Aerodynamic drag and hydrodynamic resistance", published by author.

472.** 1958 N. Tetervin, "Theoretical Distribution of Laminar-Boundary-Layer Thickness, Boundary-Layer Reynolds Number and Stability Limit, and Roughness Reynolds Number for a Sphere and Disk in Incompressible Flow", NACA Tech. Note 4350, Sept 58. Langley Aero. Labs.

473. 1957 P. Savic & G.T. Bolt, "The fluid flow associated with the impact of liquid drops with solid surfaces", Proc Heat Transfer Mech Inst, p43-84

474. ** 1956 R.H. Magarvey & B.W. Taylor, "Free fall break-up of larger drops", J Applied Phys, v27, n10, p1129-1135, Oct 56.

475.*B 1956 W.R. Lane & H.L. Green, "The mechanics of drops and bubbles", Survey in Mechanics, Edited by G.K. Batchelor & R.M. Davies, Camb Univ Press.

476.** 1956 R.D. Ingebo, "Drag Coefficient for Droplets and Solid Spheres in Clouds Accelerating in Airstreams". NACA TN3762, Sept 1956

477. 1955 S. Hu & R.G. Kinter, "The fall of single liquid drops through water.", AIChE J, V 1, P43-49

478. 1955 J.O. Hinze, "Fundamentals of the hydrodynamic mechanism of splitting in dispersion processes", A.I.Ch.E. Journal, v1,n3, p289-295

479. 1955 O.G. Engel, "Water drop collisions with solid surfaces", J Res Nat Bur Stand, v54(5), p281-298

480.*B 1954 W.H. McAdams, "Heat Transmission", McGraw-Hill., 3rd Edition.

481.*B 1953 A.H. Shapiro, "The Dynamics and Thermodynamics of Compressible Fluid Flow", Volume 1, The Ronald Press Co.

482. 1952 W.E. Ranz & W.R. Marshall, "Evaporation from drops", Chem Eng Prog, v48, p141-146 & p173-180

483. * 1952 H. Kober, "Dictionary of Conformal Representations", Dover Publications.

484. 1951 G.D. Kinzer & R. Gunn, "The evaporation and thermal relaxation of freely falling water drops", J Metrology, v8, n2, p71-83

485. ** 1951 W.R. Lane, "Shatter of drops in streams of air.", Indust. Engng. Chem, v43, n6, p1312-1317.

486. ** 1950 G. Taylor, "The instability of liquid surfaces when accelerated in a direction perpendicular to their planes", Proc. Roy. Soc., Series A, v201, p192

487. 1950 D.J. Kewis, "The instability of liquid surfaces when accelerated in a direction perpendicular to their planes", Proc R Soc Lond A, v202(1068), p81-96

488. 1949 A.N. Kologorov, "The break-up of droplets in a turbulent stream", Doklady Akademia Nayk SSSR, v66, p825-828

489. **1949** **W.R. Gunn & G.D. Kinzer, "The terminal velocity of fall for water droplets in stagnant air", J Meteorology, v6, p243-248, Aug 49**
490.** 1949 J.O. Hinze, "Critical speeds and sizes of liquid globules", Appl Sci Res A, v1(4), p273-288
491. 1948 M.S. Volynski, "On the break-up of droplets in air streams", Doklady Akad. Nauk SSSR v 62, p 301-304 (Russian)
492. ** 1948 J.O. Hinze, "Forced Deformations of Viscous Liquid Globules", Appl Sci Res A1, v1(4), p263-272
493. 1948 D.C. Blanchard, General Electric Research Lab., Schenectady (Project Cirrus, Occasional Report N 7, 1948), 13pp. (free-fall drop size)
494. ** 1947 A.C. Merrington and E.G. Richardson, "The Break-up of Liquid Jets", Proc Phys Soc, v59, n331, p1, Jan 1947
495. 1940 C.E. Lapple, C.B. Shepherd, Ind. Eng. Chem. v 32, p 005-617. (Standard drag curve for rigid spheres)
496. 1936 J.L. Shereshefsky & Steckler, "A study of the evaporation of small drops and of the relationship between surface tension and curvature", J Chem Phys v4, n2, p108
497. 1936 W.V. Ohnesorge, "Formation of drops by nozzles and the break-up of liquid jets",, Z. Angew Math Mech, v16, p355-358
498. 1936 W.V. Ohnesorge, "Die bildung von tropfen aus dusen deim zerfall flussiger strahlen", Angew Math Mech, v16, p355-358
499. 1932,45 H. Lamb, "Hydrodynamics".
500. 1931 R.A. Castleman, "Mechanism of atomization of liquids", Technical report, U.S. Nat Bureau Std, J Res.
501. ** 1930 L.F.G. Simmons, N.S. Dewey, "Wind Tunnel Experiments with Circular Discs", report no. 1334, Air Ministry HMSO. T.2919.
502.** Sep 27 A Fage, F.C. Johanson, "The Flow of Air behind and Inclined Flat Plate of Infinite Span", Proc Roy Soc, v116, n773, p170, www.jstor.org
503. ** Jul 26 A Fage, F.C. Johanson, "The Flow of Air and of an Inviscid Fluid around and Elliptic Cylinder and an Aerofoil of Infinite Span, Especially in the Region of the Forward Stagnation Point". Roy Soc Trans. Vol 227, Reports and Memoranda No. 1097. http://www.jstor.org/
504. 1924 ME. Muller, "Math-Naturew, klasse, Abt. Ua, 133
505. ** 1922 W. Margoulis, "Joukowski Wings", From L'Aeronautique, Aug 21; NACA TM 78.
506. 1914 E. Buckingham, "On physically similar systems; illustrations of the use of dimensional equations.", Physics Review, v 4, p 347-376.
507. 1904 P. Lenard, Meteorol Z, v21, p 248-262 (1904)
508. 1900 M.S. Allen, Philos. Mag., v50, p 323-338, 519-534 (early drag data for spheres)

509. 1879 Rayleigh, "On the capillary phenomena of jets.", Proc R Soc Lond, V 29, P71-97
510. 1878 Rayleigh, "On the instability of jets", Proc London Math Soc, v10, p4-13

End